Electromagnetic Multipolarity of Gamma-Rays and Properties of Neutron-Rich, Deformed Fission Fragments

By

Jonathan Mark Eldridge

Dissertation

Submitted to the Faculty of the

Graduate School of Vanderbilt University

in partial fulfillment of the requirements

for the degree of

DOCTOR OF PHILOSOPHY

in

Physics

May 8, 2020

Nashville, Tennessee

Approved:

Professor Joseph Hamilton, Ph.D.

Professor Akunuri Ramayya, Ph.D.

Professor Sait Umar, Ph.D.

Professor David Ernst, Ph.D.

Professor Erika Grundstrom, Ph.D.

TABLE OF CONTENTS

Page

LIST OF TABLES iv

LIST OF FIGURES vi

Chapter

1. Introduction: The Fundamentals of Nuclear Physics 1

Types of Nuclear Decay 4
β-Decay 5
γ-Decay 8
Multipole Radiation and Magnetic Properties of Nuclei 9
Reduced Transition Probabilities 11
Internal Conversion 14
Fission 17
Nuclear Models Describing Excited State Properties 22
The Shell Model 24
The Collective Model 27
Rotational Bands 27
Vibrational States 28

2. Experimental Methods 30

The Gammasphere 30
Coincidence Analysis with Gammasphere 30
Integral Perturbed Angular Correlation Method with Gammasphere 32
LeRIBSS at HRIBF 35

3. Mixing Ratios of γ-Band to Yrast-Band Transitions 37

g-Factors of 2^+ excited states 37
Measured E2/M1 Mixing Ratios 40
Isotopes of Mo 40
^{102}Mo 45
^{104}Mo 50
^{106}Mo 54
^{108}Mo 57
Isotopes of Ru 58
^{108}Ru 58
^{110}Ru 63
^{112}Ru 64

Isotopes of Pd 66
^{112}Pd 69
^{114}Pd 70
^{116}Pd 71
Discussion: Trends in the Mixing Ratios 72

4. The β-decay of ^{164}Eu 75

Spectra, Coincidence Analysis, and Common Contaminants 75
Details on the intensity measurements of transitions observed in ^{164}Gd 83
Lifetime Measurements 87
Discussion 90

5. Structure of Midshell, $A \sim 150 - 170$, Rare ^{252}Cf Fission Fragments 98

^{164}Gd 98
^{163}Gd 104
^{155}Nd 108
^{159}Eu and ^{89}Br 117
Other Nuclei 119

Appendix

A. PSM and TPSM calculations for ^{163,164}Gd 120

B. Correction for Isomer Lifetime in Intensities Measured from β-Gated Singles 123

C. The Efficiency Functions For the β-decay Data 126

Singles (Primary) Efficiency Function 126
Gated Efficiency 129

BIBLIOGRAPHY 137

LIST OF TABLES

Table Page

1.1 Table of allowed and forbidden transitions in β-decay 8

1.2 Correction factors for $B(E2)$ values based on mixing of γ, β, and ground state properties 14

3.1 g-Factors measured in this work for first 2^+ excited states 38

3.2 Angular correlations measured for ^{102,104}Mo 42

3.3 Angular correlations measured for ^{106,108}Mo 43

3.4 Mixing ratios measured in this work for the isotopes of Mo 44

3.5 Angular correlations measured for isotopes of Ru. 60

3.6 Mixing ratios measured in this work for the isotopes of Ru 61

3.7 Angular correlations measured for isotopes of Pd. 65

3.8 Mixing ratios measured for isotopes of Pd 67

4.1 Levels and γ-rays in ^{164}Gd from the β-decay of ^{164}Eu 77

4.2 Internal conversion measurements for $\sim$61 keV transition 86

4.3 Level γ-feeding vs outflow for ^{164}Gd from the β-decay of ^{164}Eu 92

4.4 Reduced transition probability ratios of transitions in ^{164}Gd 95

4.5 Approximate, experimental γ-ground and γ-β mixing values found for several isotopes of Gd 96

5.1 Levels and γ-rays in ^{164}Gd from the spontaneous fission of ^{252}Cf 103

5.2 A list of levels and γ-rays observed for ^{163}Gd in the SF of ^{252}Cf 106

5.3 γ-Rays and levels observed in this work for ^{155}Nd 112

C.1 Raw data provided for the energy-dependant efficiency of the LeRIBSS. 127

C.2 Efficiency values compared to those generated by equation C.1. 127

C.3 Efficiency values compared to those generated by equation C.3. 128
C.4 Test peaks used to determine the magnitude of the discrepancy between gated and singles efficiencies 132
C.5 Comparison between gated and singles efficiencies 133

LIST OF FIGURES

Figure Page

1.1 First 2^+ excited state energies of nuclei in the $A \approx 160$ midshell region 3

1.2 Internal conversion coefficients vs. energy 16

1.3 Spontaneous fission potential energy surface for ^{252}Cf 20

1.4 Nilsson orbitals 26

2.1 Uncertainty in G_k values as a function of ϕ 34

2.2 A schematic of HRIBF 35

3.1 The $4_g^+ \rightarrow 2_g^+ \rightarrow 0_g^+$ correlations measured in this work 39

3.2 Partial Level Schemes of the Isotopes of Mo considered in this work 41

3.3 Angular correlations measured for ^{102}Mo 42

3.4 Mixing ratio ovals confirming the spin of the 1244.9 keV level in ^{102}Mo. 45

3.5 The $2_\gamma^+ \rightarrow 2_g^+ \rightarrow 0_g^+$ correlations measured in this work 47

3.6 The $3_\gamma^+ \rightarrow 2_g^+ \rightarrow 0_g^+$ correlations measured in this work 48

3.7 The $4_\gamma^+ \rightarrow 4_g^+ \rightarrow 2_g^+$ correlations measured in this work 49

3.8 Angular correlations measured for ^{104}Mo 50

3.9 The $5_\gamma^+ \rightarrow 4_g^+ \rightarrow 2_g^+$ correlations measured in this work 51

3.10 The $7_\gamma^+ \rightarrow 6_g^+ \rightarrow 4_g^+$ correlations measured in this work 52

3.11 The $9_\gamma^+ \rightarrow 8_g^+ \rightarrow 6_g^+$ correlation measured in this work for ^{104}Mo 53

3.12 Angular correlations measured for ^{106}Mo 55

3.13 The $6_\gamma^+ \rightarrow 6_g^+ \rightarrow 4_g^+$ correlation measured in this work for ^{106}Mo 56

3.14 Angular correlations measured for ^{108}Mo 57

3.15 Partial Level Schemes of the isotopes of Ru considered in this work 59

3.16 Angular correlations measured for ^{108}Ru 62

3.17 Angular correlations measured for ^{110}Ru 63

3.18 Angular correlations measured for ^{112}Ru 66
3.19 The partial level schemes of the isotopes of Pd considered in this work. 68
3.20 Angular correlations measured for ^{112}Pd 69
3.21 Angular correlations measured for ^{114}Pd 70
3.22 Angular correlations measured for ^{116}Pd 71
3.23 Plot of mixing ratios measured in this work compared with Walter Greiner's theory 73

4.1 The level scheme of ^{164}Gd as seen by the β-decay of ^{164}Eu 76
4.2 Singles and β-gated singles spectra from the ^{164}Eu β-decay data 78
4.3 Gates on the 169 and 854 keV transitions from the ^{164}Eu β decay data 80
4.4 A comparison of the singles spectra from both the $A = 164$ and $A = 165$ β-decay data 84
4.5 Isomer lifetime decay measurement 88
4.6 Measurement of ^{164}Eu β-decay half-life 91

5.1 The level scheme of ^{164}Gd as seen in the SF of ^{252}Cf 99
5.2 Gates on 1455.1/168.6 and 1455.1/667.1 keV in Cf data 100
5.3 Gates on 168.6/854.9/43.1 and 73.0/43.1/962.4 keV in Cf data 101
5.4 Systematics for γ-vibrational bands in isotopes of Gd. 105
5.5 The level scheme of ^{163}Gd as observed in this work 107
5.6 A double gate on 704.1/863.6 keV from ^{86}Se 109
5.7 The level scheme of ^{155}Nd as found in this work 110
5.8 Systematics of bands across ^{153,155}Nd, and ^{155,157}Sm 113
5.9 Nd-Sr Yields Curves 115
5.10 Double gate on 836.7/1308.7 keV from ^{94}Sr 116
5.11 Triple gates for ^{155}Nd 118

A.1 Calculated energy levels for ^{164}Gd compared with experimental levels 121

A.2 Calculated energy levels for ^{163}Gd compared with experimental levels 121

C.1 A comparison of the singles γ-ray spectra from each clover 129

Chapter 1

Introduction: The Fundamentals of Nuclear Physics

The study of nuclear physics is important in the understanding of the fundamentals of creation. An atomic nucleus is a unique proving ground for Quantum Mechanics, where too few particles are present for statistical methods to work but yet too many particles for exact/analytical solutions to the Schrödinger (or Dirac) equation to exist. Furthermore, little is known about the form of the strong force, the strongest of the four fundamental forces, which underpins the forces binding positively charged protons together with neutrons, overpowering the Electromagnetic force, that would normally repel them. As for the neutron-rich nuclei studied in this work, many questions still remain about the r-process, believed to be the explanation of the distribution of nuclei we see in nature today, as well as the happenings inside a nuclear reactor. Because the nucleus is too complex to be solved easily, theorists need data to which they can compare their theories. This dissertation seeks to provide a small sliver of these data, thus further enabling future work both in experiment and theory towards answering these fundamental questions.

Beyond these general considerations, a number of more specific motivations underline the work discussed in this dissertation. Chapter 3 will discuss *multipole mixing ratios* – or the ratio of the probability of a state emitting radiation of one multipolarity over another – for transitions from γ-vibrational bands to the ground state bands of several nuclei. Because γ-vibrational-bands are a type of quadrupole vibration, γ-rays emitted when a nucleus decays from the γ-band to the yrast band is expected to be pure quadrupole, as will be explained in section 1.2.2.2. Previous work by Goodin [1] has called this prediction into question for some transitions in ^{102,104,106,108}Mo, ^{108,110,112}Ru, and ^{112,114,116}Pd. This work will seek to correct Goodin's measurements and to establish, by γ-γ angular correlation studies, that this E2 prediction is correct in these 10 isotopes.

Furthermore, while the absolute sign of the mixing ratios is a matter of convention (as will be explained in section 1.1.2.1), a change in the sign from one nucleus to another can be indicative of a change in nuclear shape since the mixing ratio is proportional to the quadrupole operator. Chapter 3 will also seek to confirm the prediction by Krane [2] that such a shape change should occur at around ^{110,112}Ru, being observable by a sign change in the mixing ratios.

Questions have been raised recently concerning deformation in the region between the nuclear magic numbers (see section 1.2.1) $N = 82$ and $N = 126$ and between $Z = 50$ and $Z = 82$. One expects, by a simple or naive approximation, that the nucleus at the exact center of this region at $N = 104$ and $Z = 66$, or ^{170}Dy, would be the most deformed. However, by the best measurements of deformity available currently – first 2^+ excited states of even-even nuclei – the $Z = 60$ (Nd) chain appears to have the greatest deformation. This effect is shown in figure 1.1. This work, in chapters 4 and 5, will seek to provide data on nuclei in this region, so that theorists may produce better models by which to solve this puzzle of an apparent 6 proton shift in maximum deformity from the expectation.

However, before any of these the experimental results can be discussed, some theoretical context is required to make sense of the results presented in later chapters of this work. In nuclear physics (similar for other quantum regimes), a single nucleus will have a fixed probability per unit time of decaying from one state to a lower energy state. This means that for a large collection of nuclei, the number of nuclei that will decay per unit time is proportional to the total number of nuclei present;

$$\frac{\partial N}{\partial t} = -\lambda N \tag{1.1}$$

The solution to this differential equation is the well known exponential decay law;

$$N(t) = N_0 e^{-\lambda t} \tag{1.2}$$

Figure 1.1: A plot showing the variation of known first 2^+ excited state energies in the region around ^{164}Gd, and other isotopes studied in this work. Because lower first 2^+ excited state energy is an indicator of higher deformation, one can clearly see the $N = 100$ up-tick for several nuclei, and the unexpected minimum of the $_{60}$Nd chain, rather than the $_{66}$Dy chain. However, the expected $N = 104$ 2^+ energies are a minimum for the $_{66}$Dy, $_{68}$Er, $_{70}$Yb, and $_{72}$Hf chains.

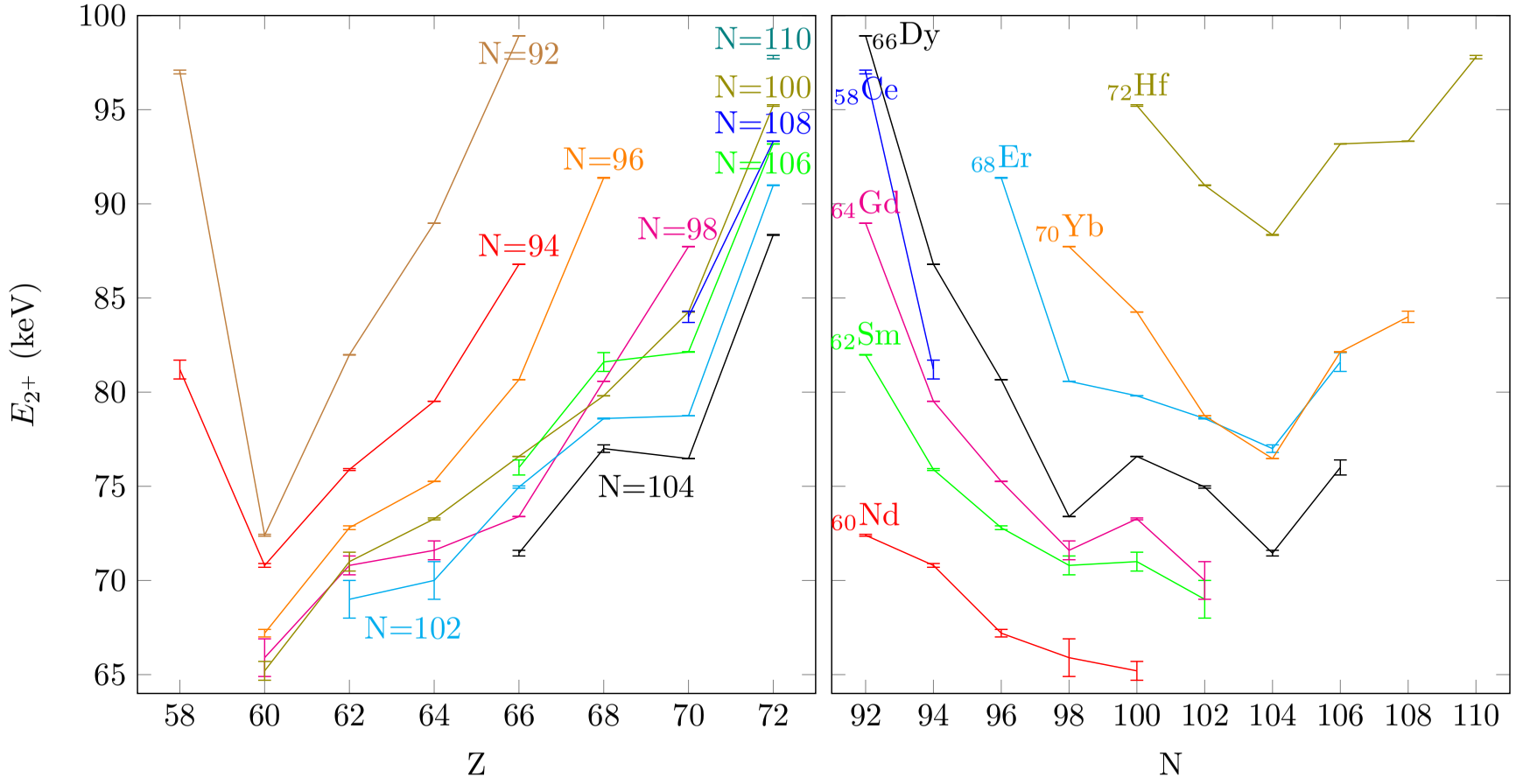

where $N(t)$ is the number of parent nuclei at time t, N_0 is the number of parent nuclei at $t = 0$, and λ is known as the decay constant and has units of $[time]^{-1}$. A more physically useful number is the nuclear lifetime, τ, or the average time it takes for a single nucleus to decay. While λ and τ are mathematically convenient, it is traditional to speak of nuclear half-lives, $t_{1/2}$, or the time it takes for half the nuclei to decay (i.e. $N(t_{1/2}) = \frac{1}{2}N_0$). From these definitions it should be obvious that

$$\lambda = \frac{1}{\tau} = \frac{\ln 2}{t_{1/2}} \tag{1.3}$$

Furthermore, if a nucleus is being produced at a rate, P, then equation 1.1 becomes

$$\frac{\partial N}{\partial t} = P - \lambda N \tag{1.4}$$

for which the solution – if we assume P is constant – is

$$N(t) = \frac{P}{\lambda}\left(1 - e^{-\lambda t}\right) + N_0 e^{-\lambda t} \tag{1.5}$$

Normally, in a case of production, $N_0 = 0$, thus (in terms of τ);

$$N(t) = P\tau\left(1 - e^{-t/\tau}\right) \tag{1.6}$$

If P is not constant, then the solutions to equation 1.4 depend on the form of $P(t)$. In all cases considered in this work, P can be assumed or approximated to be constant.

1.1 Types of Nuclear Decay

There are three primary modes of decay for a nucleus, traditionally known as α, β, and γ decay. Alpha decay typically occurs in heavy nuclei, and consists of the emission of a ^{4}He, nucleus;

$${}^{A}_{Z}X_N \rightarrow {}^{A-4}_{Z-2}X'_{N-2} + {}^{4}_{2}\mathrm{He}_2 + \text{energy} \tag{1.7}$$

where ${}^{A}_{Z}X_{N}$ is an arbitrary isotope of an element consisting of Z protons, N neutrons, and $Z+N=A$ total nucleons. Beta decay occurs for nuclei that have too many neutrons resulting in a neutron changing into a proton by emission of an electron and an anti-electron-neutrino;

$$ {}^{A}_{Z}X_{N} \rightarrow {}^{A}_{Z+1}X'_{N-1} + \mathrm{e}^{-} + \bar{\nu}_{e} + \text{energy} \tag{1.8} $$

Gamma decay occurs when a nucleus, being in an excited state (often denoted by *), emits a photon;

$$ {}^{A}_{Z}X^{*}_{N} \rightarrow {}^{A}_{Z}X_{N} + {}^{0}_{0}\gamma_{0} \tag{1.9} $$

In addition to these three primary modes, nuclei may also decay by spontaneous fission (SF), internal conversion (IC), positron emission (β^{+}), orbital electron capture (EC), neutron emission, proton emission, pair production, and cluster emission. Furthermore, a nucleus may be caused to decay by external stimuli in processes such as neutrino absorption, neutron (or otherwise) induced fission, and inverse internal conversion[1]. Only β-decay, γ-decay, IC, SF, and proton induced fission are relevant to this work. Extensive details for all of these decay modes, as well as others not listed here, can be found in most introductory nuclear physics textbooks, such as Yang and Hamilton [4] or Krane [5].

1.1.1 β-Decay

As noted with equation 1.8, β-decay occurs when a neutron changes into a proton by emission of an electron and an anti-electron neutrino. As with all physical processes, energy must be conserved during β-decay. In nuclear physics, the mass of a nucleus is less than the sum of the masses of the individual nucleons. This mass difference, in accordance with Einsteins famous equation of mass energy equivalence,

$$ E = mc^{2} \tag{1.10} $$

[1] only recently observed experimentally; see Chiara *et al.* [3].

is the energy of the strong interaction binding the nucleons together, better known as the binding energy, B. Because of its mathematical convenience, it is common to work in terms of the "mass excess" of the nucleus, $\Delta(A,Z)$, defined as the difference in energy between the mass energy equivalence of A atomic mass units[2] and the actual mass of the atom, including electrons;

$$\Delta(A,Z) = [M(A,Z) - A \times (1\text{ u})]\,c^2 \tag{1.11}$$

Where M is the mass of an atom, including electrons. Thus it can be shown that for energy to be conserved in β-decay, the total energy shared among the electron, neutrino, and the daughter nucleus must be

$$\begin{aligned} Q_\beta &= [m(A,Z) - (m(A,Z+1) + m_e)]\,c^2 \\ &= [M(A,Z) - M(A,Z+1)]\,c^2 \\ &= \Delta(A,Z) - \Delta(A,Z+1) \end{aligned} \tag{1.12}$$

where m represents the mass of a nucleus (without electrons) and m_e is the mass of an electron. Tables of experimental values of Δ for all known nuclei can be found in Yang and Hamilton [4] and many other sources.

The decay energy (Q_β), colloquially called the Q-value, is very important in the study of β-decay. In fact, many times a measurement of the Q-value of a particular β-decay is used to measure the mass of the parent nucleus, and other important related quantities. However, in this present work, the most important use of Q_β is the constraint it places on what excited states could be populated in the daughter nucleus. As stated above, Q_β is split between four sources, the kinetic energy of the electron, neutrino, and daughter, plus the excitation of the daughter. Thus, the excitation of the daughter, in which this work is most interested, should always be less than Q_β.

[2] An atomic mass unit is defined such that ^{12}C (including electrons) has a mass of exactly 12 u. Thus $\Delta(12,6) = 0$, for ^{12}C.

However, a better constraint comes not from the energetics of β-decay, but from the relationship between the spin and parity of the parent nucleus and the excited and ground states of the daughter. Since angular momentum (spin) must be conserved, the sum of the angular momenta of the daughter, electron, and neutrino must add up to the spin of the parent. Since the electron and neutrino are both spin 1/2 particles with odd wave functions (such particles are called Fermions), the total angular momentum carried away by them can be either 1 or 0, when the spin of the electron and the neutrino are aligned or anti-aligned, respectively This means that β-decay can only populate levels whose spin is 0 or 1 $\hbar$ different from that of the parent nucleus, with no parity change.

However, experiments observe β decays with and without parity changes and spin changes of 2 or more. This is because the above analysis assumes that the nucleus is a point particle, when in fact it is not. If the electron or the neutrino is emitted tangential to the nucleus, then it will have orbital angular momentum in addition to its spin, allowing both its spin and parity to change by greater amounts. For historic reasons, nuclear physicists call β-decay transitions with 0 or 1 spin change and no parity change "allowed" and assign degrees of "forbiddenness" to other transitions, as shown in table 1.1. Furthermore, certain β-decays are considered superallowed. This occurs when the parent and daughter states involved are nearly identical, such as in "mirror nuclei" where Z,N of the parent equals N,Z of the daughter. Superallowed β-decay have no direct bearing on this work and won't be discussed further.

In principal, in most β-decay experiments, one should expect to see all allowed β-transitions that are also allowed according to the Q-value as well as many first forbidden decays. By contrast, unless one has absurdly amazing statistics and low background, no second or higher order forbiddenness should be observed. The $\log ft$ values, known as comparative half lives, shown in table 1.1 are a direct measure of how probable a β-decay transition is, since t is simply the specific half life for a transition, and f effectively removes some of the physical distinctions between levels, allowing the value of ft to be more use-

Table 1.1: Table of allowed and forbidden transitions in β-decay. Shown is a quick reference, showing the spin and parity changes for each label, with an approximate $\log_{10} ft$ range, indicating how likely the β-transition is to occur.

Forbiddenness	ΔJ	$\Delta\pi$	$\log_{10} ft$
Superallowed	0	no	$\sim 3-4$
Allowed	0,1	no	$\sim 4-6$
First Forbidden	0,1,2	yes	$\sim 5-10$
Second Forbidden	1,2,3	no	$\sim 11-14$
Third Forbidden	2,3,4	yes	$\sim 17-19$

fully compared. Typically, f and t are difficult to independently measure, and can range in orders of magnitude as widely as half lives can, thus it is customary to report $\log_{10} ft$. Now f is defined as,

$$f = \int_1^{T_0} T(T^2-1)^{1/2}(T_0-T)^2 F(Z,T)\, dT \tag{1.13}$$

where T is the kinetic energy of the electron emitted, T_0 is the combined energy of the electron and neutrino (i.e. Q_β minus excitation of the daughter), and F is known as the Fermi function and is defined as

$$F(Z,T) = \frac{\xi}{1-\exp(-\xi)} \tag{1.14}$$

where

$$\xi = \pm \frac{Ze^2}{\hbar v} \tag{1.15}$$

for $\beta^{\mp}$ decay, with e and v being the charge and velocity of the electron, respectively.

1.1.2 γ-Decay

The study of γ-rays emitted by an excited nucleus has long been a valuable tool in the study of nuclear structure. Indeed, nearly all of the experimental data discussed in this work comes from the direct observations of γ-rays, or photons, emitted from nuclei. From

the measured properties of these massless emissaries of the nuclear world, many properties of the nuclei that emitted them may be determined.

1.1.2.1 Multipole Radiation and Magnetic Properties of Nuclei

In particular the *multipole mixing ratios* of a γ-ray can give much information about the spins and parities (J^{π}) of nuclear energy levels. When a nucleus decays from an excited state, in order for angular momentum to be conserved, the multipole order of the γ-ray, L, must be

$$|J_i - J_f| \leq L \leq J_i + J_f \tag{1.16}$$

where J_i and J_f are the spins of the initial and final nuclear states, respectively. In practice, for a given γ-ray transition, only the lowest two multipolarities allowed by equation 1.16 are seen. Additionally, parity must also be conserved in any electromagnetic nuclear decay producing additional selection rules. Electric radiation of multipolarity L has parity $\pi_E = (-1)^L$ while magnetic radiation has parity $\pi_M = (-1)^{L+1}$. In this work, the multipolarity of a γ-ray is denoted by ΠL, where $\Pi = E$, for electric transitions or M for magnetic transitions, and L is the multipole order. By using these selection rules, a γ-decay from a 2^+ state into a 1^+ state permits $M1$, $E2$, or $M3$ radiation but only the $M1$ and $E2$ components are ever observed experimentally.

In principal, the lowest two multipole orders for any given transition may compete, making it convenient to define a mixing ratio $\delta(\Pi(L+1)/\Pi' L)$ (where Π and Π' must be different) such that

$$\delta^2(\Pi(L+1)/\Pi' L) = \frac{P(\Pi(L+1))}{P(\Pi' L)} \tag{1.17}$$

where $P(\Pi L)$ represents the probability of the γ-ray to be emitted having multipolarity ΠL. Because electric multipole radiation is strongly favored over its magnetic counterpart, $M(L+1)/EL$ mixtures are extremely rare and it can nearly always be assumed that

$\delta^2(M(L+1)/EL) = 0$. The Krane-Steffen convention for the sign of the mixing ratio [6] has been used in this work.

Walter Greiner, in a 1966 paper [7] produced a theory exploring the consequences of differing proton and neutron deformation parameters, resulting from differing proton and neutron pairing forces. This theory allows one to calculate mixing ratios for primarily rotational nuclei by

$$\left(\frac{\delta}{E}\right)_{J_i \to J_f} = \left(8.6 \times 10^{-6} \frac{\beta_p^2 (1-0.72\beta_p)^2}{f^2(1-2f)^2} A^{\frac{10}{3}} \times \frac{\langle J_f 0, 22 | J_i 2 \rangle^2}{\langle J_f 1, 11 | J_i 2 \rangle^2} \frac{1}{J_f(J_f+1)}\right)^{1/2} MeV^{-1} \tag{1.18}$$

and for $2^+_\gamma \to 2^+_g$ transitions in primarily vibrational nuclei;

$$\left(\frac{\delta}{E}\right)_{2^+_\gamma \to 2^+} = 8.6 \times 10^{-4} \frac{A^{5/3}\beta_0}{(1-2f)f} \tag{1.19}$$

where f is a quadrupole correction factor defined by

$$f = \frac{\beta_2 - \beta_p}{\beta_2} = 1 - \frac{A}{N\frac{\beta_n}{\beta_p} + Z} \tag{1.20}$$

In these eqs., β_2, β_p, and β_n are the nuclear, proton, and neutron quadrupole deformations, respectively, β_0 is an effective, or mean, deformation factor for a vibrating nucleus, and $\langle j_1 m_1, j_2 m_2 | jm \rangle$ is a Clebsch-Gordan coefficient. In this work, we have made the simplifying assumption that $\beta_0 = \beta_2$. The various deformation parameters discussed in equations 1.18 through 1.20 are related by

$$\beta_2 = \frac{N\beta_n + Z\beta_p}{A} \tag{1.21}$$

and

$$\frac{\beta_p}{\beta_n} = \sqrt{\frac{G_n}{G_p}} \tag{1.22}$$

where G_n and G_p are proton and neutron pairing forces, respectively. According to Dudek *et al.* [8], these pairing forces can be found by;

$$G_p = \frac{17.90 + 0.176(N-Z)}{A} \tag{1.23}$$

$$G_n = \frac{18.95 - 0.078(N-Z)}{A} \tag{1.24}$$

It is worth noting that these values are from fits of nuclei in the rare earth region and tend to predict slightly lower values than actual for lighter nuclei. However, as will be discussed in section 3.2.4, the pairing forces of Dudek *et al.* [8], when used in Greiner's theory, reasonably predict some of the mixing ratios measured in this work. It should be noted, however, that Greiner's theory predicts only the magnitude of the mixing ratios, not their sign. For a better understanding of deformation, see section 1.2, below.

1.1.2.2 Reduced Transition Probabilities

The probability per unit time, λ, that a nucleus will undergo a certain transition from state $|J_i\rangle$ to state $|J_f\rangle$ by emitting a photon of energy E and angular momentum L, with either magnetic ($\Pi = M$) or electric ($\Pi = E$) qualities is

$$\lambda(\Pi L; J_i \to J_f) = \frac{8\pi(L+1)}{L((2L+1)!!)^2}\frac{1}{\hbar}\left(\frac{E}{\hbar c}\right)^{2L+1}\left|\left\langle J_f\left|\hat{O}(\Pi L)\right|J_i\right\rangle\right|^2 \tag{1.25}$$

where $\hat{O}$ is the multipole transition operator, and $x!! \equiv 1 \times 3 \times 5 \times \cdots \times x$ is a double factorial. This λ is the same as defined in equation 1.3. It is common to define a reduced transition probability, $B(\Pi L; J_i \to J_f)$, that is independent of energy, and only depends on the nuclear properties of the two states involved. When this is done, equation 1.25 becomes

$$\lambda(\Pi L; J_i \to J_f) = \frac{8\pi(L+1)}{L((2L+1)!!)^2}\frac{1}{\hbar}\left(\frac{E}{\hbar c}\right)^{2L+1} B(\Pi L; J_i \to J_f) \tag{1.26}$$

Greater detail on the derivation of equations 1.25 and 1.26 can be found in Eisenberg and Greiner [9].

The experimental techniques discussed in this work are incapable of directly measuring $B(\Pi L)$ values. However, the ratios of such values for transitions from the same state are still useful. In general when multiple transitions de-excite the same nuclear state, their measured intensities, I, will be proportional to their respective transition probabilities, T. Thus we can use equation 1.26 to find a general relationship between the reduced transition probabilities and measured intensities of transitions from the same state;

$$\frac{B(\Pi_1 L_1; J_i \rightarrow J_f)}{B(\Pi_2 L_2; J_i \rightarrow J'_f)} = \frac{(L_2+1)L_1((2L_1+1)!!)^2}{(L_1+1)L_2((2L_2+1)!!)^2}(\hbar c)^{2(L_1-L_2)}\frac{I_1 E_2^{2L_2+1}}{I_2 E_1^{2L_1+1}} \tag{1.27}$$

In most cases $\Pi_1 L_1 = \Pi_2 L_2 \equiv \Pi L$, and thus

$$\frac{B(\Pi L; J_i \rightarrow J_f)}{B(\Pi L; J_i \rightarrow J'_f)} = \frac{I_1 E_2^{2L+1}}{I_2 E_1^{2L+1}} \tag{1.28}$$

which is an elegantly simple equation useful for calculating experimental $B(\Pi L)$ ratios.

Furthermore, for collective states, especially those involving quadrupole vibrations, the ratio of $B(EL)$ values for transitions out of the same state can be calculated simply by the ratio of the square of Clebsch Gordon Coeficients;

$$\frac{B(EL : J_i \rightarrow J_f)}{B(EL : J_i \rightarrow J'_f)} = \frac{\langle J_i K_i, L\Delta K | J_f K_f \rangle^2}{\langle J_i K_i, L\Delta K' | J'_f K'_f \rangle^2} \tag{1.29}$$

Where K is the projection of the nuclear spin on the nuclear axis of symetry (usually the same as the spin of the bandhead), and $\Delta K = K_f - K_i$. Equation 1.29 allows one to calculate what are known as Alaga rules which are useful tools giving a first order approximation for $B(E2)$ ratios, and can be very powerful for identifying the K values for various band structures seen in data, thus aiding in the assignment of observed bands with different structure properties. In our case, it will be used for transitions into the ground state band

($K = 0$) from newly discovered bands, to assist in their identification. A deeper discussion of Alaga rules can be found in Casten [10].

Equation 1.29 assumes that the properties of the collective bands it connects are unmixed. This assumption is rarely valid for β- and γ-vibrational bands, meaning that the experimental $B(E2)$ ratios rarely match equation 1.29. We can define γ-ground, β-ground, and γ-β mixing parameters respectively as

$$\begin{aligned} Z_\gamma &\equiv \sqrt{24}\varepsilon_\gamma \left(\frac{\langle 00|\hat{O}(E2)|00\rangle}{\langle 12|\hat{O}(E2)|00\rangle} \right) \\ Z_\beta &\equiv 2\varepsilon_\beta \left(\frac{\langle 00|\hat{O}(E2)|00\rangle}{\langle 10|\hat{O}(E2)|00\rangle} \right) \\ Z_{\beta\gamma} &\equiv \sqrt{6}\varepsilon_{\beta\gamma} \left(\frac{\langle 12|\hat{O}(E2)|00\rangle}{\langle 10|\hat{O}(E2)|00\rangle} \right) \end{aligned} \tag{1.30}$$

where $|nK\rangle$ is the band head of a band consisting of n quadrupole phonons with a projection K of the spin on the symmetry axis, and the ε_i are constants dependent on the nuclear moment of inertia and the exact form of the Hamiltonian. The effect of this mixing can be found as a multiplicative correction to the $B(E2)$ values found by equation 1.29 by

$$B(E2;J_i \to J_f) = B_0(E2;J_i \to J_f)\left[1 + Z_\gamma F_\gamma(J_i,J_f) + Z_{\beta\gamma}F_{\beta\gamma}(J_i,J_f)\right]^2 \tag{1.31}$$

where $B_0(E2)$ is the unmixed $B(E2)$ (as given by equation 1.29) and

$$\begin{aligned} F_\gamma(J_i,J_f) &= \frac{1}{\sqrt{24}}\left(f_\gamma(J_f)\frac{\langle J_i 2, 20|J_f 2\rangle}{\langle J_i 2, 2-2|J_f 0\rangle} - \frac{1}{2}\left(1+(-1)^{J_i}\right) f_\gamma(J_i)\frac{\langle J_i 0, 20|J_f 0\rangle}{\langle J_i 2, 2-2|J_f 0\rangle} \right) \\ F_{\beta\gamma}(J_i,J_f) &= \frac{1}{2}\left(1+(-1)^{J_i}\right)\frac{f_\gamma(J_i)}{\sqrt{6}}\frac{\langle J_i 0, 20|J_f 0\rangle}{\langle J_i 2, 2-2|J_f 0\rangle} \end{aligned} \tag{1.32}$$

with $f_\gamma(J) \equiv \sqrt{J(J-1)(J+1)(J+2)}$. Equations 1.31 and 1.32 result in relatively simple corrections to theoritical $B(E2)$ values as tabulated in table 1.2. These results (equations 1.31 and 1.32 and table 1.2) are specifically for γ-band to ground state band transitions.

Table 1.2: Correction Factors for $B(E2)$ values based on equations 1.31 and 1.32. The correction factors listed here are only valid for γ-band to ground state band transitions. Z_γ and $Z_{\beta\gamma}$ are defined in equation 1.30. These correction factors first appeard in Lipas [11], though this work uses the sign conventions of Riedinger [12] and Marshalek [13].

J_i	J_f	$\frac{B(E2;J_i\to J_f)}{B_0(E2;J_i\to J_f)}$
$J-2$	J	$\left[1+(2J+1)Z_\gamma+J(J-14)Z_{\beta\gamma}\right]^2$
$J-1$	J	$\left[1+(J+2)Z_\gamma\right]^2$
J	J	$\left[1+2Z_\gamma-\frac{1}{3}J(J+1)Z_{\beta\gamma}\right]^2$
$J+1$	J	$\left[1-(J-1)Z_\gamma\right]^2$
$J+2$	J	$\left[1-(2J+1)Z_\gamma+(J+1)(J+2)Z_{\beta\gamma}\right]^2$

For more information on this theory, including its application to β-band to ground band transitions, see Lipas [11], Riedinger [12], and Marshalek [13]. More recent theories, such as described in Gupta [14], still explain deviations from the Alaga rules in terms of mixing between the β-, γ-, and yrast-bands, but tend to rely on complex computer codes which are beyond the scope of this work.

1.1.3 Internal Conversion

Not only, as in equation 1.9, can a nucleus decay from an excited state by γ-emission, but it can also decay by a process known as internal conversion (IC).[3] IC occurs when the nucleus gives energy directly to one of the most bound atomic electrons orbiting the nucleus. This does not occur by γ emission that is then absorbed by the orbital electron, but rather occurs by a direct electromagnetic interaction (by virtual photon) occurring when the wave functions of the electron and nucleus overlap, which is why the most bound electrons are the most likely to be internally converted.

Because IC usually occurs when γ-decay is also possible, it is useful to define an internal conversion coefficient, α (or ICC), which is characteristic of any transition within a

[3]Technically a nucleus can undergo α-, β-, Fission, and other kinds of decay from excited states, but I'm speaking here of decays where A, N, and Z of the parent remain unchanged by the decay.

nucleus's structure;

$$\alpha = \frac{I_{IC}}{I_\gamma} \tag{1.33}$$

where I_{IC} is the measured intensity of IC electrons and I_γ is the measured intensity of γ-rays emitted. In the experiments discussed in this work, a direct count of IC electrons is not possible, thus values of α are calculated theoretically by use of the brIcc tool and brIccFO database [15]. Thus, it should be obvious from equation 1.33 that the total intensity of a transition is

$$I_{tot} = I_{IC} + I_\gamma = (\alpha + 1) I_\gamma \tag{1.34}$$

a form commonly used to estimate total decay intensities for γ-transitions measured in this work[4].

Unlike β-decay electrons, IC electrons have discrete energies determined by the energy of the transition and the binding energy of the electron that gets converted;

$$E_{e;IC} = E_\gamma - B_e \tag{1.35}$$

where $E_{e;IC}$ is the kinetic energy of the conversion electron, E_γ is the energy of the transition (which is the energy of the emitted γ-ray, if the transition decays by γ instead of IC), and B_e is the binding energy of the orbital electron. This inherently means that there is a minimum transition energy before IC is possible, namely B_e. However, this depends on which electron is internally converted, the more bound the electron (and thus the greater overlap between electron and nuclear wave functions) the higher the energy threshold for IC, causing discontinuities in the value α vs transition energy. Additionally, with the exception of these discontinuities, α increases as the transition energy decreases. The energy dependence of α is seen clearly in figure 1.2.

[4]While technically incorrect, it is common to speak of IC as a special case of γ-decay. It might be more correct to speak of both IC and γ-decay as different kinds of *internal transitions*, where a nucleus decays within its own structure (i.e. A, Z, and N remain unchanged by the decay). Because this nomenclature is common in the literature, it has been adopted here.

Figure 1.2: Four different plots of internal conversion coefficients as a function of Energy for different values of Z and transition multipolarities. Top left; $Z = 25$. Top right; $Z = 50$. Bottom left; $Z = 75$. Bottom right; $Z = 100$. These graphs were generated by brIcc using the brIccFO database [15].

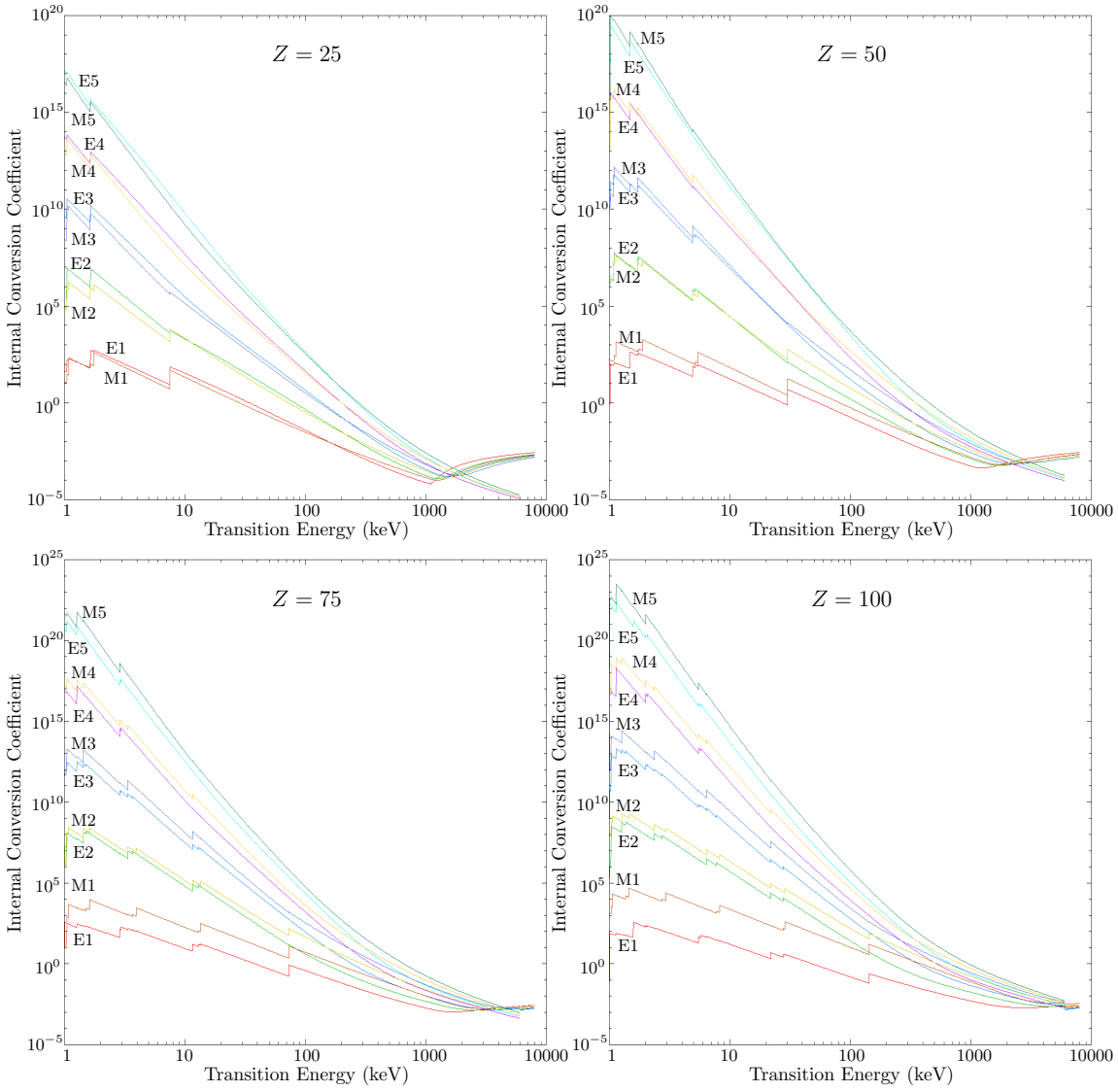

Furthermore, α (equation 1.33) is also dependent on Z such that, as Z increases, the probability of IC increases for two connected reasons. Since there are more electrons orbiting a nucleus with higher Z (number of electrons = Z), there are more candidates for internal conversion. Of greater effect, however, is the generally greater amount of charge present in the system, especially the nucleus itself, causing the strength of the interaction between the nucleus and the electrons to increase. This means that the most bound electrons are more and more tightly bound with increasing Z, causing their wave functions to be in greater overlap with the wave function of the nucleus. Figure 1.2 shows plots for four different values of Z; 25, 50, 75, and 100.

For γ-ray transitions, as shown in equations 1.25 through 1.29, the lifetime of decay increases as the multipole order increases and magnetic transitions typically have longer lifetimes than electric. These lengthening of the γ-ray lifetimes provides more opportunities for orbital electrons to be internally converted, causing the multipolarity dependence of α shown in figure 1.2. Since γ-ray transitions are impossible for $0^{\pm} \rightarrow 0^{\pm}$ ($E0$ or $M0$) transitions, $E0$ and $M0$ transitions always transition by IC (or decay by β- or other mode), being equivalent to $\alpha = \infty$. Because nearly all data discussed in this work are from γ-decay, no $\Pi 0$ transitions are observed.

1.1.4 Fission

Typically only heavy nuclei will fission, splitting into two smaller nuclei plus a a few neutrons;

$$ {}^{A}_{Z}X_{N} \rightarrow {}^{A'}_{Z'}X'_{N'} + {}^{A-A'-x}_{Z-Z'}X''_{N-N'-x} + x\left({}^{1}_{0}n_{1}\right) + \text{energy} \tag{1.36} $$

The daughters, ${}^{A'}X'$ and ${}^{A-A'-x}X''$, are left in excited states, usually with large spin, in addition to the kinetic energy of both daughters and the x neutrons. Like β-decay, the total energy, Q_F, of the excitation and kinetic energies must be less than the mass difference

between the fissioning nucleus and the daughters and neutrons;

$$Q_{\mathrm{F}} = \Delta(A,Z) - \Delta(A',Z') - \Delta(A-A'-x, Z-Z') - x\Delta(1,0) \tag{1.37}$$

However, Q_F is typically so large that it is of no concern when studying the structure of the daughters (as is the goal of this work). For example, for the fission reaction

$$^{252}\mathrm{Cf} \rightarrow {}^{104}\mathrm{Mo} + {}^{144}\mathrm{Ba} + 4n$$

one finds that $Q_F \approx 196$ MeV.

The larger concern for structure research is the neutron separation energy. A neutron or proton separation energy is a characteristic energy for a nucleus which is required to remove a neutron or proton from the nucleus. The neutron separation energy tends to be a loose upper limit for the excitation of a nucleus in many experiments, not just those populated by fission. The greater a nucleus's excitation is above the neutron (or proton) separation energy, the more likely the nucleus is to decay by neutron (proton) emission;

$${}^{A}_{Z}X_N \rightarrow {}^{A-1}_{Z}X'_{N-1} + n + \text{energy} \tag{1.38}$$

rather than γ-ray or IC. With good statistics, one may observe γ-rays emitted from a few states above the lower separation energy, however this is extremely rare, and not observed for any of the nuclei studied in this work.

In fact, the neutrons emitted by fission are typically emitted by *primary fragments*, the highly excited nuclei directly produced by the fission process, and not emitted in the fission process itself. Fission occurs in stages, with the primary fragments being populated well above their neutron separation energies in under 10^{-20} s during the "saddle to scission" phase. The prompt neutron emission phase occurs when the primary fragments emit neutrons by around 10^{-18} s, producing the excited daughters, or *secondary fragments*, as

shown in equation 1.36. At around 10^{-16}s, the daughter nuclei will emit prompt γ-rays, which are the emissaries from the nuclear world studied in this work (as described in section 1.1.2 above). Finally, from 10^{-6} s to infinity, one will often see β-delayed neutrons and γ-rays, as the ground states (or isomers) of the secondary fragments β-decay, causing both neutrons and γ-rays to be emitted from their daughters, who also will eventually β-decay, continuing the process until the nuclei decay to stability.

The term "saddle to scission" refers to the path the fissioning nucleus takes from a saddle point in its potential energy surface to the point that the nucleus actually scissions into two distinct nuclei. Fission (and α-decay) occurs by quantum tunneling through a potential energy barrier in the nucleus's deformation potential energy surface. As will be described in greater detail in section 1.2.2 below, the shape of a nucleus can be described in terms of deformation parameters, β_i, where i represents the multipole order of the electromagnetic field produced by the charge distribution of the nucleus. Figure 1.3a shows the potential energy surface for ^{252}Cf, as a function of β_2 and β_3, along with a few different paths the nucleus might take as it tunnels through the fission barrier to scission. Figure 1.3b shows an one dimensional slice of the potential energy surface, showing the shape of the potential energy barrier that a nucleus must tunnel through before scision.

Equations 1.36 and 1.37 and figure 1.3 assume that it is the ground state of a nucleus that is fissioning. When the ground state of a nucleus fissions without an external stimulus, this is known as *spontaneous fission* (or SF). While ^{252}Cf – whose decay products are studied in this work – spontaneously fissions $\sim 3\%$ of the time[5], most fission reactions studied by physicists are *induced fission*. Induced fission occurs when an external stimulus excites the nucleus to an energy where tunneling across the fission barrier is substantially easier, or perhaps even above the barrier altogether;

$$ {}^{1}_{0}n_1 + {}^{A}_{Z}X_N \rightarrow {}^{A'}_{Z'}X'_{N'} + {}^{A-A'-x+1}_{Z-Z'}X''_{N-N'-x} + x\left({}^{1}_{0}n_1\right) + \text{energy} \tag{1.39} $$

[5]The other $\sim 97\%$ is α-decay

Figure 1.3: (a) A two dimensional potential energy surface for spontaneous fission as a function of quadrupole (β_2) and octupole (β_3) deformation paramaters with dotted lines representing possible paths ^{252}Cf might take toward scission. (b) one dimensional potential for the fission path along $\beta_3 = 0$, with points marked corresponding to points shown in a. Additionally "GS" represents the ground state of ^{252}Cf and "sph" represents the $\beta_2 = \beta_3 = 0$ point of perfect spherical symmetry. This figure is copied from Ter-Akopian *et al.* [16]

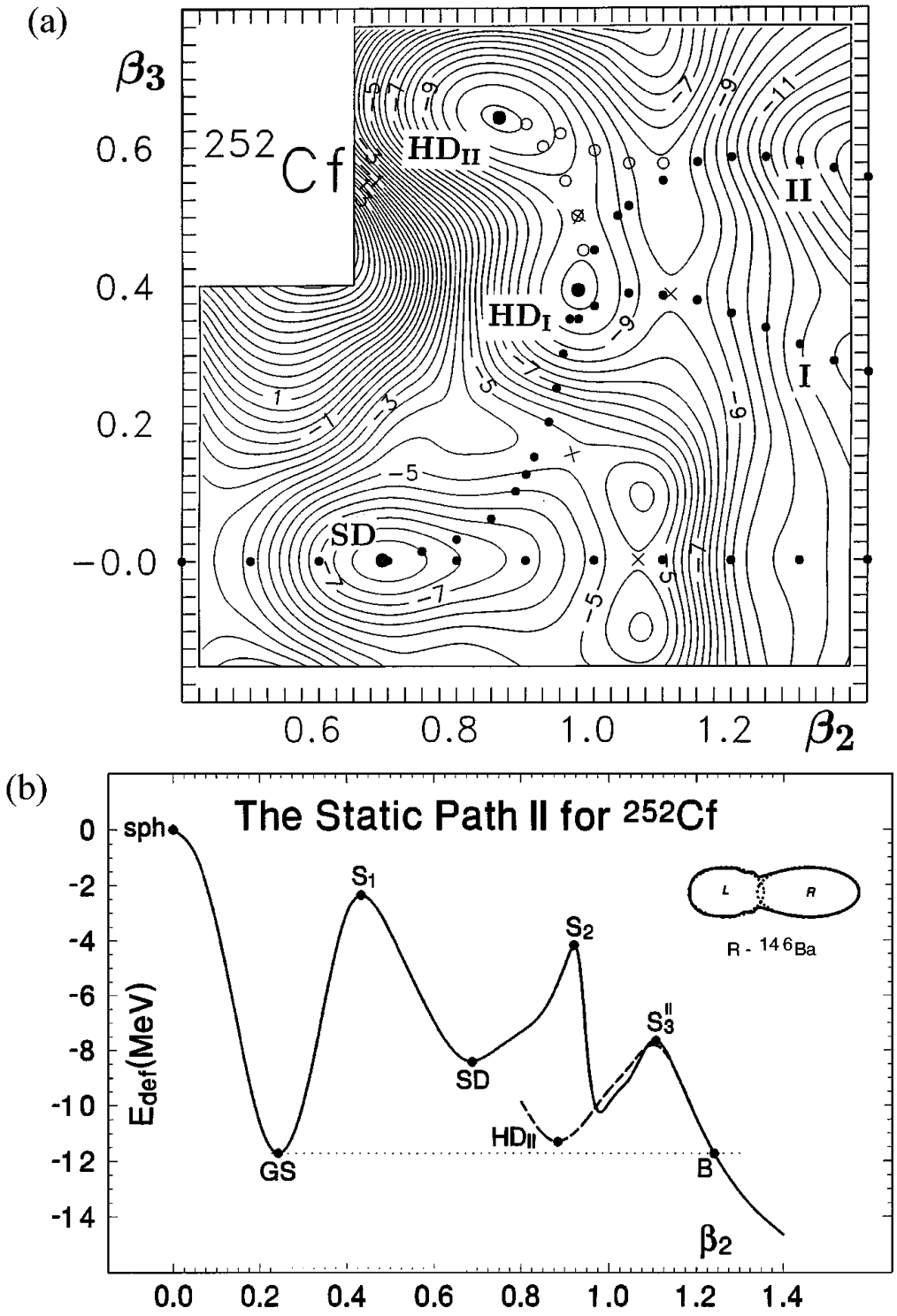

Neutron induced fission is commonly used in nuclear power reactors, because the excess neutrons produced by one fission event can be used to start other fission events, causing a chain reaction. However, neutrons, being neutral, are difficult to accelerate to precise energies, or directions. Thus, one of the experiments in this work uses proton induced fission;

$$ {}^{1}_{1}\mathrm{H}_0 + {}^{A}_{Z}X_N \rightarrow {}^{A'}_{Z'}X'_{N'} + {}^{A-A'-x}_{Z-Z'}X''_{N-N'-x} + x\left({}^{1}_{0}n_1\right) + \text{energy} \tag{1.40} $$

to produce isotopes of interest.

Because uranium can be found in nature, but doesn't (commonly) spontaneously fission, it is typically significantly cheaper to use induced fission in an experiment. However, because the inducing particle (be it proton, neutron, α-particle or other) has initial kinetic energy, induced fission is a significantly more complicated process. The inducing particle adds a significant amount of energy to the fissioning nucleus, meaning that its properties at the time of fission are not knowable with current experimental techniques. This lack of knowledge about the spin, parity, and energy of the fissioning state, makes it more difficult to trace the products of fission backward to the fission process, since the initial conditions are not uniform. Additionally, for spontaneous fission, the fission fragments can be stopped, preventing the need of Doppler correction for the γ-rays. Because of the initial kinetic energy and momentum of the inducing particle in the laboratory frame, one must use a Doppler correction to study any prompt γ-rays emitted by the secondary fragments of induced fission. This is only aggravated by the fact that the precise kinetic energies of the secondary fragments is not known and difficult to measure, making any Doppler correction highly inaccurate. To get around this issue, the one induced fission experiment discussed in this work does not deliver the fission products to the detectors until after the prompt γ-rays have all been emitted, leaving only the β-delayed γ-rays and neutrons for study.

1.2 Nuclear Models Describing Excited State Properties

While β-decay and fission are used in this work to produce the nuclei of interest and γ-decays are used as emissaries from the nuclei of interest, in the present work it is primarily the structure, or excited state properties of these nuclei with which we are concerned. The two most crucial properties of any nuclear state are its spin and parity, represented in this work by J^{π}. The nuclear spin, J, is the sum of the individual spins of the nucleons as well as their orbital angular momentum and collective motion of the nucleus. The orbital angular momentum of individual nucleons and the collective angular momentum of the whole nucleus will be discussed in sections 1.2.1 and 1.2.2 below, respectively. Protons and neutrons are both $J = \frac{1}{2}\hbar$ particles that "prefer" to pair off (protons with protons and neutrons with neutrons) with anti-aligned spins, making the total spin become 0 for the pair. This means the ground states of all even-even nuclei have spin 0, and, for at least the lowest lying levels, the spin and parity of all other nuclei are determined by the properties of the last odd proton and/or neutron.

Closely related to the spin of a nuclear state is its *gyromagnetic ratio*, or g-factor, a dimensionless quantity which characterizes the magnetic properties of the nucleus in that state. A g-factor is defined by the ratio of the nuclear state's magnetic moment, $\boldsymbol{\mu}$, to its spin angular momentum, $\boldsymbol{J}$;

$$\boldsymbol{\mu} = g\frac{\mu_N}{\hbar}\boldsymbol{J} \tag{1.41}$$

where $\mu_N \equiv \frac{e\hbar}{2m_p}$ is the nuclear magneton. The spin, J, of a state is simply the projection of $\boldsymbol{J}$ on the z axis. The g-factors of a nucleus's excited states can be used to determine many unique and interesting properties of it. Of particular interest in this work is the relationship between g and the angle, ϕ, through which the nucleus will rotate while in a particular state;

$$\phi = -B\tau g\frac{\mu_N}{\hbar} \tag{1.42}$$

where B is the external magnetic field and τ is the lifetime of the nuclear state as defined in equation 1.3.

The parity of the nuclear state refers to the evenness or oddness of the total wave function describing the state. Even parity happens when a function is perfeclty reflected across the origin, i.e. $f(x) = f(-x)$, while odd occurs when a function is negatively reflected across the origin, i.e. $f(x) = -f(-x)$. Parity combines multiplicatively such that $f_{odd}(x)g_{even}(x) = f_{even}(x)g_{odd}(x) = h_{odd}(x)$ while $f_{odd}(x)g_{odd}(x) = f_{odd}(x)g_{even}(x) = h_{even}(x)$. For this reason, even parity is often called positive and odd parity is often called negative. Any given proton or neutron has negative parity from being a fermion and either odd or even parity from its orbit. Since the proton/neutron pairs coupling to zero spin discussed above inhabit the same states (see section 1.2.1), they have the same orbital wave functions, and thus the same parity, meaning that their parity will be positive. Thus the ground states of all even-even nuclei will have even parity in addition to 0 spin. Thus, just like with spin, parities of nuclear ground states are determined by the odd neutron and/or proton remaining unpaired.

Two major models have been used to explain other patterns in spins, parities, and other properties of nuclear ground and excited states. Maria Geoppert Mayer and J. Hans D. Jensen won the Nobel Prize in Physics in 1963 for the success of their nuclear shell model which they proposed in 1948 [17] and 1949 [18]. Mayer published a more complete theoretical approach in 1950 [19, 20], but a full description of the theory did not come until Mayer and Jensen's jointly written book in 1955 [21]. In 1975 the Nobel Prize in Physics was awarded to Aage N. Bohr, Ben R. Mottelson, and Leo J. Rainwater for the discovery of the collective model of nuclei. Rainwater proposed the idea that nuclei may not be spherical and Bohr and Mottelson fleshed out the implications of Rainwater's proposal for nuclear collective motion in 1953 [22]. Later, Bohr and Mottelson published a seminal two-volume work on both models titled *Nuclear Structure* [23].

1.2.1 The Shell Model

Mayer and Jensen took inspiration from the atomic shell model – which had both explained the discrete line spectra emitted by the hydrogen atom and the periodicity of the periodic table of the elements – to explain many of the mysteries of nuclear physics. Neither a square well potential, nor a harmonic oscillator potential alone could explain the observed higher stability of nuclei with a "magic number" (2, 8, 20, 28, (40), 50, 82, and 126) of either protons or neutrons. For nuclei with odd numbers of protons or neutrons, no potential nor modeling the nucleus as a liquid drop, was able to adequately explain the spins and parities of ground states, let alone excited states.

Mayer and Jensen's breakthrough, however, was actually in the nuclear shell model's distinction from the atomic shell model. The spin orbit coupling for nucleons in nuclei is significantly larger in magnitude and of opposite sign from electrons in atoms. Spin orbit coupling, in both atoms and nuclei, causes the base orbitals to split into spin aligned and spin anti-aligned. Reversing the sign causes the lower spin split to be higher in energy for nuclei and the larger magnitude makes the size of the splitting greater. The difference occurs because of the greater strength and differing nature for the strong nuclear force compared to the Coulomb force. Once this difference was in place, Mayer and Jensen were able to accurately calculate large gaps in energy at the magic numbers, as well as the spins and parities of many nuclei, especially near magic numbers.

Mayer and Jensen's shell model still had issues. The further a nucleus was from a magic number of protons and neutrons, the less likely its structure was to be found in agreement with the nuclear shell model. Mayer and Jensen assumed that nuclei were spherical but it was soon discovered that many nuclei are not spherical, but instead can often take the shape of spheroids;

$$\frac{x^2}{a^2}+\frac{y^2}{b^2}+\frac{z^2}{c^2}=1 \tag{1.43}$$

For most nuclei, two of the axes have the same length. When the third axes is longer than the two identical axes, a nucleus is called *prolate*, while a shorter third axes is called *oblate*.

Equation 1.43 can be rewritten in terms of spherical coordinates;

$$r(\theta.\phi) = R_0\left(1+\beta_2\cos\gamma Y_{20}(\theta,\phi)+\frac{1}{\sqrt{2}}\beta_2\sin\gamma[Y_{22}(\theta,\phi)+Y_{2-2}(\theta,\phi)]\right) \qquad (1.44)$$

where r is the radius of the nucleus in the direction determined by the angles θ down from the z axis and ϕ around from the x axis, $Y_{lm}(\theta,\phi)$ is a spherical harmonic, and β_2 and γ are deformation parameters (this is the same β_2 referenced in equations 1.18 through 1.24 section 1.1.2.1). By using the variables of equation 1.44, $\beta_2 = 0$ represents a spherical nucleus, while a prolate nucleus lies along $\gamma = 0^\circ$ and oblate nuclei lie along $\gamma = 60^\circ$. Values of $0^\circ < \gamma < 60^\circ$ corresponds to triaxial nuclei ($a \neq b \neq c$).

Sven G. Nilsson, in conjunction with Bohr and Mottelson and others, expanded the spherical shell model to other spheroidal shapes, showing how the levels predicted by the spherical shell model shift and further split as the deformation changes. A plot showing Nilsson orbitals as a function of deformation is shown in figure 1.4. With the new non-spherical shell model, or *Nilsson model*, nearly all nuclear ground states and many more excited states became explainable. Furthermore, the weaker magic number observed at N or Z of 40, is explained by the opening of a new gap in the orbitals at 40 nucleons.

By using either the spherical or Nilsson shell models, for nuclei with an odd number of protons or neutrons, many excited states can be explained as the excitation of a single proton or neutron from one state to another. For nuclei with an odd number of protons or neutrons it is common to define most states (including the ground state) by which orbital the odd particle is in. This is typically noted by $\pi J^\pi[Nn_z\Lambda]$ for odd proton or $\nu J^\pi[Nn_z\Lambda]$ for odd neutron, where N is the nuclear equivalent of the principal quantum number and $n_z + \Lambda = N$. Each of the lines in figure 1.4 are marked with the appropriate spin and identifying numbers while solid lines represent positive parity and dashed lines represent negative parity. Because exciting an even-even nucleus in this way requires breaking a pair of nucleons, one must note both unpaired particles and which state they are in as well as

Figure 1.4: A Nilsson orbital diagram are shown here for neutron orbitals for neutron numbers $82 \leq N \leq 126$ reproduced from Firestone [24]. Firestone also holds Nilsson orbital diagrams for proton orbitals and orbitals for other number of neutrons. Sold lines represent states with positive parity, while dotted lines represent states with negative parity. Here the deformation parameter $\varepsilon_2 = 15\beta_2/(4\sqrt{5\pi} + 5\beta_2)$ is used on the x axis and energy on the y. One can see, along $\varepsilon_2 = 0$ the spherical shells predicted by the spherical shell model of Mayer and Jensen at 82 and 126.

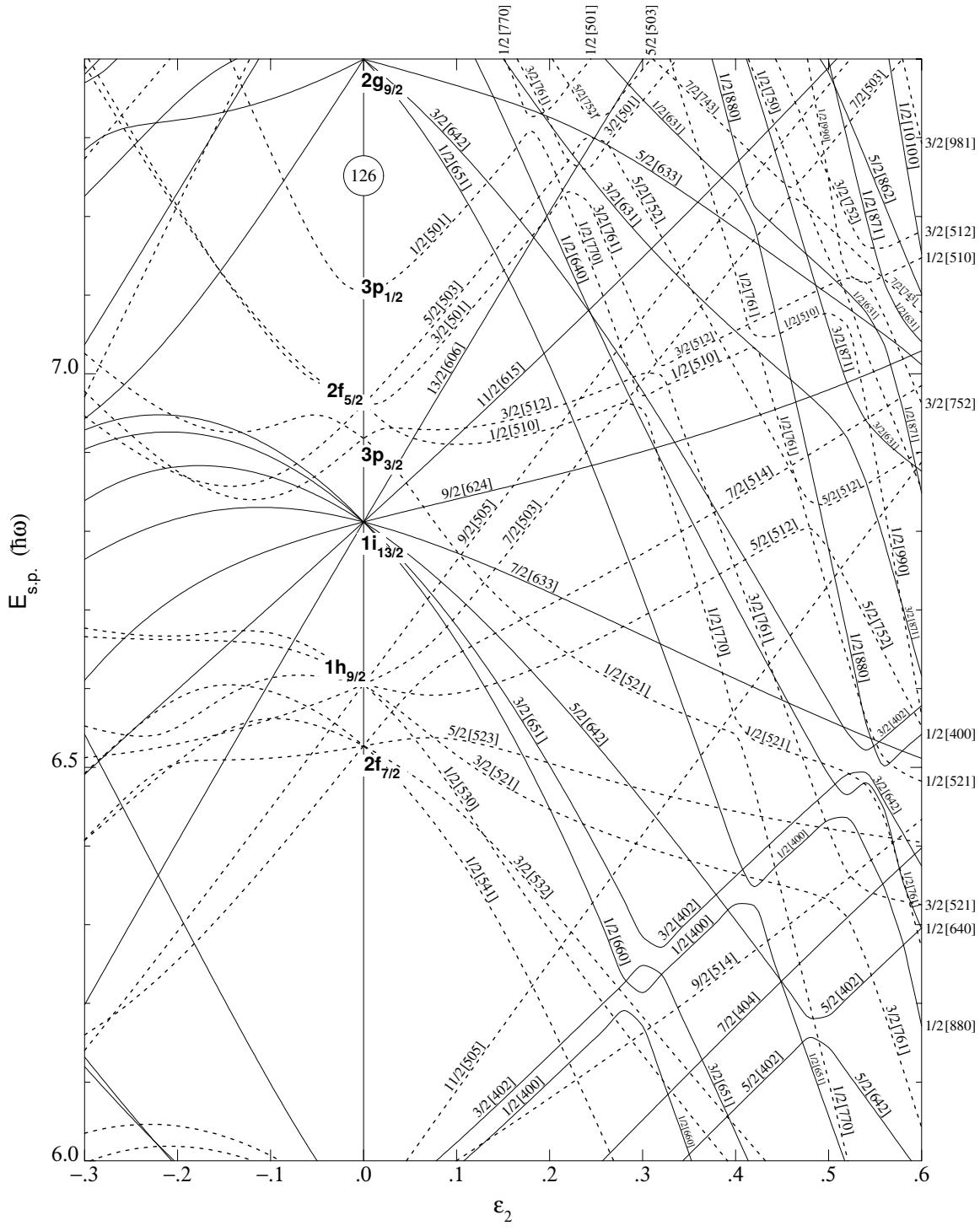

what spin to which the particles couple[6]. Thus one has either $J_f^\pi \left(\pi J_1^\pi [N n_z \Lambda] \otimes J_2^\pi [N' n_z' \Lambda']\right)$ for protons or $J_f^\pi \left(\nu J_1^\pi [N n_z \Lambda] \otimes J_2^\pi [N' n_z' \Lambda']\right)$ for neutrons.

1.2.2 The Collective Model

However, not all nuclear excited states can be easily explained by single particle excitations in a spherical or deformed shell model. In fact, the vast majority of excited states discussed in this work cannot be explained by either shell model discussed above. Two common modes of *collective excitation* are known for deformed nuclei; rotation and vibration.

1.2.2.1 Rotational Bands

Quantum mechanically, it is impossible for a nucleus to rotate about an axis of symmetry, and thus impossible for a spherical nucleus to rotate about any axis. This is because, quantum mechanically, two indistinguishable states are in fact, the same state, thus any rotation about an axes of symmetry reproduces the original state that was rotated.

It is well known that the eigenvalues of quantum mechanical angular momentum operator L^2 are $l(l+1)\hbar^2$, where l is any non-negative integer. Thus it should be obvious that the eigenvalues of the quantum mechanical rotational Hamiltonian, $H_{rot} = \frac{L^2}{2\mathscr{L}}$ (assuming no external potential) are $l(l+1)\frac{\hbar^2}{2\mathscr{L}}$, where $\mathscr{L}$ is the moment of inertia of the system about the axis of rotation[7]. For nuclei, the quantum number l corresponds to the spin, J, of the nuclear state. Thus when a deformed nucleus rotates, the energy of each successively more rapidly rotating state is

$$E_{rot} = J(J+1)\frac{\hbar^2}{\mathscr{L}}, \tag{1.45}$$

for any non-spherical nucleus with moment of inertia $\mathscr{L}$.

[6]Recall that, in quantum mechanics, two angular momentum vectors, $\boldsymbol{J}$ and $\boldsymbol{L}$, may combine to any integer value from $|J-L|$ to $J+L$. Thus multiple spins may be allowed for the same configuration, and in nuclear physics, these spins may not be degenerate in energy.

[7]For a full derivation and definition of these operators see Shankar [25] or another introductory quantum mechanics textbook.

In principal, any non-spherical state of a nucleus can rotate, not just the ground state. Thus, for all of the nuclei observed in this work, multiple *rotational bands* are observed. Since most excited states – be they single particle, vibrational, or otherwise – have rotational bands built on top of them, it is common to refer to a rotational band by the properties of its band-head. For example the rotation of the ground state is called often the yrast band[8] or ground state band, while a rotational band built on a single particle state in an odd neutron nucleus would be commonly called a $\nu J^{\pi}[Nn_z\Lambda]$ band. In such a rotational band (at least to a first order approximation), each state in the band has the same properties as the band-head; the only difference is that the higher energy states are rotating. Thus, equation 1.45 applies not to the absolute excitation, but to the excitation relative to the band-head of the rotational band.

1.2.2.2 Vibrational States

Most nuclei can vibrate. Such vibrations will typically follow, approximately, the even energy spacing between states characteristic of a quantum harmonic oscillator, though plenty of nuclei have been observed to exhibit varying levels of anharmonicity. Typically vibrations observed are phonons built upon the ground state of the nucleus, but some nuclei have been observed to exhibit vibrations of an excited single-particle state [26].

There are two kinds of vibrations important in this work; β-vibrations and γ-vibrations of a prolate shape. Both are quadrupole in nature and have already been addressed indirectly in section 1.1.2.2. These two vibrational modes are most easily understood from equation 1.44, because a β-vibration is essentially an oscillation of the β_2 deformation parameter, while a γ-vibration is the same for the γ deformation parameter.

To understand what is meant by a quadrupole vibration, one should recall classical electricity an magnetism. Classically, there are two kinds of closely related multipoles;

[8]Technically a yrast state is the lowest energy state of a given spin, especially in even-even nuclei. For all the nuclei studied in this work, the ground state rotational bands are all yrast states, and thus the nomenclature "yrast band" is used interchangeably in this work with "ground state rotational band."

those defined by charge distributions and those observed as radiation sources. All nuclei have a relatively large monopole moment (Q_0), directly proportional to their charge, $+Ze$. The simplicity of the nuclear monopole moment causes it to be trivial and rarely discussed. An electric dipole requires opposing positive and negative charge in close proximity. Thus an atom may have a dipole moment (Q_1), but the nucleus, on its own, does not. Thus the leading order for an electric moment of significance in nuclear physics is the quadrupole moment, Q_2 (not to be confused with the Q-value for nuclear decay, see equation 1.12 or 1.37). In fact, a nucleus's deformation β_2 can be related to its quadrupole moment by

$$\beta_2 = \frac{Q_2\sqrt{5\pi}}{3ZR_0A^{1/3}} \tag{1.46}$$

where $R_0 \approx 1.2$ fm. Thus β_2 is called the quadrupole deformation parameter. Thus it is not surprising that the two most important kinds of vibrations for nuclei are quadrupole in nature, since the leading electric multipole order of any significance for nuclei is quadrupole.

Classically any accelerating charge will radiate.[9] Specifically, a harmonic vibration of a multipole distribution, as described above, will produce radiation of that same multipole order. These multipole radiations have unique angular distributions which can be used to identify them. Both of these facts remain true in the quantum world. Thus one would expect both γ and β vibrational states to emit quadrupole radiation when decaying to non-vibrational states, and that one could identify this radiation by its angular distribution. More on the impact of multipole radiation and angular distributions for this work will be discussed in section 2.1.2. For a complete discussion of classical multipole distributions and radiations see Jackson [27]. For further detail on the nuclear applications of the quantized multipole radiations see Frauenfelder and Steffen [28] or Bohr and Mottelson [23].

[9]The loss of energy due to this radiation is one of the main reasons the Rutherford model of the atom was later replaced by the Bohr (and even later the Schrödinger-Heisenberg) quantum mechanical model.

Chapter 2

Experimental Methods

Two primary experiments were employed in this work. The first involved the spontaneous fission of ^{252}Cf inside the Gammasphere detector array, while the other concerned the β-decay of ^{164}Eu observed by the Low Energy Radioactive Ion Beam Spectroscopy Station (LeRIBSS) at Oak Ridge National Laboratory (ORNL).

2.1 The Gammasphere

Most of the work described in this dissertation comes from the analysis of data from an experiment which was conducted using the Gammasphere detector array in August and November of 2000, at Lawrence Berkley National Laboratory (LBNL)[1]. A 62 μCi source of ^{252}Cf was placed between iron foils inside Gammasphere yielding 5.7×10^{11} $\gamma-\gamma-\gamma$ and higher coincidence events, of which 1.9×10^{11} were $\gamma-\gamma-\gamma-\gamma$ events. Because the iron foils were thick enough to stop the fission fragments, no Doppler corrections were needed on the measurements. At the time of the experiment, 101 of Gammasphere's 110 Hyper-Pure Germanium (HPGe) γ-ray detectors were working. These detectors are arranged spherically about the source, with 64 possible angles between any two detectors. More details on this experimental setup can be found in Luo *et al.* [29].

2.1.1 Coincidence Analysis with Gammasphere

The large number of higher order coincidence events observed in this experiment, enables us to isolate rare transitions by setting *gates*. To set a gate, we select a slice of the $\gamma-\gamma-\gamma$ or $\gamma-\gamma-\gamma-\gamma$ data in one of their dimensions, effectively reducing the dimensionality of the data. Thus a single gate on 100 keV will turn triple coincidence data into a two dimensional $\gamma-\gamma$ matrix of all events occurring *in coincidence* with a 100 keV γ-ray

[1] Gammasphere is now located at Argonne National Laboratory (ANL)

signal in any detector. In this experiment a 1 μs *coincidence window* – or the maximum time after the triggering event that a subsequent event will be considered "in coincidence" with the triggering event – was used. Normally, one will set gates on multiple dimensions simultaneously in order to reduce the final result to a more manageable 1 dimensional histogram. Thus when working with the $\gamma-\gamma-\gamma$ compilation of the data, we will select two γ-ray energies to gate on (called a double gate) and thus produce a 1 dimensional histogram, or spectrum, which lists how many times every γ-ray energy was observed in coincidence with *both* of the γ-rays upon which we gated. Similarly, triple gating on the $\gamma-\gamma-\gamma-\gamma$ compilation of the data, produces a 1 dimensional spectrum of all events observed in coincidence with *all three* chosen γ-rays.

Setting gates in this way has two key advantages. First, it enables one to isolate γ-rays in the total spectrum that actually belong to a nucleus of interest by selecting only γ-rays as gates which are already known to belong to the nucleus of interest or to one of its fission partners. Second, it enables us to better construct the ordering of the γ-rays within the structure of a nucleus, as each nucleus has multiple paths by which it may decay to ground, many of which are anti-coincident with each other. However, there is one major drawback to this method; contamination. Because the spectra produced from the SF of ^{252}Cf come from hundreds of possible secondary fragments and β-delayed emissions, it is likely that a single gate on an energy in one nucleus will be close in energy to other transitions observed in other nuclei. This is, of course, minimized by double- and even triple-gating, but even in high order gates, occasionally more than one transition will be similar in energy to the energies of the desired nuclei. Furthermore, sometimes random background fluctuations, or non-γ-ray-interactions with the HPGe crystals, will cause false positives, increasing the likelihood of contaminant coincidence. This is especially true when one of the γ-rays gated upon is at around 600 keV, because neutron interaction creates a platform at around 600 keV consistent across all gates. When analyzing the coincidence spectra, care has been taken to account for contamination.

2.1.2 Integral Perturbed Angular Correlation Method with Gammasphere

Another tool used with this Gammasphere data is known as Integral Perturbed Angular Correlation. The IPAC method measures the distribution of angles between two γ-rays in coincidence and the distribution is fitted to

$$W(\theta) = 1 + G_2 A_2 P_2(\cos\theta) + G_4 A_4 P_4(\cos\theta) \tag{2.1}$$

where P_l is a Legendre polynomial and G_k is a constant attenuation factor, to be discussed below. The parameters A_k can either be used as fit parameters or theoretically calculated as functions of the mixing ratios of the two γ-rays, δ_1 and δ_2, respectively. When one mixing ratio is held fixed, the theoretical values of A_2^{thry}, A_4^{thry} become a parametric equation which forms an oval as δ, starting at $-\infty$, comes back around to the same A_2^{thry}, A_4^{thry} at $\delta = +\infty$. For details on how the A_k^{thry} parameters are calculated see Frauenfelder and Steffen [28]. Before the experimental results were fit to eq. (2.1), in order that there would be more statistics behind each data point, the 64 angular bins innate to Gammasphere were combined to 17 angle bins, which were subsequently combined in pairs across the $\cos\theta = 0$ axis of symmetry to an effective 9 bins. Once A_2^{exp}, A_4^{exp} are thus measured, they are compared to the oval by a χ^2 minimization analysis to determine the closest corresponding values of A_2^{thry}, A_4^{thry}, which fall exactly on the oval. Because there is a 1 to 1 correspondence between values of δ and pairs of A_2^{thry}, A_4^{thry}, we thus know the value of δ once A_2^{thry}, A_4^{thry} have been determined. Typically only A_2^{exp} was used in these calculations, since its uncertainty is usually smaller than A_4^{exp} and small contaminations in the correlation affect A_4^{exp} to a greater extent. To preform these χ^2 minimization calculations, the program DELTA, provided by the National Nuclear Data Center, was used [30]. Because DELTA uses the depth and width of the minimum value of χ^2 to determine the uncertainties in δ, the uncertainties of δ will frequently be smaller than the uncertainties of A_2^{exp}, A_4^{exp}, and only occasionally larger.

Because IPAC depends on the angle between two γ-rays, any rotation the nucleus undergoes while in the intermediate nuclear state will attenuate the resultant angular correlation. If the attenuations factors, G_k, in eq. (2.1) are known, one can correct for this attenuation. G_k is defined as the ratio of the experimental and theoretical A_k factors;

$$G_k \equiv \frac{A_k^{exp}}{A_k^{thry}} \tag{2.2}$$

For a correlation whose unattenuated A_2^{thry},A_4^{thry} we know, we can indirectly measure the angle through which the nucleus rotates, ϕ;

$$G_k = \frac{1}{2k+1}\left(1+2\sum_{q=1}^{k}\frac{1}{1+q^2\phi^2}\right) \tag{2.3}$$

Combining eqs. (1.42) and (2.3), we can use G_k to find the g-factor of an excited state. The g-factors of the 2_g^+ excited states of the nuclei discussed in this paper were measured using the $4_g^+ \rightarrow 2_g^+ \rightarrow 0_g^+$ angular correlation in each isotope. For these correlations, G_2 was found by equation (2.2). Then equations (2.3) and (1.42) were solved for ϕ and g. These values of g and ϕ were then used in eq. (2.3) to find G_4. Since this method of calculating the g-factor depends on the difference between theoretical and experimental values of A_2,A_4, the uncertainty of the g-factor (and subsequently G_4) would be expected to increase as this difference decreases, as shown in figure 2.1.

Often, multiple fission products of ^{252}Cf will have extremely similar energies in their cascades. This can be especially true for isotopes of the same element. Since IPAC is an essentially $\gamma-\gamma$ coincidence method, we can take full advantage of the $\gamma-\gamma-\gamma$ coincidence nature of our data to eliminate much of this source of background contamination by requiring that the cascades of interest be in coincidence with another γ-ray, either from the nuclide in question or from one of its fission partners. Our software is set up to allow us to select up to 10 such gates, requiring that the cascade of interest be in coincidence with *at least* one of them. More information on our implementation of IPAC (including corrections

Figure 2.1: Two plots to demonstrate the uncertainty of G_k values as a function of nuclear procession angle, ϕ (see equation 2.3). In the top graph one can easily see that, for small values of ϕ, the derivatives of G_k with respect to ϕ become larger. The uncertainty of G_k also depends on $\left|\frac{d\phi}{dG_k}\right|$. Thus the bottom plot demonstrates that both low and high rates of rotation cause the uncertainty of G_k to increase, giving limits to the usefulness of the IPAC method with Gammasphere. This figure has been reproduced from Goodin [1].

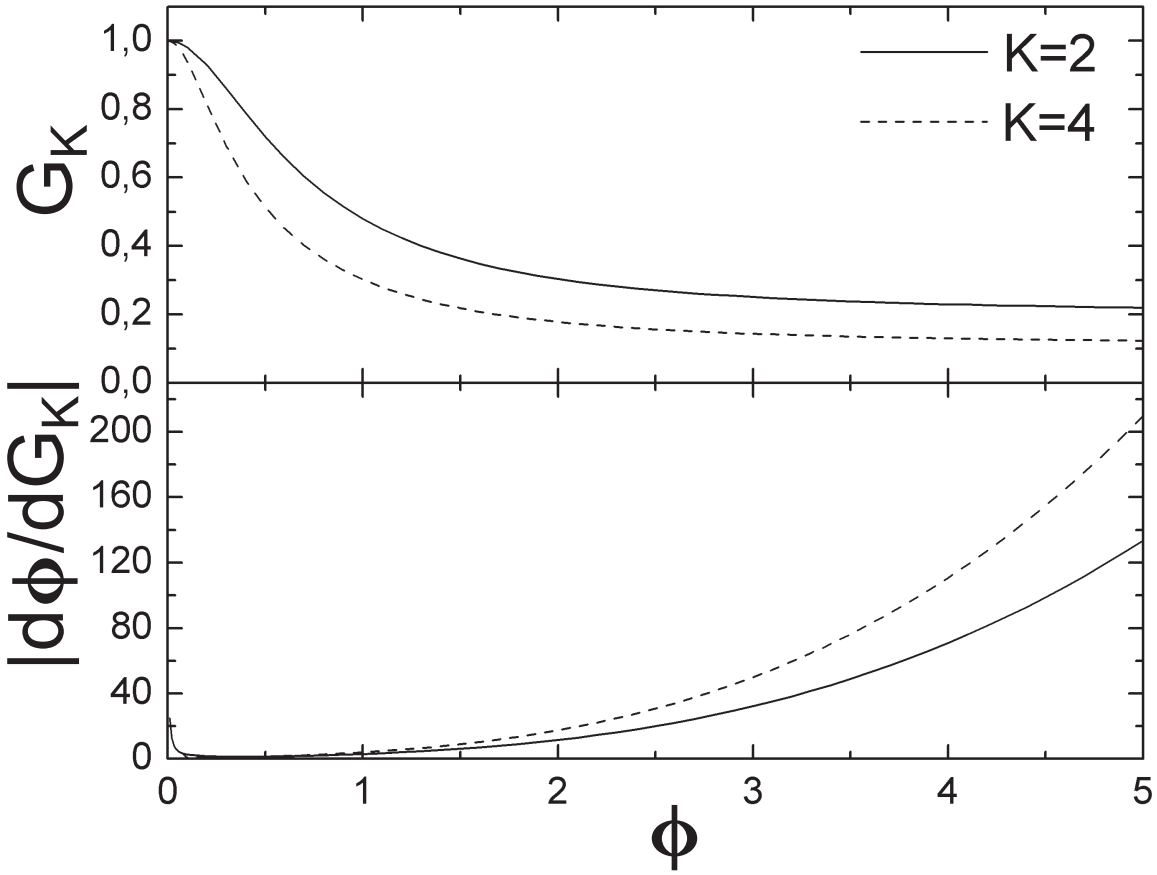

Figure 2.2: A Schematic of the Holifield Radioactive Ion Beam Facility at Oak Ridge National Laboratory.

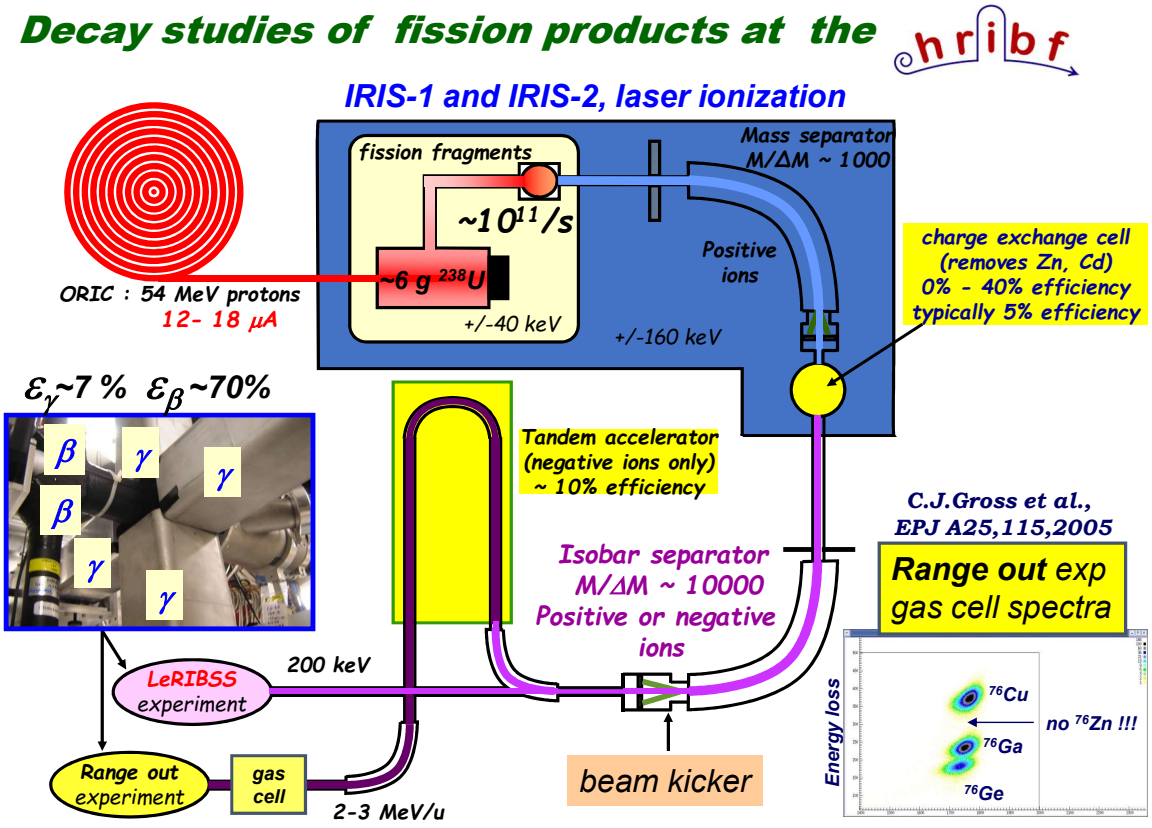

for differences in the individual detectors and the number of detectors in each angular bin) can be found in Daniel *et al.* [31] and Goodin [1].

2.2 LeRIBSS at HRIBF

Another experiment was conducted at the Holifield Radioactive Ion Beam Facility (HRIBF) at Oak Ridge National Laboratory (ORNL). A diagram of HRIBF is shown in figure 2.2. This experiment used proton induced fission of ^{238}U to generate fission fragments which were then mass-separated to isolate ^{164}Eu to study its β-decay into ^{164}Gd. The Oak Ridge Isochronous Cyclotron (ORIC) was used to accelerate protons to around 54 MeV, and the beam was incident on a 6 g target of ^{238}U in the form of UC_x, producing around 10^{11} fission fragments per second. These fission fragments are then separated by their charge to mass ratios to a precision of mass over the spread in mass is $\sim 10^4$ within

the beam . The fission fragments – in our case, ^{164}Eu ions in a 2^+ charge state – are deposited onto a moving tape which is passed through the Low-energy Radioactive Ion Beam Spectroscopy Station (LeRIBSS), which consists of 4 clover HPGe gamma ray detectors and two β-particle detectors. The beam was tuned to maximize the detection of 168 keV γ-rays, the strongest transition previously known in ^{164}Gd, to about 28 events per minute.

These data were taken in 16 s cycles for 109 minutes. The beam is implanted on the tape directly in the center of the LeRIBSS station's detectors for 8 s, and then was shut-off by a Faraday-cup beam kicker for another 8 s. At the end of these 16 s, the section of tape inside the detector was removed behind a wall of lead bricks, and the cycle began anew. This cycle allowed for a consistent pattern of grow-in and decay-out, while minimizing the presence of ^{164}Tb, the β-decay daughter of ^{164}Gd.

These data were then compiled by using a 1 μs "rolling" coincidence window, meaning that the compiler closed an event after 1 μs had passed without the detection of a β or γ. This "rolling" coincidence increases the statistics in coincidence spectra, while still limiting the number of false coincidences that would occur with a wider traditional coincidence window (as used for the ^{252}Cf data discussed in section 2.1, above). This setup resulted in 2.0×10^7 single γ-ray events, 9.8×10^5 $\beta - \gamma$ coincidence events, and 1.3×10^6 $\gamma - \gamma$ coincidence events. The tandem accelerator and Range Out Stations shown in figure 2.2 were not used in this experiment, and will not be discussed here. More details on this experiment and the LeRIBSS station at HRIBF can be found in Brewer [32], Alshudifat *et al.* [33], and Liu *et al.* [34]. See also the LeRIBSS's websites from the University of Tennessee Knoxville [35] and ORNL [36].

Chapter 3

Mixing Ratios of γ-Band to Yrast-Band Transitions

Results are presented here for the angular correlations measured using IPAC and Gammasphere, as described in section 2.1.2. These angular correlations yielded both g-factors of first 2_g^+ excited states and mixing ratios ($\delta(E2/M1)$) for γ-vibrational-band to ground-state-band transitions in ^{102,104,106,108}Mo, ^{108,110,112}Ru, and ^{112,114,116}Pd. These results have confirmed the spin assignment of the 1244.9 keV, $3_\gamma^{(+)}$ level in ^{102}Mo. The rest of the mixing ratios presented demonstrate that, as theoretically predicted, these transitions are nearly pure E2, and agree with Krane's [2] predicted shape transition. However, Walter Greiner's theory [7], defined in equations 1.18 and 1.19, is reasonably able to predict the order of magnitude for some of the values of $\delta(E2/M1)$ in this region, but is not much more accurate than that except in a few cases. The errors given in this work for A_2^{exp}, A_4^{exp} are primarily statistical and represent 1 standard deviation (1σ). Considering how A_2, A_4 depend on δ, the uncertainty on values of δ measured represent 1σ in A_2, A_4 space, rather than on the δ number-line. As explained in section 2.1.2, the uncertainties of the values of δ also tend to be slightly lower than the uncertainty of A_2, A_4 in A_2, A_4 space.

3.1 g-Factors of 2^+ excited states

In some cases, as discussed in section 2.1.2, the raw angular correlations were attenuated due to rotation of the nucleus. To correct for this attenuation, the g-factors of the intermediate states needed to be measured (see equations 1.42, 2.2, and 2.3). Thus, the $4_g^+ \to 2_g^+ \to 0_g^+$ correlations listed in tables 3.2, 3.3, 3.5, and 3.7 were used to measure the attenuation factors (G_k) and g-factors for the isotopes considered in this work.

Figure 3.1 and table 3.1 display the results of the analysis of these $4_g^+ \to 2_g^+ \to 0_g^+$ angular correlations. According to theory, these angular correlations should all fall at the point $A_2, A_4 = 0.10204, 0.00907$ [37], which corresponds to $0 = \delta_1(M3/E2) = \delta_2(M3/E2)$.

Table 3.1: Attenuation factors and g-factors of 2_g^+ excited states measured by $4_g^+ \rightarrow 2_g^+ \rightarrow 0_g^+$ angular correlations for which $A_2^{thry}, A_4^{thry} = 0.10204, 0.00907$ [37]. The Hyper-Fine Magnetic Fields experienced by each nuclide are taken from Rao [38]. For the Isotopes of Mo, $B = 25.6(5)$ T. For Ru, $B = 50.0(10)$ T. For Pd, $B = 54.7(38)$ T. The nuclear lifetimes, τ, are taken from refs. [39, 40, 41, 42, 43, 44, 45, 46]. An uncertainty of ∞ indicates that the parameter could not be determined with any reasonable precision. The uncertainties of both g and G_4 grow large for both large and small values of ϕ (G_2 is unaffected since it is directly experimentally determined), as seen in figure 2.1. As shown in equation 1.42, ϕ is proportional to the lifetime of the nuclear state, thus exceptionally large or small lifetimes will cause larger uncertainties in G_4 and g.

Nuclide	A_2^{exp}, A_4^{exp}	τ (ns)	G_2, G_4	g-factor	
				This Work	Previous
^{102}Mo	0.105(8), 0.00(2)	0.180(6)	1.03(8),0.9(7)	0.8(6)	0.42(7)*,0.4(2)†‡
^{104}Mo	0.082(4),0.015(6)	1.40(12)	0.80(4),0.60(10)	0.22(3)	0.27(2)*†‡
^{106}Mo	0.076(8),0.014(12)	1.80(4)	0.74(8),0.54(15)	0.21(5)	0.21(2)*†‡
^{108}Mo	0.080(15),0.00(2)	0.7(4)	0.79(14),0.6(5)	0.5(2)	0.5(3)*†‡
Average for $^{104-108}$Mo: $G_2, G_4 = 0.79(3), 0.58(8)$					
^{108}Ru	0.090(14),0.02(2)	0.52(4)	0.88(13),0.7(7)	0.2(2)	0.23(4)†,0.28(4)*‡
^{110}Ru	0.083(6),0.021(9)	0.46(3)	0.81(6),0.62(15)	0.34(7)	0.42(6)*,0.44(7)†‡
^{112}Ru	0.087(9),0.000(14)	0.46(4)	0.85(9),0.67(12)	0.29(11)	0.44(9)*†‡
Average for $^{108-112}$Ru: $G_2, G_4 = 0.83(5), 0.65(9)$					
^{112}Pd	0.101(5),0.019(8)	0.121(20)	0.99(5),1(2)	0.2(6)	-
^{114}Pd	0.108(4),-0.004(6)	0.118(20)	1.06(4),-	-	0.24(13)*,0.09(5)†‡,0.24(11)‡
^{116}Pd	0.096(6),0.022(10)	0.16(4)	0.94(6),0.9(5)	0.5(3)	0.2(1)*†‡
$G_2 = G_4 = 1$ Used for ^{102}Mo and ^{112,114,116}Pd					

*From Chamoli *et al.* [47] who cite Smith *et al.* [48, 49] for some measurements.

†From Smith, Patel, *et al.* [48].

‡From Smith, Orlandi, *et al.* [49], a near-copy of Smith, Patel, *et al.* [48] in a different journal.

Figure 3.1: A Plot of all the $4^+_g \rightarrow 2^+_g \rightarrow 0^+_g$ correlations measured in this work compared to the 4(2,3)2(2)0 oval, zoomed in to see the details.

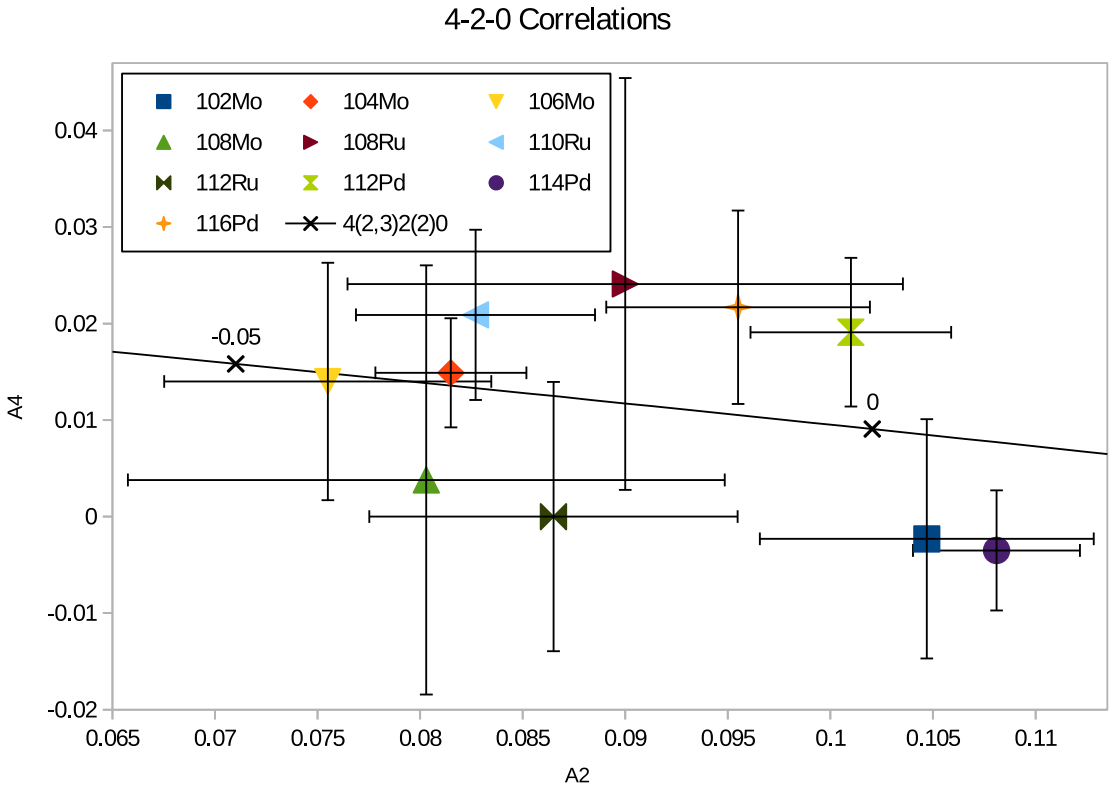

For ^{102}Mo and ^{112,114,116}Pd, the attenuation factors, G_2, G_4, were determined to be close enough to 1 that no correction was used for these nuclides. The values for the attenuation factors for ^{104,106,108}Mo and for ^{108,110,112}Ru were averaged, to reduce uncertainties. For ^{104,106,108}Mo it was determined that $G_2, G_4 = 0.79(3), 0.58(8)$, while for the isotopes of ^{108,110,112}Ru, $G_2, G_4 = 0.83(5), 0.65(9)$. These averages were used to correct the $2^+_\gamma \rightarrow 2^+_g \rightarrow 0^+_g$ and $3^+_\gamma \rightarrow 2^+_g \rightarrow 0^+_g$ correlations for these isotopes. It has been assumed that the lifetimes of 4^+_g and higher states are short enough that there is no attenuation (as was found in Goodin [1]).

The g-factors measured in this work generally agree with those cited in Chamoli *et al.* [47], and two papers by Smith *et al.* [48, 49], though the uncertainties in the present

work are generally larger than those cited in these previous works. Of particular note, however, is the g-factor for ^{112}Pd, for which – though its uncertainty is extremely large – no value for it has been previously reported in the literature. Since the IPAC method can only give the magnitude of the g-factors, we have adopted the sign given in these previous works, which is positive for all g-factors considered.

3.2 Measured E2/M1 Mixing Ratios

Tables 3.4, 3.6, and 3.8 contain information about the angular correlations measured and the subsequent calculations of mixing ratios for γ-band to ground-state-band transitions measured in this work. Typically, these calculations of δ used only A_2. Because possible values of δ make an oval in A_2, A_4 space, a given value of A_2 will usually have two possible values of A_4 (and vice versa), corresponding to two different values of δ. In these three tables only solutions possible within 3σ of A_2^{exp}, A_4^{exp} have been given, but those solutions which are also greater than 1.5σ have been marked off with square braces, to indicate that they are less likely. The measured $2^+_\gamma \rightarrow 2^+_g \rightarrow 0^+_g$ correlations, $3^+_\gamma \rightarrow 2^+_g \rightarrow 0^+_g$ correlations, $4^+_\gamma \rightarrow 4^+_g \rightarrow 4^+_g$ correlations, and $5^+_\gamma \rightarrow 4^+_g \rightarrow 2^+_g$ correlations can be seen compared to the appropriate respective δ ovals in figs. 3.5, 3.6, 3.7, and 3.9, respectively.

3.2.1 Isotopes of Mo.

Partial level schemes of the isotopes of Mo considered in this work are shown in figure 3.2. The complete level scheme of ^{102}Mo can be found in Yang *et al.* [50] and Wang *et al.* [51]. For ^{104}Mo and ^{106}Mo see Jones *et al.* [52] and Musangu *et al.* [53]. For ^{108}Mo see Ding *et al.* [54].

Tables 3.2 and 3.3 list all the angular correlations measured in this work for isotopes of Mo. Table 3.4 lists the $\delta(E2/M1)$ ratios measured from these angular correlations for ^{102,104,106,108}Mo.

Figure 3.2: Partial Level Schemes of the Isotopes of Mo considered in this work

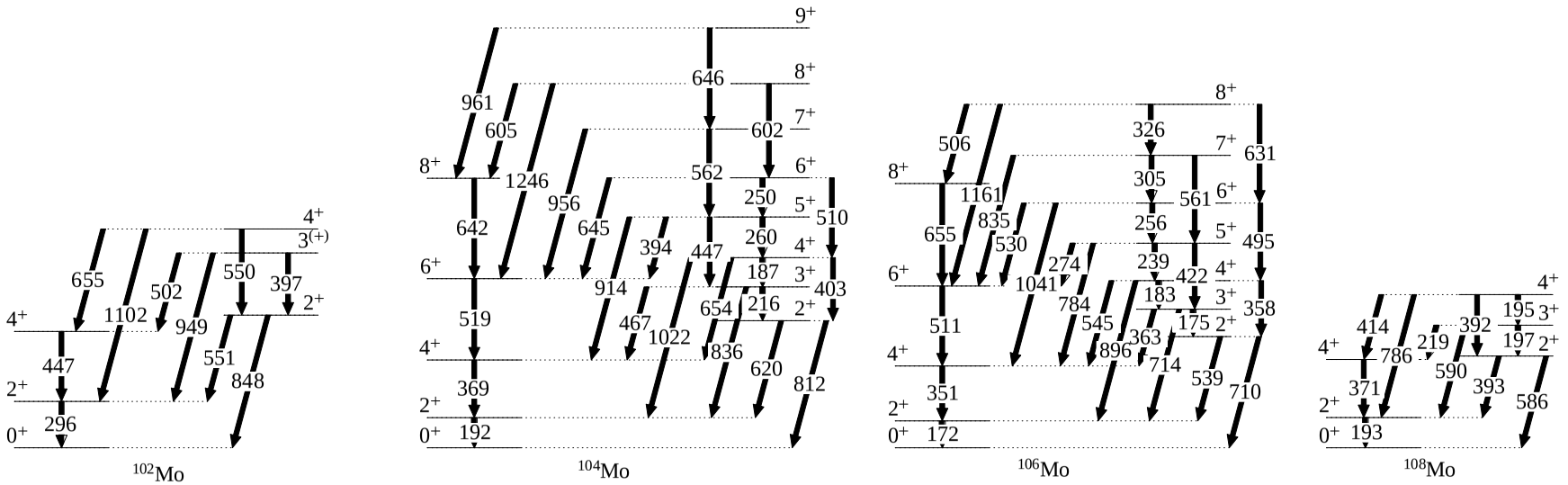

Table 3.2: Angular correlations measured for ^{102,104}Mo

Correlation $J^\pi \xrightarrow{(keV)} J^\pi \xrightarrow{(keV)} J^\pi$	Additional Gates (keV)	A_2^{raw},A_4^{raw}
^{102}Mo		
$4_g^+ \xrightarrow{447.2} 2_g^+ \xrightarrow{296.1} 0_g^+$	584.4;690.9;181.3*	0.105(8),-0.002(12)
$2_\gamma^+ \xrightarrow{551.6} 2_g^+ \xrightarrow{296.1} 0_g^+$	397.4, 574.4, 1021.4, 1597.7, 1022.5	-0.15(2),0.29(4)
$3_\gamma^+ \xrightarrow{948.8} 2_g^+ \xrightarrow{296.1} 0_g^+$	1235.2, 624.2, 1200.2, 331.1*, 1376.3, 181.5*, 444.9*, 752.1	-0.29(3),-0.07(3)
$4_\gamma^+ \xrightarrow{654.7} 4_g^+ \xrightarrow{447.2} 2_g^+$	296.0, 1082.4, 181.4*, 332.6*, 1223.2, 199.5*, 1265.4, 431.0*	-0.18(2),0.13(3)
^{104}Mo		
$4_g^+ \xrightarrow{368.6} 2_g^+ \xrightarrow{192.4} 0_g^+$	519.4, 641.5, 734.0, 799.5, 860.4	0.082(4),0.015(6)
$2_\gamma^+ \xrightarrow{619.7} 2_g^+ \xrightarrow{192.4} 0_g^+$	771.3, 477.6, 330.9*, 199.6*, 431.5*, 509.4*, 240.8, 343.3*, 402.7, 215.8	-0.12(2),0.23(3)
$3_\gamma^+ \xrightarrow{835.5} 2_g^+ \xrightarrow{192.4} 0_g^+$	555.5, 199.6*, 477.7, 331.0*	-0.146(9),-0.069(13)
$4_\gamma^+ \xrightarrow{653.8} 4_g^+ \xrightarrow{368.6} 2_g^+$	192.4, 509.6, 331.1*, 199.6*, 431.5*, 368.7, 477.7, 112.9*, 117.6*, 260.0	-0.155(13),0.16(2)
$5_\gamma^+ \xrightarrow{913.7} 4_g^+ \xrightarrow{368.6} 2_g^+$	192.4, 561.1, 646.0, 199.5*	-0.105(11),-0.06(2)
$7_\gamma^+ \xrightarrow{956.3} 6_g^+ \xrightarrow{519.4} 4_g^+$	192.4, 386.6, 645.9, 713.7 199.5*, 331.0*, 431.4*, 117.8*	-0.01(3),0.07(5)
$9_\gamma^+ \xrightarrow{960.9} 8_g^+ \xrightarrow{641.5} 6_g^+$	192.4, 368.6, 519.3, 199.6*, 331.2*, 117.7*, 113.2*, 431.7*, 713.4, 164.7*	0.10(6),-0.15(9)

*Indicates that this additional gate is from a fission partner

Figure 3.3: Angular correlations measured for ^{102}Mo. Top left: $4_g^+ \to 2_g^+ \to 0_g^+$. Top right: $2_\gamma^+ \to 2_g^+ \to 0_g^+$. Bottom left: $3_\gamma^+ \to 2_g^+ \to 0_g^+$. Bottom right: $4_\gamma^+ \to 4_g^+ \to 2_g^+$.

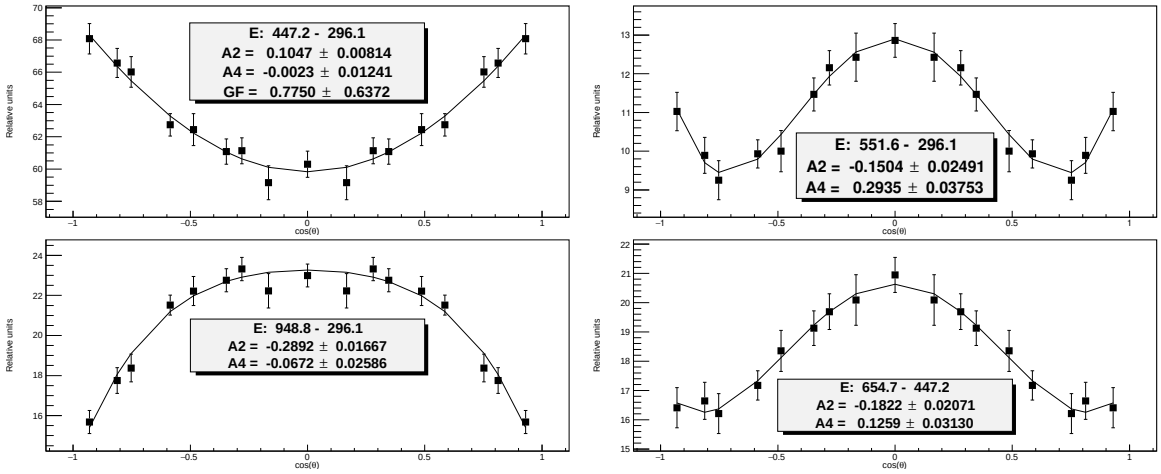

Table 3.3: Angular correlations measured for ^{106,108}Mo

Correlation $J^\pi \overset{(keV)}{\rightarrow} J^\pi \overset{(keV)}{\rightarrow} J^\pi$	Additional Gates (keV)	A_2^{raw}, A_4^{raw}
^{106}Mo		
$4_g^+ \overset{350.8}{\rightarrow} 2_g^+ \overset{171.8}{\rightarrow} 0_g^+$	654.9	0.076(8),0.014(12)
$2_\gamma^+ \overset{538.7}{\rightarrow} 2_g^+ \overset{171.8}{\rightarrow} 0_g^+$	724.4, 359.8*	-0.140(13),0.15(2)
$3_\gamma^+ \overset{713.6}{\rightarrow} 2_g^+ \overset{171.8}{\rightarrow} 0_g^+$	421.6, 1051.6, 772.5, 549.5	-0.058(8),-0.046(12)
$4_\gamma^+ \overset{545.4}{\rightarrow} 4_g^+ \overset{350.8}{\rightarrow} 2_g^+$	171.8, 495.5	-0.192(10),0.11(2)
$5_\gamma^+ \overset{784.4}{\rightarrow} 4_g^+ \overset{350.8}{\rightarrow} 2_g^+$	171.8, 561.1, 784.1, 199.5*, 359.7*	0.023(7),-0.046(11)
$6_\gamma^+ \overset{529.9}{\rightarrow} 6_g^+ \overset{510.9}{\rightarrow} 4_g^+$	171.8, 350.7	-0.07(2),0.04(3)
$7_\gamma^+ \overset{834.9}{\rightarrow} 6_g^+ \overset{510.9}{\rightarrow} 4_g^+$	None	0.08(3),-0.08(5)
^{108}Mo		
$4_g^+ \overset{371.0}{\rightarrow} 2_g^+ \overset{193.1}{\rightarrow} 0_g^+$	527.1, 662.1, 414.6	0.080(15),0.00(2)
$2_\gamma^+ \overset{393.0}{\rightarrow} 2_g^+ \overset{193.1}{\rightarrow} 0_g^+$	392.7	-0.08(3),0.19(5)
$3_\gamma^+ \overset{590.1}{\rightarrow} 2_g^+ \overset{193.1}{\rightarrow} 0_g^+$	449.3, 585.2, 916.0, 639.4, 706.9, 724.8, 1047.2, 1129.4, 991.4, 1091.7	-0.12(2),-0.03(4)
$4_\gamma^+ \overset{414.6}{\rightarrow} 4_g^+ \overset{371.0}{\rightarrow} 2_g^+$	529.7, 588.8*, 602.2*, 662.2, 658.4*, 253.9, 720.2, 779.0, 978.8	-0.12(4),0.10(6)

*Indicates that this additional gate is from a fission partner

Table 3.4: Mixing ratios (δ) measured in this work for the isotopes of Mo. The A_2^{raw},A_4^{raw} values are copied from tables 3.2 and 3.3, while A_2^{cor},A_4^{cor} are the same values corrected according to the data presented in table 3.1. Often two solutions are warranted for δ, given A_2^{exp},A_4^{exp} within 3σ. Square braces, "[ ]", indicate that A_2^{thry} (or A_4^{thry}) differs from A_2^{exp} (A_4^{exp}) by 1.5σ or more.

Transition	A_2^{raw},A_4^{raw}	A_2^{cor},A_4^{cor}	δ	A_2^{thry},A_4^{thry}
		^{102}Mo		
$2_\gamma^+ \rightarrow 2_g^+$	-0.15(2),0.29(4)	-	9^{+3}_{-2}	-0.152,0.323
$3_\gamma^+ \rightarrow 2_g^+$	-0.29(3),-0.07(3)	-	-9^{+2}_{-3} [-0.28(2)]	-0.289,-0.081 -0.285,[-0.006]
$4_\gamma^+ \rightarrow 4_g^+$	-0.18(2),0.13(3)	-	2^{+3}_{-1}	-0.179,0.131
		^{104}Mo		
$2_\gamma^+ \rightarrow 2_g^+$	-0.12(2),0.23(3)	-0.15(3),0.39(8)	9^{+4}_{-2}	-0.150,0.323
$3_\gamma^+ \rightarrow 2_g^+$	-0.146(9),-0.069(13)	-0.185(14),-0.12(3)	42^{+90}_{-17}	-0.185,-0.082
$4_\gamma^+ \rightarrow 4_g^+$	-0.155(13),0.16(2)	-	7^{+3}_{-1}	-0.156,0.148
$5_\gamma^+ \rightarrow 4_g^+$	-0.105(11),-0.6(2)	-	30^{+16}_{-8}	-0.105,-0.059
$7_\gamma^+ \rightarrow 6_g^+$	-0.01(3),0.07(5)	-	0.10(4) $[7^{+3}_{-1}]$	-0.007,-0.001 -0.007,[-0.050]
$9_\gamma^+ \rightarrow 8_g^+$	0.10(6),-0.15(9)	-	$2.9^{+1.1}_{-0.7}$ $[0.31^{+0.10}_{-0.09}]$	0.102,-0.043 0.102,[-0.004]
		^{106}Mo		
$2_\gamma^+ \rightarrow 2_g^+$	-0.140(13),0.15(2)	-0.18(2),0.27(5)	$6.6^{+1.1}_{-0.8}$	-0.178,0.319
$3_\gamma^+ \rightarrow 2_g^+$	-0.058(8),-0.046(12)	-0.074(10),-0.08(2)	$6.0^{+0.4}_{-0.3}$	-0.074,-0.079
$4_\gamma^+ \rightarrow 4_g^+$	-0.192(10),0.11(2)	-	$[2.1^{+0.6}_{-0.4}]$	[-0.177],0.123††
$5_\gamma^+ \rightarrow 4_g^+$	0.023(7),-0.046(11)	-	4.4(2)	0.023,-0.056
$6_\gamma^+ \rightarrow 6_g^+$	-0.07(2),0.04(3)	-	$1.09^{+0.14}_{-0.10}$ $[-5^{+1}_{-2}]$	-0.075,0.061 -0.075,[0.108]
$7_\gamma^+ \rightarrow 6_g^+$	0.08(3),-0.08(5)	-	$3.2^{+0.8}_{-0.6}$ $0.26^{+0.06}_{-0.05}$	0.080,-0.047 0.080,-0.003
		^{108}Mo		
$2_\gamma^+ \rightarrow 2_g^+$	-0.08(3),0.19(5)	-0.11(4),0.32(9)	$25^{+\infty}_{-16}$ $[0.49^{+0.06}_{-0.05}]$	-0.105,0.326 -0.104,[0.064]
$3_\gamma^+ \rightarrow 2_g^+$	-0.12(2),-0.03(4)	-0.15(4),-0.05(6)	14^{+25}_{-5} -0.10(4)	-0.148,-0.081 -0.148,-0.001
$4_\gamma^+ \rightarrow 4_g^+$	-0.12(4),0.10(6)	-	1.1(2) $\infty(^{>+6}_{<-9})^{\ddagger}$	-0.119,0.080 -0.118,0.152

††For this measurement, δ was calculated using both A_2^{exp} and A_4^{exp}, rather than only A_2^{exp}.

‡This solution is exactly pure E2 ($\delta = \pm\infty$). In parentheses are values allowed within 1σ.

Figure 3.4: Various δ ovals are shown here compared to the 948.8 keV – 296.1 keV angular correlation from ^{102}Mo, demonstrating the confirmation of the spin of the 1244.9 keV level.

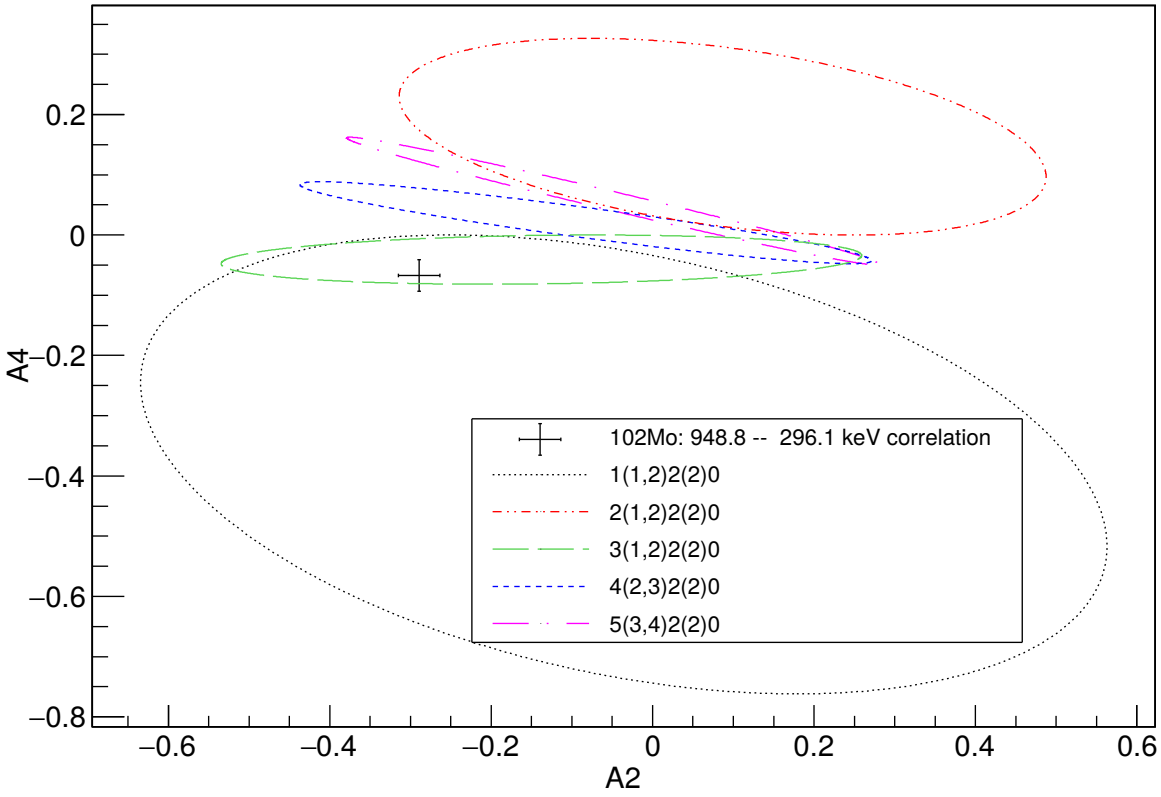

3.2.1.1 ^{102}Mo

The plots of the angular correlations measured for ^{102}Mo are shown in figure 3.3. In ^{102}Mo, the present work has confirmed the assignments of Yang *et al.* [50], that the band with the 2^+, 847.5 keV band-head is the one phonon γ-band for ^{102}Mo and their assignment of the 1244.9, (3^+) level to this band. Figure 3.4 compares the result of this correlation to the δ ovals corresponding to each of the possible spins for this level from 1 to 5. Clearly only the 3(1,2)2(2)0 oval matches the results of the correlation, thus we firmly assign a spin of 3 to the 1244.9 level. These results are also consistent with the assignments of Wang *et al.* [51].

The $2_g^+ \rightarrow 0_g^+$ transition, 296.1 keV, in ^{102}Mo is close in energy to the $4_g^+ \rightarrow 2_g^+$, 295.2 keV transition in ^{148}Ce. This meant that care had to be taken in selecting extra gates so that no contamination from this isotope entered the data for correlations which include this transition. For the $4_g^+ \rightarrow 2_g^+ \rightarrow 0_g^+$ and the $2_\gamma^+ \rightarrow 2_g^+ \rightarrow 0_g^+$ cascades, this was not a big deal since most of the contamination was removed by the requirement that the γ-ray be in coincidence with either the 447.2 keV or 551.4 keV γ-rays, which are not seen in ^{148}Ce. For the $2_\gamma^+ \rightarrow 2_g^+ \rightarrow 0_g^+$ cascade, the 401.1 keV γ-ray was not used as an additional gate, even though it is the second strongest peak in the coincidence spectrum, because it is also expected to be in coincidence with the $4_g^+ \rightarrow 2_g^+$, 295.2 keV γ-ray of ^{148}Ce. The results of this angular correlation are plotted in the top left of figure 3.3, and compared to the 2(1,2)2(2)0 oval in figure 3.5. Based on these considerations the mixing ratio for the $2_\gamma^+ \rightarrow 2_g^+$ transition is observed to be $\delta = 7.0^{+1.8}_{-0.6}$, as displayed in table 3.4.

However, for the $3_\gamma^+ \rightarrow 2_g^+ \rightarrow 0_g^+$ cascade, both γ-ray energies are found in ^{148}Ce. The $3_\gamma^+ \rightarrow 2_g^+$ transition in ^{102}Mo has energy of 948.8 keV, while the $7_\gamma^+ \rightarrow 6_g^+$ transition in ^{148}Ce has energy, 948.9 keV. This means that many of the peaks in the spectrum were from ^{148}Ce and the various isotopes of Zr, the fission partner of Ce. All of the gates chosen are from ^{102}Mo or one of the isotopes of Ba, the fission partner of Mo, and were carefully inspected to make sure they are not close to those of ^{148}Ce or $^{100-103}$Zr. This correlation is plotted in the bottom left of figure 3.3, compared with multiple δ ovals in figure 3.4, and compared to the 3(1,2)2(2)0 δ oval and the other $3_\gamma^+ \rightarrow 2_g^+ \rightarrow 0_g^+$ correlations in figure 3.6. Based on these considerations, we observe $\delta = -9^{+2}_{-3}$ for this transition, as recorded in table 3.4. However, as also noted in table 3.4, $\delta = -0.28(2)$ cannot be ruled out with 3σ confidence.

There were no surprises with the $4_\gamma^+ \rightarrow 4_g^+ \rightarrow 2_g^+$ correlation for ^{102}Mo. It is plotted in the bottom right of figure 3.3 and compared to the δ oval for 4(1,2)4(2)2 in figure 3.7. Based on these results, we extract $\delta = 2^{+3}_{-1}$ as the value for the mixing ratio for this transition.

Figure 3.5: A plot of all the $2^+_\gamma \rightarrow 2^+_g \rightarrow 0^+_g$ correlations measured in this work compared to the 2(1,2)2(2)0 δ oval.

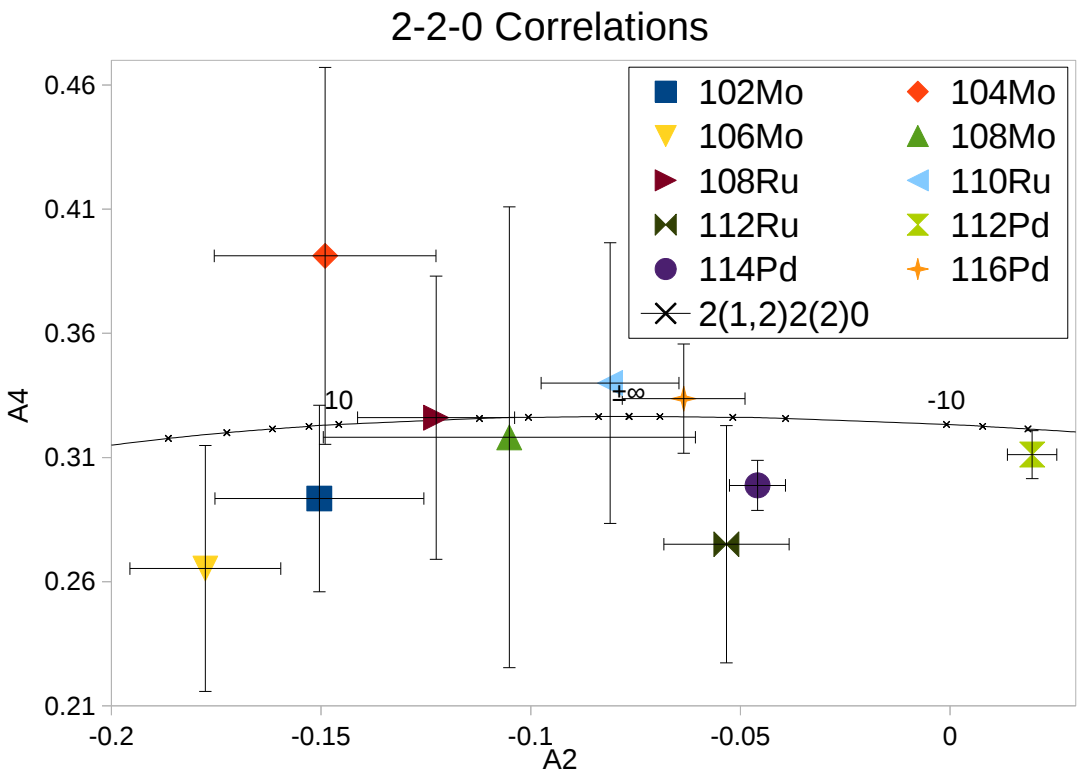

Figure 3.6: A plot of all the $3^+_\gamma \rightarrow 2^+_g \rightarrow 0^+_g$ correlations measured in this work compared to the 3(1,2)2(2)0 δ oval.

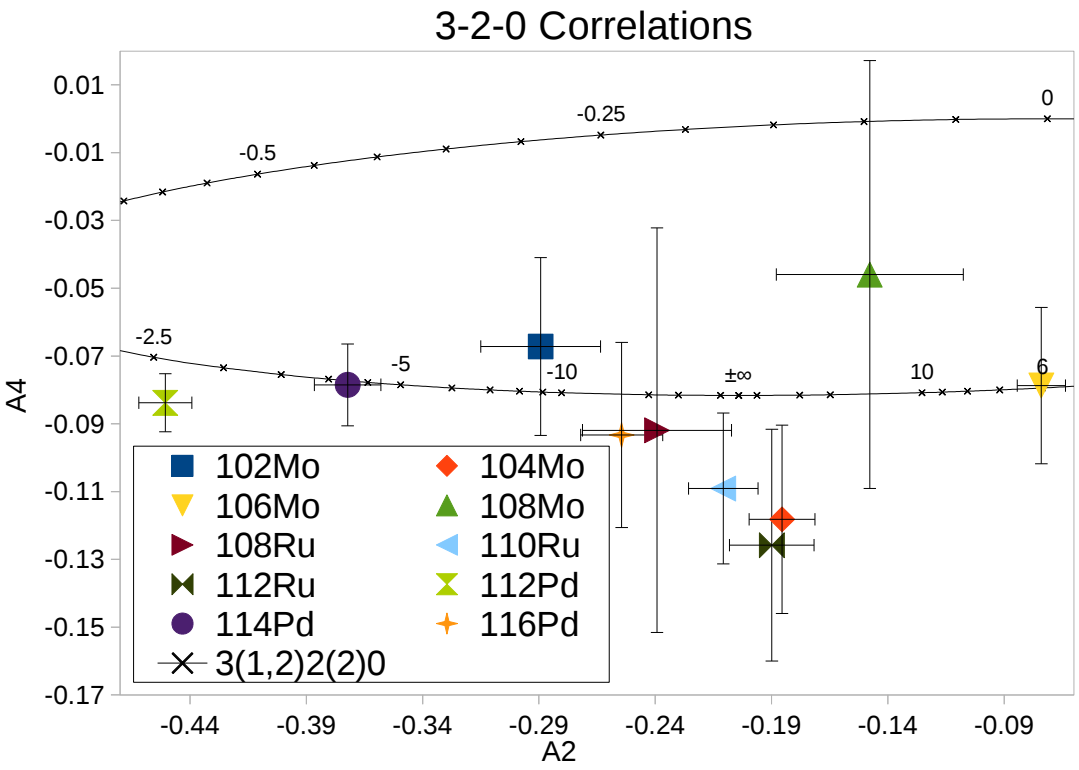

Figure 3.7: A plot of all the $4^+_\gamma \rightarrow 4^+_g \rightarrow 2^+_g$ correlations measured in this work compared to the 4(1,2)4(2)2 δ oval.

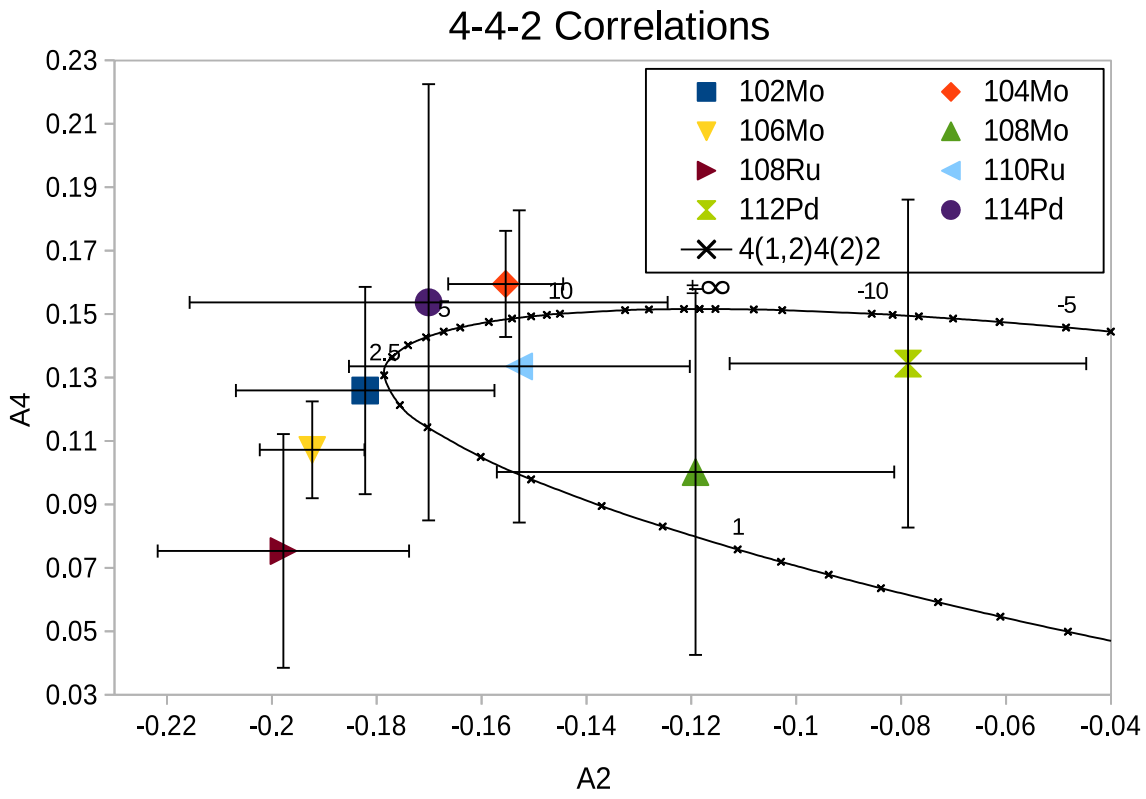

Figure 3.8: Angular correlations measured for ^{104}Mo. Top left: $4^+_g \rightarrow 2^+_g \rightarrow 0^+_g$. Top right: $2^+_\gamma \rightarrow 2^+_g \rightarrow 0^+_g$. Second left: $3^+_\gamma \rightarrow 2^+_g \rightarrow 0^+_g$. Second right: $4^+_\gamma \rightarrow 4^+_g \rightarrow 2^+_g$. Third left: $5^+_\gamma \rightarrow 4^+_g \rightarrow 2^+_g$. Third right: $7^+_\gamma \rightarrow 6^+_g \rightarrow 4^+_g$. Bottom: $9^+_\gamma \rightarrow 8^+_g \rightarrow 6^+_g$.

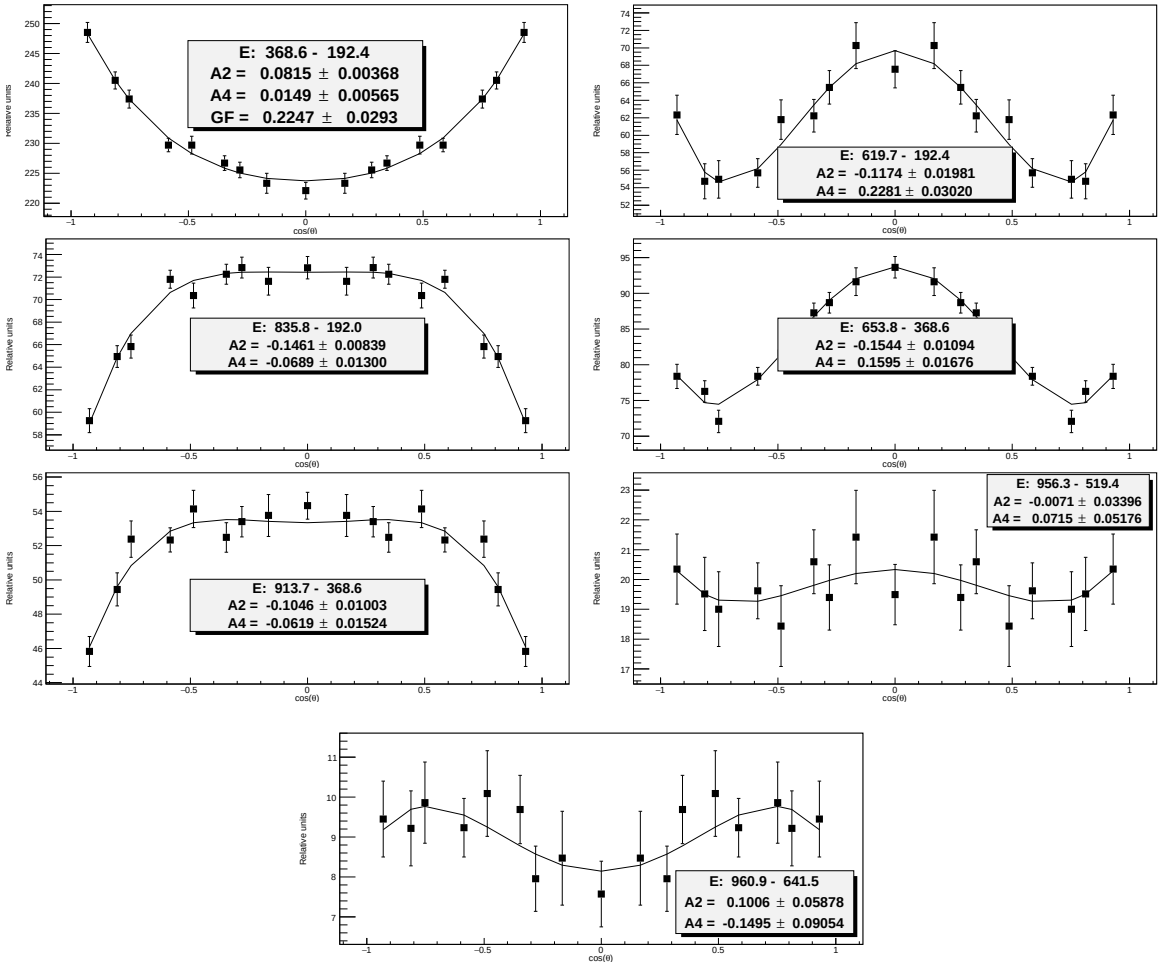

3.2.1.2 ^{104}Mo

Because ^{104}Mo and its primary fission partner ^{144}Ba are the two most common products of the spontaneous fission (SF) of ^{252}Cf, our data had sufficient statistics to measure the mixing ratios up to that of the $9^+_\gamma \rightarrow 8^+_g$ transition.

Because we have such good statistics concerning ^{104}Mo, especially the transitions lower in its level scheme, the correlations for measuring the mixing ratios for the transitions from the 2^+_γ, 3^+_γ, 4^+_γ, and 5^+_γ were all straight forward. These are plotted in figure 3.8. The A_2,A_4 values given for the $2^+_\gamma \rightarrow 2^+_g \rightarrow 0^+_g$ and the $3^+_\gamma \rightarrow 2^+_g \rightarrow 0^+_g$ were each subsequently

Figure 3.9: A plot of all the $5^+_\gamma \rightarrow 4^+_g \rightarrow 2^+_g$ correlations measured in this work compared to the 5(1,2)4(2)2 δ oval.

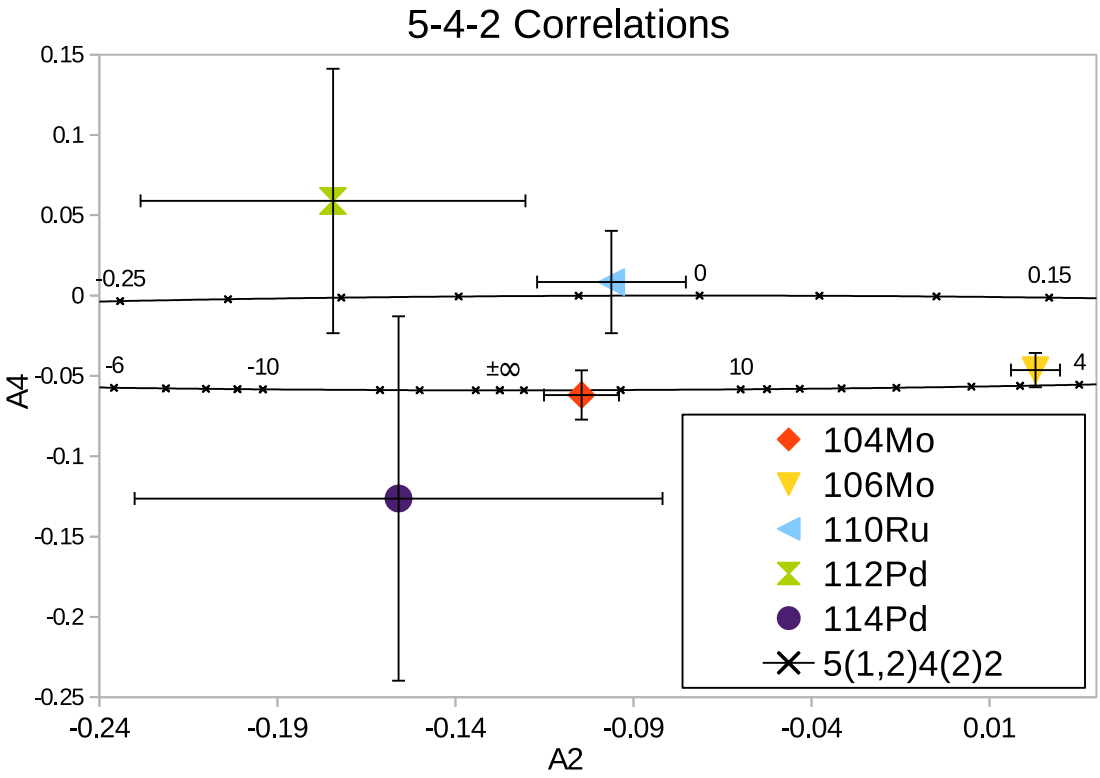

corrected for attenuation according to Table 3.1. These are compared with their respective δ ovals in figures 3.5, 3.6, 3.7, and 3.9. We have observed values of $\delta = 9^{+4}_{-2}$, 42^{+90}_{-17}, 7^{+3}_{-1}, and 30^{+16}_{-8} for the $2^+_\gamma \rightarrow 2^+_g$, $3^+_\gamma \rightarrow 2^+_g$, $4^+_\gamma \rightarrow 4^+_g$, and $5^+_\gamma \rightarrow 4^+_g$ transitions, respectively.

The statistics for the $6^+_\gamma \rightarrow 6^+_g \rightarrow 4^+_g$ correlation were insufficient to overcome the contamination from similar energies from the 2 neutron fission partner of ^{104}Mo, ^{146}Ba and from its own $8^+_g \rightarrow 6^+_g$ transition. Therefore, no satisfactory measurement of the mixing ratio was able to be determined for this transition.

Though the statistics were still relatively low for the $7^+_\gamma \rightarrow 6^+_g \rightarrow 4^+_g$ correlation, they were still significantly higher than for the $6^+_\gamma \rightarrow 6^+_g \rightarrow 4^+_g$. There also were no major sources of contamination. The results of this angular correlation are plotted in figure 3.8. The value of A_4 for this result placed it decently above the δ oval as shown in figure 3.10.

Figure 3.10: A plot of all the $7^+_\gamma \rightarrow 6^+_g \rightarrow 4^+_g$ correlations measured in this work compared to the 7(1,2)6(2)4 δ oval.

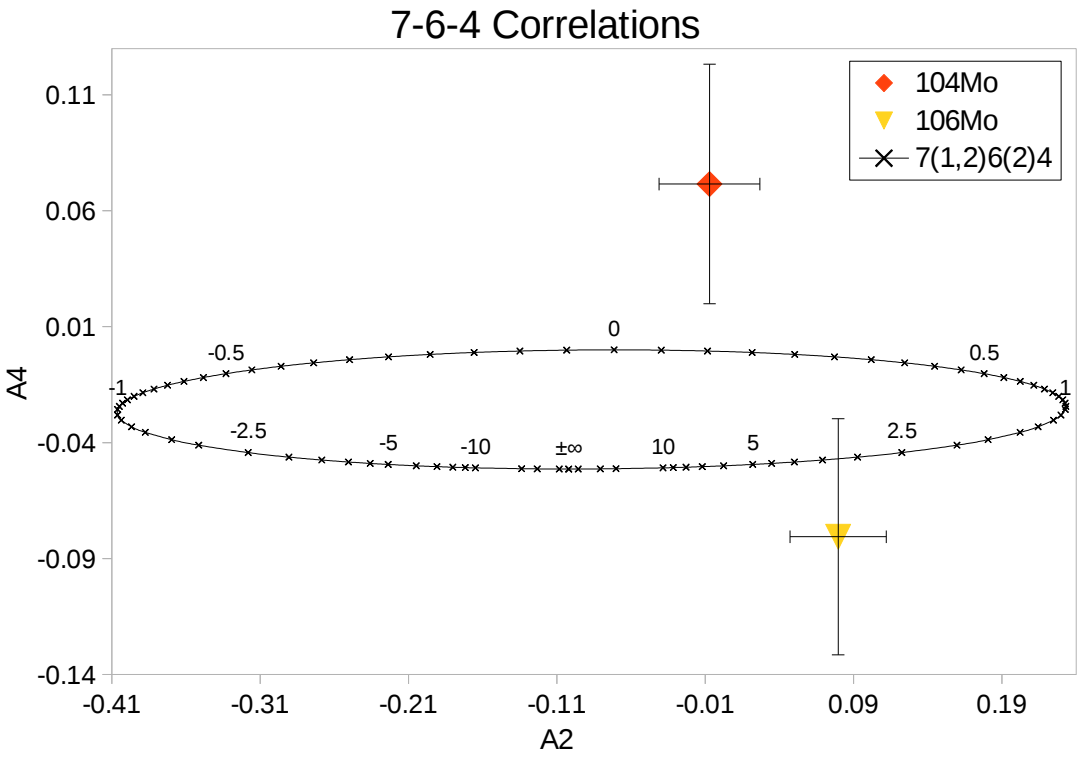

Figure 3.11: A plot the $9^+_\gamma \rightarrow 8^+_g \rightarrow 6^+_g$ correlation measured in this work for ^{104}Mo compared to the 9(1,2)8(2)6 δ oval.

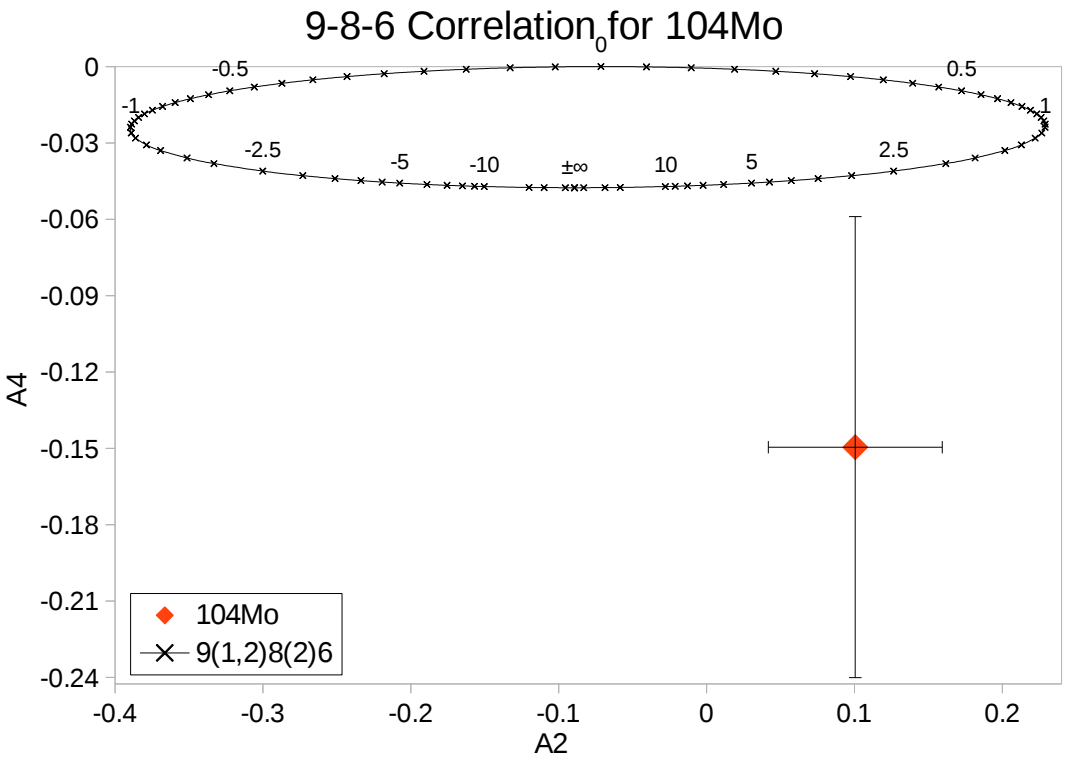

A low value of $\delta = 0.10(4)$, indicating about only 1 %E2, can be assigned to this transition with about 1.4σ variation from the experimental value of A_4. If, on the other hand, up to 2.4σ variation is allowed, a solution of $\delta = 7^{+3}_{-1}$, corresponding to approximately 98 %E2, can be assigned. Both of these solutions are shown in table 3.4.

A clear determination of the mixing ratio for the $8^+_\gamma \rightarrow 8^+_g$, 604.8 keV transition could not be made because the low statistics were insufficient to distinguish it from platform in our data that occurs at about 595 to 610 kev, due to neutron interactions with the HPGe crystals.

The $9^+_\gamma \rightarrow 8^+_g \rightarrow 6^+_g$ correlation is at the limit, statistically, of our angular correlation procedure. However, there were no major sources of contamination allowing us to make a decent determination of the mixing ratio for this transition. The correlation is plotted in

the bottom right of figure 3.8 and compared with the δ oval in figure 3.11. Based on these results, a value of $\delta = 2.9^{+1.1}_{-0.7}$ is the best observation of the mixing ratio for the $9^+_\gamma \rightarrow 8^+_g$ transition in ^{104}Mo. However, as shown in table 3.4, $\delta = 0.31^{+0.10}_{-0.09}$ cannot be ruled out with 3σ certainty.

3.2.1.3 ^{106}Mo

Like ^{104}Mo, ^{106}Mo is a frequent product of the SF of ^{252}Cf. For this reason we were able to make determinations of the mixing ratios of γ-band to ground-state-band transitions from as high as the 8^+_γ level. The partial level scheme considered in this work for ^{106}Mo is given in figure 3.2.

As with ^{104}Mo, the first few transitions from the γ-band to the yrast-band in ^{106}Mo were straightforward because of the high statistics in our data. In accordance with the information in table 3.1, the $2^+_\gamma \rightarrow 2^+_g \rightarrow 0^+_g$ and $3^+_\gamma \rightarrow 2^+_g \rightarrow 0^+_g$ correlations as shown in figure 3.12, were corrected by attenuation factors, $G_2, G_4 = 0.78(6), 0.6(2)$ before being compared to their respective δ ovals in figures 3.5 and 3.6. Based on these analyses we have observed a value of $\delta = 6.6^{+1.1}_{-0.8}$ and $\delta = 6.0^{+0.4}_{-0.3}$ as the mixing ratios of the $2^+_\gamma \rightarrow 2^+_g$ and $3^+_\gamma \rightarrow 2^+_g$ transitions respectively.

The mixing ratios for the $4^+_\gamma \rightarrow 4^+_g$ and $5^+_\gamma \rightarrow 4^+_g$ transitions were also straightforward. The correlations for these transitions are shown in figure 3.12. These correlations are then compared to their respective δ ovals in figures 3.7 and 3.9. Based on these analyses we extract a value of $\delta = 2.1^{+0.6}_{-0.4}$ for the $4^+_\gamma \rightarrow 4^+_g$ transition and $\delta = 4.4(2)$ for the $5^+_\gamma \rightarrow 4^+_g$ transition, as stated in table 3.4.

The $6^+_\gamma \rightarrow 6^+_g \rightarrow 4^+_g$ and $7^+_\gamma \rightarrow 6^+_g \rightarrow 4^+_g$ correlations both had the same difficulty; the energy of the $6^+_g \rightarrow 4^+_g$ transition is 510.9 keV. In ^{144}Ba, the $8^+_g \rightarrow 6^+_g$, 509.5 keV and $5^- \rightarrow 4^+_g$, 509.0 keV transitions are both strong in intensity, bringing in some contamination to the spectrum from this 2-neutron fission partner of ^{106}Mo. However, and more importantly,

Figure 3.12: Angular correlations measured for ^{106}Mo. Top left: $4^+_g \rightarrow 2^+_g \rightarrow 0^+_g$. Top right: $2^+_\gamma \rightarrow 2^+_g \rightarrow 0^+_g$. Second left: $3^+_\gamma \rightarrow 2^+_g \rightarrow 0^+_g$. Second right: $4^+_\gamma \rightarrow 4^+_g \rightarrow 2^+_g$. Third left: $5^+_\gamma \rightarrow 4^+_g \rightarrow 2^+_g$. Third right: $6^+_\gamma \rightarrow 6^+_g \rightarrow 4^+_g$. Bottom: $7^+_\gamma \rightarrow 6^+_g \rightarrow 4^+_g$.

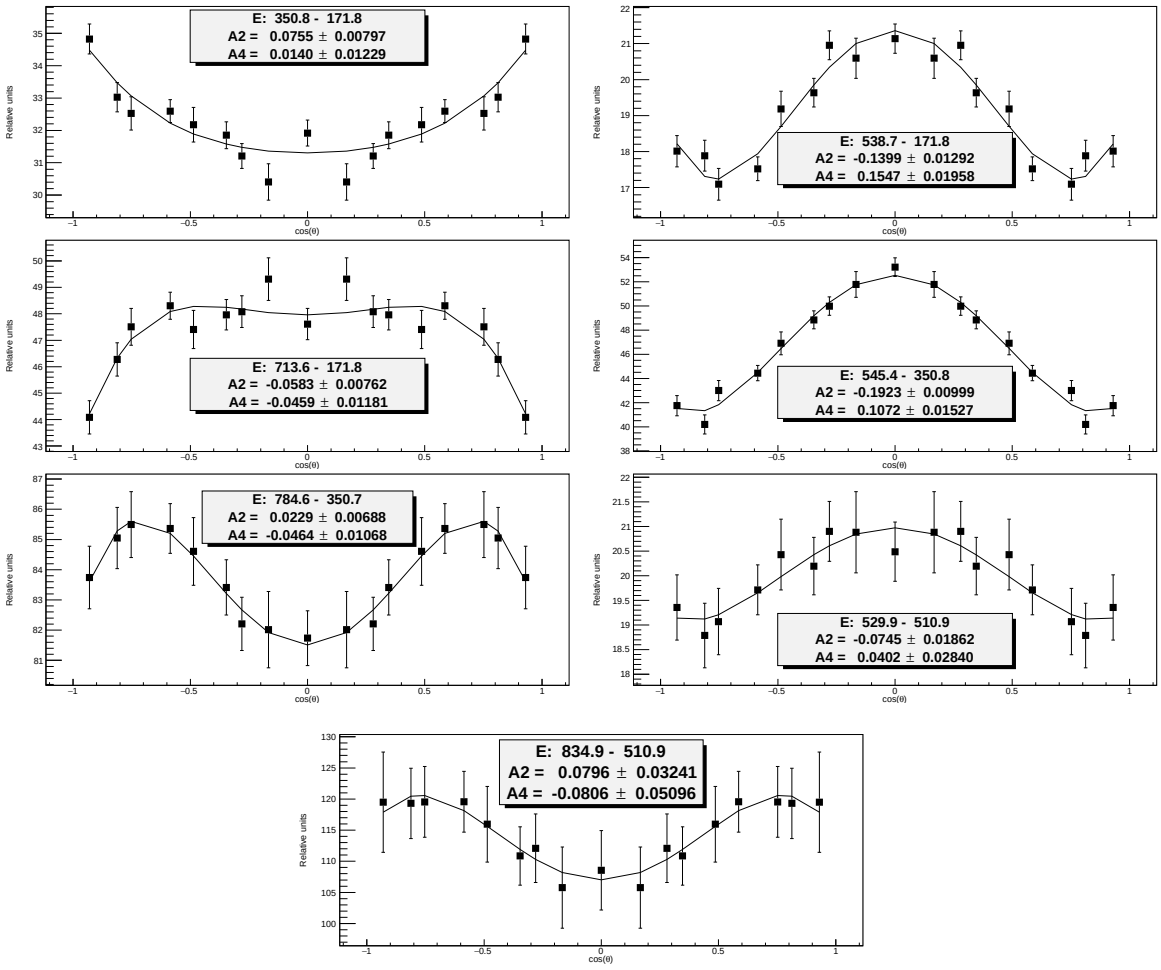

Figure 3.13: A plot the $6^+_\gamma \rightarrow 6^+_g \rightarrow 4^+_g$ correlation measured in this work for ^{106}Mo compared to the 6(1,2)6(2)4 δ oval.

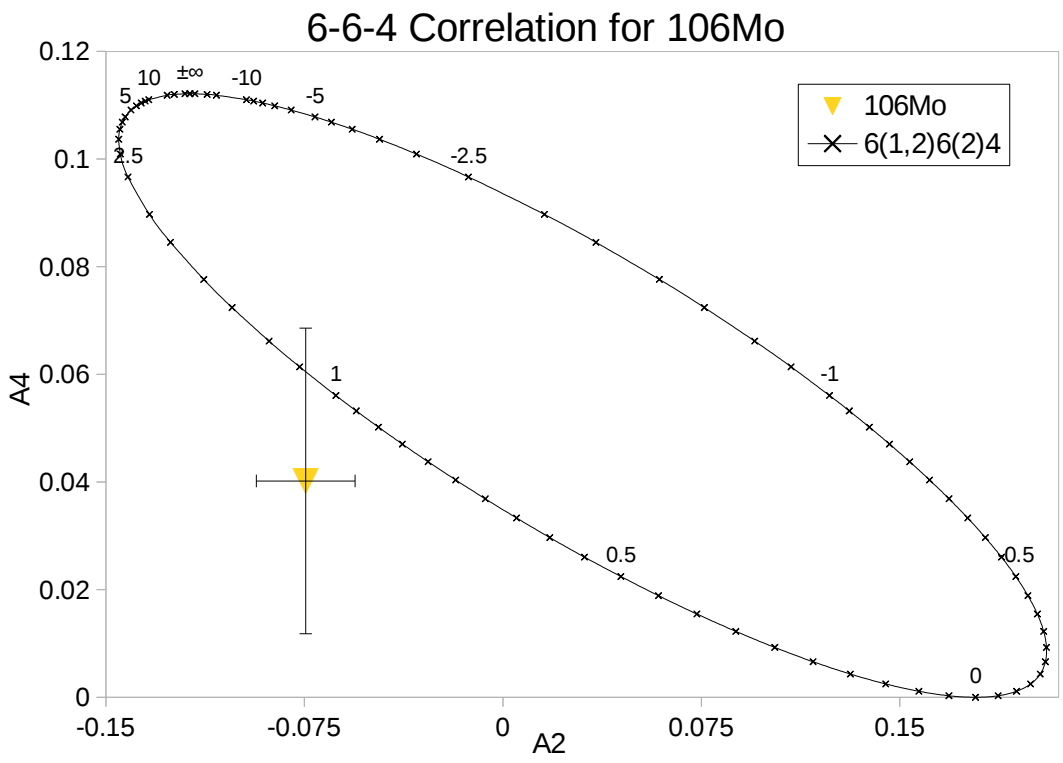

our data commonly see 511.0 keV γ-rays from the annihilation of positrons. For these reasons, the uncertainties from these two correlations are larger.

The $6^+_\gamma \rightarrow 6^+_g \rightarrow 4^+_g$ correlation is shown figure 3.12 and compared to the δ oval in figure 3.13. Based on these results, the best solution (falling at 0.7σ for A_4^{exp}) is $\delta = 1.09^{+0.14}_{-0.10}$. However, since the error bars are statistical, it is plausible to allow even larger deviations. Thus, if 2.4σ deviation is allowed for A_4^{exp} we can assign a value of $\delta = -5^{+1}_{-2}$ for this transition's mixing ratio. Both of these solutions are displayed in table 3.4.

The $7^+_\gamma \rightarrow 6^+_g \rightarrow 4^+_g$ correlation is plotted on the bottom left of figure 3.12 and compared to the δ oval in figure 3.10. From figure 3.10 it should be clear that there are two solutions for the mixing ratio of the $7^+_\gamma \rightarrow 6^+_g$ of ^{106}Mo within 1.5σ. The first, and more likely,

Figure 3.14: Angular correlations measured for ^{108}Mo. Top left: $4^+_g \rightarrow 2^+_g \rightarrow 0^+_g$. Top right: $2^+_\gamma \rightarrow 2^+_g \rightarrow 0^+_g$. Bottom left: $3^+_\gamma \rightarrow 2^+_g \rightarrow 0^+_g$. Bottom right: $4^+_\gamma \rightarrow 4^+_g \rightarrow 2^+_g$.

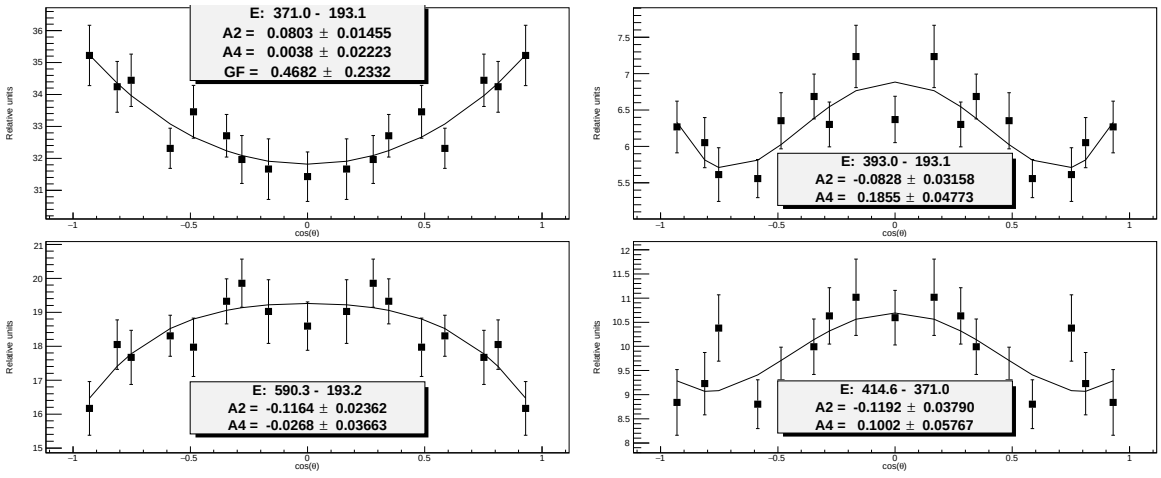

solution lies at 0.7σ in A_4 and is $3.2^{+0.8}_{-0.6}$. The second solution, $0.26^{+0.06}_{-0.05}$, falls at 1.3σ in A_4. Both of these solutions are displayed in table 3.4.

3.2.1.4 ^{108}Mo

The lower frequency with which ^{108}Mo is produced in the SF of ^{252}Cf than the other isotopes of Mo meant we were only able to make determinations of the mixng ratios up to transitions from the 4^+_γ state. The partial level scheme of ^{108}Mo is given in figure 3.2.

The similarity in energies between the $4^+_\gamma \rightarrow 2^+_\gamma$, 392.5 keV transition and the $2^+_\gamma \rightarrow 2^+_g$, 393.0 keV transition caused difficulty in measuring the $2^+_\gamma \rightarrow 2^+_g \rightarrow 0^+_g$ angular correlation. Several different extra gate combinations were tried to remove this contamination. Ultimately it was determined that using only the $4^+_\gamma \rightarrow 2^+_\gamma$ itself produced the least attenuated and clearest correlation. This correlation is plotted in the top right of figure 3.14. The values corrected according to table 3.1 are then compared to the δ oval in figure 3.5. Often the uncertainty in A_2, A_4 space will include the point where $\delta = \pm\infty$. This is usually signified by an error of $+\infty$ on positive values or $-\infty$ on negative values, and means that Pure E2 as well as both positive and negative values of δ are within 1σ in A_2, A_4 space. For ^{108}Mo, one solution lies at $\delta = 23^{+\infty}_{-14}$. In this case, in addition to indicating that pure E2 lies within

1σ, the $+\infty$ uncertainty indicates that values of $\delta < -51$ are allowed within 1σ in A_2, A_4 space.

The $3^+_\gamma \rightarrow 2^+_g \rightarrow 0^+_g$ correlation was straightforward, though the statistics were relatively low, causing the uncertainty to be high. This correlation is plotted as the bottom left of figure 3.14. This correlation was corrected for attenuation according to table 3.1 and then compared to the δ oval in figure 3.6. This result produced two possible solutions within 1σ. At about 0.6σ in A_4 is $\delta(E2/M1) = 14^{+25}_{-5}$, while at about 0.7σ lies $\delta(E2/M1) = -0.10(4)$. Both values are listed as possibilities for the mixing ratio for the $3^+_\gamma \rightarrow 2^+_g$ transition in table 3.4.

The $4^+_\gamma \rightarrow 4^+_g \rightarrow 2^+_g$ correlation was also straightforward but with low statistics. This correlation is plotted in the bottom right of figure 3.14 and compared to the δ oval in figure 3.7. Based on these results, and the relatively large uncertainties on A_2^{exp}, A_4^{exp}, there were two solutions within 1σ. The first solution, at about 0.4σ in A_4^{exp}, is $\delta(E2/M1) = 1.1(2)$. The second solution, at about 0.9σ in A_4^{exp}, is exactly pure E2, or $\delta(E2/M1) = \pm\infty$ with uncertainties that allow positive values > 6 or negative values < -9. Both solutions are shown in table 3.4.

3.2.2 Isotopes of Ru.

Partial level schemes of the isotopes of Ru considered in this work can be found in figure 3.15. The complete level schemes for the isotopes of Ru considered in this work can be found in Luo *et al.* [55] and Zhu *et al.* [56].

The raw angular correlations for isotopes of Ru are shown in table 3.5. Their analysis to find $\delta(E2/M1)$ mixing ratios is shown in table 3.6.

3.2.2.1 ^{108}Ru

The first few transitions in the Yrast Bands of ^{108}Ru and ^{110}Ru are extremely similar. This caused difficulty measuring the $4^+_g \rightarrow 2^+_g \rightarrow 0^+_g$ correlations for these two isotopes. Only transition energies seen in one isotope, but not the other, were chosen as additional

Figure 3.15: Partial Level Schemes of the isotopes of Ru considered in this work

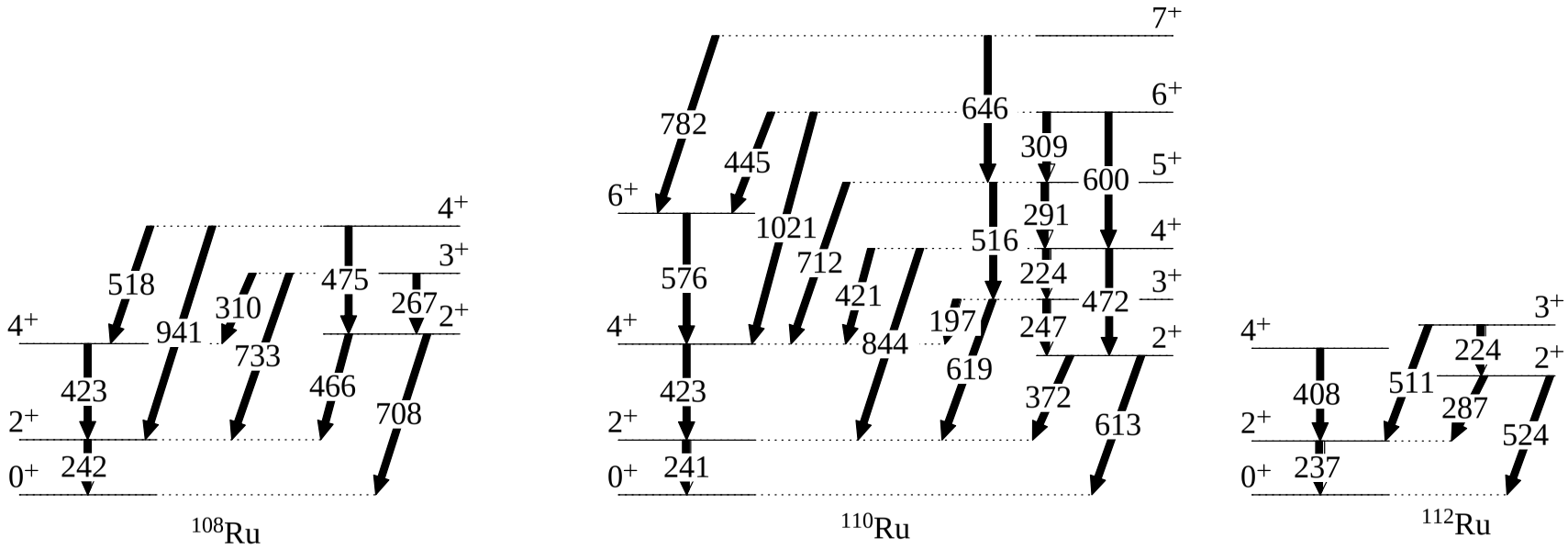

Table 3.5: Angular correlations measured for isotopes of Ru.

Correlation $J^\pi \overset{(keV)}{\rightarrow} J^\pi \overset{(keV)}{\rightarrow} J^\pi$	Additional Gates (keV)	A_2^{raw},A_4^{raw}
^{108}Ru		
$4_g^+ \overset{422.9}{\rightarrow} 2_g^+ \overset{242.3}{\rightarrow} 0_g^+$	1445.5, 797.7, 517.7, 162.5, 442.9, 1232.2	0.090(14),0.02(2)
$2_\gamma^+ \overset{465.7}{\rightarrow} 2_g^+ \overset{242.3}{\rightarrow} 0_g^+$	None	-0.102(14),0.21(2)
$3_\gamma^+ \overset{732.6}{\rightarrow} 2_g^+ \overset{242.1}{\rightarrow} 0_g^+$	521.2, 851.0, 637.1, 669.1, 182.2, 710.7, 199.5, 725.5, 443.2, 771.1	-0.20(2),-0.06(4)
$4_\gamma^+ \overset{518.5}{\rightarrow} 4_g^+ \overset{422.3}{\rightarrow} 2_g^+$	242.5, 376.8*, 579.4, 457.5*, 483.7*, 571.5*, 582.5*, 588.8*, 585.4*, 77.1*	-0.20(2),0.08(4)
^{110}Ru		
$4_g^+ \overset{422.6}{\rightarrow} 2_g^+ \overset{240.8}{\rightarrow} 0_g^+$	705.3, 815.0	0.083(6),0.021(9)
$2_\gamma^+ \overset{372.2}{\rightarrow} 2_g^+ \overset{240.9}{\rightarrow} 0_g^+$	471.8, 599.8, 247.3, 712.8, 515.5, 291.0	-0.067(13),0.22(2)
$3_\gamma^+ \overset{619.1}{\rightarrow} 2_g^+ \overset{240.8}{\rightarrow} 0_g^+$	515.5, 645.6, 867.9, 394.6	-0.175(8),-0.071(11)
$4_\gamma^+ \overset{421.0}{\rightarrow} 4_g^+ \overset{422.6}{\rightarrow} 2_g^+$	599.9, 712.9, 291.0, 931.8	-0.15(3),0.13(5)
$5_\gamma^+ \overset{711.9}{\rightarrow} 4_g^+ \overset{422.6}{\rightarrow} 2_g^+$	654.6, 756.0, 867.6, 394.5	-0.10(2),0.01(3)
^{112}Ru		
$4_g^+ \overset{408.2}{\rightarrow} 2_g^+ \overset{236.8}{\rightarrow} 0_g^+$	589.0*, 483.6*, 400.0*, 723.0, 1220.2*	0.087(9),0.000(14)
$2_\gamma^+ \overset{286.8}{\rightarrow} 2_g^+ \overset{237.0}{\rightarrow} 0_g^+$	457.2, 224.3, 589.4	-0.044(12),0.18(2)
$3_\gamma^+ \overset{510.8}{\rightarrow} 2_g^+ \overset{236.8}{\rightarrow} 0_g^+$	487.9, 605.8, 693.7	-0.157(12),-0.08(2)

*Indicates that this additional gate is from a fission partner

Table 3.6: Table of delta values measured in this work for the isotopes of Ru. The A_2^{raw},A_4^{raw} values are copied from table 3.5, while A_2^{cor},A_4^{cor} are the same values corrected according to the data presented in table 3.1. Often two solutions are warranted for δ, given A_2^{exp},A_4^{exp} within 3σ. Square braces, "[ ]", indicate that A_2^{thry} (or A_4^{thry}) differs from A_2^{exp} (A_4^{exp}) by 1.5σ or more. For some solutions the point in A_2,A_4 space corresponding to $\delta = \pm\infty$ is within 1σ. These cases have been marked with a $+\infty$ or $-\infty$, and the text contains more details.

Transition	A_2^{raw},A_4^{raw}	A_2^{cor},A_4^{cor}	δ	A_2^{thry},A_4^{thry}
		^{108}Ru		
$2_\gamma^+ \rightarrow 2_g^+$	-0.102(14),0.21(2)	-0.12(2),0.33(6)	15^{+7}_{-4}	-0.123,0.325
$3_\gamma^+ \rightarrow 2_g^+$	-0.20(2),-0.06(4)	-0.24(3),-0.09(6)	-22^{+11}_{-20} -0.22(3)	-0.239,-0.081 -0.239,-0.004
$4_\gamma^+ \rightarrow 4_g^+$	-0.20(2),0.08(4)	-	$1.8^{+0.9}_{-0.4}$	-0.172,0.117†
		^{110}Ru		
$2_\gamma^+ \rightarrow 2_g^+$	-0.067(13),0.22(2)	-0.08(2),0.34(6)	$158^{+\infty}_{-123}$	-0.081,0.327
$3_\gamma^+ \rightarrow 2_g^+$	-0.175(8),-0.071(11)	-0.211(15),-0.11(2)	$-118^{+82}_{-\infty}$	-0.211,-0.082
$4_\gamma^+ \rightarrow 4_g^+$	-0.15(3),0.13(5)	-	7^{+96}_{-6}	-0.154,0.149
$5_\gamma^+ \rightarrow 4_g^+$	-0.10(2),0.01(3)	-	-0.04(2) $[22^{+28}_{-8}]$	-0.096,0.000 -0.096,[-0.059]
		^{112}Ru		
$2_\gamma^+ \rightarrow 2_g^+$	-0.044(12),0.18(2)	-0.053(15),0.28(5)	-32^{+11}_{-38}	-0.053,0.326
$3_\gamma^+ \rightarrow 2_g^+$	-0.157(12),-0.08(2)	-0.19(2),-0.13(3)	$55^{+\infty}_{-31}$	-0.190,-0.082

†For this measurement, δ was calculated using both A_2^{exp} and A_4^{exp}, rather than only A_2^{exp}.

Figure 3.16: Angular correlations measured for ^{108}Ru. Top left: $4^+_g \rightarrow 2^+_g \rightarrow 0^+_g$. Top right: $2^+_\gamma \rightarrow 2^+_g \rightarrow 0^+_g$. Bottom left: $3^+_\gamma \rightarrow 2^+_g \rightarrow 0^+_g$. Bottom right: $4^+_\gamma \rightarrow 4^+_g \rightarrow 2^+_g$.

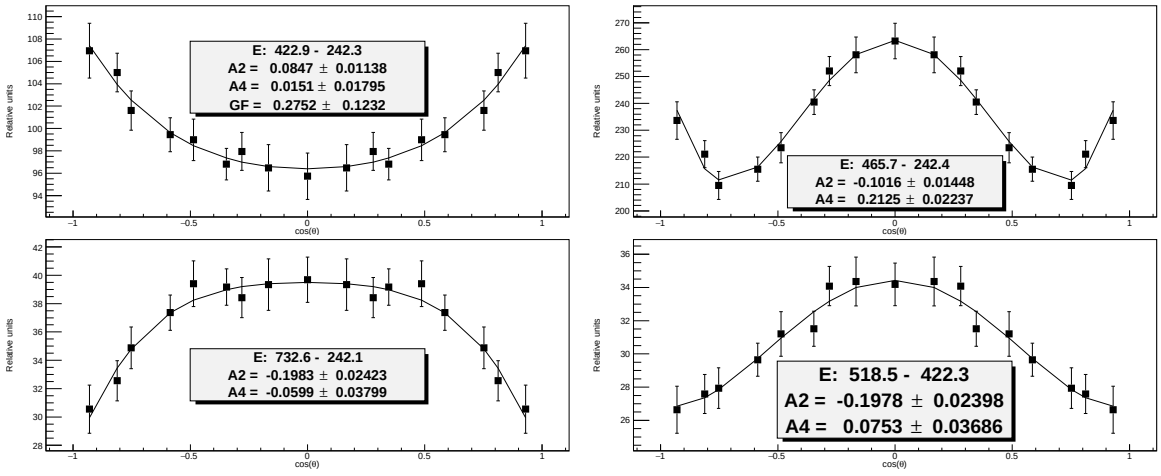

gates to ensure that the correlation measured was actually that of the desired isotope. However, the γ bands of these two isotopes are different enough that the similarities in the Yrast-band transitions caused little issue.

The $2^+_\gamma \rightarrow 2^+_g \rightarrow 0^+_g$ correlation for ^{108}Ru is plotted in figure 3.16. Based on the work shown in table 3.1, this correlation has been corrected – according to equation 2.2 – by $G_2, G_4 = 0.83(5), 0.65(9)$. The corrected value for this transition is plotted in figure 3.5. Based on these results, a value of 15^{+7}_{-4} is extracted for the mixing ratio for the $2^+_\gamma \rightarrow 2^+_g$ transition in ^{108}Ru.

The $3^+_\gamma \rightarrow 2^+_g \rightarrow 0^+_g$ correlation is plotted in figure 3.16. Once corrected for attenuation according to table 3.1, this correlation is compared to the appropriate δ oval in figure 3.6. Based on these results both $\delta(E2/M1) = -22^{+11}_{-20}$ and $-0.22(3)$ are allowed for the mixing ratio for the $3^+_\gamma \rightarrow 2^+_g$ transition at 0.18σ and 1.47σ in A_4, respectively. The first solution is clearly statistically favored. Both are shown in table 3.6.

Figure 3.16 holds the plot of the $4^+_\gamma \rightarrow 4^+_g \rightarrow 2^+_g$ correlation for ^{108}Ru. Since no correction for attenuation was used, this correlation is compared directly with the δ oval in figure 3.7. Based on the these results, $\delta(E2/M1) = 1.8^{+0.9}_{-0.4}$ is observed as the mixing ratio for the $4^+_\gamma \rightarrow 4^+_g$ transition.

Figure 3.17: Angular correlations measured for ^{110}Ru. Top left: $4^+_g \rightarrow 2^+_g \rightarrow 0^+_g$. Top right: $2^+_\gamma \rightarrow 2^+_g \rightarrow 0^+_g$. Middle left: $3^+_\gamma \rightarrow 2^+_g \rightarrow 0^+_g$. Middle right: $4^+_\gamma \rightarrow 4^+_g \rightarrow 2^+_g$. Bottom: $5^+_\gamma \rightarrow 4^+_g \rightarrow 2^+_g$.

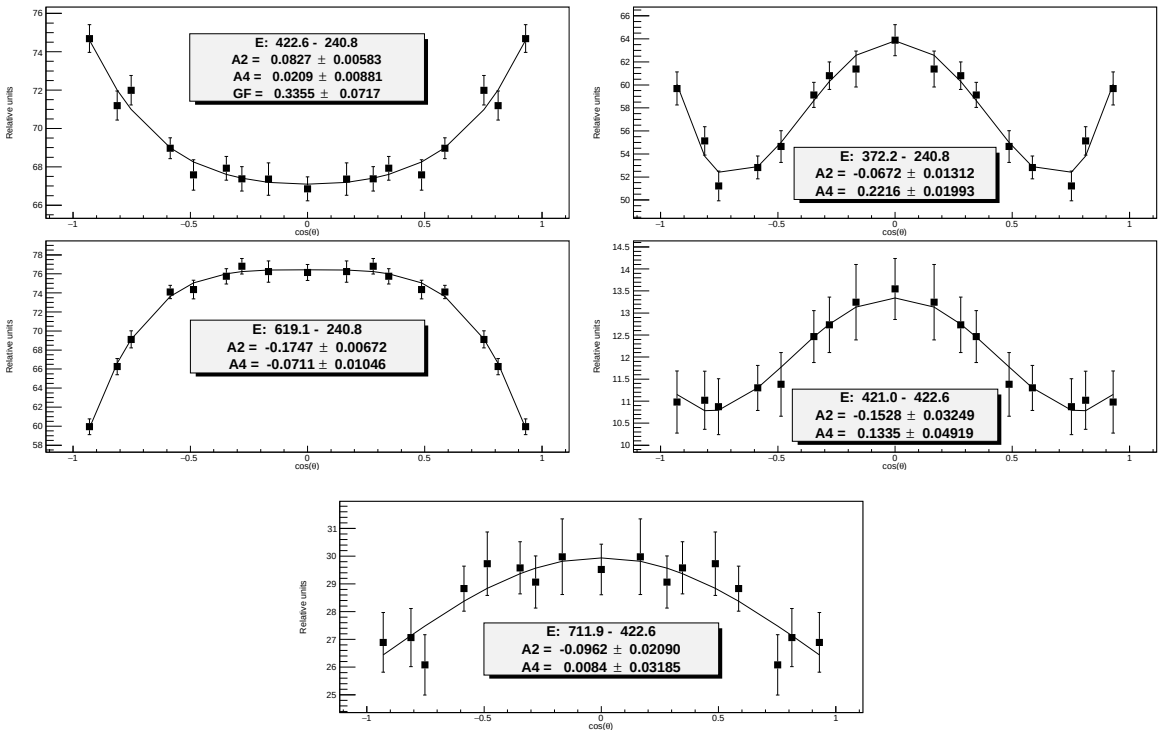

3.2.2.2 ^{110}Ru

Because ^{110}Ru is the most commonly produced isotope of Ru in the SF of ^{252}Cf, we were able to measure the mixing ratios of transitions from as high as the 5^+_γ state.

The $2^+_\gamma \rightarrow 2^+_g \rightarrow 0^+_g$ and $3^+_\gamma \rightarrow 2^+_g \rightarrow 0^+_g$ correlations are both plotted figure 3.17. These correlations were corrected for attenuation according to table 3.1. The corrected correlations are plotted with their respective δ ovals in figures 3.5 and 3.6. Based on these results we have observed values of $\delta(E2/M1) = 158^{+\infty}_{-123}$ and $-118^{+82}_{-\infty}$, to the $2^+_\gamma \rightarrow 2^+_g$ and $3^+_\gamma \rightarrow 2^+_g$ transitions, respectively. As noted in section 3.2.1.4, concerning the mixing ratio of the $4^+_\gamma \rightarrow 4^+_g$ transition of ^{108}Mo, the $\pm\infty$ errors on these values indicate that $\delta = \pm\infty$ is within 1σ in A_2,A_4 space. Furthermore, for the $2^+_\gamma \rightarrow 2^+_g$ of ^{108}Ru, this indicates that values of $\delta(E2/M1) < -62$ are also within 1σ. And similarly, for the $3^+_\gamma \rightarrow 2^+_g$ of ^{108}Ru, values > 95 are allowable within 1σ. Both of these values are shown in table 3.6.

The $4^+_\gamma \rightarrow 4^+_g \rightarrow 2^+_g$ correlation is plotted in the middle right of figure 3.17 and compared to the δ oval in figure 3.7. Based on these results a large range of values are possible for the mixing ratio of the $4^+_\gamma \rightarrow 4^+_g$ transition; $\delta(E2/M1) = 7^{+96}_{-6}$, as shown in table 3.6.

The $5^+_\gamma \rightarrow 4^+_g \rightarrow 2^+_g$, 711.9 – 422.6 keV correlation for ^{110}Ru was the only other major such issue. This is primarily due to its proximity in energy to the $9^+_\gamma \rightarrow 7^+_\gamma$, 710.4 keV and $4^+_g \rightarrow 2^+_g$, 422.9 keV transitions from ^{108}Ru, and its own $8^+_\gamma \rightarrow 6^+_\gamma$, 712.7 keV transition. After trying a number of additional combinations to weed out these sources of contamination, the four known transitions from ^{110}Ru found in coincidence with its $5^+_\gamma \rightarrow 4^+_g \rightarrow 2^+_g$ cascade, but not its $8^+_\gamma \rightarrow 6^+_\gamma$ transition were deemed to produce the clearest and least attenuated correlation. The results of this analysis are shown in figures 3.16 and 3.9, and resulted in two possible solutions for δ within our standard bounds of 3σ, as shown in table 3.6. The first solution, $\delta(E2/M1) = -0.04(2)$, is 0.3σ from A_4, which could make it more likely than the 2.1σ, $\delta(E2/M1) = 22^{+28}_{-8}$ solution.

3.2.2.3 ^{112}Ru

Due to the relative infrequency with which ^{112}Ru is produced in the SF of ^{252}Cf, we were only able to determine the mixing ratios of the $2^+_\gamma \rightarrow 2^+_g$ and $3^+_\gamma \rightarrow 2^+_g$ transitions.

The $2^+_\gamma \rightarrow 2^+_g \rightarrow 0^+_g$ and $3^+_\gamma \rightarrow 2^+_g \rightarrow 0^+_g$ uncorrected correlations are plotted in figure 3.18. These were subsequently corrected for attenuation due to the lifetime of the 2^+_g state, according to table 3.1. The corrected correlations are plotted with their respective δ ovals in figures 3.5 and 3.6. Based on these results, the the mixing ratio for the $2^+_\gamma \rightarrow 2^+_g$ transition is observed to be $\delta(E2/M1) = -32^{+11}_{-38}$, while $55^{+\infty}_{-31}$ corresponds to the $3^+_\gamma \rightarrow 2^+_g$ transition. The $+\infty$ uncertainty on the $3^+_\gamma \rightarrow 2^+_g$ mixing ratio indicates that it is indistinguishable from a pure E2 transition and that negative values, < -198, are also within 1σ of A_2, A_4.

Table 3.7: Angular correlations measured for isotopes of Pd.

Correlation $J^\pi \overset{(keV)}{\rightarrow} J^\pi \overset{(keV)}{\rightarrow} J^\pi$	Additional Gates (keV)	A_2^{raw},A_4^{raw}
^{112}Pd		
$4_g^+ \overset{534.4}{\rightarrow} 2_g^+ \overset{348.7}{\rightarrow} 0_g^+$	None	0.101(5),0.019(8)
$2_\gamma^+ \overset{388.1}{\rightarrow} 2_g^+ \overset{348.7}{\rightarrow} 0_g^+$	359.8	0.020(6),0.311(10)
$3_\gamma^+ \overset{747.9}{\rightarrow} 2_g^+ \overset{348.7}{\rightarrow} 0_g^+$	560.3, 1098.5, 662.8, 1658.7, 352.7*	-0.451(11),-0.084(9)
$4_\gamma^+ \overset{479.4}{\rightarrow} 4_g^+ \overset{534.4}{\rightarrow} 2_g^+$	348.8, 640.5, 423.9*, 352.6*	-0.08(3),0.13(5)
$5_\gamma^+ \overset{876.4}{\rightarrow} 4_g^+ \overset{534.4}{\rightarrow} 2_g^+$	None	-0.17(5),0.06(8)
^{114}Pd		
$4_g^+ \overset{520.1}{\rightarrow} 2_g^+ \overset{332.8}{\rightarrow} 0_g^+$	648.4, 715.5, 643.9, 583.8	0.108(4),-0.004(6)
$2_\gamma^+ \overset{362.1}{\rightarrow} 2_g^+ \overset{332.8}{\rightarrow} 0_g^+$	317.2, 619.2, 625.6	-0.046(7),0.299(10)
$3_\gamma^+ \overset{679.3}{\rightarrow} 2_g^+ \overset{332.8}{\rightarrow} 0_g^+$	None	-0.372(14),-0.079(12)
$4_\gamma^+ \overset{467.5}{\rightarrow} 4_g^+ \overset{520.1}{\rightarrow} 2_g^+$	333.0, 664.0	-0.17(5),0.15(7)
$5_\gamma^+ \overset{778.4}{\rightarrow} 4_g^+ \overset{520.1}{\rightarrow} 2_g^+$	333.0, 659.5, 1279.0*, 992.9, 296.9*, 889.5, 325.0*, 1508.6, 1150.6*	-0.16(7),-0.13(11)
^{116}Pd		
$4_g^+ \overset{537.6}{\rightarrow} 2_g^+ \overset{340.5}{\rightarrow} 0_g^+$	None	0.096(6),0.022(10)
$2_\gamma^+ \overset{397.8}{\rightarrow} 2_g^+ \overset{340.5}{\rightarrow} 0_g^+$	328.4, 635.6, 652.4, 744.1, 465.9	-0.064(15),0.33(2)
$3_\gamma^+ \overset{726.2}{\rightarrow} 2_g^+ \overset{340.5}{\rightarrow} 0_g^+$	6523., 744.0, 466.0, 549.3, 774.0, 1150.5*,1279.1*	-0.25(2),-0.09(3)

*Indicates that this additional gate is from a fission partner

Figure 3.18: Angular correlations measured for ^{112}Ru. Top left: $4^+_g \rightarrow 2^+_g \rightarrow 0^+_g$. Top right: $2^+_\gamma \rightarrow 2^+_g \rightarrow 0^+_g$. Bottom: $3^+_\gamma \rightarrow 2^+_g \rightarrow 0^+_g$.

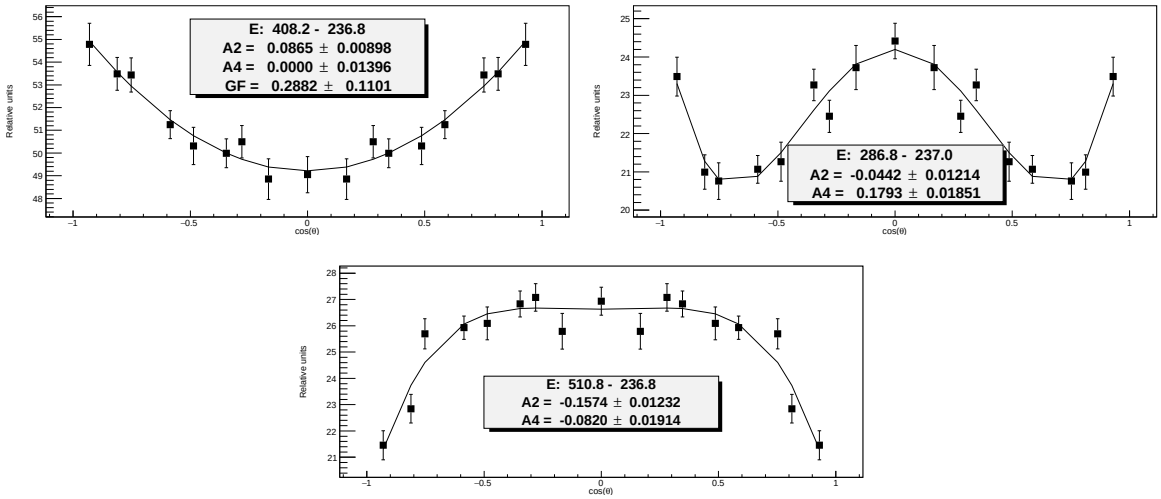

3.2.3 Isotopes of Pd

The raw angular correlations measured for the isotopes of Pd considered in this work are shown in table 3.7, while their analysis to yield $\delta(E2/M1)$ mixing ratios are shown in table 3.8.

The partial level schemes of ^{112,114,116}Pd, as considered in this work, can be found in figure 3.19. The complete level schemes of these isotopes of Pd are published in Luo *et al.* [57].

No major sources of commonalities between the transition energies of interest and transition energies from other nuclides were found. This lack of contamination and the lack of need for corrections for attenuation (see table 3.1) combined to cause the uncertainties for the isotopes of Pd to be generally lower than their counterpart measurements in either Mo or Ru. Another consequence was that measuring mixing ratios of transitions from higher spin states were possible for the isotopes of Pd than for those of Ru, even though the isotopes of Ru are more frequently produced in the SF of ^{252}Cf.

Table 3.8: Table of delta values measured in this work for the isotopes of Pd. Because, as shown in table 3.1, no correction for attenuation was needed for the isotopes of Pd, only one column is given for A_2^{exp},A_4^{exp} (rather than splitting it into A_2^{raw},A_4^{raw} and A_2^{cor},A_4^{cor}). Often two solutions are warranted for δ, given A_2^{exp},A_4^{exp} within the standard 3σ bounds used in this work. For the isotopes of Pd, most solutions fell within 1.5σ. Square braces, "[ ]", indicate that A_2^{thry} (or A_4^{thry}) differs from A_2^{exp} (A_4^{exp}) by more than 1.5σ.

Transition	A_2^{exp},A_4^{exp}	δ	A_2^{thry},A_4^{thry}
^{112}Pd			
$2_\gamma^+ \rightarrow 2_g^+$	0.020(6),0.311(10)	$-7.9^{+0.3}_{-0.4}$	0.019,0.321
$3_\gamma^+ \rightarrow 2_g^+$	-0.451(11),-0.084(9)	$-2.57^{+0.12}_{-0.13}$	-0.451,-0.071
$4_\gamma^+ \rightarrow 4_g^+$	-0.08(3),0.13(5)	$-8^{+\ 4}_{-47}$ $0.8^{+0.12}_{-0.11}$	-0.079,0.150 -0.079,0.062
$5_\gamma^+ \rightarrow 4_g^+$	-0.17(5),0.06(8)	-0.15(6) $-18^{+\ 8}_{-81}$	-0.171,-0.001 -0.164,-0.059
^{114}Pd			
$2_\gamma^+ \rightarrow 2_g^+$	-0.046(7),0.299(10)	$[-25^{+3}_{-2}]$	-0.047,[0.326]
$3_\gamma^+ \rightarrow 2_g^+$	-0.372(14),-0.079(12)	-4.2(3)	-0.372,-0.077
$4_\gamma^+ \rightarrow 4_g^+$	-0.17(5),0.15(7)	$4^{+40}_{-\ 3}$	-0.168,0.144†
$5_\gamma^+ \rightarrow 4_g^+$	-0.16(7),-0.13(11)	$-21^{+11}_{-\infty}$ -0.13(8)	-0.160,-0.059 -0.158,-0.001
^{116}Pd			
$2_\gamma^+ \rightarrow 2_g^+$	-0.064(15),0.33(2)	$-74^{+\ 38}_{-282}$	-0.067,0.326
$3_\gamma^+ \rightarrow 2_g^+$	-0.25(2),-0.09(3)	-15^{+3}_{-5}	-0.255,-0.081

†For this measurement, δ was calculated using both A_2^{exp} and A_4^{exp}, rather than only A_2^{exp}.

Figure 3.19: The partial level schemes of the isotopes of Pd considered in this work.

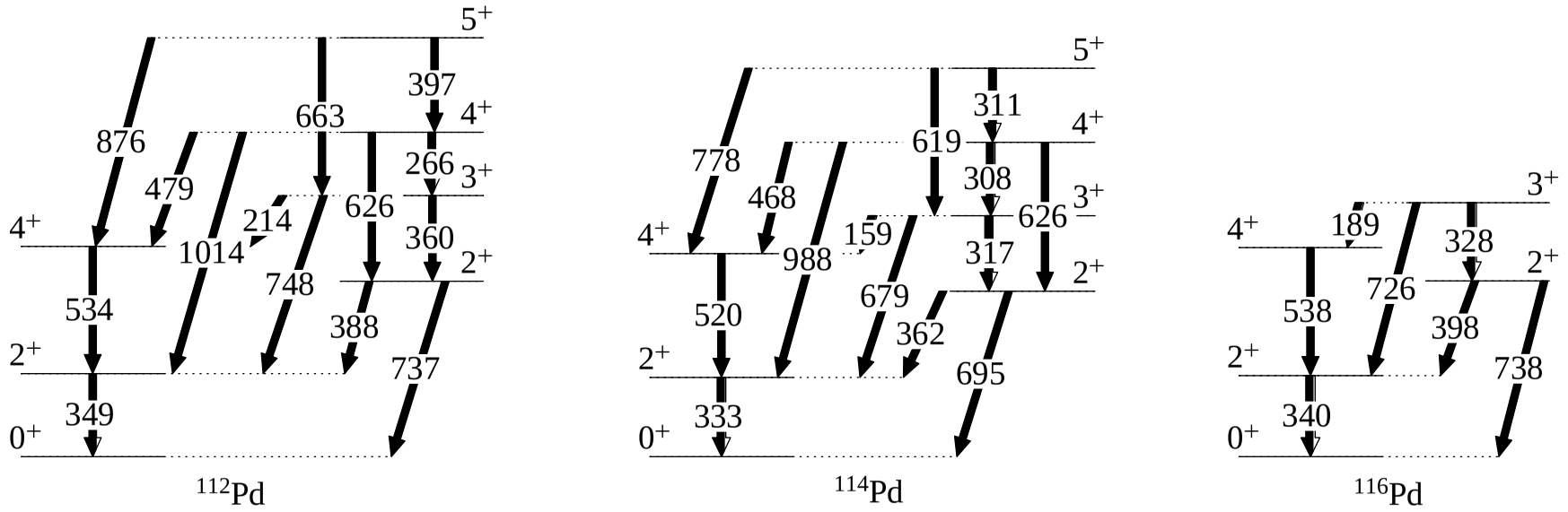

Figure 3.20: Angular correlations measured for ^{112}Pd. Top left: $4^+_g \rightarrow 2^+_g \rightarrow 0^+_g$. Top right: $2^+_\gamma \rightarrow 2^+_g \rightarrow 0^+_g$. Middle left: $3^+_\gamma \rightarrow 2^+_g \rightarrow 0^+_g$. Middle right: $4^+_\gamma \rightarrow 4^+_g \rightarrow 2^+_g$. Bottom: $5^+_\gamma \rightarrow 4^+_g \rightarrow 2^+_g$.

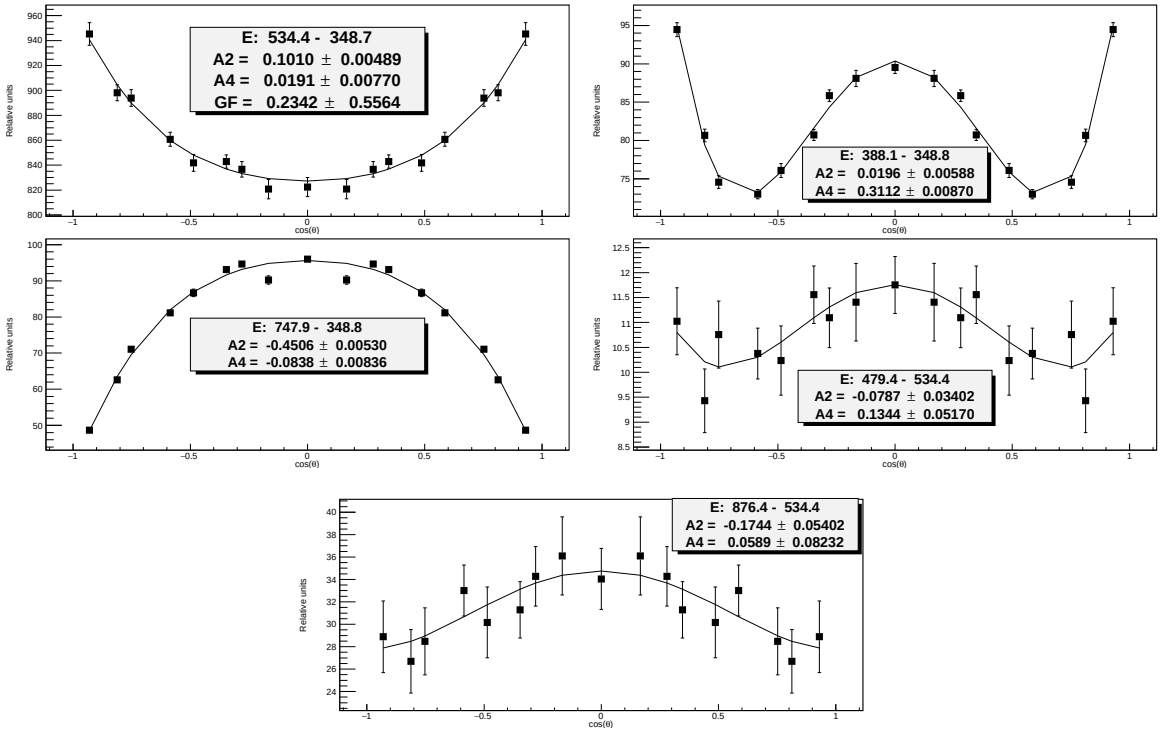

3.2.3.1 ^{112}Pd

Unlike ^{104,106,108}Mo and the Ru isotopes considered in this work, the lifetimes of the 2^+_g states of the Pd isotopes considered did not cause any appreciable attenuation, as seen in table 3.1. Thus no correction factor was used on the $2^+_\gamma \rightarrow 2^+_g \rightarrow 0^+_g$ and the $3^+_\gamma \rightarrow 2^+_g \rightarrow 0^+_g$ correlations shown in figure 3.20. These two correlations are compared to their respective δ ovals in figures 3.5 and 3.6. Based on these results, we have extracted a value of $\delta(E2/M1) = -7.9^{+0.3}_{-0.4}$ to the mixing ratio for the $2^+_\gamma \rightarrow 2^+_g$ transition and a value of $-2.57^{+0.12}_{-0.13}$ for the mixing ratio of the $3^+_\gamma \rightarrow 2^+_g$ transition, as shown in table 3.8.

The $4^+_\gamma \rightarrow 4^+_g \rightarrow 2^+_g$ and $5^+_\gamma \rightarrow 4^+_g \rightarrow 2^+_g$ correlations are shown in figure 3.20. Because of the relatively low statistics these correlations produced larger uncertainties. They are compared to their respective δ ovals in figures 3.7 and 3.9. Based on these results, a value of $\delta(E2/M1) = -8^{+4}_{-47}$ is observed for the mixing ratio of the $4^+_\gamma \rightarrow 4^+_g$ transition. There

were two solutions within 1.5σ for the $5^+_\gamma \rightarrow 4^+_g$ transition; one at about 0.7σ in A_4^{exp} is $\delta(E2/M1) = -0.15(6)$ and the other near 1.4σ in A_4^{exp} is $-18^{+\ 8}_{-81}$. Both values are possible for the $5^+_\gamma \rightarrow 4^+_g$ mixing ratio in table 3.8.

3.2.3.2 ^{114}Pd

As with ^{112}Pd, we were able to make determinations of the mixing ratios of transitions up to a transition from the 5^+_γ state. In ^{114}Pd, because the $4^+_g \rightarrow 2^+_g \rightarrow 0^+_g$ correlation showed no attenuation, the $2^+_\gamma \rightarrow 2^+_g \rightarrow 0^+_g$ and $3^+_\gamma \rightarrow 2^+_g \rightarrow 0^+_g$ correlations, shown in figure 3.21, needed no correction for attenuation. These two correlations are compared with their respective δ ovals in figures 3.5 and 3.6, respectively. Based on these results we observe a value of $\delta(E2/M1) = -25^{+3}_{-2}$ to the $2^+_\gamma \rightarrow 2^+_g$ transition and a value of $-4.2(3)$ as the mixing ratio of the $3^+_\gamma \rightarrow 2^+_g$ transition. Both results are shown in table 3.8.

Figure 3.21: Angular correlations measured for ^{114}Pd. Top left: $4^+_g \rightarrow 2^+_g \rightarrow 0^+_g$. Top right: $2^+_\gamma \rightarrow 2^+_g \rightarrow 0^+_g$. Middle left: $3^+_\gamma \rightarrow 2^+_g \rightarrow 0^+_g$. Middle right: $4^+_\gamma \rightarrow 4^+_g \rightarrow 2^+_g$. Bottom: $5^+_\gamma \rightarrow 4^+_g \rightarrow 2^+_g$.

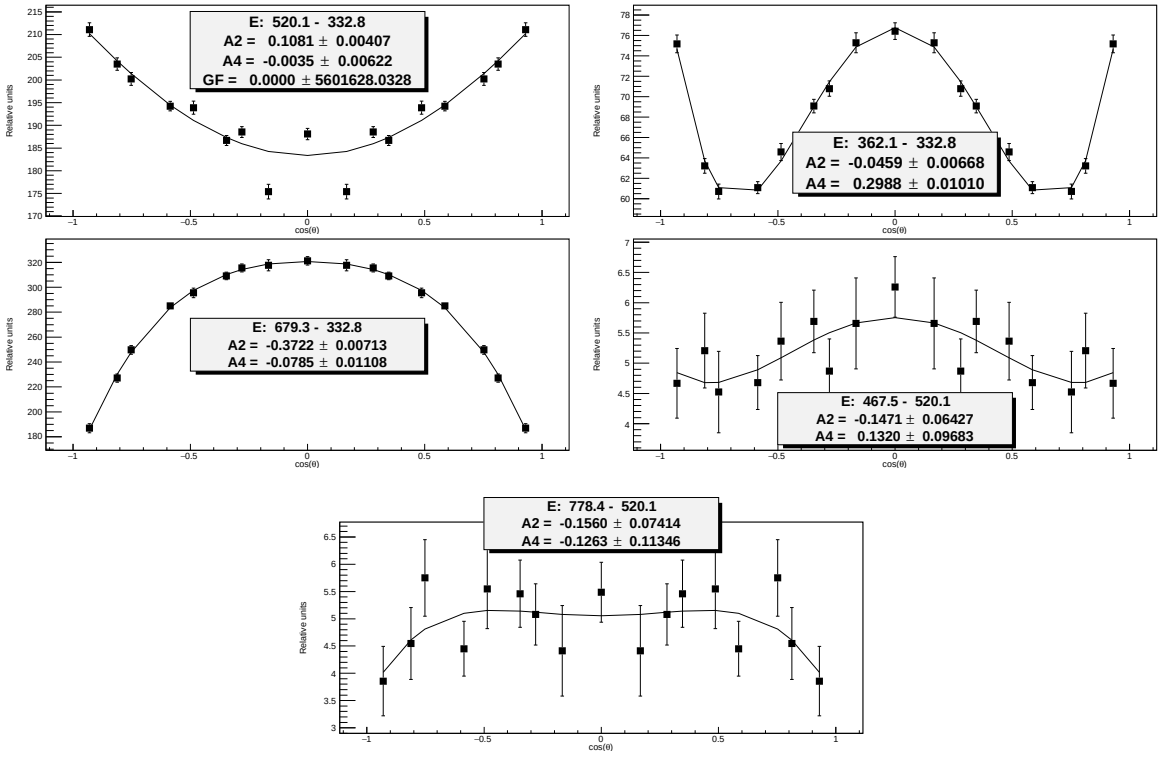

Figure 3.22: Angular correlations measured for ^{116}Pd. Top left: $4^+_g \rightarrow 2^+_g \rightarrow 0^+_g$. Top right: $2^+_\gamma \rightarrow 2^+_g \rightarrow 0^+_g$. Bottom: $3^+_\gamma \rightarrow 2^+_g \rightarrow 0^+_g$.

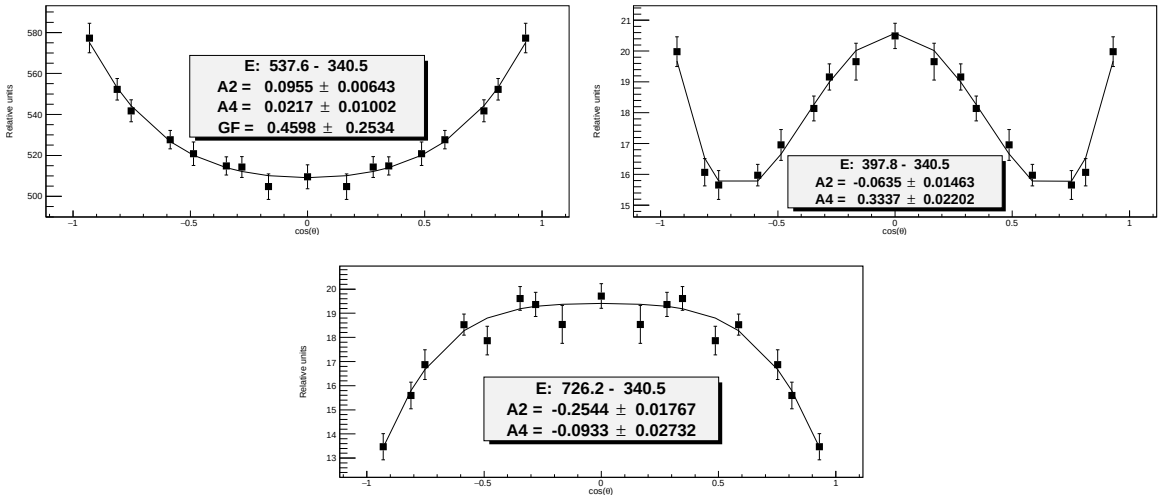

As with ^{112}Pd, the $4^+_\gamma \rightarrow 4^+_g \rightarrow 2^+_g$ and $5^+_\gamma \rightarrow 4^+_g \rightarrow 2^+_g$ correlations for ^{114}Pd have larger uncertainties due to moderately low statistics. These correlations are shown in the middle right and bottom of figure 3.21, respectively. As is the case for many of the $4^+_\gamma \rightarrow 4^+_g \rightarrow 2^+_g$ correlations plotted in figure 3.7, the error bars of this correlation from ^{114}Pd encompass a large and dense section of the 4(1,2)4(2)2 δ oval. For this reason, we observe a value of $\delta(E2/M1) = 4^{+40}_{-3}$ to the $4^+_\gamma \rightarrow 4^+_g$ mixing ratio as displayed in table 3.8.

For the mixing ratio of the $5^+_\gamma \rightarrow 4^+_g$ transition, two values of δ were possible within 1.5σ. The first, and more likely (lying at 0.6σ in A_4), value is $\delta(E2/M1) = -21^{+11}_{-\infty}$, where the $-\infty$ error indicates that values of $\delta > 15$ are also within 1σ of A_2. Similar cases are discussed in sections 3.2.1.4, 3.2.2.2, and 3.2.2.3 for ^{108}Mo and ^{110,112}Ru, respectively. The second solution, $\delta(E2/M1) = -0.13(8)$, lies at 1.1σ from A_4. Both solutions are shown in table 3.8.

3.2.3.3 ^{116}Pd

Because of the infrequency with which ^{116}Pd is produced in the SF of ^{252}Cf, we were only able to measure the mixing ratios of its $2^+_\gamma \rightarrow 2^+_g$ and $3^+_\gamma \rightarrow 2^+_g$ transitions. The

$2^+_\gamma \rightarrow 2^+_g \rightarrow 0^+_g$ and $3^+_\gamma \rightarrow 2^+_g \rightarrow 0^+_g$ correlations used to measure these mixing ratios are shown in figure 3.22 and compared to their respective δ ovals in figures 3.5 and 3.6. Since no attenuation factors were needed (see table 3.1), $\delta(E2/M1) = -74^{+38}_{-282}$ is the final value for the mixing ratio for the $2^+_\gamma \rightarrow 2^+_g$ transition while a value of -15^{+3}_{-5} is observed for the $3^+_\gamma \rightarrow 2^+_g$ mixing ratio, as shown in table 3.8.

3.2.4 Discussion: Trends in the Mixing Ratios

One can see, looking at tables 3.4, 3.6, 3.8, and fig. 3.23 that 30 of the 37 mixing ratios ($\sim$81%) measured demonstrate a pure or near-pure E2 transition (namely, $|\delta| \geq 3 \rightarrow \%E2 \geq 90\%$) within 1.5σ in A_2, A_4 space. Noting that the uncertainties in tables 3.4, 3.6, and 3.8 for values of δ represent 1σ in A_2, A_4 space, all of the 37 mixing ratios measured can be pure or near-pure E2 within 3σ. However, these results are lower than the simpler theory that states, based on the quadrupole nature of the 2^+_γ state, that these transitions should all be pure or nearly pure E2. This simplistic theory's prediction would be based primarily on statistical distributions, stating that 87% of the data (or $\sim$32 of 37) should be pure or nearly pure E2 within 1.5σ and $\sim$36.8 of 37 would be pure or nearly pure E2 within 3σ. Since the sample size here is small, it is likely that this fluctuation is random and would be resolved were more mixing ratios measured, especially since the choice of $|\delta| \geq 3$ as the benchmark is relatively arbitrary. Thus we conclude that, from a statistical standpoint, all of the mixing ratios measured in this work are pure or nearly pure E2, in accordance with theory.

Walter Greiner's theory [7], detailed in eqs. 1.18 and 1.18, however, makes much more precise predictions of these mixing ratios than simply that they should be pure or nearly pure E2. Equations 1.18 and 1.18 are plotted alongside the experimental mixing ratios measured in this work in figure 3.23. Since many of the variables in Greiner's theory are only known through experiment, appropriate 1σ uncertainties have been included in the theory. Most of the experimental variables required were found in refs. [39, 40, 41, 42,

Figure 3.23: Plots of mixing ratios measured in this work compared with Walter Greiner's rotational (solid black) and vibrational (dashed black) theories [7], given in equs. 1.18 and 1.19, respectively, with 1σ uncertainty. Since Greiner's theory predicts all positive values for δ, the negatives of his theory have also been given. Mixing ratios less than 1.5σ in the uncertainty of both A_2^{exp} and A_4^{exp} are marked with filled in shapes, while those which are between 1.5 and 3.0σ in either A_2^{exp} or A_4^{exp} are hollow shapes. The mixing ratios whose values were determined to be $\pm\infty$ do not appear on the graph, but the lower bound on positive numbers and upper bound on negative numbers can be seen. In a similar manner, mixing ratios whose values overlap with $\delta = \pm\infty$, show uncertainties which wrap around the graph.

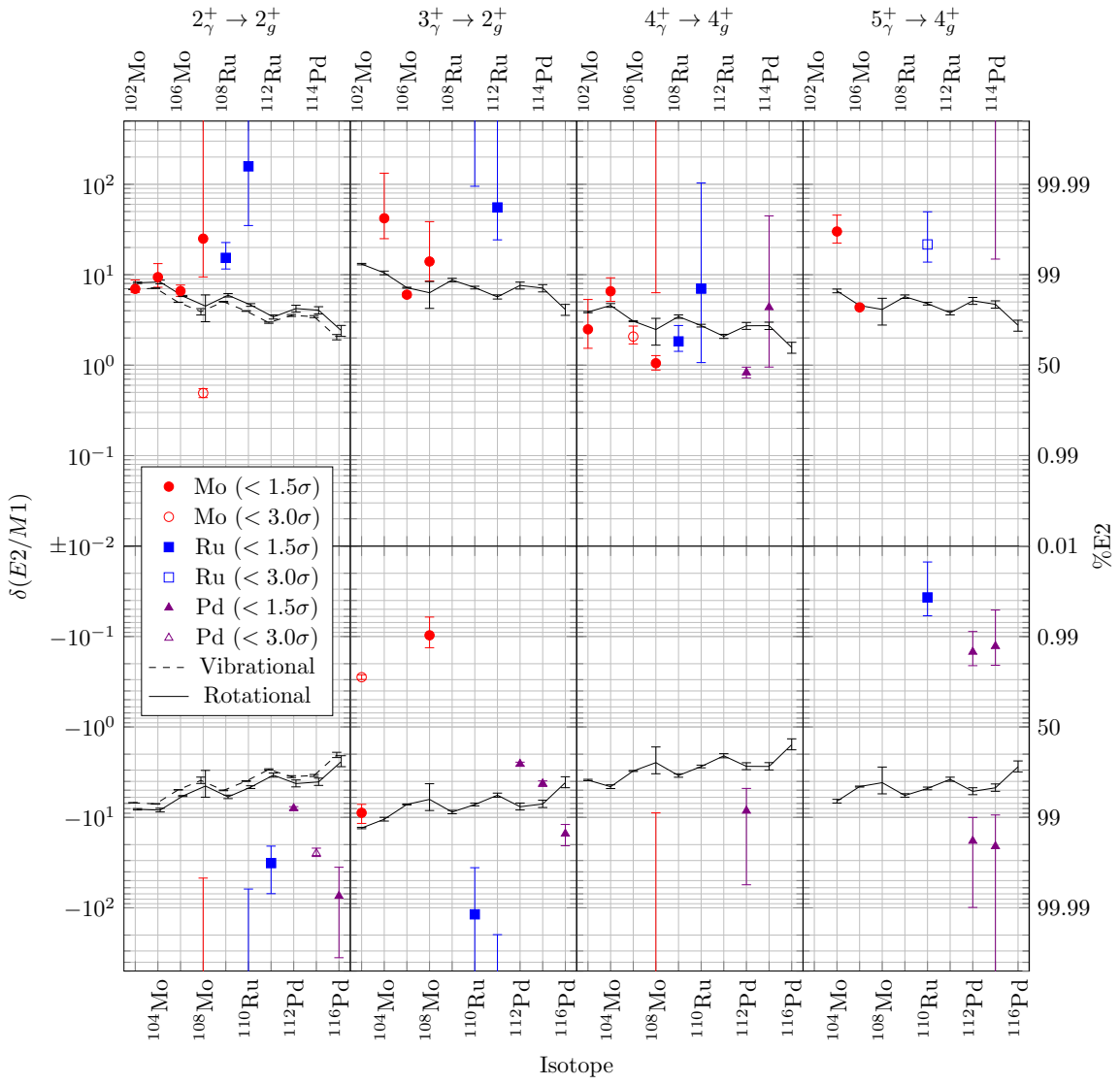

43, 44, 45, 46]. Because Greiner's theory does not predict any sign changes in the mixing ratios, both the positive and negative of it have been plotted. As can be seen in fig. 3.23, Greiner's theory consistently under-predicts the magnitude of the mixing ratios except for the $3^+_\gamma \rightarrow 2^+_g$ mixing ratio for ^{112}Pd, which is probably random, and the $4^+_\gamma \rightarrow 4^+_g$ mixing ratios, which generally have larger uncertainties. Thus Greiner's theory is not accurate for this section of the chart of nuclides.

Krane [2] predicted that there would be a shape change in nuclei at around ^{110}Ru which would correspond to a change in the relative sign in the mixing ratios of γ-band to ground-band transitions. This has been clearly observed, especially in the $2^+_\gamma \rightarrow 2^+_g$ transitions as seen in fig. 3.23. Additionally, there is a generally increasing trend among the $2^+_\gamma \rightarrow 2^+_g$ mixing ratios for Mo and Ru, where for Ru the trend crosses $\pm\infty$ at ^{110}Ru and continues in negative numbers (i.e. a decreasing trend in $1/\delta$). The Pd isotopes, however, show a decreasing trend, but are all negative. In general, the higher order mixing ratios confirm these trends, though not quite as clearly.

The work described in this chapter has been published in the European Physical Journal A [58].

Chapter 4

The β-decay of ^{164}Eu

The LeRIBSS at ORNL was used to observe γ-rays from the β-decay of ^{164}Eu (see section 2.2 for more details). This resulted in a newly developed level scheme for ^{164}Gd as shown in figure 4.1 and table 4.1 with 15 new transitions, 13 new levels, and 2 transitions that were previously observed [59] have now, for the first time, been placed into the level scheme. Three of these new transitions, four of the new levels, and one of the newly placed transitions were also observed in ^{252}Cf SF, as described in section 5.1.

4.1 Spectra, Coincidence Analysis, and Common Contaminants

Figure 4.2 shows the γ-ray singles and β-gated γ-ray singles from the β-decay of ^{164}Eu. First, the singles spectrum is generated by every γ-ray interaction with any of the 16 HPGe crystals in the 4 clovers of the LeRIBSS station, meaning that the massive background at low energies is, in part, the sum of Compton scatters of all higher energy γ-rays. Because no coincidence of any kind is required in the singles spectrum, the greatest number of noise peaks can be seen here, as well as all but the weakest peaks from ^{164}Gd. Second, the β-gated singles are just like the singles except that any γ-ray recoreded must be in coincidence with a β. This drastically reduces the contaminant peaks, and enhances the peak to background ratio of many of the peaks in which we are interested.

Figure 4.3 shows background subtracted gates on γ-rays, with no requirement of β-coincidence. Both of these coincidence spectra use "add-back", where any gamma-ray interactions in different crystals of the same clover are added back together under the assumption that they were in fact the same original γ-ray. The background subtraction in these gates was done by subtracting gates on channels immediately to the left and right of the desired gate energies from the desired channels. The 168.5 keV gate is specifically a gate on channels (1 keV/channel) 167 to 170 minus gates on 165 to 166 and 171 to 172,

Figure 4.1: The level scheme of ^{164}Gd as seen by the β-decay of ^{164}Eu. Red levels and transitions are newly observed in this work. Blue were previously observed [59], but had not been placed in the level scheme. The widths of the arrows are proportional to the intensity with white representing internal conversion. The relative intensity of the 72.9 keV transition has been halved to make the widths of the other transitions more visible.

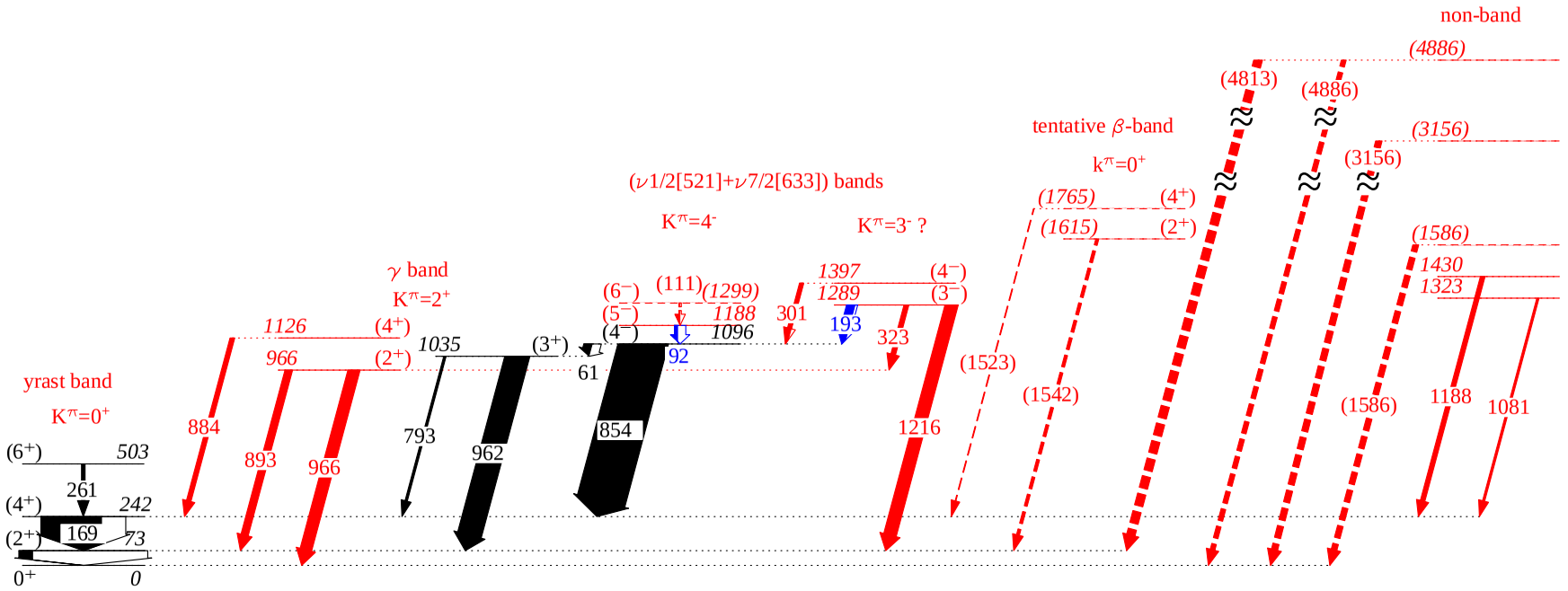

^{164}Gd

Table 4.1: Table of levels and γ-rays in ^{164}Gd. Internal Conversion Coefficients (ICC) are taken from brIccFO [15] assuming the multipolarities shown (where Π = E or M). With the exception of the 61.0 keV transition whose measurement is described in table 4.2, these multipolarities are guesses based on spins and parities and the quadrupole nature of γ-vibrations, and have not been measured or otherwise verified. Square brackets indicate that a value is tentative. Subscripts on Spin-parity labels indicate band, with γ=γ-vibrational band, β=beta vibrational band, o=octupole band, g=yrast "ground state" band, and numbers indicate the value of K for quasiparticle bands.

E_γ	I_γ	ΠL	I_{tot}	E_i	J_i^π	E_f	J_f^π
61.0(5)	13(3)	E1	28(7)	1095.7(6)[a]	$[4_4^-]$	1034.7(6)	$[3_\gamma^+]$
72.9(5)	23(6)	[E2]	214(61)	72.9(5)[b]	$[2_g^+]$	0.0[c]	0_g^+
91.6(5)[d]	5(2)	[M1]	18(6)	1187.3(8)[e]	$[5_4^-]$	1095.7(6)[a]	$[4_4^-]$
[111(2)][e]	1.6(13)	[M1]	4(3)	[1298.0(13)][e]	$[6_4^-]$	1187.3(8)[e]	$[5_4^-]$
168.5(5)	100(6)	[E2]	140(8)	241.4(7)	$[4_g^+]$	72.9(5)[b]	$[2_g^+]$
192.8(5)[d]	13(2)	[M1]	18(3)	1288.5(5)[e]	$[3_3^-]$	1095.7(6)[a]	$[4_4^-]$
260.7(5)	5.3(9)	[E2]	5.8(10)	502.1(9)	$[6_g^+]$	241.4(7)	$[4_g^+]$
300.8(5)[e]	11(4)	[M1]	12(4)	1396.5(8)[e]	$[4_3^-]$	1095.7(6)[a]	$[4_4^-]$
322.2(9)[e]	8(4)	[E1]	8(4)	1288.5(5)[e]	$[3_3^-]$	966.3(6)[e]	$[2_\gamma^+]$
793.3(6)	3.7(15)		3.7(15)	1034.7(6)	$[3_\gamma^+]$	241.4(7)	$[4_g^+]$
854.3(5)	81(7)		81(7)	1095.7(6)[a]	$[4_4^-]$	241.4(7)	$[4_g^+]$
883.9(7)[e]	8(2)		8(2)	1125.3(10)[e]	$[4_\gamma^+]$	241.4(7)	$[4_g^+]$
893.4(6)[e]	12(2)		12(2)	966.3(6)[e]	$[2_\gamma^+]$	72.9(5)[b]	$[2_g^+]$
961.8(5)	40(4)		40(4)	1034.7(6)	$[3_\gamma^+]$	72.9(5)[b]	$[2_g^+]$
966.3(8)[e]	19(6)		19(6)	966.3(6)[e]	$[2_\gamma^+]$	0.0[c]	0_g^+
1080.8(5)[e]	3.5(14)		3.5(14)	1322.2(9)[e]		241.4(7)	$[4_g^+]$
1187.8(5)[e]	7(2)		7(2)	1429.2(9)[e]		241.4(7)	$[4_g^+]$
1215.6(6)[e]	21(3)		21(3)	1288.5(5)[e]	$[3_3^-]$	72.9(5)	$[2_g^+]$
[1523.5(5)][e]	< 5		< 5	[1764.9(9)][e]	$[4_\beta^+]$	241.4(7)	$[4_g^+]$
[1542.5(5)][e]	< 17		< 17	[1615.4(7)][e]	$[2_\beta^+]$	72.9(5)	$[2_g^+]$
[1585.7(7)][e]	9(6)		9(6)	[1585.7(7)][e]		0.0[c]	0_g^+
[3156.3(10)][e]	10(4)		10(4)	[3156.3(10)][e]		0.0[c]	0_g^+
[3789.8(10)][ef]	< 10		< 10	[4885.5(6)][e]	$[3_o^-]$	1095.7(6)[a]	$[4_4^-]$
[4812.6(6)][e]	14(6)		14(6)	[4885.5(6)][e]	$[3_o^-]$	72.9(5)[b]	$[2_g^+]$
[4885.5(8)][e]	8(4)		8(4)	[4885.5(6)][e]	$[3_o^-]$	0.0[c]	0_g^+

[a]Isomeric State: $t_{1/2} = 0.59(9)$ µs, see figure 4.5.
[b]Half-life: $t_{1/2} = 2.77(14)$ ns [60].
[c]Half-life: $t_{1/2} = 45(3)$ s [61].
[d]Previously observed [59] but not placed into the level scheme until now.
[e]Newly Observed in this work.
[f]Not shown in figure 4.1

Figure 4.2: The singles (a) spectrum on a log scale and the β-gated singles (b) on a linear scale from the ^{164}Eu β-decay data. Transitions from ^{164}Gd are marked with their appropriate numbers. Various background peaks have been marked with symbols as shown in the legend. Of special note are those marked "b." These are sources of radiation in the room, some are common/known sources of background radiation while others could not be identified. None of the transitions marked "b" show any coincidence with either β or γ events in the data, and as such do not appear in the β-gated singles spectrum (b).

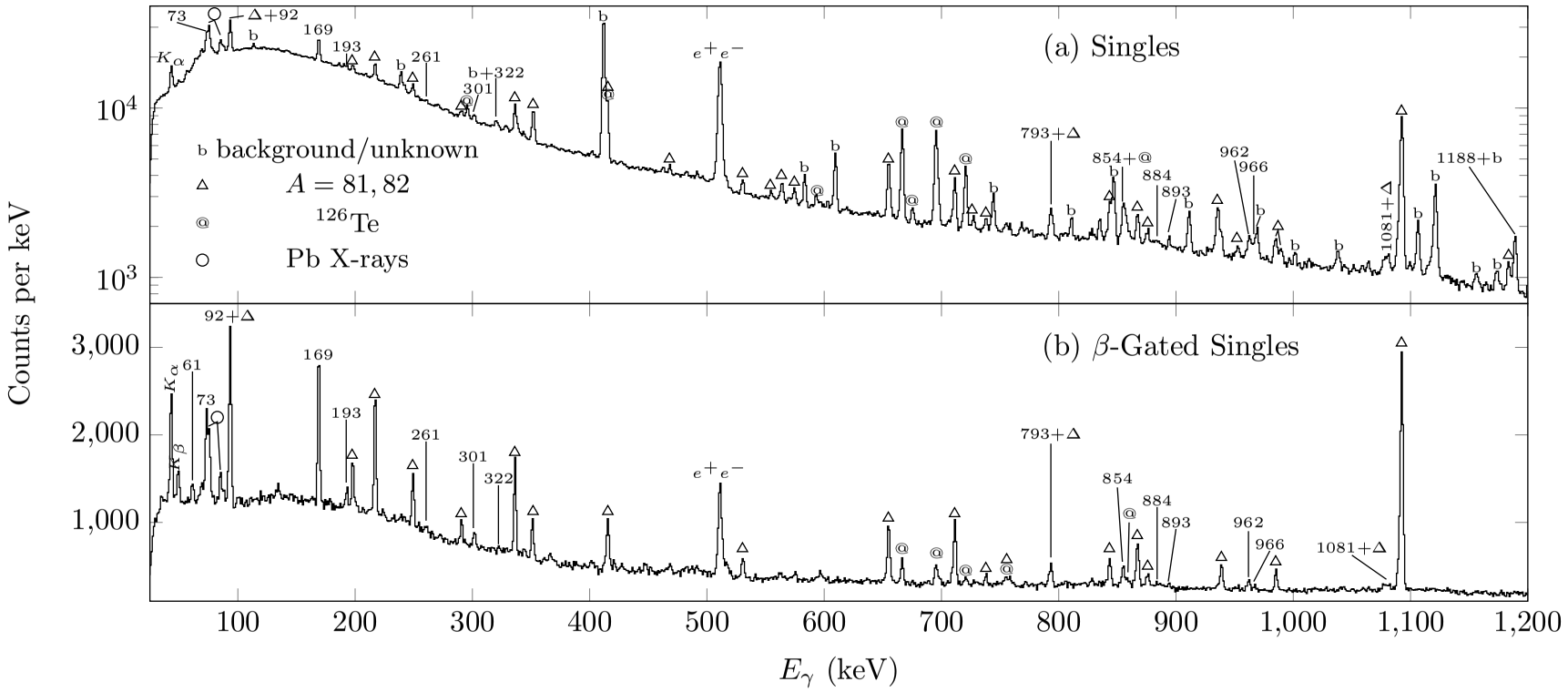

while the 854.9 keV gate is from 851 to 858 minus 847 to 850 and 859 to 862. This form of background subtraction does a great job at removing both the ambient non-linear background (as seen in both singles and β-gated singles) and any peaks that occur just because a γ-ray is emitted frequently. The one thing it does not remove is Compton cross-talk, when a higher energy γ-ray Compton scatters into a different clover. Cross talk creates diagonal lines in the 2-D histogram from which these gates were taken, meaning that the background gates see the cross talk peak at higher or lower energy than the gate energies. This creates sharp negative peaks in the final spectrum on either side of the cross talk peak, making them easier to spot. Another consequence of the diagonal nature of the cross talk peaks is that a wider gate produces wider cross talk peaks, this is clearly seen when comparing the cross talk peaks in the 168 keV gate to those in the 855 keV gate. Cross talk peaks are labled with an "S" in figure 4.3.

The most prominent contaminant in our data is from the $A = 82$ and 81 chains. Transitions from these nuclei have been marked with triangles in figure 4.2. As noted in section 2.2, our data were generated by selecting a charge to mass ratio of 2+ to 164 u. It should be obvious then, how $A = 82$ fission fragments with a 1+ charge state easily contaminate our experiment, as they have almost exactly the same mass to charge ratio. We end up with $A = 81$ nuclei in our data from $\beta - n$ decay. Most of the $A = 82$ nuclei commonly produced in ^{238}U fission have Q-values for β decay higher than the 1-neutron separation energy of their daughters, and significantly shorter half-lives than either ^{164}Eu or ^{164}Gd. For example, ^{82}Ga has a half life of 0.599(2) s and a Q-value for β-decay to ^{82}Ge of 12.484 MeV, while ^{82}Ge has a neutron separation energy of only 7.195 MeV. This means that every ^{82}Ga implanted directly by the beam or produced from the β-decay of ^{82}Zn will β-decay to ^{82}Ge during our 16 s tape cycle (see section 2.2 for details on the tape cycle) including $\sim 20\%$ that undergo $\beta - n$ decay to ^{81}Ge. In fact, a previous experiment using the same detector system used for this experiment, had trouble with $A = 164$ contaminants when studying the $A = 82$ chain, which gave rise to this experiment. The results of that experiment – including

Figure 4.3: Shown here are background subtracted gates on the 169 (a) and 854 (b) keV transitions from the ^{164}Eu β decay data. These two spectra clearly show many of the γ-rays, observed in ^{164}Gd in this work, demonstrating the coincidence relationships between them. Peaks marked with an "S" indicate Compton scatter false peaks. Be careful to note the difference in the *x*-axis scales for these two spectra.

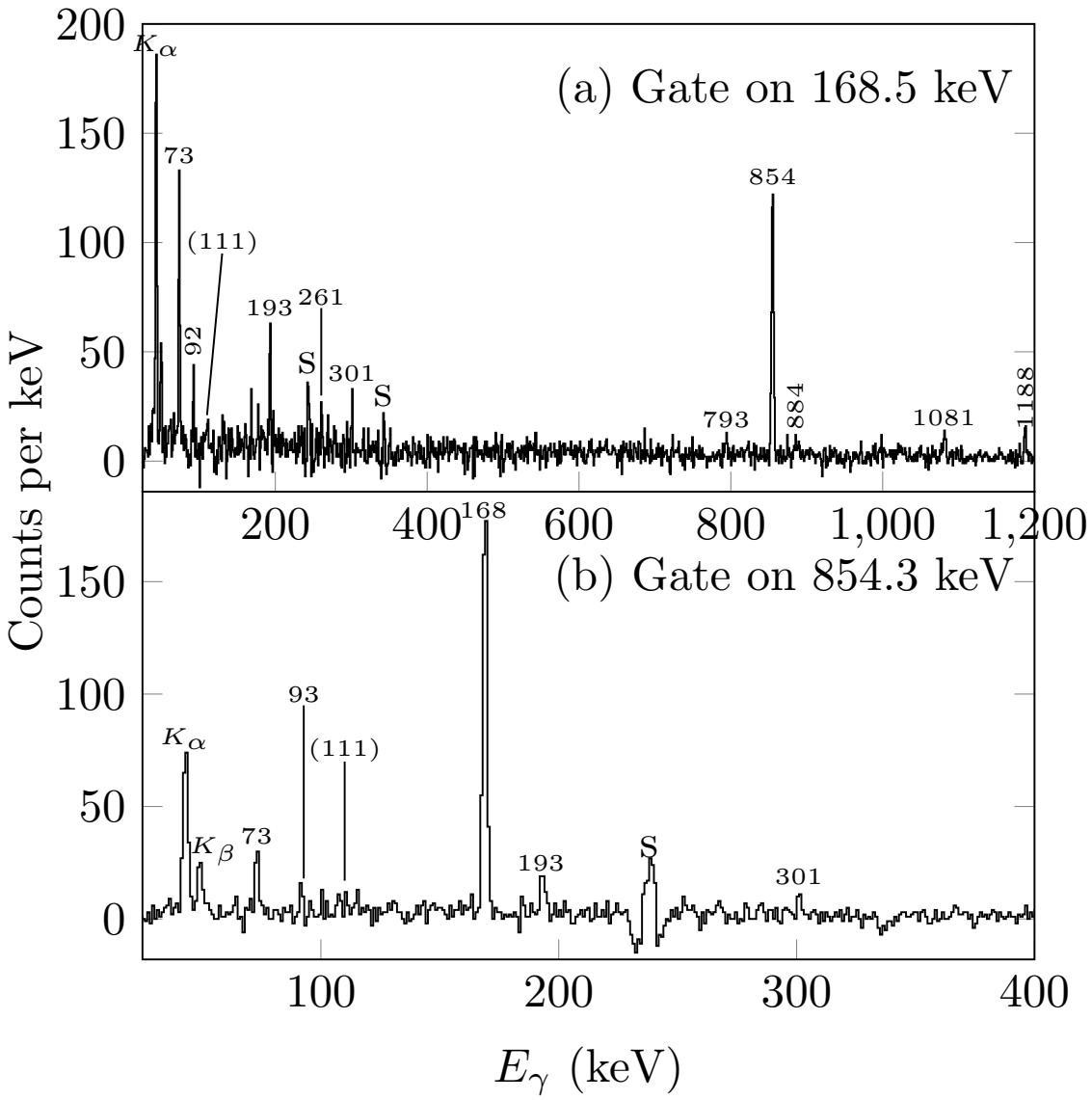

many of our contaminant γ-rays from the $A = 82$ and $A = 81$ isotopes – were published by Alshudifat *et al.* in 2016 [33]. Further details on the γ-rays produced by these $A = 81, 82$ contaminants can also be found in references [62, 63, 64, 65, 66, 67].

A number of contaminant γ-rays exhibit one distinguishing feature in common; that they experience no coincidence (aside from background) with other γ-rays or β-particles. These have been marked with a "b" in figure 4.2a. These coincidence-less peaks also show no time variation behavior, meaning that they cannot be contained in our beam or dependent on our tape cycle. The most prominent of these coincident-less γ rays lies at 411 keV and has a relative intensity of 1012(61) compared to the intensities for ^{164}Gd shown in table 4.1. Many of the coincident-less γ-rays are not observed in all of our clovers, or even in every leaf of a clover. The aforementioned 411 keV peak is only observed in three clovers (see figure C.1 in appendix C), indicating that its source is probably outside the LeRIBSS, such that one detector is shielded from it by the others and/or other objects in the room.

We found two strong possibilities to explain the 411 keV γ-ray; ^{55}Fe and ^{198}Au. First, ^{55}Fe, populated by ^{54}Fe(n,γ) [68] and/or ^{56}Fe(n,2nγ) [69] both produce 411 keV γ-rays, with extremely low production of any other γ-rays with energy below 4.5 MeV (the approximate maximum γ-ray energy detectable by LeRIBSS). Additionally, both ^{152}Eu and ^{198}Au are standard sources known to β-decay to nuclei that emit $\sim$411 keV γ-rays (see Helmer and van der Leun [70]). It is not possible for ^{152}Eu to be generating the 411 keV γ-ray, because we should also see an even stronger 344 keV γ-ray which the 411 feeds in the structure of ^{152}Gd. On the other hand, ^{198}Hg, following the β-decay of ^{198}Au, is only to emits three γ-rays with the 676 and 1088 keV γ-rays accounting for a combined $< 1\%$ of the total γ-rays emitted following the β-decay of ^{198}Au (see Hammed *et al.* [71]). Identifying an exceedingly weak ($\sim$0.1% of the 411) 1088 keV transition in our data would be impossible, since it lies on the shoulder of the extremely strong 1092 keV γ-ray from ^{82}As [63]. There is, however, a weak 676 keV γ-ray in our spectrum, but it lies directly on a peak expected from another contaminant, ^{126}Te, discussed below. Coincidence analysis cannot,

however, be used to resolve whether or not the 676 is 100% ^{126}Te, or partly ^{198}Hg, because ^{126}Te has a $\sim$415 keV transition in coincidence with its $\sim$676 keV γ-ray. For ^{198}Hg to be the source of our 411 keV γ-rays, however, ^{198}Au would either need to be contaminating the room from a previous experiment, or it would need to be produced by the ^{197}Au(n,γ) reaction from neutrons produced in the experiment from $\beta - n$ decays from the $A = 81, 82$ contaminants. Because iron is more common than gold, ^{55}Fe is favored over ^{198}Au, but ultimately we do not know the true source of the 411 keV contaminant γ-ray in our data.

Many similar sources of contamination exist in the room with LeRIBSS, because LeRIBSS was located inside the dome for the TANDEM Acclerator at HRIBF. Each of the coincidentless γ-rays occur from sources in the tandem dome with LeRIBSS – like the 411 keV – or are caused by fluctuations in the electronics, or by interactions of non-γ radiation (such as β or neutrons) with the HPGe chrystals making up our detectors. Most of these peaks are difficult to identify, precisely because of their lack of coincidence, the 411 keV being no exception. Thus no precise identification has been attempted for most of them. Several, however, are known as common sources of background radiation, which is cataloged by the Federal Radiological Monitoring and Assessment Center [72].

As mentioned above, one contaminant from the tandem dome, remaining from a previous experiment, that can be identified is ^{126}Te, due to its obvious coincidence relationships and well known energy structure [73, 74]. The transitions from ^{126}Te are marked by squares in figure 4.2. Additionally, some of the electronic states in the ^{208}Pb bricks used to shield the LeRIBSS can get activated by either γ-rays or other radiation from the experiment. The X-rays of ^{208}Pb are marked by circles in figure 4.2. Additionally, by similar means, the depopulation of the first excited state of ^{208}Pb is observable in out data, though its energy ($\sim$2615 keV) is too high to be displayed in figure 4.2. The welll-known decay scheme or ^{208}Pb can be found in Martin [75].

4.2 Details on the intensity measurements of transitions observed in ^{164}Gd

The intensities displayed in table 4.1 were measured using four different spectra, which are shown in figures 4.2 and 4.3. The first spectrum is the γ-ray singles spectra, which displays all γ-rays detected during the nearly two hours of data collection, with no coincidence requirement or attempt to correct for losses or backgrounds due to effects like internal conversion. The second spectrum used was the β-gated singles, which is the same as the singles spectrum but has the added restriction that any γ-ray included must be in coincidence with at least one electron, reducing several sources of background contamination. The third and fourth spectra were background-subtracted gates on the 168.5 and 854.3 keV γ-rays, respectively, which are identical to those shown in figure 4.3, except without add-back.

Both the singles, and β-gated singles were normalized such that the intensity of the 168.5 keV γ-ray was 100. The gate on 168.5 keV was normalized so that the 854.3 keV γ-ray was equivalent to what was measured in the singles spectrum. The 854.3 keV gate was normalized by the intensity of the 192.4 keV γ-ray, compared to its weighted average intensity in both the singles and β-gated singles spectra. In all four of these spectra some transitions were too weak to measure (which is why the singles alone were not used). The intensities of transitions which were measurable in multiple spectra were averaged using the inverse of the squares of the uncertainties as weights. Because of the delayed decay of the 1095.7 keV isomer no transitions below it in the β-gated singles could be accurately measured (specifically the 61.0, 72.9, 168.5, 793.5, 854.3, and 962.0 keV transitions). Similarly, in the 168.5 keV gate, none of the transitions above the isomer were accurately measurable (namely 92.8, 110.0, 142.9, 192.4, 300.9, and 490.6 keV). If a static coincidence (i.e. a hard cutoff) had been used, these inaccuracies due to the lifetime of the isomer could have easily been accounted for (see Appendix B, for details), but a "rolling" coincidence makes this correction nearly impossible.

Figure 4.4: Figure comparing the singles spectra from both the $A = 164$ (black) and $A = 165$ (red) β-decay data. The $A = 164$ data was normalized to the $A = 165$ data by a factor of 4.620 so that the sum of the counts from 104 to 110 keV would be the same for both spectra, as shown.

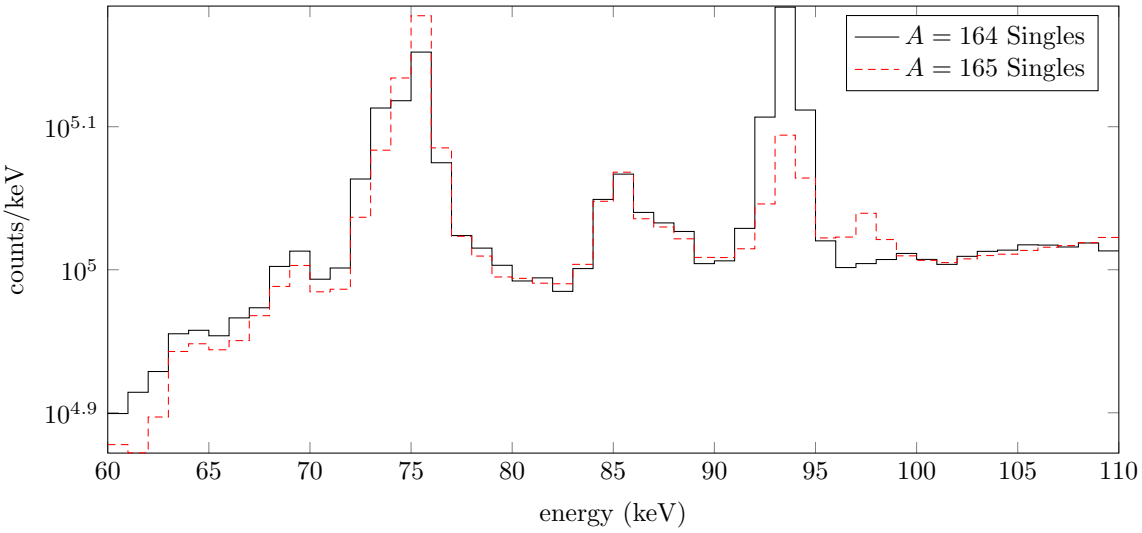

Because the 72.9 keV transition decays primarily by internal conversion *and* can not be separated easily from the 75.0 and 72.9 keV Pb X-rays, a more complicated process was needed to measure its intensity accurately. To measure the intensity of the 72.9 keV transition, the singles spectrum from ^{165}Gd data (generated by the same methods as described in section 2.2, but for $A = 165$) was compared to the singles spectrum for the ^{164}Gd data discussed in this work. These two spectra were normalized by the 104-110 keV background region, where neither spectrum has any clear peaks causing the Pb K_β X-rays at around 85 keV to be identical, and the 73-75 X-ray/desired transition peak to be nearly identical. This comparison and normalization is shown in figure 4.4. Since, after normalization, the two spectra have the same intensity K_β X-rays, their K_α X-rays should also have the same number of counts. Thus the discrepancy between the 73 to 75 keV peaks in these two spectrum should be caused by only things other than Pb in these two data sets. In the ^{164}Gd data, the only other energy in this peak is the 72.9 keV transition from ^{164}Gd. The ^{165}Gd data have three other energies in the 73-75 keV peak, all from the β-decay of ^{149}Nd, which

enters the beam when it bonds with ^{16}O.[1] There are three confirmed $\sim$74 keV γ-rays in ^{149}Pm that are known to be observed in the β-decay of ^{149}Nd. The contribution of these γ-rays to the $\sim$72-75 keV peak was determined based on their well known intensity relative to the 114 keV γ-ray from ^{149}Pm from the β-decay of ^{149}Nd (see Schneider *et al.* [76] for detailed intensity breakdown). Subtracting the contribution of these three γ-rays from the $\sim$74 keV peak in the $A = 165$ data allows us calculate $\frac{K_\beta}{K_\alpha} = 0.29(2)$ for Pb, which is in agreement with the calculations by Scofield [77] which have been experimentally confirmed by Sakar *et al.* [78]. Since we know the precise contribution of Pb to the $\sim$74 keV peak in the $A = 165$ data, and that this should be the same as the contribution to the normalized $A = 164$ data, we can determine the exact contribution of the 72.9 keV transition from ^{164}Gd. Doing so (and comparing it to the intensity of the 169 keV transition) yields an intensity of 23(6) for the 72.9 keV transition of ^{164}Gd, as shown in table 4.1.

Finally, all of the transitions under 500 keV were subsequently corrected for internal conversion. To do this a multipolarity had to be assumed for each of these transitions. The γ-ray energy and assumed multipolarity were fed into the brIccFO database [15] yielding the internal conversion coeficients used to get the intensities corrected for internal conversion shown in table 4.1. For most transitions the multipolarity used comes from the most likely result given the spins and parities of the levels involved. For some transitions, however, the multipolarity chosen is mainly a wild guess based on the spin of the state the transition feeds and the the likely spin and parity of the ground state of ^{164}Eu. The one exception to this is the 61.0 keV transition, whose internal conversion coefficient was measured directly, though the BrIcc value was still used in table 4.1. After internal conversion correction, all of the levels in ^{164}Gd demonstrate more decay out of the state than feeding into the state, within error bars.

[1] It is likely that ^{148}Nd similarly bonds with ^{16}O and is a contaminant in the beam for the ^{164}Gd experiment. However, because ^{148}Nd is stable it does not β-decay to produce more γ- and X-rays as contaminants in the $A = 164$ data.

Table 4.2: The internal conversion coefficient (ICC) of the 61.0 keV transition has been measured by a gate on the 192.7 keV transition with a 2 μs rolling coincidence window. The longer coincidence ensures that no intensity is lost due the lifetime of the the isomer, especially since the timing resolution of our Ge clovers is worse at lower energies. By measuring the relative intensities of the 793.5, 962.0, and 61.0 keV transitions, the ICC can be found by equation 4.1. The 793.5, however, was indistinguishable from background in the 192.7 keV gate. Thus its area has been deduced from the intensities given in table 4.1. From the comparison between experimental and theoritical ICC values, it is clear that the 61.0 keV transition is E1.

E_γ (keV)	I_γ (relative)	ICC of 61.0 keV transition	
		Experimental	Theoretical [15]
61.0	426(99)		E1: 1.090(16)
793.5	55(27)*	1.0(7)	M1: 8.42(12)
962.0	808(217)		E2: 16.97(42)

The internal conversion coefficient of the 61.0 keV transition was measured by gating on the 192.8(5) keV transition. The sum of the intensities of the two transitions depopulating the 1034.3 keV state fed by the 61.0 keV transition are taken as the total intensity ($\gamma + e^-$) of the 61.0 keV transition. This intensity is compared to the measured intensity of the 61.0 keV transition, which is the γ-ray intensity in equation 1.33. This means that the internal conversion coefficient of this 61.0 keV transition is

$$\alpha_{61} = \frac{I_{961} + I_{793}}{I_{61}} - 1 \tag{4.1}$$

where α is an internal conversion coefficient (defined in equation 1.33) and I_E is the measured γ-ray intensity of a transition with energy E (in keV). The one complication to this is that, in the 192.4 keV gate, the 793.5 keV transition is barely identifiable above background, and thus too week to fit. The branching ratios of the 793.5 and 962.0 keV transitions from the total γ-ray intensities in table 4.1 was used to determine the intensity of the 793.5 keV transition. These measured intensities of the 962 and 61 keV transitions and the calculated intensity of the 794 keV transition in this background subtracted 192.4 keV

gate are shown in table 4.2. The experimentally measured internal conversion coefficient for this transition is 1.0(7), consistent with an E1 transition as determined by brIcc [15] and shown in table 4.2. Rather than introduce an additional 70% uncertainty to the intensity of the $\sim$60 keV transition, the brIcc value for an E1 transition has been adopted in table 4.1.

4.3 Lifetime Measurements

The lifetime of the 1095.7 keV state has been measured to be 0.56(3) μs. This measurement was conducted by measuring the exponential decay rate from the $\beta - \gamma$ time, or the time between the detection of an electron and the detection of a γ-ray, using a 2 μs rolling coincidence for longer observation of the isomer. In the $\beta - \gamma$ time vs. γ-ray energy plot, the sum of the 854.3 and 168.5 keV γ-rays was used for this measurement. The resulting summed gate is displayed in figure 4.5.

Three key features of the $\beta - \gamma$ time data are apparent in figure 4.5. First is the large sudden rise and rapid drop starting a few ns after the detection of the electron. This initial hump is caused by fundamental limitation of our detector crystals and electrons, hiding all the prompt decays and thereby placing a lower limit on the lifetimes that are measurable in our setup. Two humps are visible in this initial formation, due to the fact that these detector/electronic limitations are energy dependent, with lower energies taking longer to both rise and fall. The second feature is caused by the decay of the isomer. An exponential decay law (equation 1.2) will appear as a straight line on a logarithmic graph, such as figure 4.5. This section of the graph has been fit to determine the lifetime of the 1095.7 keV state. The third segment of figure 4.5 is in the appearance of a shorter lifetime starting at 2 μs. This effect is caused by the nature of the "rolling" coincidence by which our data were compiled. The data were compiled using a 2 μs "rolling" coincidence window for this measurement, rather than the 1 μs "rolling" coincidence window used for the majority of the analysis described in this chapter. This means that the compiler does not close an event until 2 μs have passed without detecting any signals in any of the 6 detectors of the

Figure 4.5: A plot of sum of gates on the 854.3 keV and 168.5 keV γ-ray energies as a function of the $\beta - \gamma$ time. In our system, our β-detectors are incapable of distinguishing between conversion electrons and actual β-decay electrons. This fact, combined with properties of the electronics and limitations of the detectors' timing resolutions, causes the large "bump" at the beginning of the data. While a 1 µs "rolling" coincidence window allows for more statistics overall, it does cause an attenuation of observed transitions from isomers starting after 1 µs. To partially deal with this, the data were recompiled using a 2 µs rolling coincidence window for the lifetime measurement. However, a change of slope (i.e. apparant lifetime) can be observed starting at 2 µs. The fit shown between the end of the "bump" and 2 µs is used to determine the lifetime of the 1095.7 (4^-) isomer in ^{164}Gd.

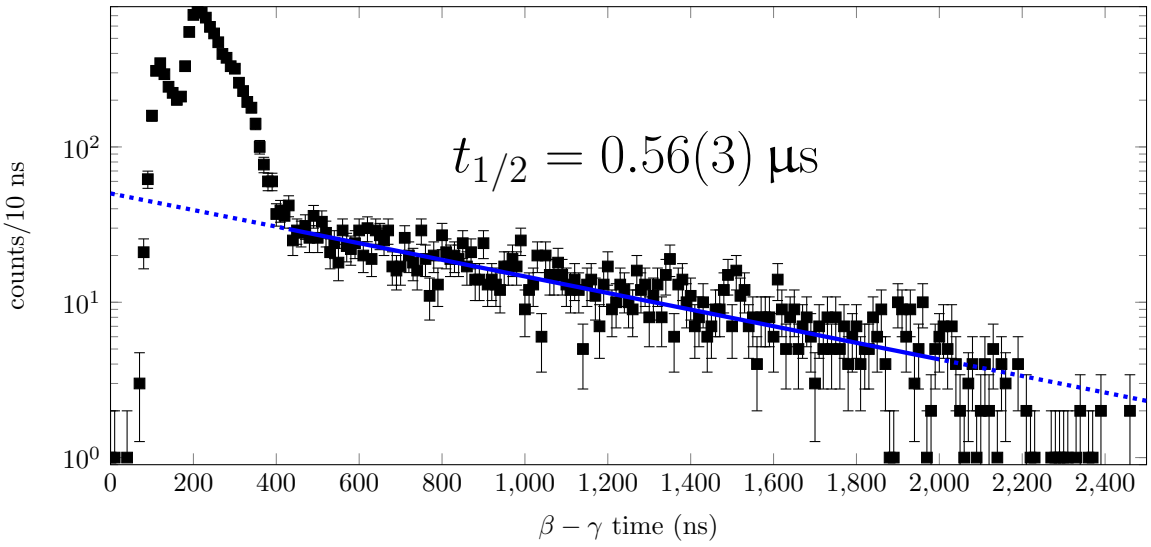

LeRIBSS. This means that the first 2 μs of an event behave like normal, but the rate of inclusion drops for all particle-detections occurring after 2 μs. This effect appears as a faster rate of decay imposed on top of all data occurring greater than 2 μ from the particle detection triggering the start of the coincidence event.[2] For this reason, this section was not included in the fit to determine the lifetime of the 1095.7 keV state.

According to Patel *et al.* [79] and Yokoyama *et al.* [80] (same research group), the decay of this 1095.7 keV level is hindered by a large change in K. For the 854 keV γ-ray, $\Delta K = -4$, even though $\Delta J = 0$. An experimental hindrance factor can be defined as $f_\nu \equiv \left(t^\gamma_{1/2}/t^W_{1/2}\right)^{1/\nu}$, where $t^W_{1/2}$ is the Weisskopf predicted half life (see Bohr and Mottelson [23], Volume I, Appendix 3C-5) for the transition, $t^\gamma_{1/2}$ is the γ-ray partial half life, $\nu = |\Delta K| - L$, and L is the multipole order of the transition (i.e. EL or ML). Patel *et al.* [79] reports $f_3 = 1.4 \times 10^3$ for the 854 keV γ-ray, while Yokoyama *et al.* [80] quotes $f_3 = 1.28(3) \times 10^3$. The difference between these two results primarily stems from differing branching ratios of the 61 keV transition compared to the 855 keV γ-ray. The present experiment has better statistics than either Patel *et al.* or Yokoyama *et al.*, and a new half life measurement which is consistent with both of their half life measurements. Based on these considerations we have found $f_3 = 1.27(6) \times 10^3$ for the 854 keV transition and $f_1 = 4.5(13) \times 10^6$ for the 61 keV transition, consistent with the measurements of Yokoyama *et al.* These two hindrance factors were measured with partial half lives $t^\gamma_{1/2}(61) = 4.5(13)\,\mu s$, $t^{IC}_{1/2}(61) = 4.1(23)\,\mu s$, and $t^\gamma_{1/2}(854) = 0.75(11)\,\mu s$, derived from the branching ratios of the 854 and 61 keV $\gamma - rays$ and the ICC of the 61 keV transition. Of course, the f_ν hindrance factor assumes that the only thing hindering the decay of the state is a high ΔK. We believe, based on the theoretical calculations discussed in appendix A, that shape coexistence may also contribute to some of the hindrance.

Finally, the lifetime of the ^{164}Eu β-decay parent of ^{164}Gd has been measured by examining the tape cycles, as shown in figure 4.6. A 2-d histogram was generated which

[2] By contrast, a standard or hard-cutoff coincidence window would observe a sharp discontinuity at 2 μs, with 0 counts in every channel at greater times.

gives γ-ray energy vs. time within a tape cycle, and consists in the sum of all tape cycles. As noted in section 2.2, the tape cycle was 8 s beam-on, followed by 8 s beam-off, for a total of 16 s. This means that our total tape cycle is only about 4 half-lives (previous: 4.2(2) s [59] and 3.80(56) s [81], see also [61]), with only two half-lives being allowed for each grow-in and decay-out, which increases the uncertainty in this lifetime measurement[3]. Background subtracted gates on 72.9, 168.5, and 854.3 were combined for more statistics. Both the grow-in and decay out were fit simultaneously with a piecewise function, combining equations 1.2 and 1.6. From this fit, we deduced the half life of ^{164}Eu to be 3.9(3) s, in agreement with the 4.15(20) s NNDC accepted half life [61]. The result of these gates and fitting is shown in figure 4.6.

4.4 Discussion

From the intensity data shown in table 4.1, we can calculate the combined β- and unobserved-γ-feeding for each level. The results of this analysis is shown in table 4.3. It is impossible, in our experimental setup, to measure the absolute β-feeding to the ground state, which would normally mean that true β-feeding measurements – including the determination of $\log ft$ values – would be impossible. However, the previously proposed spin of the ground state of ^{164}Eu is 3, with no parity assignment [61], meaning that direct β-feeding to the ground state would be second or third forbidden (see table 1.1), and thus negligible. Thus we have calculated $\log ft$ values using the LOGFT program provided by NNDC [83], under the assumptions that β-feeding to ground is negligible and that we are not missing any γ-rays. These $\log ft$ results are also shown in 4.3.

The assumption that no γ-feeding has been missed is, strictly speaking, likely not true for all states in ^{164}Gd, because, as has been shown by total absorption experiments (for example, Rasco *et al.* [84]), β-decay experiments using HPGe detectors frequently miss higher energy γ-rays due to exponentially decreasing efficiency with increasing energy.

[3] While only 2 half-lives is shorter than desired for the measurement of the ^{164}Eu half life, it does minimize some the presence of contaminants from our beam. For example, it mostly precludes population of ^{164}Tb from the β-decay of ^{164}Gd, as that half life is 45(3) s [82].

Figure 4.6: A plot of the measurement of the β-decay half-life of ^{164}Eu. Requiring β-coincidence, background subtracted γ-ray gates on 72.9, 168.5, and 854.3 keV were summed to produce the time spectrum below. These gates were on a γ-ray energy vs. time histogram which sums the results of all tape cycles that occurred during the acquisition of our data. The grow-in and decay-out were fit simultaneously to produce the curves shown. The resulting half-life is 3.9(3) s.

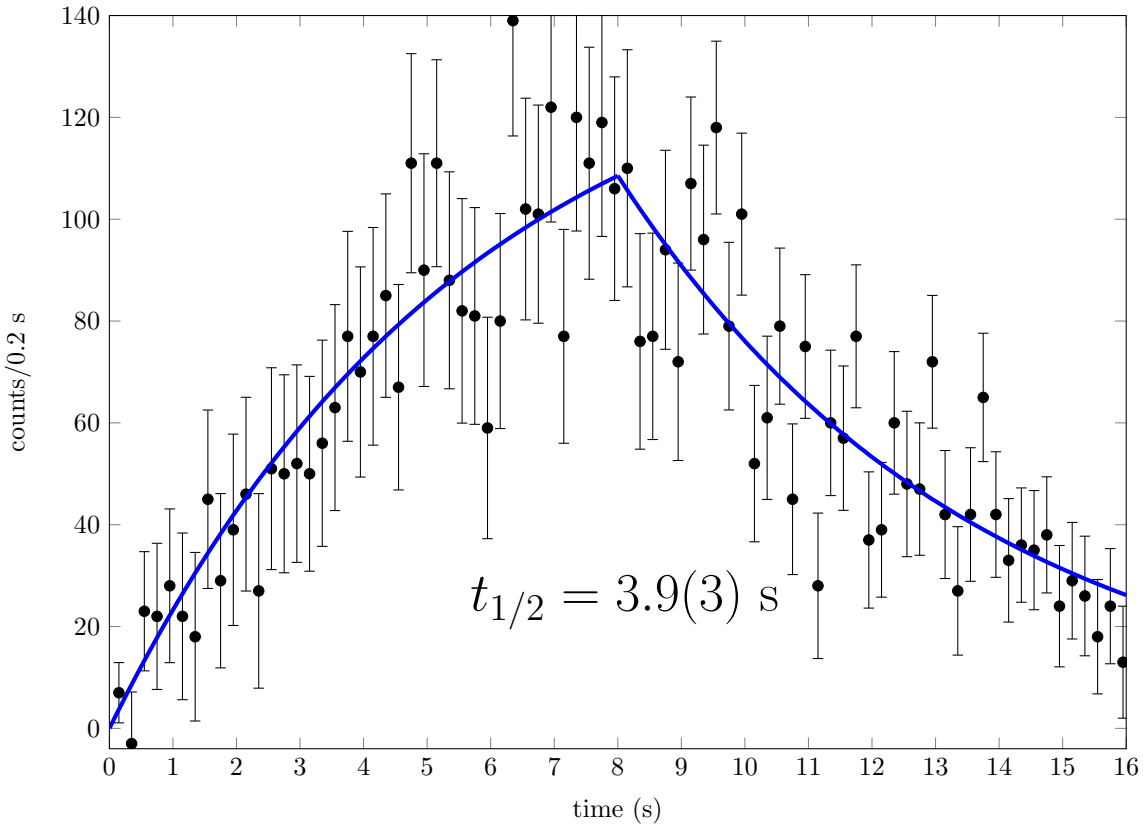

Table 4.3: The γ-ray feeding and outflow of excited levels in ^{164}Gd from the β-decay of ^{164}Eu. The difference between these values represents the relative combined β- and γ-feeding that are not directly observable in our setup. All feedings and outflows are in relative units. These data are generated from the internal conversion corrected intensities reported in table 4.1. Subscripts on spin-parity labels indicate band, following the same convention described in the caption to table 4.1. The $logft$ values are calculated using the "LOGFT" tool by Emeric and Sonzogni [83] assuming negligible β-feeding to ground and that no γ-rays from the β-decay of ^{164}Eu are left unobserved. If there is non-negligible feeding directly to the ground state, then all the $\log ft$ values here would increase. If there are unobserved γ-rays, then the levels that those γ-rays feed would have higher $\log ft$ values than what is listed (and it is more likely that weakly populated levels have unobserved γ-feeding than strongly populated ones, because it is harder to observe a weak γ-ray in coincidence with a weak one than a strong one). Thus, all of the $\log_{10} ft$ values reported here are, at worst, lower limits.

E_{level} (keV)	J^π	ob. γ-feeding	γ-outflow	β- & unob. γ-feeding	$\log ft$
0.0	0^+_g	261(57)	0	-261(57)	~ 0.0
72.9(5)	$[2^+_g]$	232(16)	214(61)	< 46	> 6.3
241.4(7)	$[4^+_g]$	108(8)	140(8)	31(11)	6.4(2)
502.1(9)	$[6^+_g]$	0	5.8(10)	5.8(10)	7.09(14)
966.3(6)	$[2^+_\gamma]$	8(4)	31(6)	24(7)	6.3(2)
1034.7(6)	$[3^+_\gamma]$	28(12)	43(4)	16(13)	6.5(4)
1095.7(6)	$[4^-_4]$	42(8)	108(14)	66(16)	5.9(2)
1125.3(10)	$[4^+_\gamma]$	0	8(2)	8(2)	6.76(14)
1187.3(8)	$[5^-_4]$	4(3)	18(6)	14(7)	6.5(3)
1288.5(5)	$[3^-_3]$	0	47(6)	47(6)	5.91(13)
[1298.0(13)]	$[6^-_4]$	0	4(3)	4(3)	7.0(4)
1322.2(9)		0	3.5(14)	3.5(14)	7.0(2)
1396.5(8)	$[4^-_3]$	0	12(4)	12(4)	6.5(2)
1429.2(9)		0	7(2)	7(2)	6.7(2)
[1585.7(7)]		0	9(6)	9(6)	6.5(4)
[1615.4(7)]	$[2^+_\beta]$	0	< 17	< 17	> 6.2
[1764.9(9)]	$[4^+_\beta]$	0	< 5	< 5	> 6.7
[3156.3(11)]		0	10(4)	10(4)	5.7(2)
[4885.5(6)]	$[3^-_o]$	0	25(10)	25(10)	4.0(2)

This problem is compounded by the fact that the density of states tends to increase with increasing excitation, meaning that the intensity of any one transition is diluted, before any detection efficiency is considered. Since the Q_β value for ^{164}Eu is 6.39(5) MeV [85], there is plenty of room in the level scheme of ^{164}Gd for higher energy levels and γ-rays beyond what is reported in tables 4.1 and 4.3. However, missing high energy γ-ray transitions would only selectively effect some states more than others, and in an experiment like ours that relies on coincidence analysis to find rare transitions, we are more likely to miss weak transitions that are feeding weekly populated states than those populating strongly populated states, as the statistics on both axes of the coincidence would have few statistics. Regardless, if either assumption is wrong, the $\log ft$ values reported in table 4.3 would increase.

From the $\log ft$ values reported in table 4.3, we can learn a few things about the structure of both ^{164}Gd and ^{164}Eu. First, since only four states have $\log ft$ values below 6, they are likely allowed β-transitions according to table 1.1. Only two of these four states have spins and parities assigned prior to analysis of the $\log ft$ values, and they are the 1095.7, (4^-) and 1288.5, (3^-) levels. In order for both of these two levels to be allowed, the spin and parity of the ground state of ^{164}Eu must be either 3^- or 4^-. This is consistent with the previous assignment [61], thus validating the assumption that there is effectively no β-feeding directly to the ground state. Furthermore, despite the known β-decaying isomers in both ^{160}Eu and ^{162}Eu [86], the lack of a large difference between the spins of known low $\log ft$ values for the levels in ^{164}Gd would indicate that ^{164}Eu has only one β-decaying state, and thus no β-decaying isomers. According to Patel *et al.* [79], ^{164}Eu does have a γ-decaying isomer, but the precise lifetime or energy of the isomer remains unknown. Because of these considerations, we assign a spin and parity of (3^-) to the ground state of ^{164}Eu.

Since the tentative 4885.5 keV state in ^{164}Gd has a 4.0(2) $\log ft$ value, it must be an allowed transition, and might even be super-allowed (see table 1.1), meaning that it most

likely has the same spin and parity as ^{164}Eu. However, a 3^- spin and parity for this state causes problems, since it is believed to decay directly to ground, as that would require an E3 transition. To explain this, we propose that the 4885.5 keV level in ^{164}Gd is from an octupole vibration, as such vibrations are known to cause enhanced E3 transition probabilities (see the 2017.52 keV state in ^{98}Mo [87], for example), just as quadrupole vibrations cause enhanced E2 transition probabilities (see chapter 3). Alternatively, since the three γ-rays[4] we observe decaying from the 4885.5 keV level have no coincidence (at their energy, the statistics are not sufficient for coincidence), it is possible that they don't in fact come from the same level. Also possible is that there are levels above the 4885.5 keV level which feed it, but that we aren't observing due to the low statistics. This seems unlikely as most levels at that high of excitation would most likely decay by multi-MeV transitions as observed for the 4885.5 keV state. Since the energies of these three, otherwise unexplainable, γ-rays observed in the data line up perfectly in energy to all be coming from the same state, we favor the 3^- octupole explanation for this level.

By using equation 1.28 and the intensity data in table 4.1, the $B(\Pi L)$ ratios can be determined for the transitions out of the 966.3, 1034.7 and 1095.7, and 1288.5 keV levels. Because there is no dependence on Π ($= E$ or M) in equation 1.27, we can still use equation 1.28 to calculate the $\frac{B(E1)}{B(M1)}$ ratios for the two $E1$ transitions from the 1288.5 keV state. All of the measured ratios are presented in table 4.4.

A number of things can be stated about this 1288.5 keV level, simply based on the $B(\Pi 1)$ ratios and final spin-parity of its three depopulating γ-rays. First, it decays to the 72.9 keV (2_g^+), 966.3 keV (2_γ^+), and 1095.7 keV (4_4^-) states, thus its own spin and parity must be 2^-, $3^\pm$, or 4^+, because only $M1$, $E1$, and $E2$ transitions are commonly observed.[5] Second, the reduced transition probabilities of the 192.8 and 322.1 keV transitions are clearly much higher than that of the 1215.6 (see table 4.4). By comparing with the reduced

[4]Note that, while all three transitions are recorded in table 4.1, one of them is not shown in figure 4.1.

[5]An observable E3 transition usually requires octupole vibration, as discussed above. Transitions with multipolarity M3 or $L = 4$ or higher are effectively never observed.

Table 4.4: Reduced transition probability ratios measured for ^{164}Gd as seen by the β-decay of ^{164}Eu. These ratios have been computed by equations 1.27 and 1.28.

E_i (keV)	J_i^π	Ratio	before ICC	After ICC
966.3	(2_γ^+)	$\frac{B(E2;966)}{B(E2;894)}$	1.1(3)	1.1(3)
1034.7	(3_γ^+)	$\frac{B(E2;962)}{B(E2;793)}$	4.1(17)	4.1(17)
1095.7	(4_4^-)	$\frac{B(E1,854)}{B(E1,61)}$	0.0027(7)	0.0013(6)
1288.5	(3_3^-)	$\frac{B(E1,1216)}{B(E1,322)}$	0.05(3)	0.05(3)
1288.5	(3_3^-)	$\frac{B(E1;1216)}{B(M1;193)}$	0.0063(13)	0.0048(9)
1288.5	(3_3^-)	$\frac{B(E1;322)}{B(M1;193)}$	0.12(7)	0.09(5)

transition probability ratios found in Lesher *et al.* [88] for ^{160}Gd, we can fairly confidently rule out nearly all collective states. In Lesher *et al.*, the levels of the γ-vibrational band of ^{160}Gd decay only to the ground state band, while the 1288.5 keV state in ^{164}Gd is observed decaying to both γ-vibrational and ground state band. Furthermore, the energy spacing for the 1288.5 keV state does not match for it to be γ-vibrational. We can also rule out $K^\pi = 0^-, 1^-$ octupole vibrational bands, as they are also observed to only decay to the ground state band in ^{160}Gd by Lesher *et al.* The most likely option by comparing with Lesher *et al.* is the 3^- member of a 2^- octupole vibrational band. Lesher *et al.* observes this state in ^{160}Gd decaying to the 4_γ^+, 3_γ^+, and 2_γ^+ with about equal intensity and the 4_g^+ with about 0.7% the reduced transition probability of the other transitions from this level. We rule this level out for ^{164}Gd, because we observe it decaying only to the 2_γ^+ instead of all three γ-vibrational states, and observe decay to the 2_g^+ state, rather than the 4_g^+ state. The 1288.5 keV level cannot be the 4_β^+ level, as decay from this state to the γ-vibrational band would be forbidden, as it simultaneously would create a γ-phonon while destroying a β-phonon. While this statement assumes no $\beta - \gamma$ mixing (i.e. $Z_{\beta\gamma} = 0$), and may not necessarily be true, comparison with the β-band of ^{160}Gd cited in Lesher *et al.* indicates that the assumption of no decay from β-band to γ-band most likely holds true for neutron-rich, even-even Gd isotopes.

Table 4.5: Table of approximate Z_γ and $Z_{\beta\gamma}$ values found for several isotopes near ^{164}Gd. Most cases are taken from the reported intensities. A weighted average of the results from the intensities depopulating the odd spin states give Z_γ and that Z_γ is used to find $Z_{\beta\gamma}$ from the even states. The one exception being the one from Riedinger's work [12], which are weighted averages of the Z_γ and $Z_{\beta\gamma}$ values he lists on p. 183. Because the 3^+_γ and 5^+_γ levels yielded significantly different values for Z_γ for ^{160}Gd,[6] these have been listed separately.

Isotope	Z_γ	$Z_{\beta\gamma}$	Reference
^{154}Gd	0.079(4)	0.010(3)	[12]
^{160}Gd, 3^+_γ	0.079(3)	-0.02(2)	[89]
^{160}Gd, 5^+_γ	0.030(5)	-0.06(2)	[89]
^{162}Gd	0.032(7)	-0.047(3)	Enhong's
^{164}Gd	-0.03(2)	0.03(4)	this work
^{166}Gd	0.05(2)	-0.010(9)	[90]

Thus we are left with the most likely cause of the 1288.5 keV level, being quasi-particle. The theoretical calculations suggest two possibilities for this level; either a (3^-), $(\nu 1/2[521] \oplus \nu 7/2[633])$ or a (4^+), $(\pi 3/2[411] \oplus \pi 5/2[413])$ level. Either assignment would be consistent with the fact that the 1216 keV transition seems to be hindered compared to both the 322 and 192 keV transitions, because high-ΔK transitions are generally hindered, as described in Patel *et al.* [79]. We have chosen to favor the spin anti-aligned partner to the (4^-), $(\nu 1/2[521] \oplus \nu 7/2[633])$, because the theoretical calculations showed that these two states should be near degenerate in energy, but the 4^- drops significantly when shape-coexistence (believed to be the cause of the 1095.7 keV isomer) is brought in. Furthermore, decay from a proton quasi-particle to a neutron quasi-particle state would be a two particle, rather than a single particle, transition, and thus should be significantly hindered, making the 192 keV transition effectively unobservable. Thus we believe that the 1288.5 keV level is likely a (3^-), $(\nu 1/2[521] \oplus \nu 7/2[633])$ state with the same shape as the ground state, and favors decay to the 1095.7, (4^-) level due to the shared configuration, but is not delayed by shape change when decaying to the ground- and γ-bands.

From the $B(E2)$ ratios of transitions from the 966.3 keV, (2^+_γ) and 1034.7 keV, (3^+_γ) states shown in table 4.4, we can use equation 1.29 and table 1.2 to find the γ-ground (Z_γ) and β-γ ($Z_{\beta\gamma}$) mixing for ^{164}Gd. First, from the 1034.7 keV level we find $Z_\gamma = -0.03(2)$. Second, by using this Z_γ, the $B(E2)$ ratio from the 966.3 keV level gives us $Z_{\beta\gamma} = 0.03(4)$. As shown in table 4.5, these results are not consistent with neighboring isotopes of Gd. Three possible explanations exist for this discrepancy. First, the intensities of the 793.5 and/or 962.0 keV transitions have been inaccurately measured in this work. This seems unlikely when compared to previous work, which agree with the low branching ratio of the 793.3 keV transition; Yokoyama *et al.* [80] does not report the transition at all, and Patel *et al.* [79], the only previous reference which includes the transition, lists it only tentatively[7]. Second, it could be indicative that the 1034.7 keV level is not γ-vibrational. This also seems unlikely, since theory calculations (figure A.1), the internal conversion coefficient of the 61 keV transition, and the spacing between the the 1034.7 and the proposed (2^+_γ) and (4^+_γ) levels all favor γ-vibrational behavior for this state. Third, interesting structure in ^{164}Gd causes it to behave differently than neighboring isotopes. This is backed up by the fact that ^{164}Gd, according to first 2^+ excited state energy, appears to be less deformed than its immediate neighbors, as shown in figure 1.1. The biggest problem, however, with this last explanation arises because there is currently no known mechanism or theory to explain such a discrepancy. Further research into the structure of ^{164}Gd beyond the capabilities of the current experimental methods is required to truly answer this question.

[6] I suspect the cause of the discrepancy to be caused by imprecision in their intensity measurements. However, without directly handling the data described in Lesher *et al.* [88] or Reich [89], determination of the validity of the discrepancy cannot be determined.

[7] None of the other previous works claim to observe the 1034.7 keV level.

Chapter 5

Structure of Midshell, $A \sim 150 - 170$, Rare ^{252}Cf Fission Fragments

5.1 ^{164}Gd

Previous work using our $\gamma-\gamma-\gamma$ ^{252}Cf, SF data (see section 2.1) by Jones *et al.* [91, 92] established the yrast band of ^{164}Gd up to 14^+. However, at the time, the data were not yet compiled into a $\gamma-\gamma-\gamma-\gamma$ format. Additionally, several new works [80, 79, 93] based on isomeric decay from a 4^- state added two new non-yrast levels and three new γ-rays to the level scheme of ^{164}Gd, including one of three γ-rays previously observed by Osa *et al.* [59] that had not been placed into the level scheme. Careful analysis of the $\gamma-\gamma-\gamma-\gamma$ and reanalysis of the $\gamma-\gamma-\gamma$ SF data yielded 11 new levels and 18 new γ-rays. This includes one of the three transitions identified by Osa *et al.* [59]. Three of these new transitions, four of the new levels, and the newly placed transition were also observed in the β-decay of ^{164}Eu, as described in chapter 4. The level scheme of ^{164}Gd, as seen in the SF of ^{252}Cf, is shown in figure 5.1.

Figures 5.2 and 5.3 show double and triple gated coincidence spectra, respectively, that give evidence for the transitions found in ^{164}Gd. The 168.6 keV $4^+_g \rightarrow 2^+_g$ transition in ^{164}Gd is the strongest transition observable in our data. For this reason a double gate on this 168.6 keV transition and the 1455.1 keV $2^+_g \rightarrow 0^+_g$ transition in ^{84}Se (the 4 neutron fission partner of ^{164}Gd) was used to observe the majority of the yrast band of ^{164}Gd and many of the side bands and is shown in the top of figure 5.2. The bottom of figure 5.2 is a gate on the first two transitions in the ground state band of ^{84}Se, and shows the majority of the transitions in ^{164}Gd. Figure 5.3 shows two triple gates used to uncover the lower energy transitions built on top of the previously observed 4^-, 1096.5 keV isomer.

The intensities of the γ-rays from ^{164}Gd produced in the SF of ^{252}Cf were measured by the relative areas underneath the peaks, corrected for detector efficiency, in the spectra

Figure 5.1: The level scheme of ^{164}Gd as seen in the SF of ^{252}Cf. In black are transitions and states previously observed by references [91, 92, 80, 79, 93]. In blue is the one transition previously observed by Osa *et al.* [59], that had not been placed into the level scheme observed in this work. In red are newly observed transitions and states.

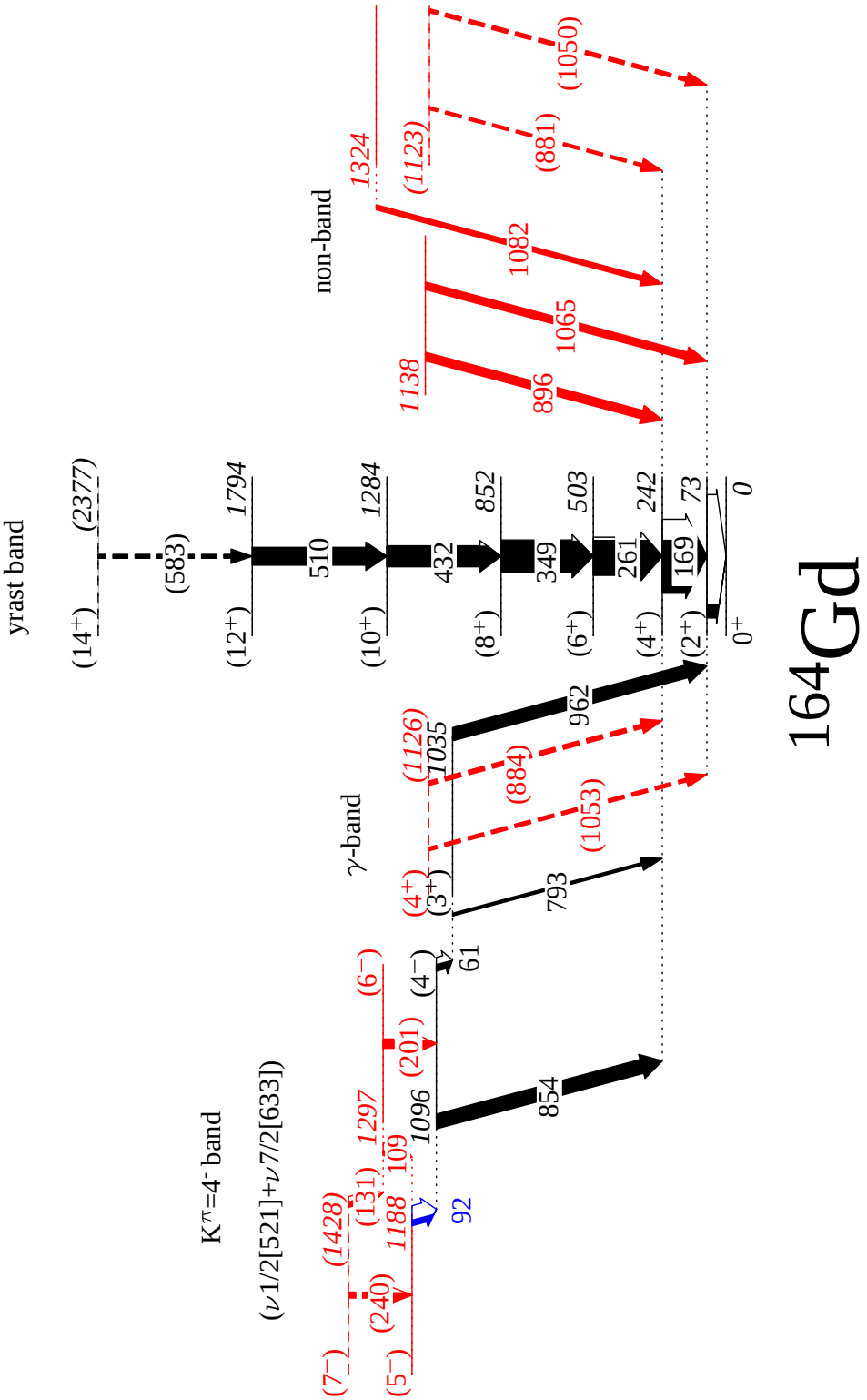

Figure 5.2: Double Gates on 1455.1/168.6 (^{84}Se/^{164}Gd), top, and 1455.1/667.1 (^{84}Se/^{84}Se), bottom, to evidence transitions observed in ^{164}Gd from the SF of ^{252}Cf.

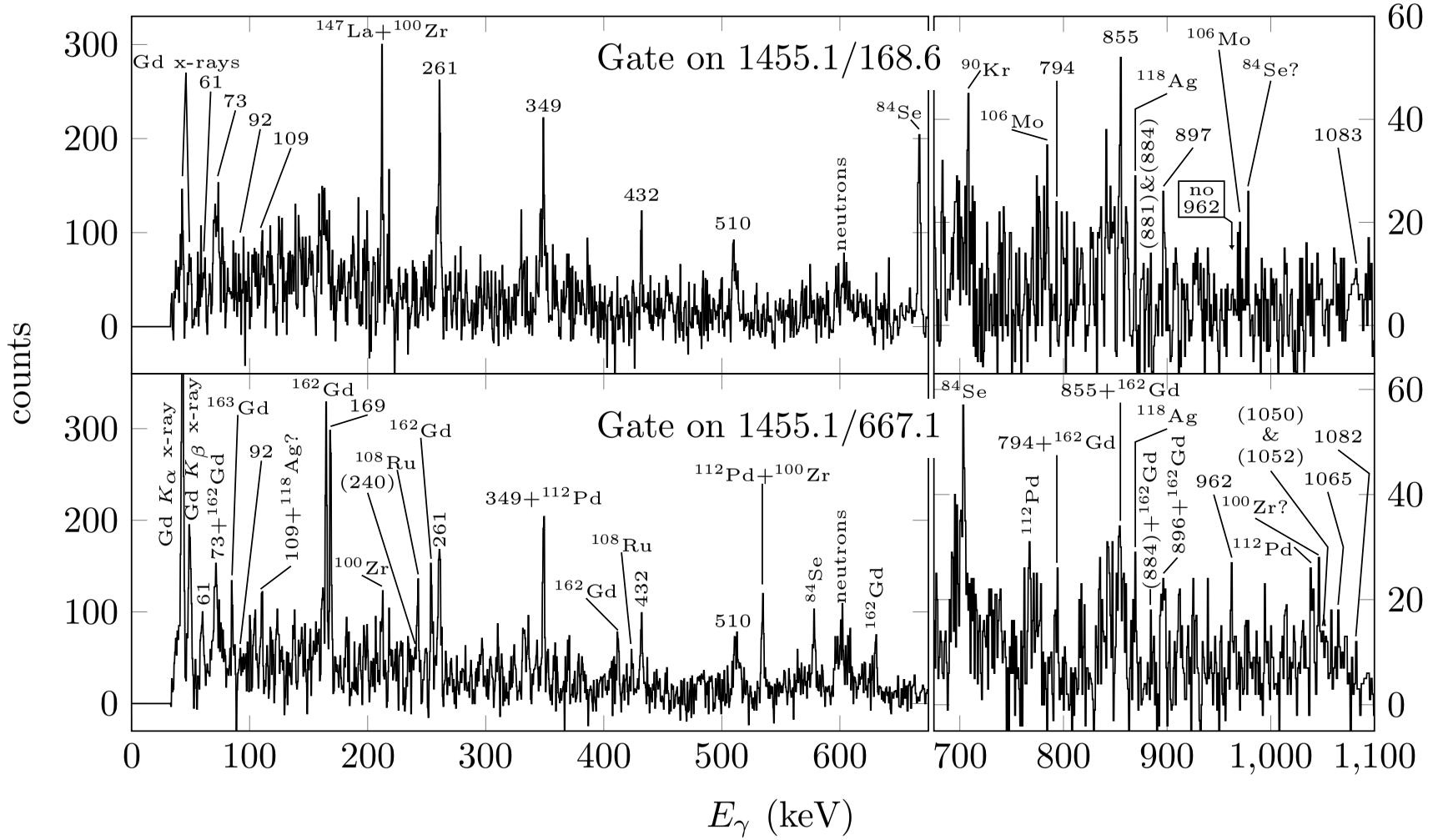

Figure 5.3: Triple Gates on 168.6/854.9/43.1 (^{164}Gd/^{164}Gd/Gd K_α x-ray), top, and 73.0/43.1/962.4 (^{164}Gd/Gd K_α x-ray/^{164}Gd), bottom, to evidence transitions observed in ^{164}Gd from the SF of ^{252}Cf.

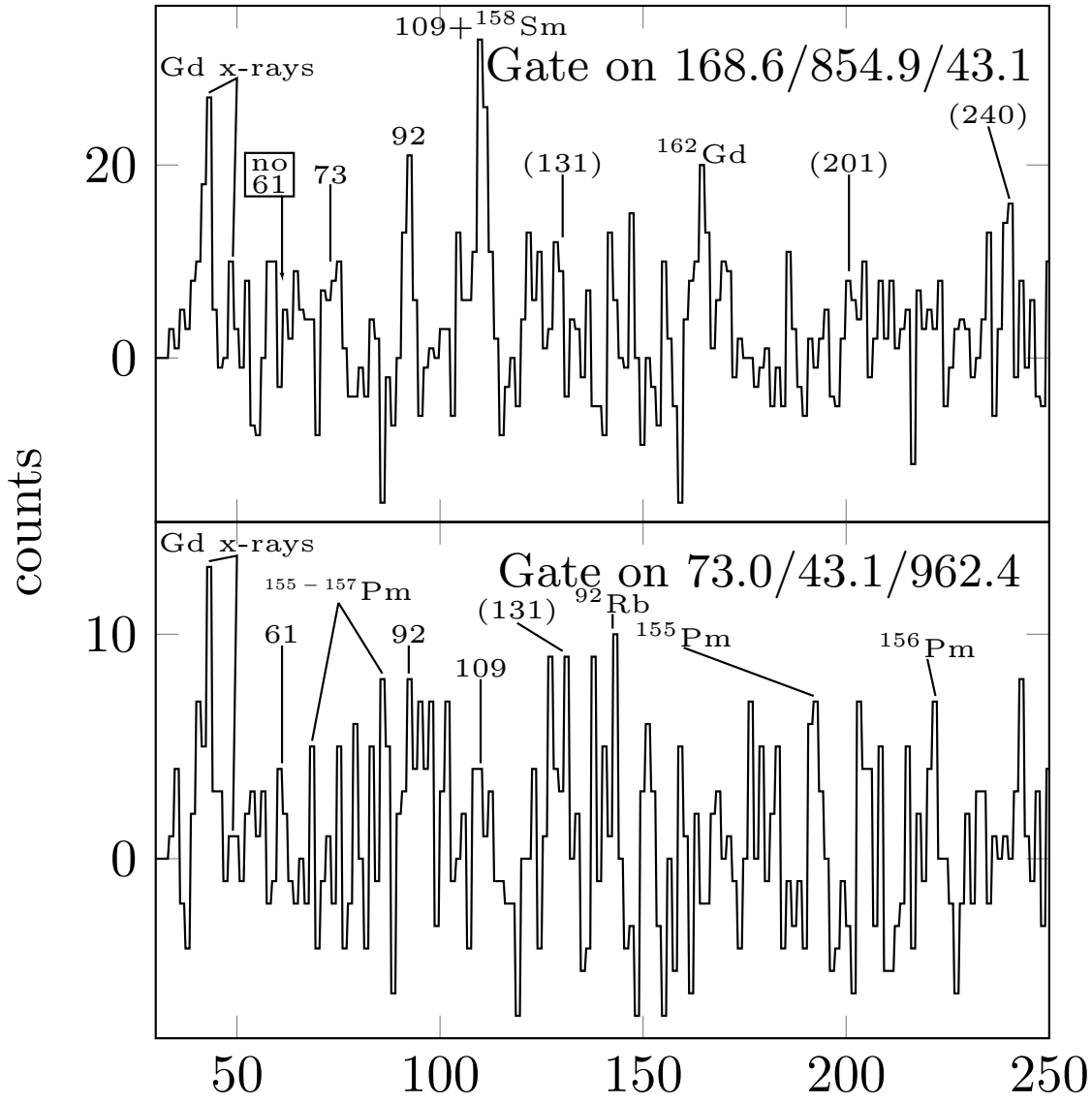

of the two double gates shown in figure 5.2. To avoid losses due to other branches from certain levels, the 1455.1/168.6 gate was used to measure the yrast band transitions, other than 73.0 and 168.6 keV, and the six other transitions directly feeding the 241.6 keV level. The rest of the transitions were measured by the 1455.1/667.1 double gate. The two gates were finally normalized to each other by the intensity of the 260.9 keV transition, as it is the strongest γ-ray accurately measurable in both gates. These results were then corrected for internal conversion according to the brIccFO database [15]. The pre- and post-internal conversion correction intensities are shown in table 5.1, and can also be seen as the width of the arrows in figure 5.1. Because there are so many different nuclei in a ^{252}Cf source, the background scatter is less certain than other, cleaner data sets. Furthermore, ^{164}Gd is extremely rare in our data, meaning that most of its transitions barely rise above the background scatter. For these two reasons, only the strongest transitions, which clearly rise above the background scatter, have been reported with absolute intensity. The majority of the transitions observed in ^{164}Gd, however, have intensities reported only as upper limits in table 5.1.

A rotational band consisting of three new spin states has been observed on top of the (4^-), $(\nu 1/2[521] \oplus \nu 7/2[633])$, 1096.5 keV, isomer with lifetime 0.56(3) μs (see section 4.3) identified in previous works [80, 79, 93], and confirmed by the theoretical calculations discussed in appendix A. The 92.0 keV transition previously observed by Osa *et al.* connects a new (5^-), 1188.4 keV state to the previously known (4^-) bandhead. Furthermore, a 1297.7 keV, (6^-), and 1428.7 keV, (7^-) states have been observed in this band, the 1428.7 keV being tentative. All the appropriate linking transitions between these four levels have been (at least tentatively) observed, and none of the three new states are observed to decay outside the band.

We believe the (3^+), 1035.4 keV state identified by references [80, 79, 93] belongs to the 1 phonon γ-vibrational band for ^{164}Gd, as seen in chapter 4. By using the intensities reported in table 5.1 for the 793.6(8) and 962.2(5) keV transitions, equation 1.28, we find

Table 5.1: Levels and γ-rays in ^{164}Gd as populated in the SF of ^{252}Cf. Uncertainties of γ-rays are ~ 0.5 keV and determine the uncertainties of the level energies. Internal Conversion Coefficients (ICC) are taken from brIccFO [15] assuming the multipolarities shown (where $\Pi =$ E or M). These multipolarities are guesses based on spins and parities and the quadrupole nature of γ-vibrations used to calculate ICCs, and have not been measured or otherwise verified. Square braces indicate that a value is tentative.

E_γ	I_γ	ΠL	$I_{\text{tot.}}$	E_i	J_i^π	E_f	J_f^π
61.2(10)	< 24	[E1]	< 50	1096.4(13)[a]	$[4_4^-]$	1035.2(11)	$[3_\gamma^+]$
73(1)	< 28	[E2]	< 260	73.0(10)[b]	$[2_g^+]$	0.0[c]	0_g^+
92.0(5)[e]	< 12	[M1]	< 41	1188.4(14)[d]	$[5_4^-]$	1096.4(13)[a]	$[4_4^-]$
109.3(11)[d]	< 15	[M1]	< 39	1297.7(18)[d]	$[6_4^-]$	1188.4(14)[d]	$[5_4^-]$
[131.0(12)][d]	< 14	[M1]	< 27	[1428.7(15)][d]	$[7_4^-]$	1297.7(18)[d]	$[6_4^-]$
168.6(6)	100(4)	[E2]	140(5)	241.6(11)	$[4_g^+]$	73.0(10)[b]	$[2_g^+]$
[201.3(12)][d]	< 16	[E2]	< 20	1297.7(18)[d]	$[6_4^-]$	1096.4(13)[a]	$[4_4^-]$
[240.3(5)][d]	< 24	[M1]	< 27	[1428.7(15)][d]	$[7_4^-]$	1188.4(14)[d]	$[5_4^-]$
261.0(5)	66(4)	[E2]	72(6)	502.6(13)	$[6_g^+]$	241.6(11)	$[4_g^+]$
349.0(5)	59(6)	[E2]	62(6)	851.6(14)	$[8_g^+]$	502.6(13)	$[6_g^+]$
431.9	39(4)	[E2]	40(4)	1283.5(14)	$[10_g^+]$	851.6(14)	$[8_g^+]$
509.6(5)	< 37	[E2]	< 37	1793.1(15)	$[12_g^+]$	1283.5(14)	$[10_g^+]$
[583.1(5)]	< 8	[E2]	< 8	[2376.2(16)]	$[14_g^+]$	1793.1(15)	$[12_g^+]$
793.6(8)	< 10	[E2]	< 10	1035.2(11)	$[3_\gamma^+]$	241.6(11)	$[4_g^+]$
854.9(6)	27(2)	[E1]	27(3)	1096.4(13)[a]	$[4_4^-]$	241.6(11)	$[4_g^+]$
[881.1(5)][d]	< 11		< 11	[1122.7(13)][d]		241.6(11)	$[4_g^+]$
[883.9(5)][d]	< 16	[E2]	< 16	[1125.5(13)][d]	$[4_\gamma^+]$	241.6(11)	$[4_g^+]$
896.5(5)[d]	< 18		< 18	1138.1(12)[d]		241.6(11)	$[4_g^+]$
962.2(5)	24(4)	[E2]	24(4)	1035.2(11)	$[3_\gamma^+]$	73.0(10)[b]	$[2_g^+]$
[1049.7(8)][d]	< 15		< 15	[1122.7(13)][d]		73.0(11)[b]	$[2_g^+]$
[1052.5(8)][d]	< 13	[E2]	< 13	[1125.5(13)][d]	$[4_\gamma^+]$	73.0(10)[b]	$[2_g^+]$
1065.1(7)[d]	< 17		< 17	1138.1(12)[d]		73.0(10)[b]	$[2_g^+]$
1082.5(5)[d]	< 11		< 11	1324.1(13)[d]		241.6(11)	$[4_g^+]$

[a]Isomeric State: $t_{1/2} = 0.59(2)$ µs, weighted average of references [80, 79, 93]

[b]Half-life; $t_{1/2} = 2.77(14)$ ns [60].

[c]Half life; $t_{1/2} = 45(3)$ s [61].

[d]Newly Observed in this work.

[e]Previously observed by Osa *et al,* [59], but not placed into the scheme.

$\frac{B(E2,793.6(8))}{B(E2,962.2(5))} < 1.1$, which is consistent with the $\frac{2}{5}$ predicted by equation 1.29. If this $B(E2)$ ratio were 0, using equation 1.31/table 1.2 we would find $Z_\gamma = -\frac{1}{6}$, which can be taken as a hard lower limit for Z_γ in ^{164}Gd. However, on the other hand, if the ratio is 1.1, then $Z_\gamma = +0.09$, which would be a 1σ upper limit[1]. This un-usefully large window for Z_γ is consistent with both the neighboring isotopes of Gd, and the value for Z_γ found by the β-decay data, which are not consistent with each other (see table 4.5 in section 4.4). In general, the intensity measurements for ^{164}Gd in our ^{252}Cf SF data are not precise enough to adequately measure Z_γ, much less $Z_{\beta\gamma}$.

For the 4^+_γ state in the γ-band, three level energy candidates have been identified in our Cf data at energies of (1122.7), (1125.5), and 1138.1 keV, respectively. For each of these candidates, transitions to both the (2^+) and (4^+) states in the ground state band have been observed, meaning that their spins and parities are probably 4^+ or 3^-, though 2^+ is also possible. Both the 1122.7 and 1125.5 would easily satisfy the expected spacing between the 4^+_γ and 3^+_γ levels equally well, while the 1138.1 keV level would indicate a slightly higher spacing, as shown in figure 5.4. Thus, the 1138.1 keV level is less likely to be the (4^+_γ) level. Second the 1125.5 keV level is also observed in β-decay (see figure 4.1 and table 4.1 in section 4) and assigned as 4^+_γ, and thus is the preferred choice for the 4^+_γ in ^{164}Gd from these three choises in the Cf data. No candidates were observed for the 2^+_γ state, nor for 5^+_γ or higher states in the ^{252}Cf data.

5.2 ^{163}Gd

Until recently, very little was known about the structure of ^{163}Gd. In 2006 Sato *et al.* [94] published 5 γ-rays, but cited no significant structure. In 2013 initial analysis of ^{163}Eu β-decay data (produced by the same methods as described in section 2.2), Nathan Brewer [32] generated an erroneous structure for ^{163}Gd, because he did not know of the 137.8 keV isomer, later observed by Hayashi *et al.* [85] in 2014 with $t_{1/2} = 23.5(10)$ s.

[1] If one uses the 5σ standard of the particle physics community, then we have $-\frac{1}{6} \leq Z_\gamma \leq 0.28$.

Figure 5.4: Systematics for γ-vibrational bands in isotopes of Gd. (a) the 1 phonon γ-vibrational-bands in ^{160,162,164,166}Gd for comparison. The levels in ^{160}Gd are from Reich [89] and those for ^{166}Gd are found in Patel, *et al.* [90]. The TPSM calculations for ^{164}Gd are discussed in appendix A, especially figure A.1. (b) The energy level spacing between levels in the γ-bands of these isotopes. All three candidates for the 4^+_γ state in ^{164}Gd are shown; the dashed lines show the tentatively observed states.

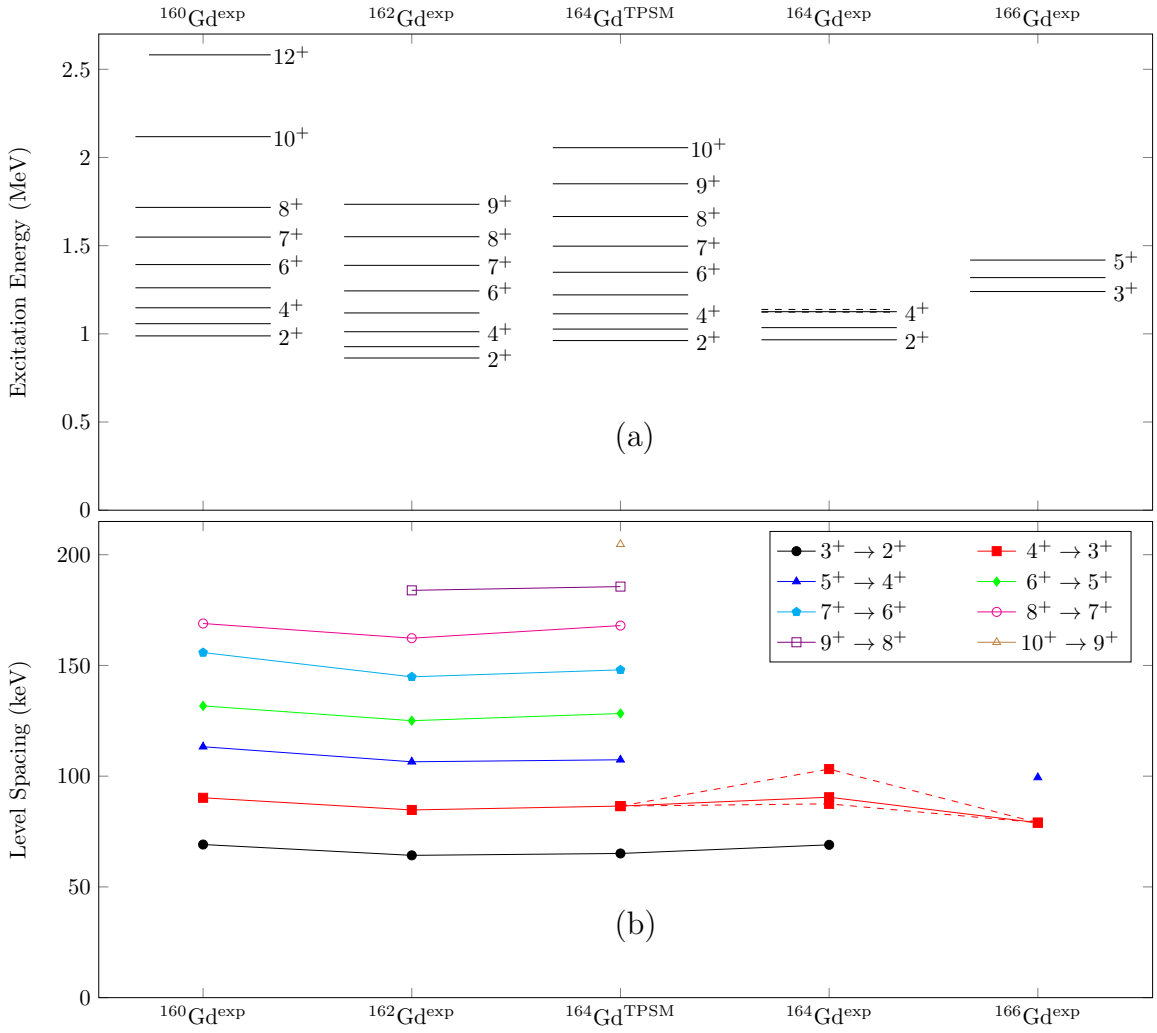

Table 5.2: A list of levels and γ-rays observed for ^{163}Gd in the SF of ^{252}Cf. Internal Conversion Coefficients are taken from the brIccFO [15] database, assuming the multipolarities shown. These multipolarities are educated guesses based on the spins and parities of the levels involved.

E_γ (keV)	I_γ (rel.)	ΠL	I_tot (rel.)	E_i (keV)	J_i^π	E_f (keV)	J_f^π
[48.9(11)][a]	< 70	[M1]	< 240	186.7(10)[a]	$3/2^-$	[137.8(5)][bc]	$1/2^-$
[71.8(5)][b]	$\ll 354$	[E2]	$\ll 3438$	209.6(7)[b]	$5/2^-$	[137.8(5)][bc]	$1/2^-$
84.8(5)	94(9)	[M1]	392(39)	84.8(5)	$9/2^+$	0	$7/2^+$
103.8(5)	100(5)	[M1]	279(15)	188.6(7)	$11/2^+$	84.8(5)	$9/2^+$
115.1(5)	75(8)	[M1]	175(18)	324.7(9)	$7/2^-$	209.6(7)[b]	$5/2^-$
122.8(5)[d]	51(6)	[M1]	109(12)	311.4(9)[d]	$(13/2^+)$	188.6(7)	$11/2^+$
138.0(5)	67(7)	[E2]	119(12)	324.7(9)	$7/2^-$	186.7(10)[a]	$3/2^-$
142.6(5)[d]	< 50	[M1]	< 86	[454.0(10)][d]	$(15/2^+)$	311.4(9)[d]	$(13/2^+)$
265.4(6)[d]	< 18	[E2]	< 19	[454.0(10)][d]	$(15/2^+)$	188.6(7)	$11/2^+$
[453.8(6)]	< 48	[E1]	< 48	[453.8(6)]	$(5/2^-)$	0	$7/2^+$

[a]Not directly measured; Calculated from level differences
[b]Not directly measured; Adopted from Zachary *et al.* [96]
[c]Known Isomer with lifetime, 23.5(10) s [85]
[d]Newly Observed in this work

Chris Zachary [95], in 2019, reanalyzing the data in Brewer [32], also observed this isomer, and built a complex level scheme for ^{163}Gd from the β-decay of ^{163}Eu, the final results of which are published in Zachary *et al.* [96], demonstrating, for the first time, the structure of ^{163}Gd with 112 total γ-rays (including the 5 observed by Sato *et al.* [94]) coming from 53 distinct excited states.

This present work attempts to build on that of Zachary *et al.* [96] by examining the ^{252}Cf data described in section 2.1. This analysis has resulted in three new transitions (two of which are tentative) depopulating two new levels (one of which is tentative) and the confirmation of seven transitions and seven excited states observed by Zachary *et al.* [96]. All of these transitions and levels are tabulated in table 5.2, while the level scheme of ^{163}Gd is shown in figure 5.5.

Because of its odd neutron number, the structure of ^{163}Gd is significantly more complex than ^{164}Gd. This means that any single fission event producing ^{163}Gd has more options on

Figure 5.5: The level scheme of ^{163}Gd as observed in this work. The width of the arrows indicates intensity (white is theoretical internal conversion). In red are the new transitions and levels newly observed in this work.

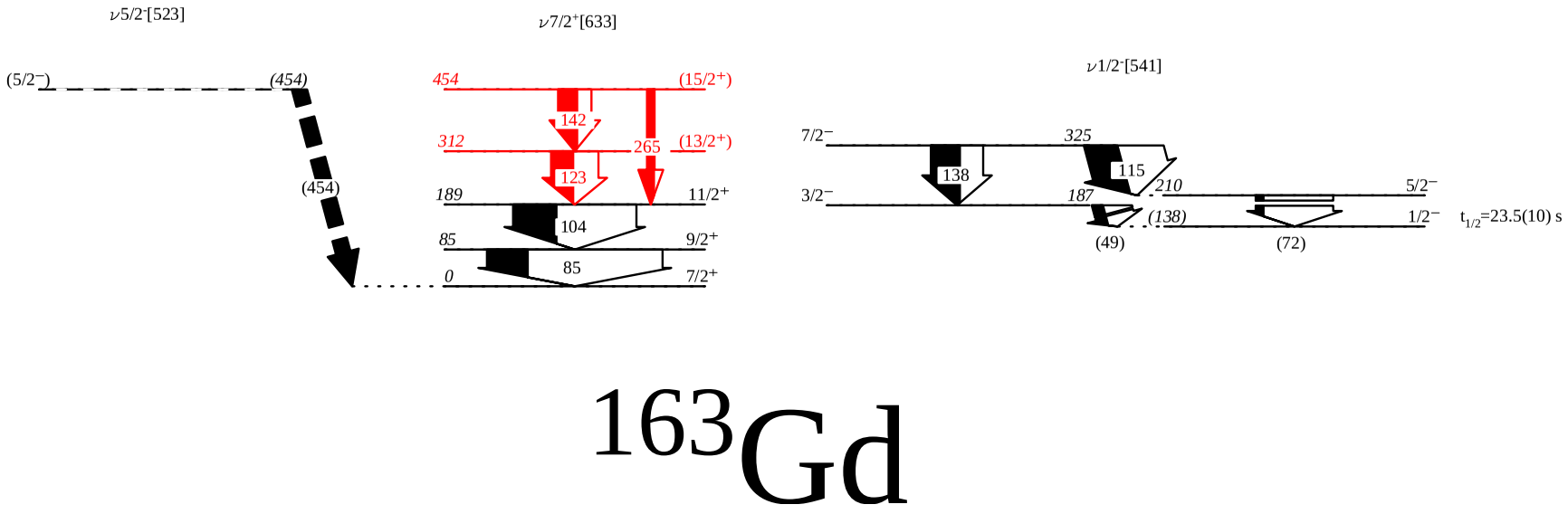

what path to take as it decays to ground than ^{164}Gd does, causing the frequency of any one transition in the level scheme to decrease. This means, despite that ^{163}Gd is produced about twice as frequently as ^{164}Gd in the SF of ^{252}Cf [97], the statistics for ^{163}Gd were minimal, evidenced by the fact that only the 85 keV transition from ^{163}Gd is visible in figure 5.2. The only gate that clearly showed transitions from ^{163}Gd is a double gate on 704.1/863.6 keV from ^{86}Se, the 3 neutron fission partner of ^{163}Gd. Furthermore, all the intensities shown in table 5.2 were measured using this double gate. This gate is shown in figure 5.6. In general, the statistics for triple gates were too low for any conclusions, though results in those gates were not contradictory with the structure shown.

Two major sources of contamination are seen in figure 5.6. First, two $\sim$704 keV transitions are known in the yrast band of ^{110}Ru at 705.3 keV ($8^+ \rightarrow 6^+$) and 703.9 keV ($14^+ \rightarrow 12^+$). When these transitions are combined with the two (albeit weak) $\sim$864 keV (861.5 and 863 keV) transitions in ^{139}Xe, the three neutron fission partner of ^{110}Ru, they produce two contaminant peaks in the spectrum shown in figure 5.6. Additionally, in the yrast band of ^{114}Pd one finds the $16^+ \overset{863.5}{\rightarrow} 14^+ \overset{703.9}{\rightarrow} 12^+$ cascade. Thus the $2^+ \overset{322.8}{\rightarrow} 0^+$ transition from ^{114}Pd can be seen in figure 5.6, as well as two other peaks generated by isotopes of Te, the fission partner of Pd.

As with ^{164}Gd, theoretical calculations for ^{163}Gd can be found in appendix A and figure A.2. The yrast band displayed in figure 5.5 agrees well with these theoretical calculations and systematics with ^{165}Dy (see Sheline *et al.* [98], Greenwood *et al.* [99], and Kaerts *et al.* [100].), which is believed to have the same ground state configuration ($\nu 7/2^+[633]$). Thus, though the coincident evidence for the ^{163}Gd level scheme from the SF of ^{252}Cf is low, we have strong confidence in the structure presented in figure 5.5.

5.3 ^{155}Nd

Previous work by Hwang *et al.* [101] established levels up to 1831.6 keV for ^{155}Nd using $\gamma - \gamma - \gamma$ coincidences from the same ^{252}Cf experiment discussed in section 2.1.

Figure 5.6: A double gate on 704.1/863.6 keV, the first two yrast transitions in ^{86}Se, in which all the transitions observed for ^{163}Gd, its 3 neutron fission partner, are visible.

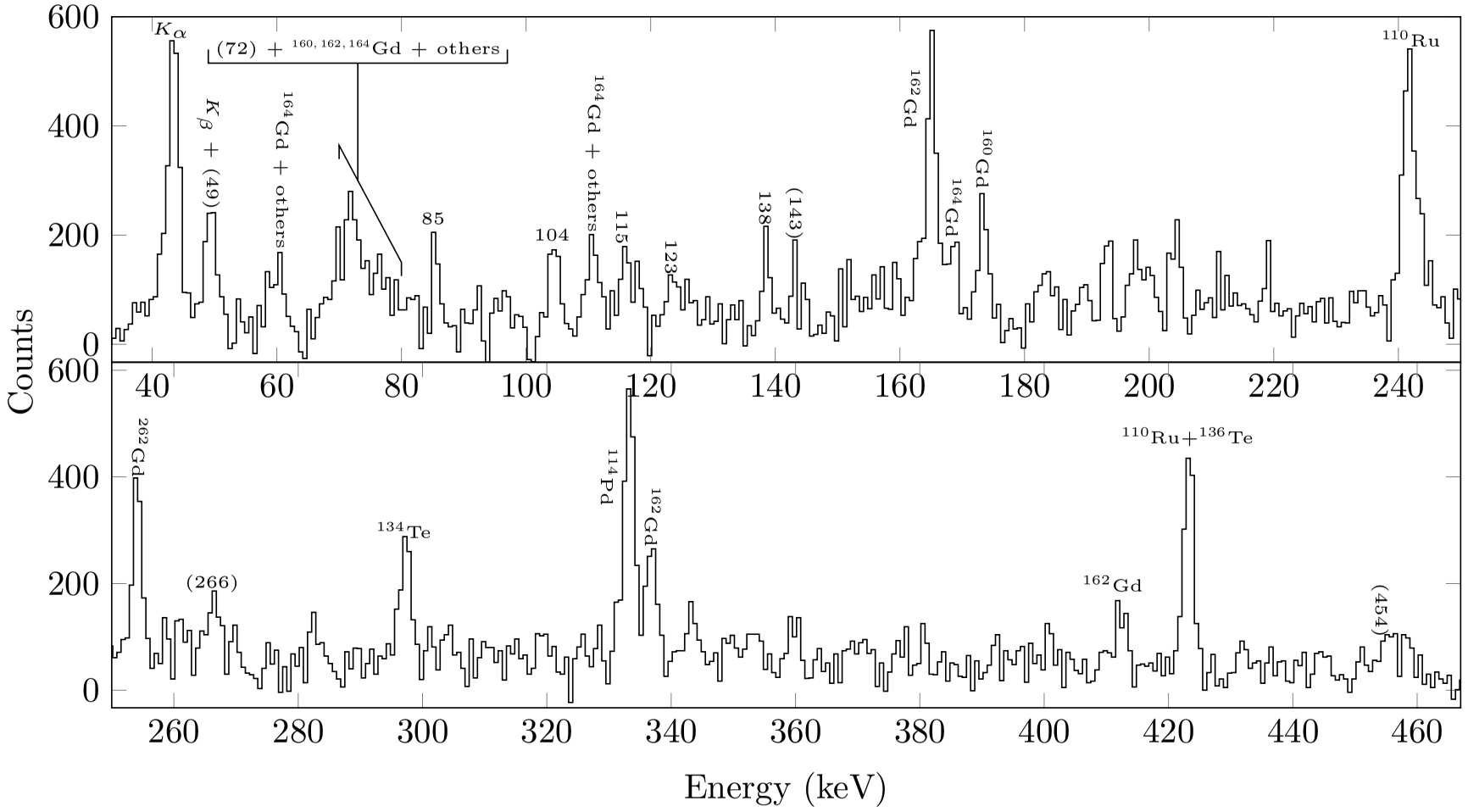

Figure 5.7: The level scheme of ^{155}Nd as found in this work.

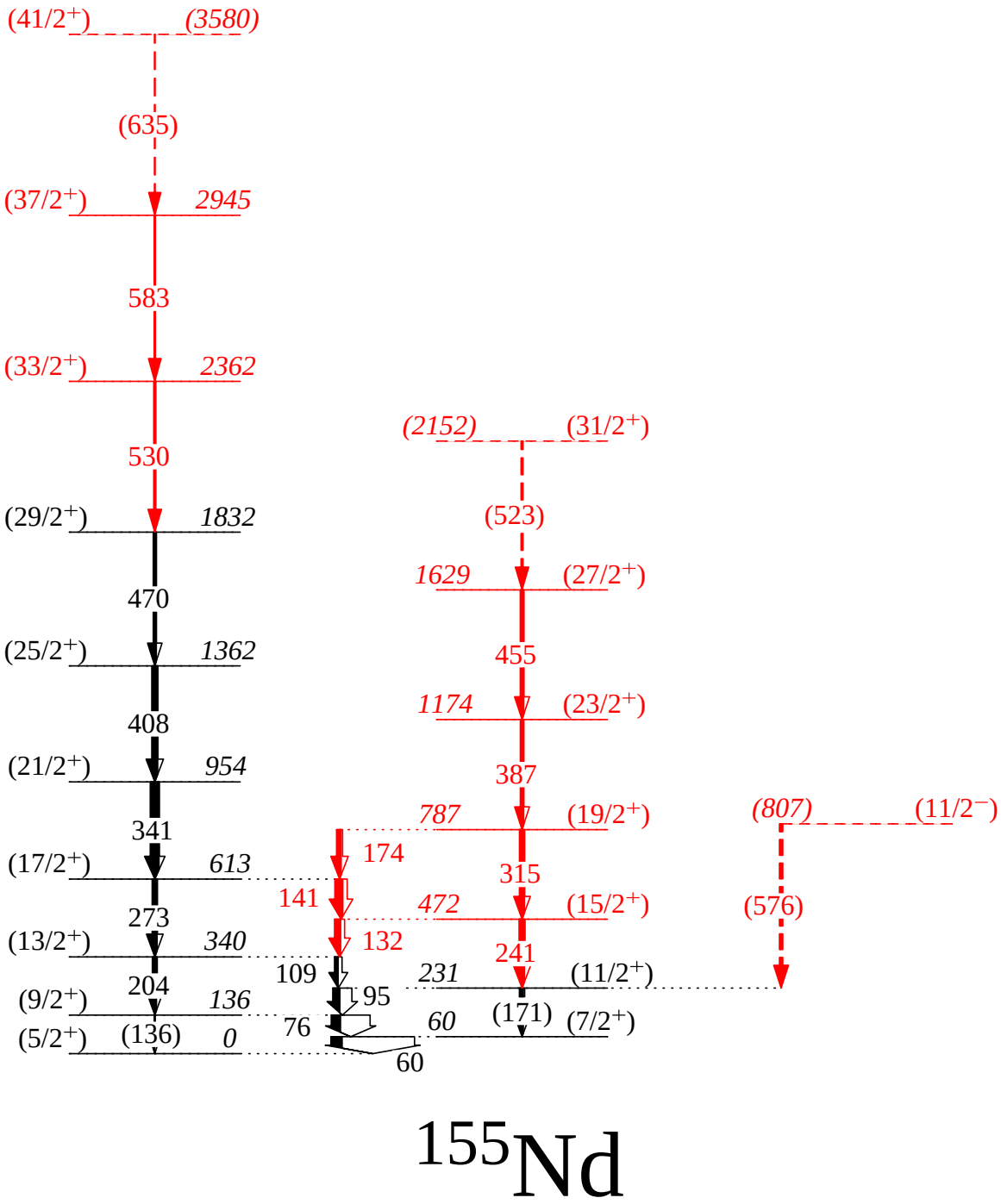

However, at the time, ^{155}Nd had not yet been compiled with $\gamma-\gamma-\gamma-\gamma$ coincidences. By use of $\gamma-\gamma-\gamma-\gamma$ coincidences, the level scheme of ^{155}Nd has been extended up to $\sim$3.5 MeV with 12 new γ-rays and 9 new levels. The newly developed levelscheme of ^{155}Nd is shown in figure 5.7 and more details about the transitions and levels can be found in table 5.3.

Furthermore, based on systematics with ^{153}Nd [101, 102], and ^{155,157}Sm [102, 103] (see also references [104, 105, 106]), we believe that the band described in [101] for ^{155}Nd is actually a $\nu 5/2^+[642]$ band instead of a $\nu 3/2^-[521]$ band. This is because, as shown in figure 5.8, the spacing of the only observed band in ^{155}Nd more closely matches the spacing of the $\nu 5/2^+[642]$ bands in ^{153}Nd and ^{155,157}Sm. Figure 5.8a shows both the $\nu 5/2^+[642]$ and $\nu 3/2^-[521]$ bands for each of these four isotopes (except ^{155}Nd, which has only one band). Figure 5.8b shows the spacing between levels as a function of spin, where one can clearly see that an assignment of $\nu 5/2^+[642]$ for the observed levels in ^{155}Nd matches the spacing of the $\nu 5/2^+[642]$ bands of the other isotopes, especially ^{153}Nd, better than the spacing of the $\nu 3/2^-[521]$ bands. Of particular note is the odd-even staggering. If an assignment of $\nu 3/2^-[521]$ were given to the band observed in ^{155}Nd, then its odd-even staggering of levels would be oposite of the odd-even staggering in the spacing of the other bands observed of either configuration for ^{153}Nd or ^{155,157}Sm. Because of these observations we *strongly* propose a new assingment of a $\nu 5/2^+[642]$ configuration – in place of the previous $\nu 3/2^-[521]$ – for the observed band in ^{155}Nd, which may or may not be the ground state.

As Hwang *et al.* [101] states, the expected ground state of ^{155}Nd is a $\nu 3/2^-[521]$, especially since this is true of ^{153}Nd and ^{155,157}Sm. Thus, based on the present work, the band-head of the band observed in this work and in Hwang *et al.* [101] is not the expected $\nu 3/2^-[521]$ ground state of ^{155}Nd, but rather a $\nu 5/2^+[642]$ excited state. Since no alternative ground states are observed for ^{155}Nd, either (1) the $\nu 5/2^+[642]$ band-head is an isomer, (2) the transition from the $\nu 5/2^+[642]$ band-head to ground is less than 33 keV

Table 5.3: γ-Rays and Levels observed in this work for ^{155}Nd. The intensities measured are corrected for internal conversion up to 500 keV, using the brIccFO [15] database assuming the multipolarity (ΠL) shown. Transitions and levels marked wth an asterisk (*) are newly observed in this work. Square brackets indicate that a transition or level is tentative.

E_γ	I_γ	ΠL	$I_{\text{tot.}}$	$E_i - X$	J_i^π	$E_f - X$	J_f^π
59.6(5)	< 316	[M1]	< 2270	59.6(5)	$\left(\frac{7}{2}^+\right)$	0	$\left(\frac{5}{2}^+\right)$
75.8(5)	< 260	[M1]	< 1070	135.4(8)	$\left(\frac{9}{2}^+\right)$	59.6(5)	$\left(\frac{7}{2}^+\right)$
94.9(5)	100(8)	[M1]	264(22)	230.3(9)	$\left(\frac{11}{2}^+\right)$	135.4(8)	$\left(\frac{9}{2}^+\right)$
109.4(5)	< 99	[M1]	< 207	339.7(7)	$\left(\frac{13}{2}^+\right)$	230.3(9)	$\left(\frac{11}{2}^+\right)$
132.5(5)*	86(12)	[M1]	143(21)	472.2(7)*	$\left(\frac{15}{2}^+\right)$	339.7(7)	$\left(\frac{13}{2}^+\right)$
[135.4(7)]	< 13	[E2]	< 22	135.4(8)	$\left(\frac{9}{2}^+\right)$	0	$\left(\frac{5}{2}^+\right)$
140.9(6)*	112(19)	[M1]	171(29)	613.1(6)	$\left(\frac{17}{2}^+\right)$	472.2(7)*	$\left(\frac{15}{2}^+\right)$
[170.7(8)]	55(9)	[E2]	74(12)	230.3(9)	$\left(\frac{11}{2}^+\right)$	59.6(5)	$\left(\frac{7}{2}^+\right)$
173.7(6)*	65(10)	[M1]	84(13)	786.8(6)*	$\left(\frac{19}{2}^+\right)$	613.1(6)	$\left(\frac{17}{2}^+\right)$
204.3(5)	58(9)	[E2]	69(10)	339.7(7)	$\left(\frac{13}{2}^+\right)$	135.4(8)	$\left(\frac{9}{2}^+\right)$
241.9(5)*	76(12)	[E2]	84(13)	472.2(7)*	$\left(\frac{15}{2}^+\right)$	230.3(9)	$\left(\frac{11}{2}^+\right)$
273.4(5)	69(18)	[E2]	74(19)	613.1(6)	$\left(\frac{17}{2}^+\right)$	339.7(7)	$\left(\frac{13}{2}^+\right)$
314.6(5)*	70(10)	[E2]	73(11)	786.8(6)*	$\left(\frac{19}{2}^+\right)$	472.2(7)*	$\left(\frac{15}{2}^+\right)$
341.3(5)	123(17)	[E2]	127(17)	954.4(8)	$\left(\frac{21}{2}^+\right)$	613.1(6)	$\left(\frac{17}{2}^+\right)$
386.6(5)*	47(7)	[E2]	48(7)	1173.4(8)*	$\left(\frac{23}{2}^+\right)$	786.8(6)*	$\left(\frac{19}{2}^+\right)$
407.5(6)	83(12)	[E2]	85(12)	1361.9(10)	$\left(\frac{25}{2}^+\right)$	954.4(8)	$\left(\frac{21}{2}^+\right)$
455.4(5)*	49(9)	[E2]	49(9)	1628.8(9)*	$\left(\frac{27}{2}^+\right)$	1173.4(8)*	$\left(\frac{23}{2}^+\right)$
469.7(5)	43(15)	[E2]	43(15)	1831.6(11)	$\left(\frac{29}{2}^+\right)$	1361.9(10)	$\left(\frac{25}{2}^+\right)$
[522.7(5)]*	27(6)		27(6)	[2151.5(11)]*	$\left(\frac{31}{2}^+\right)$	1628.8(9)*	$\left(\frac{27}{2}^+\right)$
529.6(6)*	29(4)		29(4)	2361.2(13)*	$\left(\frac{33}{2}^+\right)$	1831.6(11)	$\left(\frac{29}{2}^+\right)$
[576.8(5)]*	47(8)		47(8)	[807.1(10)]*	$\left(\frac{11}{2}^-\right)$	230.3(9)	$\left(\frac{11}{2}^+\right)$
583.3(7)*	17(4)		17(4)	2944.5(15)*	$\left(\frac{37}{2}^+\right)$	2361.2(13)*	$\left(\frac{33}{2}^+\right)$
[635.6(5)]*	10(3)		10(3)	[3580.1(15)]*	$\left(\frac{41}{2}^+\right)$	2944.5(15)*	$\left(\frac{37}{2}^+\right)$

Figure 5.8: Systematics of bands across ^{153,155}Nd, and ^{155,157}Sm. (a) the $\nu 3/2^-[521]$ and $\nu 5/2^+[642]$ bands for each isotope. Since, as discussed in the text, the exact excitation of the lowest observed state in ^{155}Nd is not known, the levels for ^{155}Nd are plotted starting from 0 keV to ensure that they fit in the plot better. Except for ^{155}Nd, which has only one known band, the $\nu 3/2^-[521]$ band is plotted on the left while the $\nu 5/2^+[642]$ band is plotted on the right for each isotope. The spins have been labeled for most levels. (b) a plot of the spacing between any two levels whose spins differing by 1. The dashed lines indicate the $\nu 3/2^-[521]$ bands while the solid lines indicate the $\nu 5/2^+[642]$ bands. The line for the $\nu 3/2^-[521]$ band of ^{155}Nd is what the spins would be if the only observed band were that configuration, rather than the $\nu 5/2^+[642]$ configuration assumed by this work. On can clearly see that the $\nu 5/2^+[642]$ assignment for ^{155}Nd matches closely with the spacing for the same of ^{153}Nd, while somewhat matching the spacing for the Sm isotopes. Also, the odd-even staggering of the $\nu 3/2^-[521]$ for ^{155}Nd is opposite of that for any of the bands of either configuration from the other isotopes considered.

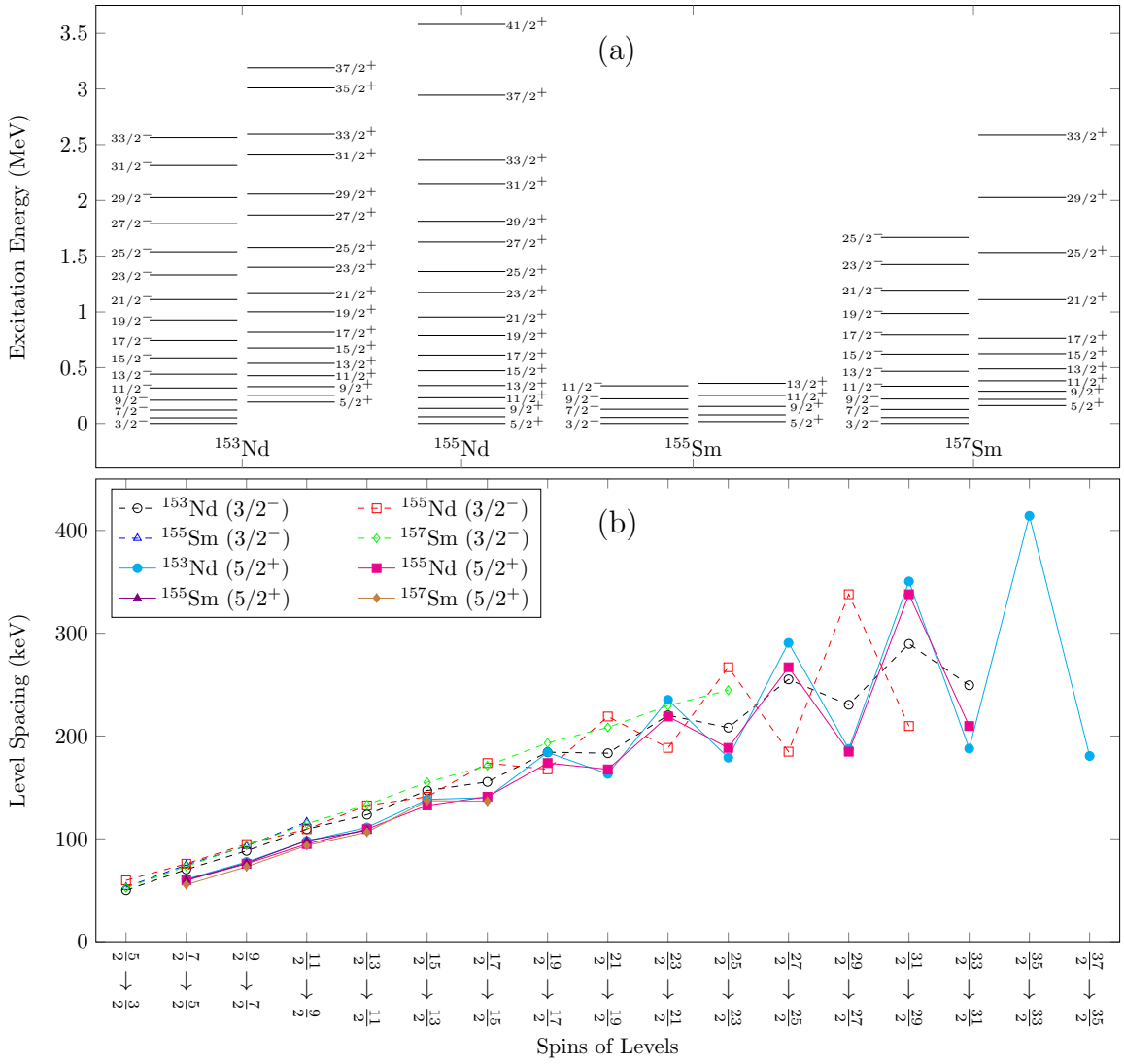

(the minimum detectable energy in our data), (3) the assignment of Hwang *et al.* [101] is correct and the assignment of this work is wrong, or (4) the energies of the $\nu 5/2^+[642]$ and $\nu 3/2^-[521]$ bands are swapped for ^{155}Nd compared to its neighbors. Option (3) would be in direct contradiction with the observations of figure 5.8. While option (4) is not, strictly speaking, impossible concerning the observations in figure 5.8, it is unlikely, since ^{153}Nd and ^{155,157}Sm all observe a $\nu 3/2^-[521]$ ground state and a $\nu 5/2^+[642]$ excited state. Furthermore, option (1) could be consistent with the observed 2.8(5) and 1.06(5) μs half-lives of the $\nu 5/2^+[642]$ states in ^{155}Sm [102] and ^{153}Nd [106], respectively.[2] Thus, based on the systematic shown in figure 5.8, this work favors a combination of options (1) and (2) to explain why the $\nu 3/2^-[521]$ state is not observed in this work.

By looking at the data provided by Musangu *et al.* [107], one can, in principal, check to see if ^{155}Nd has an unobserved ground-state, separate from the $\nu 5/2^+[642]$ state. Musangu *et al.* produced yield curves for the Nd-Sr pair in the spontaneous fission of ^{252}Cf as a function of neutron number. If ^{155}Nd has a $\nu 3/2^-[521]$ band, like its neighbors, that is in fact the ground-state, one would expect that Musangu *et al.* [107] would have missed some of the yield of ^{155}Nd due to this not being known at the time of their analysis. By plotting the yields of Nd for each isotope of Sr as shown in Musangu *et al.* [107], one does indeed find that ^{155}Nd is has a slightly lower yield than the curve, in most cases, as shown in figure 5.9. However, this discrepancy is incredibly small, and could be explained by statistical variation. Furthermore, their analysis primarily uses the 94.9 keV γ-ray (after internal conversion correction) to measure the yields of ^{155}Nd. This means that, without missing the true ground-state of ^{155}Nd, one would already expect their yields to error low for ^{155}Nd, as the 75.8 keV and 59.6 keV transitions could be populated by other means. Thus, the yield curves of Nd-Sr reported in Musangu *et al.* [107], are inconclusive for determining whether or not the lowest level reported in figure 5.7 is the ground state or not.

[2]The lifetime of the $\nu 5/2^+[642]$ state in ^{157}Sm is not known in the literature.

Figure 5.9: Plots of the ^{252}Cf SF yields of Sr isotopes as function of Nd mass number (A). These data are taken from Musangu *et al.* [107]. One can clearly see that ^{155}Nd is slightly low in each curve, creating a concave-up effect. However, in most cases, it is within uncertainty.

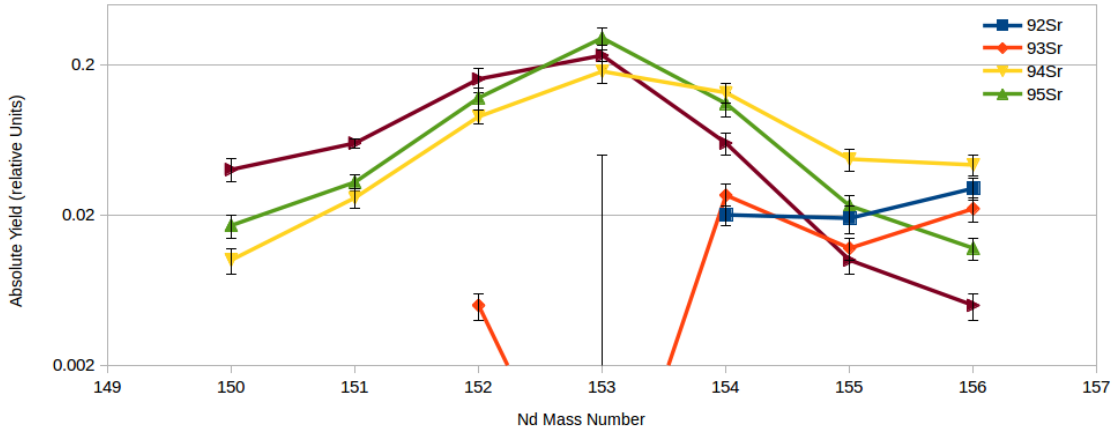

As with the other isotopes analyzed using the ^{252}Cf SF data, the level scheme in figure 5.7 and table 5.3 were found by multidimensional coincidence gates. Figure 5.10 shows a double gate on the first two yrast transitions of ^{94}Sr, the 3 neutron fission partner of ^{155}Nd. In that figure one can see transitions from $^{152\text{-}156}$Nd, including every transition from ^{155}Nd observed in this work. The primary difficulty in examining gates for ^{155}Nd, as shown in figure 5.10, is the similarity of energies across Nd isotopes. In fact, it is this similarity that is partially used for the band assignments as shown in figure 5.8. Fortunately, for identifying new transitions in ^{155}Nd, as typical for neighboring isotopes, this similarity diverges with increasing energy.

Most of the important coincident relationships within the structure of ^{155}Nd (as shown in figure 5.7) can be seen in figure 5.11, which shows eight different triple gates on γ-ray transitions within the structure of ^{155}Nd. the transitions up to the 455 keV in the odd-half-integer[3] part of the observed ^{155}Nd band can be seen in the left half of figure 5.11, to varying levels of clarity. The tentative 523 keV is seen most clearly in the 273/174/387

[3]Odd-half-integers are odd integers plus $\frac{1}{2}$, or the numbers 1.5, 3.5, 5.5, *etc*. Similarly even-half-integers are the numbers 0.5, 2.5, 4.5, *etc*.

Figure 5.10: A double gate on 836.7/1308.7 keV, the first two yrast transitions from ^{94}Sr, the 3 neutron fission partner of ^{155}Nd. In this spectrum, every transition from ^{155}Nd, as well as many from other isotopes of Nd and from ^{94}Sr itself, can be seen (though this spectrum may not be the best evidence for each). Labels ending in a question mark indicate that, either, the transition is previously unidentified or that (for a previously identified transition) the intensity is significantly stronger than expected.

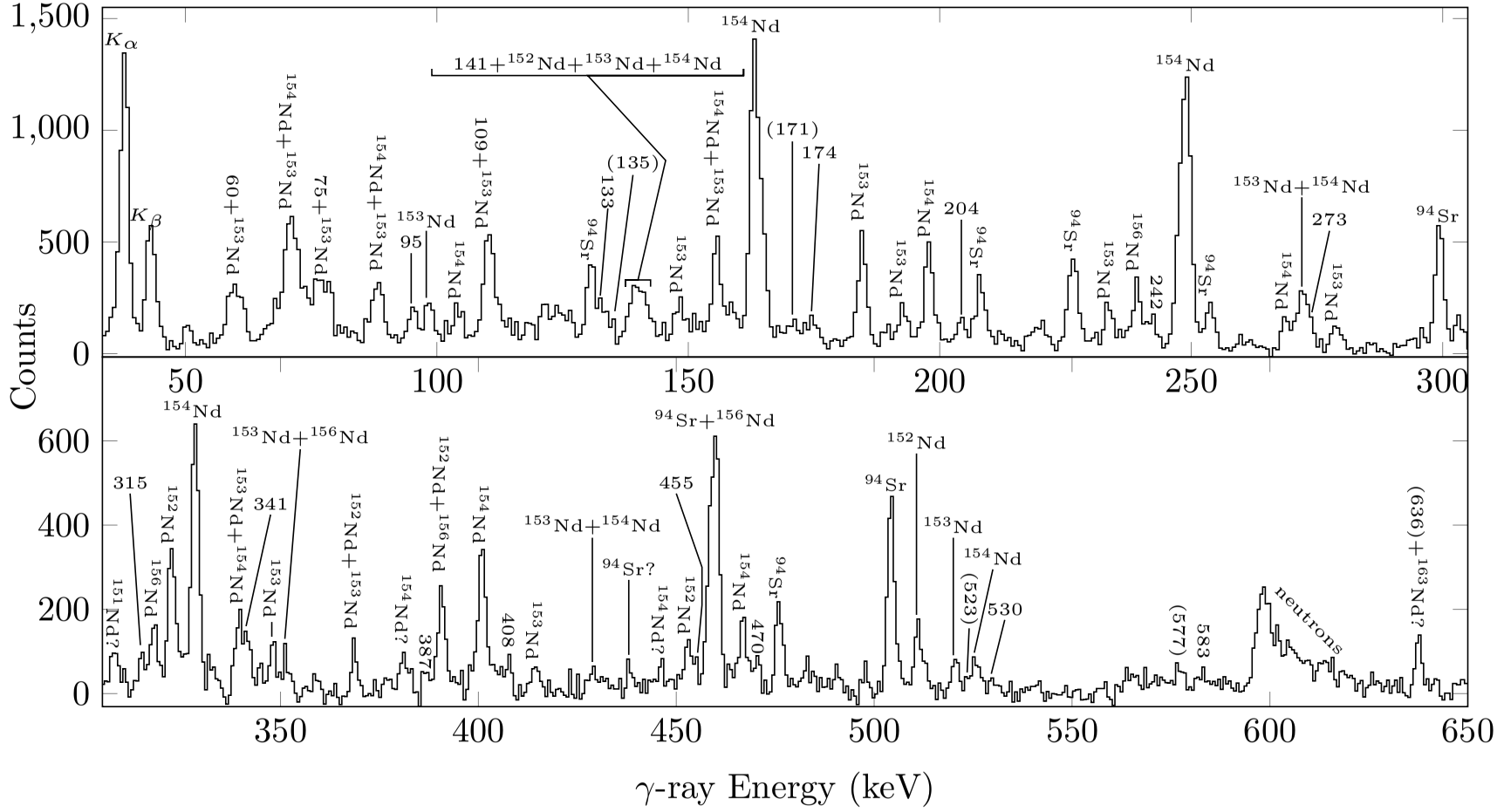

keV gate on the bottom left it is marked tentative, because it is only seen clearly there, and could still just be background fluctuation.

On the right of figure 5.11 are triple gates on the (probably) E2 transitions from the even-half spin states. The transitions in this half of the band are even clearer than those for the odd-half-integer spin levels. One can clearly see, as the gates chosen climb up the band, the transitions being gated on disappear, and all of the others are visible. The one exception is the tentative 636 keV transition that is only clear in one of the gates shown in figure 5.11.

The one transition not visible in figure 5.11 is the highly tentative 577 keV transition from the 807 keV level. The tentative 807 keV level is a candidate for a $\nu 11/2^{-}[505]$ extruder state, which is also observed in ^{155}Sm, and expected in other isotopes in the region. Though not shown here, a gate on the 577 keV transition weakly shows the 95 keV transition, and the 577 keV transition can be seen (weakly) in the fission partner gate shown in figure 5.10.

For both the left and right of figure 5.11 many transitions are still fairly weak and – when only one gate is taken into account – could simply be slightly high background fluctuation. However, when the same slightly above background fluctuation peak shows up in several of the gates shown in figure 5.11 (as well as gates not shown), it lends strong credence to the transition's existence. This is why so many gates are shown in figure 5.11; several transitions were only confidently identifiable when many gates were taken together. The net result of these and other gates are shown in figure 5.7 and table 5.3, amounting to 12 new γ-rays from 9 new levels, as well as the new spin assignment of $\nu 5/2^{+}[642]$ for the lowest energy state observed.

5.4 ^{159}Eu and ^{89}Br

The isotope, ^{159}Eu, has only been studied twice before. First, Burke *et al.* [108], using the ^{160}Gd$(t,\alpha)^{159}$Eu reaction, with polarized tritons, uncovered 31 levels. By comparing

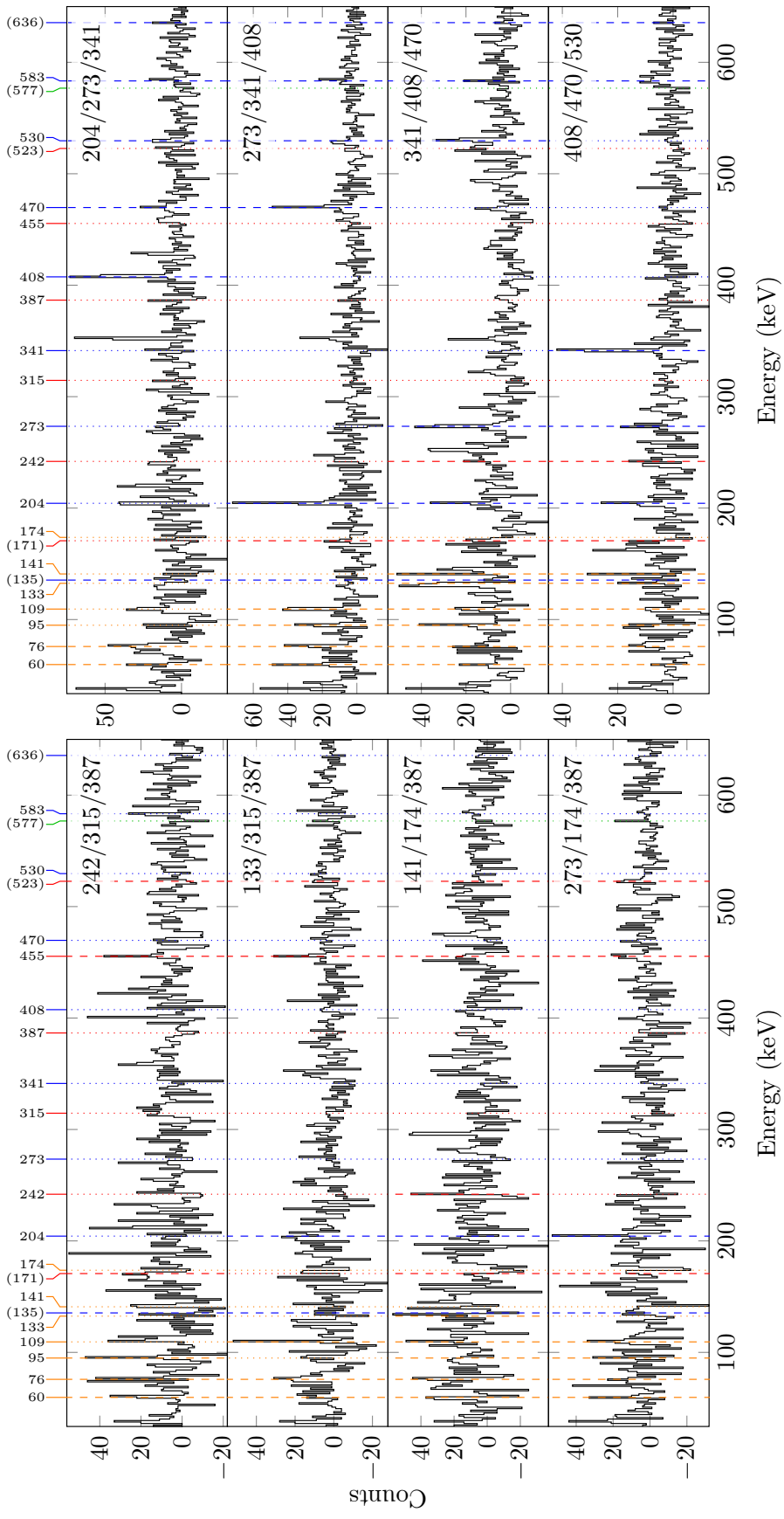

Figure 5.11: Eight different triple gates from within the structure of ^{155}Nd. Vertical lines corresponding to each transition observed have been added as a visual aid to the reader. Dashed lines indicate that a gate should see the transition, while dotted indicate that a transition should not. As to the colors; blue indicates $\Delta J = 2$ transitions from states with even-half-integer (5/2,9/2,13/2,...) spin, red indicates $\Delta J = 2$ transitions from odd-half-integer (7/2,11/2,15/2,...) spin states, orange indicates $\Delta J = 1$ transitions, and the tentative 577 keV transition is green, being from a different band.

the ^{157}Eu data in the same paper to the values recorded in the Nuclear Data Sheets [109], (for which much more is known), most of the levels discovered by Burke *et al.* are 1-3 keV higher than the values found by other methods. Later, Willmes *et al.* [110] studied the β-decay of ^{159}Sm, observing γ-rays and more precice values of some of the levels observed by Burke *et al.* [108]. Furthermore, there has been some recent theoretical interest int the region, as evidenced by Pandit *et al.* [111, 112], who published his work in two different journals, citing himself in the second.

Another complication in the study of ^{159}Eu is that ^{89}Br, the 4 neutron fission partner of ^{159}Eu has only one publication discussing excited states or γ-rays in its structure; Nyakó *et al.* [113] who do not give explicit level or γ-ray energies for ^{89}Br (though they did for ^{87}Br, discussed in the same paper). These factors, however, were insufficient to determine any precise γ-ray energies for either ^{159}Eu or ^{89}Br, though ^{159}Eu is produced only half as much as ^{155}Nd and a full order of magnitude more than ^{164}Gd in the spontaneous fission of ^{252}Cf.

5.5 Other Nuclei

Despite having a few known γ-rays (see Patel *et al.* [79]) in ^{164}Eu, the statistics in our Cf data were insufficient to make any confident determinations concerning the structure of ^{164}Eu, being produced about an order of magnitude less than ^{164}Gd in the SF of ^{252}Cf [97].

Despite being produced in the SF of ^{252}Cf at about the same frequency as ^{164}Gd [97], evidences of ^{156,157}Eu could not be confirmed in our data. The majority of the strong transitions in both ^{156,157}Eu are under 150 keV [114, 115, 116], which, as discussed elsewhere in this dissertation, is a region with many transitions from many nuclei. This, combined with the fact that the overwhelmingly preferred decay mode in this energy region is by internal conversion, not γ-ray emission, made isolating the ^{156,157}Eu transitions from the spectrum impossible.

Appendix A

PSM and TPSM calculations for ^{163,164}Gd

Theorists with whom we collaborate provided us with calculations concerning ^{163,164}Gd. Their results are shown in figures A.1 and A.2. They used the *projected shell model* (PSM), and its counterpart, the *triaxial projected shell model* (TPSM). Both PSM and TPSM are attempts to extend the shell model (see section 1.2.1) into deformed shapes/regions of the chart of nuclides in a way that is friendly to computation.

The PSM typically assumes that $\gamma = 0^\circ$ and allows positive and negative values of β_2 (see equation 1.44 – negative values of β_2 are equivalent to $\gamma = 60^\circ$). The PSM uses the hamiltonian

$$\hat{H}_{PSM} = \hat{H}_0 - \frac{\chi}{2}\sum_{\mu}\hat{Q}^{\dagger}_{\mu}\hat{Q}_{\mu} - G_M\hat{P}^{\dagger}\hat{P} - G_Q\sum_{\mu}\hat{P}^{\dagger}_{\mu}\hat{P}_{\mu} \tag{A.1}$$

where H_0 is the nuclear harmonic oscillator Hamiltonian with proper spin-orbit coupling (see section 1.2.1), typically given by the Hartree-Fock mean field approximation;

$$\hat{H}_0 = \sum_{i=1}^{A}\left(-\frac{\hbar^2}{2m}\nabla_i^2 + V_{Coulomb}(i) + V_{Nuclear}(i)\right) \tag{A.2}$$

where the first term is the kinetic energy of each individual nucleon and the Coulomb and nuclear potentials are taken assuming that each nucleon experiences an average potential, rather than explicitly calculated the nucleon-nucleon central force interactions. The other operators in equation A.1 are defined as

$$\hat{Q}_{\mu} = \sum_{\alpha\beta} Q_{\mu\alpha\beta}c^{\dagger}_{\alpha}c_{\beta} \tag{A.3}$$

$$\hat{P}^{\dagger} = \frac{1}{2}\sum_{\alpha} c^{\dagger}_{\alpha}c^{\dagger}_{\bar{\alpha}} \tag{A.4}$$

Figure A.1: Calculated energy levels for ^{164}Gd and comparison with the experiment, courtesy of theorists with whom we collaborate.

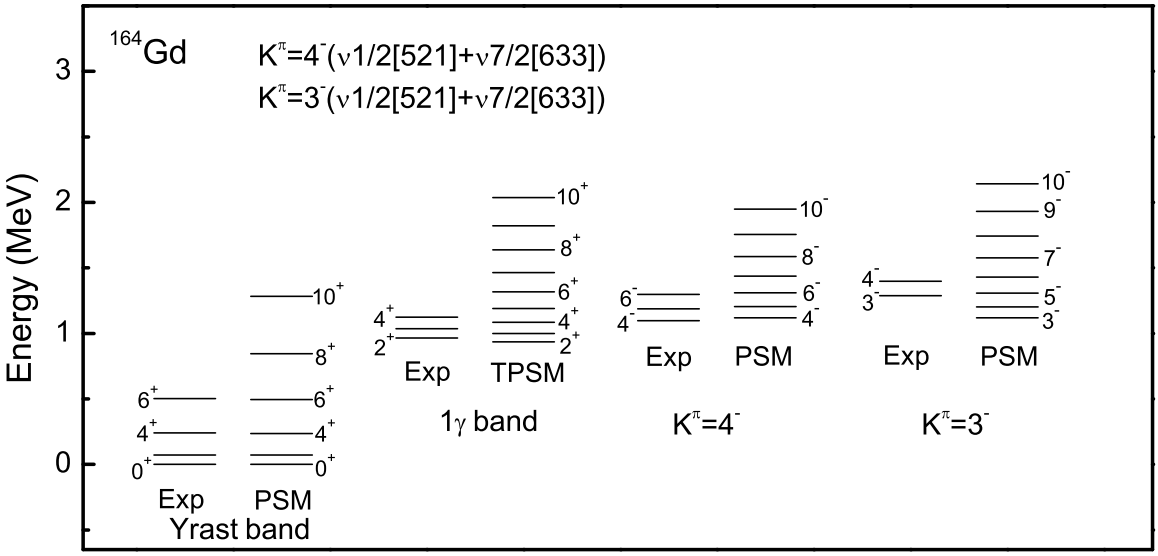

Figure A.2: Calculated energy levels for ^{163}Gd and comparison with the experiment, courtesy of theorists with whom we collaborate.

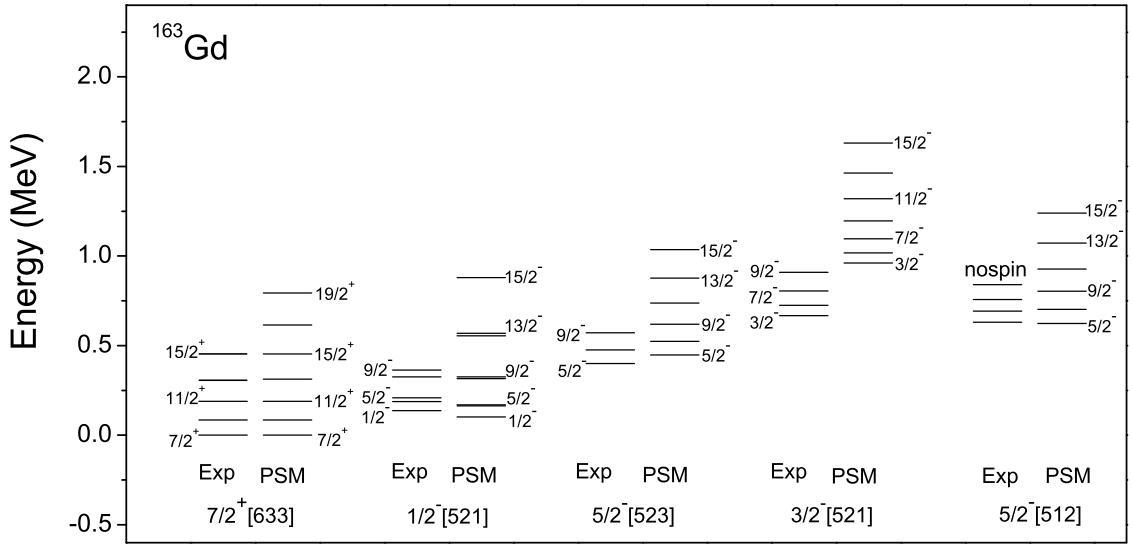

and

$$\hat{P}^{\dagger}_{\mu} = \frac{1}{2}\sum_{\alpha\beta} Q_{\mu\alpha\beta} c^{\dagger}_{\alpha} c^{\dagger}_{\bar{\beta}}, \tag{A.5}$$

The quadrupole matrix elements are defined as

$$Q_{\mu\alpha\beta} = \delta_{nn'} \left(\alpha \left| Q_{\mu} \right| \beta \right) \tag{A.6}$$

where, in equations A.3 through A.6, $\alpha = \{njm\}$ (and $\beta = \{n'j'm'\}$) represents the full slate of nuclear quantum numbers and $\bar{\alpha}$ ($\bar{\beta}$) is the time-reversed state of α (β).

By contrast, instead of equation A.1 (which approximates the Nilsson potential), the TPSM uses

$$\hat{H}_{TPSM} = \hat{H}_0 - \frac{2}{3}\hbar\omega \left(\varepsilon_2 \hat{Q}_{20} + \frac{\varepsilon'_2}{\sqrt{2}} (\hat{Q}_{22} + \hat{Q}_{2-2}) \right) \tag{A.7}$$

where ε_2 is the same deformation parameter used in figure 1.4 (which assumes $\varepsilon'_2 = 0$), and a second, similar, deformation parameter ε'_2 is used to generate triaxiality. In equation A.7, the multipole operator $\hat{Q}_{lm}$ is the qunantum mechanical equivalant of the classical multipole moments, Q_{lm}, with $\hat{Q}_{2m}$, specifically are the quadrupole operators[1]. For more information of the PSM and TPSM approaches see Sheikh and Hara [117], and the references therein.

[1] Elsewhere in this work (such as equation 1.46) only Q_l is used, because m is assumed to be 0.

Appendix B

Correction for Isomer Lifetime in Intensities Measured from β-Gated Singles

Now I have used the β-gated singles to help me measure the intensities of γ-rays in the β-decay data set for ^{164}Gd, and one of my states is an isomer. This means that any γ-rays depopulating this isomer will be attenuated by the lifetime of the isomer as some of the decays will happen outside the coincidence window. Furthermore, any γ-rays depopulating states which these γ-rays feed will be attenuated because some of the attenuation of the first γ-rays. In total, six γ-rays are affected by this attenuation, specifically the 61, 73, 168, 793, 855, and 962 keV γ-rays.

To begin, we need to figure out the base attenuation factor, A, caused by the isomer's lifetime. The half-life of the isomer in question is $t_{1/2} = 0.64(5)$ (see section 4.3). Since I have been given the half life, it will be easier to work in powers of 2, rather than e (recall that $2^x = e^{x\ln 2}$). Thus, the normalized decay function for this level is

$$\frac{N(t)}{N_0} = \frac{\ln 2}{t_{1/2}} 2^{-t/t_{1/2}} \tag{B.1}$$

the fraction of decays happening during the coincidence window comes from integrating this function from $t = 0$ to the end of the coincidence window, $t = w$. This is the attenuation factor, a;

$$a = \int_0^w \frac{\ln 2}{t_{1/2}} 2^{-t/t_{1/2}} dt = 1 - 2^{w/t_{1/2}} = 0.66(3) \tag{B.2}$$

recalling that the general formula for error propagation is

$$\Delta x(y_1, y_2, \ldots)^2 = \Delta y_1^2 \left(\frac{\partial x}{\partial y_1}\right)^2 + \Delta y_2^2 \left(\frac{\partial x}{\partial y_2}\right)^2 + \ldots$$

or

$$\Delta A = \frac{\Delta t_{1/2} w 2^{-w/t_{1/2}} \ln 2}{t_{1/2}^2}$$

in our case.

Since A is the fraction of decays during the coincidence window, this means that the intensities of the two gamma rays directly depopulating the isomer are simply

$$I_{61} = A I'_{61} \tag{B.3}$$

$$I_{855} = A I'_{855} \tag{B.4}$$

where I is the measured intensity, and I' is the actual intensity, including depopulations occurring after the end of the coincidence window.

Now the other four γ-rays affected by this are a bit more tricky, as they can be populated by other γ-rays or by direct β-feeding, and the sum of these sources of extra feeding are fundamentally unmeasurable in our data. In general, the absolute intensity of the 962 keV gamma ray should be

$$I'_{962} = \left(F_{1035} + I'_{60}(1+\alpha_{60})\right) B_{962} \tag{B.5}$$

where F is the sum of all other sources of feeding, α is an internal conversion coefficient, and B is the branching ratio of a transition such that the sum of the values of B for each transition depopulating a state equals 1. In our case, $B_{962} + B_{793} = 1$, and all other branching ratios needed are 1. Only the term including I_{60} experiences attenuation due to the isomer, thus

$$I_{962} = \left(F_{1035} + A I'_{60}(1+\alpha_{60})\right) B_{962} = \left(F_{1035} + I_{60}(1+\alpha_{60})\right) B_{962} \tag{B.6}$$

We can combine equations B.5 and B.6 to cancel our F to find;

$$I'_{962} = I_{962} + (I'_{60} - I_{60})(1+\alpha_{60}) B_{962} \tag{B.7}$$

Similarly, since the 794 keV γ-ray depopulates the same state, we find that

$$I'_{793} = I_{793} + (I'_{60} - I_{60})(1 + \alpha_{60})B_{793} \tag{B.8}$$

If we use similar logic it should be obvious that

$$I'_{168} = F_{241} + I'_{794} + I'_{855} \tag{B.9}$$

and

$$I_{168} = F_{241} + I_{794} + I_{855} \tag{B.10}$$

When equations B.9 and B.10 are combined, we find

$$I'_{168} = I_{168} + (I'_{794} - I_{794}) + (I'_{855} + I_{855}) = I_{168} + (I'_{60} - I_{60})(1 + \alpha_{60})B_{794} + (I'_{855} + I_{855}) \tag{B.11}$$

Finally, for the 73 keV γ-ray, the same logic leads to

$$I'_{73} = I_{73} + (I'_{168} - I_{168}) + (I'_{962} + I_{962}) = I_{73} + (I'_{168} - I_{168}) + (I'_{60} - I_{60})(1 + \alpha_{60})B_{962} \tag{B.12}$$

Thus, for ^{164}Gd, equations, B.3, B.4, B.7, B.8, B.11, and B.12 can be used to correct their respective γ-rays for attenuation caused by the lifetime of the 1095 keV isomer, when using β-gated singles to measure the intensities of ^{164}Gd.

However, this has not actually been done in the present work. The above derivation assumes hard cutoff in the coincidence windows used for gating, This, however, as noted in section 2.2, is not the case for our data. We use a "rolling" coincidence that waits for 1 μs to pass without any detections in any of the detectors, rather than cutting an event off after 1 μs, regardless of when interactions occurred within the event.

Appendix C

The Efficiency Functions For the β-decay Data

C.1 Singles (Primary) Efficiency Function

For our beta decay data, we were provided with a list of energies and efficiencies for the LeRIBSS, which are displayed in table C.1. These efficiency data were generated with a standard ^{122}Cd source, whose activity was known using a singles spectrum without add-back[1]. The efficiencies shown in table C.1 are the measured activity divided by the expected activity of the source.

Provided with the raw efficiency data was a suggested polynomial fit and a suggested uncertainty of 3%. The polynomial fit used the $\log_{10}(E)$ values, rather than the direct energy value:

$$P_S^{\text{poly}}(E) = 0.1248x^5 - 1.9102x^4 + 11.514x^3 - 34.029x^2 + 48.958x - 27.046 \qquad \text{(C.1)}$$

Where P_S is the singles efficiency (*P*robability of *S*ingles), and $x = \log_{10}(E)$. However, after examining equation C.1 closely, it does not fit the efficiency data well. Table C.2 displays the relationship between this polynomial and the data. The %error column is the standard %error taught to undergraduates:

$$\%\text{error} = \left| \frac{x_{\text{actual}} - x_{\text{measured}}}{x_{\text{actual}}} \right| \qquad \text{(C.2)}$$

with, in this case, x_{actual} being the raw efficiency data, and x_{measured} being the efficiency given by the C.1. The %error should be a direct measure of the uncertainty that enters the intensity calculation simply from the fit being different from the data. It is clear from table C.2 that, when using equation C.1, a blanket 3% uncertainty is woefully insufficient.

[1] This spectrum was generated the same way as the spectrum in figure 4.2a (but is not the same spectrum as displayed there).

Table C.1: Raw data provided for the energy-dependant efficiency of the LeRIBSS.

Energy (keV)	$\log_{10}(E)$	Measured Efficiency
47	1.6720978579	0.2058723210
60	1.7781512504	0.2596024902
88	1.9444826722	0.3035052498
122	2.0863598307	0.2935814468
166	2.2201080880	0.2301108032
392	2.5932860670	0.1196065102
662	2.8208579894	0.0723621348
898	2.9532763367	0.0546961155
1173	3.0692980121	0.0457983607
1333	3.1248301494	0.0406348159
1836	3.2638726769	0.0302451259

Table C.2: Efficiency values compared to those generated by equation C.1.

Energy (keV)	Measured Efficiency	Equation C.1	%error
47	0.2058723210	0.2018789064	1.94%
60	0.2596024902	0.2710738528	4.42%
88	0.3035052498	0.3010510100	0.81%
122	0.2935814468	0.2797086556	4.73%
166	0.2301108032	0.2397854552	4.20%
392	0.1196065102	0.1170376034	2.15%
662	0.0723621348	0.0678411955	6.25%
898	0.0546961155	0.0499950025	8.59%
1173	0.0457983607	0.0391986004	14.41%
1333	0.0406348159	0.0351334571	13.54%
1836	0.0302451259	0.0266084214	12.02%

Table C.3: Efficiency values compared to those generated by equation C.3.

Energy (keV)	Measured Efficiency	Equation C.3	%error
47	0.2058723210	0.2023128823	1.73%
60	0.2596024902	0.2664882147	2.65%
88	0.3035052498	0.3021990137	0.43%
122	0.2935814468	0.2827299467	3.70%
166	0.2301108032	0.2412062871	4.82%
392	0.1196065102	0.1164414081	2.65%
662	0.0723621348	0.071696351	0.92%
898	0.0546961155	0.0560771547	2.52%
1173	0.0457983607	0.0458188088	0.04%
1333	0.0406348159	0.0413534258	1.77%
1836	0.0302451259	0.0295627565	2.26%

Perhaps 3% covers the error in the raw efficiency data itself, but it cannot account for the error of equation C.1.

For this reason, I sought out a better fit function. I eventually settled on a 5^{th} order polynomial times e^{-x}, still using $\log_{10}(E)$;

$$P_S(E) = \left(a(x-b) + d(x-b)^2 + f(x-b)^3 + g(x-b)^4 + h(x-b)^5\right) e^{-c(x-b)} \qquad \text{(C.3)}$$

where $x = \log_{10}(E)$ and

$$a = 1.20106 \times 10^{-7}$$

$$b = 1.38734297755673$$

$$c = 1.47978212167891$$

$$d = 6.20343779083261$$

$$f = -9.94472994014238$$

$$g = 5.62629699447533$$

$$h = -1.09250273060072$$

Figure C.1: The singles γ-ray spectra from each clover in LeRIBSS compared to each other. From these spectra one can clearly see that each clover has a different efficiency function. The singles spectrum shown in figure 4.2a is the sum of the four spectra shown here.

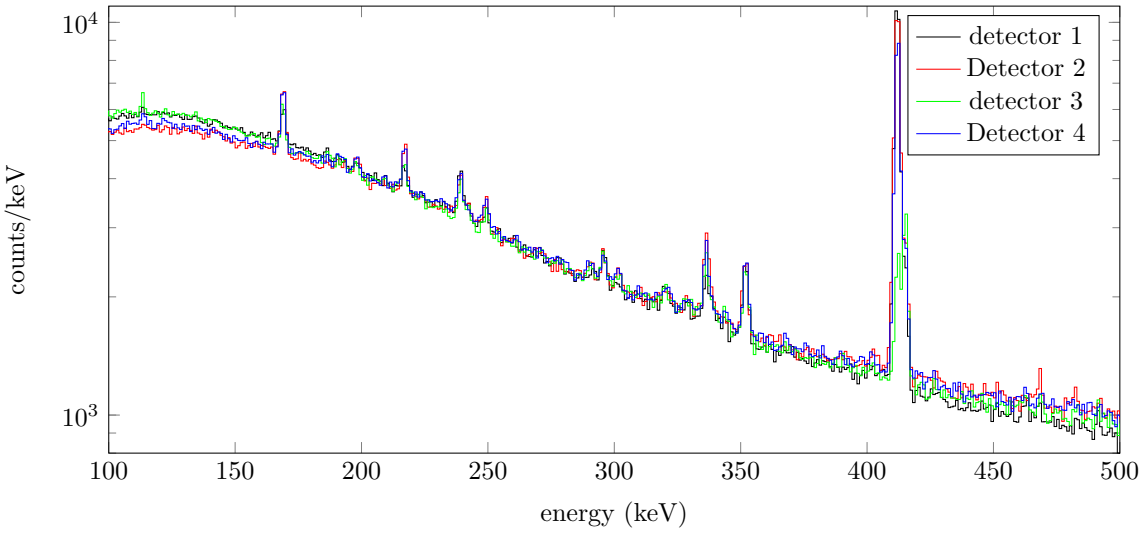

These fit values were obtained by using Mathematica 9. The reason for choosing this function is that xe^{-x} has approximately the right shape. Higher orders were used in order to attain better accuracy compared to the data from table C.1. The comparison of equation C.3 to the measured efficiency from table C.1 is shown in table C.3. It is clear from table C.3, that equation C.3 fits the data significantly better than equation C.1. For this reason, equation C.3 was used for all of the intensity calculations shown in table 4.1. It was assumed that the efficiency fit added (in quadrature) a blanket 5% uncertainty to the intensity calculation. However, the intensities found in gates had an additional 5% added (in quadrature) to their uncertainties, as described in section C.2 below.

C.2 Gated Efficiency

The reason an extra 5% was added (in quadrature) to gated intensities stems from the fact that gated efficiency is not necessarily the same as singles efficiency. For a system of

N detectors, the singles efficiency is

$$P_S(E) \propto P_1(E) + P_2(E) + \cdots = \sum_{i=1}^{N} P_i(E) \tag{C.4}$$

where P_S is the total singles efficiency, and P_i is the efficiency of a single detector. By contrast, the Gated efficiency (only $\gamma - \gamma$ coincidence, not higher orders) is

$$\begin{aligned} P_G(E_1,E_2) &\propto P_1(E_1)P_2(E_2) + P_1(E_1)P_3(E_2) + \cdots + P_2(E_1)P_3(E_2) + \cdots + P_1(E_2)P_2(E_1) + \cdots \\ &= \left(\sum_{i=1}^{N-1} P_i(E_1) \sum_{j=i+1}^{N} P_j(E2) \right) + \left(\sum_{i=1}^{N-1} P_i(E_2) \sum_{j=i+1}^{N} P_j(E1) \right) \end{aligned} \tag{C.5}$$

where E_1 is the gate energy and E_2 is the energy of the resulting spectrum[2]. In the limit that all of the detectors are the same (i.e. $P_i = P_j$ for all i, and j), it must be true that

$$\frac{P_G(E1,E)}{P_S(E)} = \frac{P_G(E1,E')}{P_S(E')} \tag{C.6}$$

It should be obvious that, in the limit where all the detectors are the same, equations C.4 and C.5 reduce to

$$\begin{aligned} P_S(E) &= NP(E) \\ P_G(E_1,E_2) &= 2(N-1)!P(E1)P(E2), \end{aligned} \tag{C.7}$$

respectively. When the forms of the efficiencies in equation C.7 are plugged into equation C.6, one gets

$$\begin{aligned} \frac{2(N-1)!P(E1)P(E)}{NP(E)} &= \frac{2(N-1)!P(E1)P(E')}{NP(E')} \\ \frac{2(N-1)!}{N}P(E1) &= \frac{2(N-1)!}{N}P(E1) \\ P(E1) &= P(E1) \end{aligned} \tag{C.8}$$

[2]Technically, in equation C.5, E_1 and $E2$ can take either role. This specification of E_1 as gate energy and E_2 as energy within the resulting spectrum will be helpful later in this derivation.

which satisfies equation C.6. However, in our data, the four clover detectors are clearly not equal, as shown in figure C.1. This means we cannot assume that the singles efficiency is valid or useful in gated spectra.

From equations C.6 and C.8 an important fact can be learned, which enables us to test our gated efficiency; for a given gated energy, an ideal detector system will give a gated efficiency curve proportional to the singles efficiency. This gives us an easy test to determine the magnitude of the deviation of our gated efficiency from our singles efficiency. If we examine the proportionality (or lack there of) between the gated efficiency from various gates and the singles efficiency, we will have a good idea of the magnitude of the deviation of our gated efficiency from our singles efficiency. As a test, the value of the functions can be obtained for specific energy values (which would need to be fit to find a continuous function) by

$$P_i(E_j) = \frac{A_i(E_j)}{A_S(E_j)} P_S(E_j) \tag{C.9}$$

where E_j is a specific energy, A_i is the measured area underneath the peak in detector i, and A_S is the area measured underneath the peak in the total singles spectrum. Six such test peaks were chosen. Two, taken at 168.5 and 1092.1 keV, are from the ^{164}Gd data (described in section 2.2) while four of the test peaks are from the ^{163}Gd data, which was recorded on the same day and with the same methods as the ^{164}Gd data, and should, therefore, have the same efficiency functions. These test peaks and the values of their respective efficiency functions at the test energies are shown in table C.4. Equation C.9 was used to find the efficiency of each individual clover, while the singles efficiency (the efficiency of all four clovers together) is from C.3.

To actually determine the discrepancy between our singles and gated efficiencies, these 6 test peaks provide 36 points in the gated efficiency plane, which can each be compared to the singles efficiency. By treating E_1 as the gated energy and E_2 as the energy of interest, we can see how much our gated efficiency deviates from an ideal system by testing the proportionality of each of these 36 points to the singles efficiency at $E2$. Table C.5

Table C.4: Table of test peaks used to determine the magnitude of the discrepancy between gated and singles efficiencies. The efficiencies in the rows labeled "all" are taken from equation C.3, the rest use equation C.9.

E (keV)	clover	area	efficiency
85.3	all	93977	0.3020
	1	15745	0.0506
	2	29591	0.0951
	3	19919	0.0640
	4	28367	0.0912
168.5	all	16966	0.2391
	1	2711	0.0382
	2	5676	0.0800
	3	3415	0.0481
	4	5146	0.0725
288.0	all	59991	0.1558
	1	10527	0.0273
	2	20785	0.0540
	3	11824	0.0307
	4	17049	0.0443
1036.9	all	15585	0.0503
	1	3226	0.0104
	2	5034	0.0163
	3	3461	0.0112
	4	4162	0.0134
1092.1	all	23620	0.0484
	1	4207	0.0086
	2	8073	0.0165
	3	5204	0.0107
	4	6285	0.0129
2275.5	all	5382	0.0200
	1	942	0.0035
	2	1662	0.0062
	3	1464	0.0054
	4	1249	0.0046

Table C.5: By using the data shown in table C.4, this table shows the comparison between the gated and singles efficiency of the LeRIBSS. The gated efficiencies are taken from equation C.5 (with $N = 4$), while the singles efficiency is taken from equation C.3. The Gated efficiency has been further normalized for each E_1 (gated energy) to the value of the singles efficiency at 85.3 keV. The %error is taken from equation C.2 (with $P_S = x_{\text{actual}}$).

E_1 (keV)	E_2 (keV)	$P_G(E_1, E_2)$	$P_S(E_2)$	%error
85.3	85.3	0.3020	0.3020	0.00%
85.3	168.5	0.2390	0.2391	0.05%
85.3	288.0	0.1567	0.1558	0.57%
85.3	1036.9	0.0518	0.0503	3.02%
85.3	1092.1	0.0479	0.0484	1.08%
85.3	2275.5	0.0200	0.0200	0.10%
168.5	85.3	0.3020	0.3020	0.00%
168.5	168.5	0.2388	0.2391	0.13%
168.5	288.0	0.1566	0.1558	0.48%
168.5	1036.9	0.0519	0.0503	3.07%
168.5	1092.1	0.0479	0.0484	1.04%
168.5	2275.5	0.0200	0.0200	0.22%
288.0	85.3	0.3020	0.3020	0.00%
288.0	168.5	0.2388	0.2391	0.14%
288.0	288.0	0.1564	0.1558	0.36%
288.0	1036.9	0.0518	0.0503	2.88%
288.0	1092.1	0.0478	0.0484	1.20%
288.0	2275.5	0.0200	0.0200	0.06%
1036.9	85.3	0.3020	0.3020	0.00%
1036.9	168.5	0.2391	0.2391	0.00%
1036.9	288.0	0.1565	0.1558	0.44%
1036.9	1036.9	0.0516	0.0503	2.61%
1036.9	1092.1	0.0477	0.0484	1.45%
1036.9	2275.5	0.0199	0.0200	0.37%
1092.1	85.3	0.3020	0.3020	0.00%
1092.1	168.5	0.2391	0.2391	0.00%
1092.1	288.0	0.1565	0.1558	0.46%
1092.1	1036.9	0.0516	0.0503	2.64%
1092.1	1092.1	0.0476	0.0484	1.55%
1092.1	2275.5	0.0199	0.0200	0.60%
2275.5	85.3	0.3020	0.3020	0.00%
2275.5	168.5	0.2393	0.2391	0.07%
2275.5	288.0	0.1567	0.1558	0.54%
2275.5	1036.9	0.0516	0.0503	2.54%
2275.5	1092.1	0.0475	0.0484	1.78%
2275.5	2275.5	0.0198	0.0200	1.07%

shows the results of this analysis. Specifically, each chain of 6 E_2 values associated with a specific value of $E1$ was normalized such that $P_G(E_1, 85.3) = P_S(85.3)$, allowing us to see how much the other 5 values vary from the singles efficiency. The %error (equation C.2) between the gated and singles efficiency is used in each case to suggest an approximate amount of error that would be introduced to a measurement using a gate, but still using the singles efficiency function. As can be clearly seen in table C.5, the largest error that would be introduced in any of the 36 test cases was 3.07%. Thus it was concluded that the effort required to implement a complete gated efficiency function for use in measuring intensities was not worth the small return of a less than 4% correction on a few intensity data points, as that would be already smaller than the existing error on our intensity measurements. Instead we decided to add an additional blanket 5%, in quadrature (to the already 5% error of our efficiency curves, bringing it to about 7% total), to the uncertainty of our efficiency function for instances where the efficiency function was used on gated data.

In our data, the primary cause of the deviation for each detector is geometric. In the photograph of the LeRIBSS embedded in figure 2.2, one can see clearly that two HPGe Clover detectors are slightly closer to the source than the other two. This means that the two closer will have a slightly higher efficiency than the two further away, since the measured intensity falls off by $1/r^2$. However, it also means that the two further away are more likely to get Compton scatters from the two closer to the source than the other way around. Additionally, any contaminant sources outside the center of the four clovers will favor one detector over the others. All three of these effects are seen in figure C.1. Detectors 1 and 3 are slightly further from the source, and have a higher background at the lowest energies, but a lower background at higher energies. Additionally, with all of the ^{164}Gd and mass 82 & 81 (things in the beam) γ-rays shown, the intensity of detectors 2 and 4 are slightly higher than the intensities of detectors 1 and 3. This pattern is clearly not followed in the 113 and 411 keV γ-rays shown, indicating that they lie outside of our detectors and favor/disfavor

the various detectors differently. This fact was used to help identify which peaks in singles may be contaminants and which might be real.

BIBLIOGRAPHY

[1] C. Goodin, *Angular Correlations of Prompt Gamma-Rays from the Spontaneous Fission of* ^{252}*Cf*. PhD thesis, Vanderbilt University, Nashville, TN, 2008.

[2] K. S. Krane, "$\frac{E2}{M1}$ multipole mixing ratios of γ transitions in even-even deformed nuclei," *Physical Review C*, vol. 8, pp. 1494–1499, Oct 1973.

[3] C. J. Chiara, J. J. Carroll, M. P. Carpenter, J. P. Greene, D. J. Hartley, R. V. F. Janssens, G. J. Lane, J. C. Marsh, D. A. Matters, M. Polasik, J. Rzadkiewicz, D. Seweryniak, S. Zhu, S. Bottoni, A. B. Hayes, and S. A. Karamian, "Isomer depletion as experimental evidence of nuclear excitation by electron capture," *Nature*, vol. 554, p. 216, 2018.

[4] F. Yang and J. H. Hamilton, *Modern Atomic and Nuclear Physics*. Hackensack, NJ: World Scientific, revised ed., 2010.

[5] K. S. Krane, *Introductory Nuclear Physics*. New York: John Wiley & Sons, Inc., 1988.

[6] K. S. Krane and R. M. Steffen, "Determination of the $\frac{E2}{M1}$ multipole mixing ratios of the gamma transitions in Cd^{110}," *Physical Review C*, vol. 2, pp. 724–734, Aug 1970.

[7] W. Greiner, "Magnetic properties of even nuclei," *Nuclear Physics*, vol. 80, no. 2, pp. 417–433, 1966.

[8] J. Dudek, A. Majhofer, and J. Skalski, "Adjustment of the pairing force strength to the experimental data and the optimised woods-saxon potential spectrum-comparison with the nilsson model," *Journal of Physics G: Nuclear Physics*, vol. 6, pp. 447–454, Apr 1980.

[9] J. M. Eisenberg and W. Greiner, *Nuclear Models*, vol. 1. Amsterdam: North-Holland Physics Publishing, 3rd ed., 1987.

[10] R. Casten, *Nuclear Structure From a Simple Perspective*, vol. 13 of *Oxford Studies in Nuclear Physics*. New York: Oxford University Press, 1990.

[11] P. O. Lipas, "Perturbation corrections to energies of collective states in deformed even nuclei," *Nuclear Physics*, vol. 39, pp. 468 – 478, 1962.

[12] L. L. Riedinger, *Studies of the Collective States in ^{152}Gd, ^{152}Sm, and ^{154}Gd*. PhD thesis, Vanderbilt University, Nashville, TN, 1969.

[13] E. R. Marshalek, "Self-consistent perturbation of hartree-fock-bogoliubov equations and nuclear rotational spectra. ii," *Physical Review*, vol. 158, pp. 993–1010, Jun 1967.

[14] J. B. Gupta, "The nature of $K^\pi = 0_2^+$, 0_3^+ bands in ^{158}Gd," *Nuclear Physics A*, vol. 990, pp. 162 – 182, 2019.

[15] T. Kibédi, T. W. Burrows, M. B. Trzhaskovskaya, P. M. Davidson, and C. W. Nestor, "Evaluation of theoretical conversion coefficients using BrIcc," *Nuclear Instruments and Methods in Physics Research Section A: Accelerators, Spectrometers, Detectors and Associated Equipment*, vol. 589, no. 2, pp. 202 – 229, 2008.

[16] G. M. Ter-Akopian, J. H. Hamilton, Y. T. Oganessian, A. V. Daniel, J. Kormicki, A. V. Ramayya, G. S. Popeko, B. R. S. Babu, Q.-H. Lu, K. Butler-Moore, W.-C. Ma, S. Ćwiok, W. Nazarewicz, J. K. Deng, D. Shi, J. Kliman, M. Morhac, J. D. Cole, R. Aryaeinejad, N. R. Johnson, I. Y. Lee, F. K. McGowan, and J. X. Saladin, "New spontaneous fission mode for ^{252}Cf: Indication of hyperdeformed ^{144,145,146}Ba at scission," *Physical Review Letters*, vol. 77, pp. 32–35, Jul 1996.

[17] M. G. Mayer, "On closed shells in nuclei," *Physical Review*, vol. 74, pp. 235–239, Aug 1948.

[18] O. Haxel, J. H. D. Jensen, and H. E. Suess, "On the "magic numbers" in nuclear structure," *Physical Review*, vol. 75, pp. 1766–1766, Jun 1949.

[19] M. G. Mayer, "Nuclear configurations in the spin-orbit coupling model. i. empirical evidence," *Physical Review*, vol. 78, pp. 16–21, April 1950.

[20] M. G. Mayer, "Nuclear configurations in the spin-orbit coupling model. ii. theoretical considerations," *Physical Review*, vol. 78, pp. 22–23, April 1950.

[21] M. G. Mayer and J. H. D. Jensen, *Elementary Theory of Nuclear Shell Structure*. New York: John Wiley & Sons.

[22] A. Bohr and B. R. Mottelson, "Collective and individual-particle aspects of nuclear structure," *Det Kongelige Danske Videnskabernes Selskab: Matematisk-fysiske Meddeleser*, vol. 27, no. 16, 1953.

[23] A. Bohr and B. R. Mottelson, *Nuclear Structure*. New York: W. A. Benjamin Inc., 1975.

[24] R. B. Firestone, *Table of Isotopes*, vol. II: $A = 151 - 272$. New York: John Wiley & Sons, Inc., eighth ed., 1996.

[25] R. Shankar, *Principles of Quantum Mechanics*. New York: Springer, 2nd ed., 1980.

[26] G. E. Brown, J. A. Evans, and D. J. Thouless, "Vibrations of spherical nuclei," *Nuclear Physics*, vol. 24, no. 1, pp. 1 – 17, 1961.

[27] J. D. Jackson, *Classical Electrodynamics*. John Wiley & Sons, Inc., 3rd ed., 1999.

[28] H. Frauenfelder, R. M. Steffen, S. R. de Groot, H. A. Tolhoek, and W. J. Huiskamp, "Angular distribution of nuclear radiation," in *Alpha-, Beta- and Gamma-Ray Spec-*

troscopy (K. Siegbahn, ed.), vol. II, ch. XIX, pp. 997–1195, North-Holland Publishing Company, 1965.

[29] Y. X. Luo, J. O. Rasmussen, A. V. Ramayya, J. H. Hamilton, X. Q. Zhang, J. K. Hwang, C. J. Beyer, J. Kormicki, G. M. Ter-Akopian, Y. T. Oganessian, A. V. Daniel, K. E. Gregorich, T. N. Ginter, P. Zielinski, C. M. Folden, I. Y. Lee, P. Fallon, A. Macchiavelli, R. Donangelo, M. A. Stoyer, S. Asztalos, and S. C. Wu, "Fission γ spectra and levels in ^{139}Ba," *Physical Review C*, vol. 64, p. 054306, Oct 2001.

[30] L. P. Ekström, "Delta - a computer program to analyze gamma-gamma angular correlations from unaligned states," *Computer Physics Communications*, vol. 34, pp. 399–411, 1984.

[31] A. V. Daniel, C. Goodin, K. Li, A. V. Ramayya, N. J. Stone, J. K. Hwang, J. H. Hamilton, J. R. Stone, Y. X. Luo, J. O. Rasmussen, M. A. Stoyer, S. J. Zhu, G. M. Ter-Akopian, and I. Y. Lee, "Technique for measuring angular correlations and g-factors of excited states with large multi-detector arrays: An application to neutron rich nuclei produced by the spontaneous fission of ^{252}Cf," *Nuclear Instruments and Methods in Physics Research Section B: Beam Interactions with Materials and Atoms*, vol. 262, no. 2, pp. 399–406, 2007.

[32] N. Brewer, *Measurements from the Prompt and Delayed Radiation of Fission Fragments: Deformation Properties of Neutron Rich Nuclei*. PhD thesis, Vanderbilt University, Nashville, TN, 2013.

[33] M. F. Alshudifat, R. Grzywacz, M. Madurga, C. J. Gross, K. P. Rykaczewski, J. C. Batchelder, C. Bingham, I. N. Borzov, N. T. Brewer, L. Cartegni, A. Fijałkowska, J. H. Hamilton, J. K. Hwang, S. V. Ilyushkin, C. Jost, M. Karny, A. Korgul, W. Królas, S. H. Liu, C. Mazzocchi, A. J. Mendez, K. Miernik, D. Miller, S. W. Padgett, S. V. Paulauskas, A. V. Ramayya, D. W. Stracener, R. Surman, J. A. Winger,

M. Woli ńska Cichocka, and E. F. Zganjar, "Reexamining gamow-teller decays near ^{78}Ni," *Physical Review C*, vol. 93, p. 044325, Apr 2016.

[34] Y. Liu, C. U. Jost, A. J. M. II, D. W. Stracener, C. L. Williams, C. J. Gross, R. K. Grzywacz, M. Madurga, K. Miernik, D. Miller, S. Padgett, S. V. Paulauskas, K. P. Rykaczewski, and M. Wolinska-Cichocka, "On-line commissioning of the hribf resonant ionization laser ion source," *Nuclear Instruments and Methods in Physics Research Section B: Beam Interactions with Materials and Atoms*, vol. 298, pp. 5 – 12, 2013.

[35] K. Rykaczewski and R. Grzywacz, "UTK | Nuclear | LeRIBSS." URL: http://www.phys.utk.edu/expnuclear/LeRIBSS.html. Accessed June 25, 2019.

[36] URL: https://www.phy.ornl.gov/hribf/equipment/leribss/. Requires ORNL Login Credentials, but seems to be the standard citation in the literature for LeRIBSS. Access Attempted on June 29, 2019.

[37] H. W. Taylor, B. Singh, F. S. Prato, and R. McPherson, "A tabulation of gamma-gamma directional-correlation coefficients," *Nuclear Data Tables*, vol. A9, pp. 1–83, 1971.

[38] G. N. Rao, "Table of hyperfine fields for impurities in Fe, Co, Ni, Gd and Cr," *Hyperfine Interactions*, vol. 26, no. 1-4, pp. 1119–1193, 1985.

[39] D. De Frenne, "Nuclear data sheets for A = 102," *Nuclear Data Sheets*, vol. 110, no. 8, pp. 1745–1915, 2009.

[40] J. Blachot, "Nuclear data sheets for A = 104," *Nuclear Data Sheets*, vol. 108, no. 10, pp. 2035–2172, 2007.

[41] D. De Frenne and A. Negret, "Nuclear data sheets for A = 106," *Nuclear Data Sheets*, vol. 109, no. 4, pp. 943–1102, 2008.

[42] J. Blachot, "Nuclear data sheets for A = 108," *Nuclear Data Sheets*, vol. 91, no. 2, pp. 135–296, 2000.

[43] G. Gürdal and F. G. Kondev, "Nuclear data sheets for A = 110," *Nuclear Data Sheets*, vol. 113, no. 5, pp. 1315–1561, 2012.

[44] S. Lalkovski and F. G. Kondev, "Nuclear data sheets for A = 112," *Nuclear Data Sheets*, vol. 124, pp. 157–412, 2015.

[45] J. Blachot, "Nuclear data sheets for A = 114," *Nuclear Data Sheets*, vol. 113, no. 2, pp. 515–714, 2012.

[46] J. Blachot, "Nuclear data sheets for A = 116," *Nuclear Data Sheets*, vol. 111, no. 3, pp. 717–895, 2010.

[47] S. K. Chamoli, A. E. Stuchbery, S. Frauendorf, J. Sun, Y. Gu, R. F. Leslie, P. T. Moore, A. Wakhle, M. C. East, T. Kibédi, and A. N. Wilson, "Measured g factors and the tidal-wave description of transitional nuclei near $A = 100$," *Physical Review C*, vol. 83, p. 054318, May 2011.

[48] A. G. Smith, D. Patel, G. S. Simpson, R. M. Wall, J. F. Smith, O. J. Onakanmi, I. Ahmad, J. P. Greene, M. P. Carpenter, T. Lauritsen, C. J. Lister, R. V. F. Janssens, F. G. Kondev, D. Seweryniak, B. J. P. Gall, O. Dorvaux, and B. Roux, "The influence of $\nu h_{11/2}$ occupancy on the magnetic moments of collective 2_1^+ states in $A \sim 100$ fission fragments," *Physics Letters B*, vol. 591, no. 1, pp. 55 – 60, 2004.

[49] A. G. Smith, R. Orlandi, D. Patel, G. S. Simpson, R. M. Wall, J. F. Smith, O. J. Onakanmi, I. Ahmad, J. P. Greene, M. P. Carpenter, T. Lauritsen, C. J. Lister, R. V. F. Janssens, F. G. Kondev, D. Seweryniak, B. J. P. Gall, O. Dorvaux, and B. Roux, "The magnetic properties of collective states in $A \sim 100$ fission fragments," *Journal of Physics G: Nuclear and Particle Physics*, vol. 31, pp. S1433–S1438, Sep 2005.

[50] S.-J. Zhu, J. H. Hamilton, A. V. Ramayya, J. K. Hwang, J. O. Rasmussen, Y. X. Luo, K. Li, J.-G. Wang, X.-L. Che, H.-B. Ding, S. Frauendorf, V. Dimitrov, X. Qiang, G. Long, and Y.-Y. Yang, "Search for chiral bands in $A \sim 110$ neutron-rich nuclei," *Chinese Physics C*, vol. 33, pp. 145–147, Mar 2009.

[51] E. Wang, J. Hamilton, G. Bhat, S. Jehangir, J. Sheikh, A. V. Ramayya, C. J. Zachary, J. M. Eldridge, B. Musangu, Y. Luo, J. Rasmussen, S. J. Zhu, G. Ter-Akopian, and Y. Oganessian, "Identification of β and γ vibrational bands in ^{102}Mo," in *85th Annual Meeting of the APS Southeastern Section*, Nov 2018.

[52] E. F. Jones, P. M. Gore, S. J. Zhu, J. H. Hamilton, A. V. Ramayya, J. K. Hwang, R. Q. Xu, L. M. Yang, K. Li, Z. Jiang, Z. Zhang, S. D. Xiao, X. Q. Zhang, W. C. Ma, J. D. Cole, M. W. Drigert, I. Y. Lee, J. O. Rasmussen, Y. X. Luo, and M. A. Stoyer, "Collective bands in ^{104,106,108}Mo," *Physics of Atomic Nuclei*, vol. 69, pp. 1198–1203, Jul 2006.

[53] B. Musangu, E. H. Wang, J. H. Hamilton, S. Frauendorf, C. J. Zachary, J. M. Eldridge, A. V. Ramayya, W. H. Brantley, J. O. Rasmussen, Y. X. Luo, G. M. Ter-Akopian, Y. T. Oganessian, and S. J. Zhu, "Chiral vibrations and collective bands in ^{104}Mo," in *Proceedings of the Sixth International Conference on Fission and Properties of Neutron-Rich Nuclei* (J. H. Hamilton, A. V. Ramayya, and P. Talou, eds.), (Singapore), pp. 255–259, World Scientific, 2017.

[54] H. B. Ding, S. J. Zhu, J. H. Hamilton, A. V. Ramayya, J. K. Hwang, Y. X. Luo, J. O. Rasmussen, I. Y. Lee, X. L. Che, J. G. Wang, and Q. Xu, "Collective band structures in neutron-rich ^{108}Mo nucleus," *Chinese Physics Letters*, vol. 24, pp. 1517–1520, Jun 2007.

[55] Y. X. Luo, S. J. Zhu, J. H. Hamilton, A. V. Ramayya, C. Goodin, K. Li, X. L. Che, J. K. Hwang, I. Y. Lee, Z. Jiang, G. M. Ter-Akopian, A. V. Daniel, M. A. Stoyer,

R. Donangelo, S. Frauendorf, V. Dimitrov, J. Y. Zhang, J. D. Cole, N. J. Stone, and J. O. Rasmussen, "Odd-parity bands of ^{108,110,112}Ru," *International Journal of Modern Physics E*, vol. 18, no. 08, pp. 1697–1716, 2009.

[56] S. J. Zhu, Y. X. Luo, J. H. Hamilton, A. V. Ramayya, X. L. Che, Z. Jiang, J. K. Hwang, J. L. Wood, M. A. Stoyer, R. Donangelo, J. D. Cole, C. Goodin, and J. O. Rasmussen, "Even-parity bands of ^{108,110,112}Ru," *International Journal of Modern Physics E*, vol. 18, no. 08, pp. 1717–1739, 2009.

[57] Y. Luo, J. Rasmussen, J. Hamilton, A. Ramayya, S. Frauendorf, J. Hwang, N. Stone, S. Zhu, N. Brewer, E. Wang, I. Lee, S. Liu, G. TerAkopian, A. Daniel, Y. Oganessian, M. Stoyer, R. Donangelo, W. Ma, J. Cole, Y. Shi, and F. Xu, "New insights into the nuclear structure in neutron-rich ^{112,114,115,116,117,118}Pd," *Nuclear Physics A*, vol. 919, pp. 67 – 98, 2013.

[58] J. M. Eldridge, B. Fenker, J. H. Hamilton, C. Goodin, C. J. Zachary, E. Wang, A. V. Ramayya, A. V. Daniel, G. M. Ter-Akopian, Y. T. Oganessian, Y. X. Luo, J. O. Rasmussen, and S. J. Zhu, "E2/M1 mixing ratios in transitions from the gamma vibrational bands to the ground state rotational bands of ^{102,104,106,108}Mo, ^{108,110,112}Ru, and ^{112,114,116}Pd," *The European Physical Journal A*, vol. 54, p. 15, Feb 2018.

[59] A. Osa, S. ichi Ichikawa, M. Matsuda, T. K. Sato, and S.-C. Jeong, "Ion source development for the on-line isotope separator at JAEA," *Nuclear Instruments and Methods in Physics Research Section B: Beam Interactions with Materials and Atoms*, vol. 266, no. 19, pp. 4394 – 4397, 2008. Proceedings of the XVth International Conference on Electromagnetic Isotope Separators and Techniques Related to their Applications.

[60] D. Nagae, T. Ishii, R. Takahashi, M. Asai, H. Makii, A. Osa, T. K. Sato, S. Ichikawa, Y. R. Shimizu, and T. Shoji, "Lifetime measurements for the first 2^+ states in

^{162,164}Gd populated by the β decay of ^{162,164}Eu," *AIP Conference Proceedings*, vol. 1224, no. 1, pp. 156–160, 2010.

[61] B. Singh and J. Chen, "Nuclear data sheets for $A = 164$," *Nuclear Data Sheets*, vol. 147, pp. 1 – 381, 2018.

[62] A. Etilé, D. Verney, N. N. Arsenyev, J. Bettane, I. N. Borzov, M. Cheikh Mhamed, P. V. Cuong, C. Delafosse, F. Didierjean, C. Gaulard, N. Van Giai, A. Goasduff, F. Ibrahim, K. Kolos, C. Lau, M. Niikura, S. Roccia, A. P. Severyukhin, D. Testov, S. Tusseau-Nenez, and V. V. Voronov, "Low-lying intruder and tensor-driven structures in ^{82}As revealed by β decay at a new movable-tape-based experimental setup," *Physical Review C*, vol. 91, p. 064317, Jun 2015.

[63] P. Hoff and B. Fogelberg, "Properties of strongly neutron-rich isotopes of germanium and arsenic," *Nuclear Physics A*, vol. 368, no. 2, pp. 210 – 236, 1981.

[64] K. Miernik, K. P. Rykaczewski, C. J. Gross, R. Grzywacz, M. Madurga, D. Miller, J. C. Batchelder, N. T. Brewer, C. U. Jost, K. Kolos, A. Korgul, C. Mazzocchi, A. J. Mendez, Y. Liu, S. V. Paulauskas, D. W. Stracener, J. A. Winger, M. Woli ńska Cichocka, and E. F. Zganjar, "Excited states in ^{82}As studied in the decay of ^{82}Ge," *Physical Review C*, vol. 90, p. 034311, Sep 2014.

[65] S. Padgett, M. Madurga, R. Grzywacz, I. G. Darby, S. N. Liddick, S. V. Paulauskas, L. Cartegni, C. R. Bingham, C. J. Gross, K. Rykaczewski, D. Shapira, D. W. Stracener, A. J. Mendez, J. A. Winger, S. V. Ilyushkin, A. Korgul, W. Królas, E. Zganjar, C. Mazzocchi, S. Liu, J. H. Hamilton, J. C. Batchelder, and M. M. Rajabali, "β decay of ^{81}Zn and migrations of states observed near the $n = 50$ closed shell," *Physical Review C*, vol. 82, p. 064314, Dec 2010.

[66] C. M. Baglin, "Nuclear data sheets for $A = 81$," *Nuclear Data Sheets*, vol. 109, no. 10, pp. 2257 – 2437, 2008.

[67] J. K. Tuli and E. Browne, "Nuclear data sheets for $A = 82$," *Nuclear Data Sheets*, vol. 157, pp. 260 – 494, 2019.

[68] S. E. Arnell, R. Hardell, A. Hasselgren, L. Jonsson, and Ö. Skeppstedt, "Thermal neutron capture gammas measured with Ge(Li)-spectrometers and internal reactor targets," *Nuclear Instruments and Methods*, vol. 54, no. 2, pp. 165 – 180, 1967.

[69] V. Corcalciuc, B. Holmqvist, A. Marcinkowski, and G. A. Prokopets, "A study of the neutron induced reactions for ^{19}F, ^{56}Fe and ^{59}Co in the energy interval 16 to 22 MeV," *Nuclear Physics A*, vol. 307, no. 3, pp. 445 – 471, 1978.

[70] R. G. Helmer and C. van der Leun, "Recommended standards for γ-ray energy calibration (1999)," *Nuclear Instruments and Methods in Physics Research Section A: Accelerators, Spectrometers, Detectors and Associated Equipment*, vol. 450, no. 1, pp. 35 – 70, 2000.

[71] M. A. Hammed, I. M. Lowles, and T. D. Mac Mahon, "Decay scheme data for ^{154}Eu, ^{198}Au and ^{239}Np," *Nuclear Instruments and Methods in Physics Research Section A: Accelerators, Spectrometers, Detectors and Associated Equipment*, vol. 312, no. 1, pp. 308 – 316, 1992.

[72] Federal Radiological Monitoring and Assessment Center, Sandia National Laboratories, Albuquerque, NM, *FRMAC Gamma Spectroscopist Knowledge Guide*, 2019.

[73] L.-C. He, Y. Zheng, L.-H. Zhu, H.-L. Ma, X.-G. Wu, C.-Y. He, G.-S. Li, L.-L. Wang, X. Hao, Y. Liu, X.-Q. Li, B. Pan, Z.-Y. Li, and H.-B. Ding, "Collective states and shape competition in ^{126}Te," *Chinese Physics C*, vol. 41, p. 044003, Apr 2017.

[74] J. Katakura and K. Kitao, "Nuclear data sheets for A = 126," *Nuclear Data Sheets*, vol. 97, no. 3, pp. 765 – 926, 2002.

[75] M. Martin, "Nuclear data sheets for $A = 208$," *Nuclear Data Sheets*, vol. 108, no. 8, pp. 1583 – 1806, 2007.

[76] E. W. Schneider, M. D. Glascock, W. B. Walters, and R. A. Meyer, "Radioactive decay of 1.7-h ^{149}Nd to levels of transitional ^{149}Pm," *Zeitschrift für Physik A Atoms and Nuclei*, vol. 291, pp. 77–86, Mar 1979.

[77] J. H. Scofield, "Exchange corrections of K x-ray emission rates," *Physical Review A*, vol. 9, pp. 1041–1049, Mar 1974.

[78] E. Sakar, A. Gurol, and A. Bastug, "Experimental K X-ray intensity ratios of some heavy elements," *Radiation Physics and Chemistry*, vol. 131, pp. 105 – 107, 2017.

[79] Z. Patel, P. M. Walker, Z. Podolyák, P. H. Regan, T. A. Berry, P.-A. Söderström, H. Watanabe, E. Ideguchi, G. S. Simpson, S. Nishimura, Q. Wu, F. R. Xu, F. Browne, P. Doornenbal, G. Lorusso, S. Rice, L. Sinclair, T. Sumikama, J. Wu, Z. Y. Xu, N. Aoi, H. Baba, F. L. Bello Garrote, G. Benzoni, R. Daido, Z. Dombrádi, Y. Fang, N. Fukuda, G. Gey, S. Go, A. Gottardo, N. Inabe, T. Isobe, D. Kameda, K. Kobayashi, M. Kobayashi, T. Komatsubara, I. Kojouharov, T. Kubo, N. Kurz, I. Kuti, Z. Li, M. Matsushita, S. Michimasa, C.-B. Moon, H. Nishibata, I. Nishizuka, A. Odahara, E. Şahin, H. Sakurai, H. Schaffner, H. Suzuki, H. Takeda, M. Tanaka, J. Taprogge, Z. Vajta, A. Yagi, and R. Yokoyama, "Isomer-delayed γ-ray spectroscopy of $A = 159 - 164$ midshell nuclei and the variation of K-forbidden $E1$ transition hindrance factors," *Physical Review C*, vol. 96, p. 034305, Sep 2017.

[80] R. Yokoyama, S. Go, D. Kameda, T. Kubo, N. Inabe, N. Fukuda, H. Takeda, H. Suzuki, K. Yoshida, K. Kusaka, K. Tanaka, Y. Yanagisawa, M. Ohtake, H. Sato, Y. Shimizu, H. Baba, M. Kurokawa, D. Nishimura, T. Ohnishi, N. Iwasa, A. Chiba, T. Yamada, E. Ideguchi, T. Fujii, H. Nishibata, K. Ieki, D. Murai, S. Momota, Y. Sato, J. W. Hwang, S. Kim, O. B. Tarasov, D. J. Morrissey, B. M. Sherrill,

G. Simpson, and C. R. Praharaj, "New k isomers in the neutron-rich $n = 100$ isotones ^{162}Sm,^{163}Eu, and ^{164}Gd," *Physical Review C*, vol. 95, p. 034313, Mar 2017.

[81] J. Wu, S. Nishimura, G. Lorusso, P. Möller, E. Ideguchi, P.-H. Regan, G. S. Simpson, P.-A. Söderström, P. M. Walker, H. Watanabe, Z. Y. Xu, H. Baba, F. Browne, R. Daido, P. Doornenbal, Y. F. Fang, N. Fukuda, G. Gey, T. Isobe, Z. Korkulu, P. S. Lee, J. J. Liu, Z. Li, Z. Patel, V. Phong, S. Rice, H. Sakurai, L. Sinclair, T. Sumikama, M. Tanaka, A. Yagi, Y. L. Ye, R. Yokoyama, G. X. Zhang, D. S. Ahn, T. Alharbi, N. Aoi, F. L. Bello Garrote, G. Benzoni, A. M. Bruce, R. J. Carroll, K. Y. Chae, Z. Dombradi, A. Estrade, A. Gottardo, C. J. Griffin, N. Inabe, D. Kameda, H. Kanaoka, I. Kojouharov, F. G. Kondev, T. Kubo, S. Kubono, N. Kurz, I. Kuti, S. Lalkovski, G. J. Lane, E. J. Lee, T. Lokotko, G. Lotay, C.-B. Moon, D. Murai, H. Nishibata, I. Nishizuka, C. R. Nita, A. Odahara, Z. Podolyák, O. J. Roberts, H. Schaffner, C. Shand, Y. Shimizu, H. Suzuki, H. Takeda, J. Taprogge, S. Terashima, Z. Vajta, and S. Yoshida, "94 β-decay half-lives of neutron-rich $_{55}$Cs to $_{67}$Ho: Experimental feedback and evaluation of the r-process rare-earth peak formation," *Physical Review Lett.*, vol. 118, p. 072701, Feb 2017.

[82] R. A. Anderl and R. C. Greenwood, "Nuclear decay studies of fission-product nuclides using an on-line mass separation technique," *Journal of Radioanalytical and Nuclear Chemistry*, vol. 142, pp. 203–213, Sep 1990.

[83] M. Emeric and A. Sonzogni, "LOGFT." available on the National Nuclear Data Center website at https://www.nndc.bnl.gov/logft/.

[84] B. C. Rasco, M. Wolińska-Cichocka, A. Fijałkowska, K. P. Rykaczewski, M. Karny, R. K. Grzywacz, K. C. Goetz, C. J. Gross, D. W. Stracener, E. F. Zganjar, J. C. Batchelder, J. C. Blackmon, N. T. Brewer, S. Go, B. Heffron, T. King, J. T. Matta, K. Miernik, C. D. Nesaraja, S. V. Paulauskas, M. M. Rajabali, E. H. Wang, J. A. Winger, Y. Xiao, and C. J. Zachary, "Decays of the three top contributors to the re-

actor $\overline{\nu}_e$ high-energy spectrum, ^{92}Rb, ^{96gs}Y, and ^{142}Cs, studied with total absorption spectroscopy," *Physical Review Letters*, vol. 117, p. 092501, Aug 2016.

[85] H. Hayashi, M. Shibata, M. Asai, A. Osa, T. Sato, M. Koizumi, A. Kimura, and M. Oshima, "Performance of a total absorption clover detector for Q_β measurements of neutron-rich nuclei far from the β-stability line," *Nuclear Instruments and Methods in Physics Research Section A: Accelerators, Spectrometers, Detectors and Associated Equipment*, vol. 747, pp. 41 – 51, 2014.

[86] D. J. Hartley, F. G. Kondev, R. Orford, J. A. Clark, G. Savard, A. D. Ayangeakaa, S. Bottoni, F. Buchinger, M. T. Burkey, M. P. Carpenter, P. Copp, D. A. Gorelov, K. Hicks, C. R. Hoffman, C. Hu, R. V. F. Janssens, J. W. Klimes, T. Lauritsen, J. Sethi, D. Seweryniak, K. S. Sharma, H. Zhang, S. Zhu, and Y. Zhu, "Masses and β-decay spectroscopy of neutron-rich odd-odd ^{160,162}Eu nuclei: Evidence for a subshell gap with large deformation at $N = 98$," *Physical Review Letters*, vol. 120, p. 182502, May 2018.

[87] B. Singh and Z. Hu, "Nuclear data sheets for A = 98," *Nuclear Data Sheets*, vol. 98, no. 2, pp. 335 – 513, 2003.

[88] S. R. Lesher, C. Casarella, A. Aprahamian, L. M. Robledo, B. P. Crider, R. Ikeyama, I. R. Marsh, M. T. McEllistrem, E. E. Peters, F. M. Prados-Estévez, M. K. Smith, Z. R. Tully, J. R. Vanhoy, and S. W. Yates, "Lifetime measurements of low-spin negative-parity levels in ^{160}Gd," *Physical Review C*, vol. 95, p. 064309, Jun 2017.

[89] C. W. Reich, "Nuclear data sheets for $A = 160$," *Nuclear Data Sheets*, vol. 105, no. 3, pp. 557 – 774, 2005.

[90] Z. Patel, P.-A. Söderström, Z. Podolyák, P. H. Regan, P. M. Walker, H. Watanabe, E. Ideguchi, G. S. Simpson, H. L. Liu, S. Nishimura, Q. Wu, F. R. Xu, F. Browne, P. Doornenbal, G. Lorusso, S. Rice, L. Sinclair, T. Sumikama, J. Wu, Z. Y. Xu,

N. Aoi, H. Baba, F. L. Bello Garrote, G. Benzoni, R. Daido, Y. Fang, N. Fukuda, G. Gey, S. Go, A. Gottardo, N. Inabe, T. Isobe, D. Kameda, K. Kobayashi, M. Kobayashi, T. Komatsubara, I. Kojouharov, T. Kubo, N. Kurz, I. Kuti, Z. Li, M. Matsushita, S. Michimasa, C.-B. Moon, H. Nishibata, I. Nishizuka, A. Odahara, E. Şahin, H. Sakurai, H. Schaffner, H. Suzuki, H. Takeda, M. Tanaka, J. Taprogge, Z. Vajta, A. Yagi, and R. Yokoyama, "Isomer decay spectroscopy of ^{164}Sm and ^{166}Gd: Midshell collectivity around $N = 100$," *Physical Review Letters*, vol. 113, p. 262502, Dec 2014.

[91] E. F. Jones, J. H. Hamilton, P. M. Gore, A. V. Ramayya, J. K. Hwang, A. P. deLima, S. J. Zhu, Y. X. Luo, C. J. Beyer, J. Kormicki, X. Q. Zhang, W. C. Ma, I. Y. Lee, J. O. Rasmussen, S. C. Wu, T. N. Ginter, P. Fallon, M. Stoyer, J. D. Cole, A. V. Daniel, G. M. Ter-Akopian, R. Donangelo, S. J. Asztalos, T. Cornelius, P. Fleischer, M. Bender, T. Bürvenich, S. Schramm, J. A. Maruhn, and P.-G. Reinhard, "Identification of levels in ^{162,164}Gd and decrease in moment of inertia between $N = 98 - 100$," *Journal of Physics G: Nuclear and Particle Physics*, vol. 30, pp. L43–L48, Oct 2004.

[92] E. F. Jones, J. H. Hamilton, P. M. Gore, A. V. Ramayya, J. K. Hwang, and A. P. deLima, "Identification of levels in ^{162,164}Gd and decrease in moment of inertia between $N = 98 - 100$," *The European Physical Journal A - Hadrons and Nuclei*, vol. 25, pp. 467–468, Sep 2005.

[93] L. Gaudefroy, S. Péru, N. Arnal, J. Aupiais, J.-P. Delaroche, M. Girod, and J. Libert, "Impact of coriolis mixing on a two-quasi-neutron isomer in ^{164}Gd$_{100}$ and other $N = 100$ isotones," *Physical Review C*, vol. 97, p. 064317, Jun 2018.

[94] T. K. Sato, A. Osa, K. Tsukada, M. Asai, H. Hayashi, Y. Kojima, M. Shibata, and S. Ichikawa, "Decay studies of new neutron-rich isotopes ^{163,164,165}Eu," *JAEA-Review*, vol. 029, p. 31, 2006.

[95] C. J. Zachary, *New Insights into the Structure of Neutron Rich Nuclei ^{157}Sm, ^{163}Gd, and ^{163}Tb*. PhD thesis, Vanderbilt University, Nashville, TN, 2019.

[96] C. J. Zachary, N. T. Brewer, J. C. Batchelder, E. Wang, J. H. Hamilton, J. M. Eldridge, B. M. Musangu, A. V. Ramayya, C. J. Gross, K. P. Rykaczewski, R. Grzywacz, M. Madurga, D. Miller, D. W. Stracener, C. Jost, E. F. Zganjar, J. A. Winger, M. Karny, S. V. Paulauskas, S. H. Liu, M. Wolińska-Cichocka, S. W. Padgett, T. Mendez, K. Miernik, A. Fijałkowska, S. V. Ilyushkin, A. C. Dai, F. R. Xu, Y. X. Liu, and Y. Sun, "Identification of new transitions and levels in ^{163}Gd from β decay studies." unpublished.

[97] M. B. Chadwick, M. Herman, P. Obložinský, M. E. Dunn, Y. Danon, A. C. Kahler, D. L. Smith, B. Pritychenko, G. Arbanas, R. Arcilla, R. Brewer, D. A. Brown, R. Capote, A. D. Carlson, Y. S. Cho, H. Derrien, K. Guber, G. M. Hale, S. Hoblit, S. Holloway, T. D. Johnson, T. Kawano, B. C. Kiedrowski, H. Kim, S. Kunieda, N. M. Larson, L. Leal, J. P. Lestone, R. C. Little, E. A. McCutchan, R. E. MacFarlane, M. MacInnes, C. M. Mattoon, R. D. McKnight, S. F. Mughabghab, G. P. A. Nobre, G. Palmiotti, A. Palumbo, M. T. Pigni, V. G. Pronyaev, R. O. Sayer, A. A. Sonzogni, N. C. Summers, P. Talou, I. J. Thompson, A. Trkov, R. L. Vogt, S. C. van der Marck, A. Wallner, M. C. White, D. Wiarda, and P. G. Young, "ENDF/B-VII.1 nuclear data for science and technology: Cross sections, covariances, fission product yields and decay data," *Nuclear Data Sheets*, vol. 112, no. 12, pp. 2887 – 2996, 2011. Special Issue on ENDF/B-VII.1 Library.

[98] R. K. Sheline, W. N. Shelton, H. T. Motz, and R. E. Carter, "Energy levels of Dy^{165}," *Physical Review*, vol. 136, pp. B351–B365, Oct 1964.

[99] R. C. Greenwood, R. J. Gehrke, J. D. Baker, D. H. Meikrantz, and C. W. Reich, "Identification of a new isotope, ^{165}Tb," *Physical Review C*, vol. 27, pp. 1266–1270, Mar 1983.

[100] E. Kaerts, P. van Assche, S. Kerr, F. Hoyler, H. BÃűrner, R. Casten, and D. Warner, "A study of the low-energy level structure of ^{165}Dy," *Nuclear Physics A*, vol. 514, no. 2, pp. 173 – 224, 1990.

[101] J. K. Hwang, A. V. Ramayya, J. H. Hamilton, K. Li, C. Goodin, Y. X. Luo, J. O. Rasmussen, and S. J. Zhu, "High spin states in ^{153}Nd and first identification of excited states in ^{155}Nd," *Physical Review C*, vol. 78, p. 014309, Jul 2008.

[102] G. S. Simpson, W. Urban, J. A. Pinston, J. C. Angelique, I. Deloncle, H. R. Faust, J. Genevey, U. Köster, T. Materna, R. Orlandi, A. Scherillo, A. G. Smith, J. F. Smith, T. Rząca-Urban, I. Ahmad, and J. P. Greene, "Near-yrast structure of $N = 93$ neutron-rich lanthanide nuclei," *Physical Review C*, vol. 81, p. 024313, Feb 2010.

[103] C. J. Zachary, E. H. Wang, N. T. Brewer, J. H. Hamilton, *et al.*, "New analysis of ^{167,169}Sm from ^{252}Cf spontaneous fission." unpublished, currently sitting in our level scheme book and awaiting publication, likely with Chris as first author.

[104] J. K. Hwang, A. V. Ramayya, J. H. Hamilton, S. H. Liu, N. T. Brewer, Y. X. Luo, J. O. Rasmussen, S. J. Zhu, and R. Donangelo, "High spin states in ^{151,153}Pr, ^{157}Sm, and ^{93}Kr," *Physical Review C*, vol. 82, p. 034308, Sep 2010.

[105] W. Urban, J. A. Pinston, G. S. Simpson, A. G. Smith, J. F. Smith, T. Rząca-Urban, and I. Ahmad, "The $11/2^-[505]$ neutron extruder orbital in ^{159}Sm," *Physical Review C*, vol. 80, p. 037301, Sep 2009.

[106] S. Yamada, A. Taniguchi, Y. Toh, and K. Okano, "A new isomeric state in ^{153}Nd," *Journal of the Physical Society of Japan*, vol. 65, no. 10, pp. 3390–3391, 1996.

[107] B. M. Musangu, A. H. Thibeault, T. H. Richards, E. H. Wang, J. H. Hamilton, C. J. Zachary, J. M. Eldridge, A. V. Ramayya, Y. X. Luo, J. O. Rasmussen, G. M. Ter-Akopian, Y. T. Oganessian, and S. J. Zhu, "Anomalous neutron yields confirmed for

Ba-Mo and newly observed for Ce-Zr from spontaneous fission of ^{252}Cf," *Physical Review C*, vol. 101, p. 034610, Mar 2020.

[108] D. G. Burke, G. Løvhøiden, E. R. Flynn, and J. W. Sunier, "Single-proton states in ^{157}Eu and ^{159}Eu studied with the $(\vec{t},\alpha)$ reaction," *Nuclear Physics A*, vol. 318, no. 1, pp. 77 – 96, 1979.

[109] N. Nica, "Nuclear data sheets for $A = 157$," *Nuclear Data Sheets*, vol. 132, pp. 1 – 256, 2016.

[110] H. Willmes, R. A. Anderl, J. D. Cole, R. C. Greenwood, and C. W. Reich, "Level structure of ^{159}Eu from the β^- decay of the recently discovered isotope ^{159}Sm," *Physical Review C*, vol. 36, pp. 1540–1545, Oct 1987.

[111] R. K. Pandit, B. Slathia, R. Devi, and S. K. Khosa, "Study of rotational bands and electromagnetic properties of odd mass $^{153-159}$Eu," *International Journal of Modern Physics E*, vol. 26, no. 06, p. 1750040, 2017.

[112] R. K. Pandit, R. Devi, S. K. Khosa, G. H. Bhat, and J. A. Sheikh, "A systematic study of band structure and electromagnetic properties of neutron rich odd mass Eu isotopes in the projected shell model framework," *The European Physical Journal A*, vol. 53, p. 201, Oct 2017.

[113] B. M. Nyakó, J. Timár, M. Csatlós, Z. Dombrádi, A. Krasznahorkay, I. Kuti, D. Sohler, T. G. Tornyi, M. Czerwiński, T. Rząca-Urban, W. Urban, P. Bączyk, L. Atanasova, D. L. Balabanski, K. Sieja, A. Blanc, M. Jentschel, U. Köster, P. Mutti, T. Soldner, G. de France, G. Simpson, and C. Ur, "Medium-spin states of the neutron-rich ^{87,89}Br isotopes: configurations and shapes," *Journal of Physics: Conference Series*, vol. 724, p. 012051, jun 2016.

[114] C. Ekström and L. Robertsson, "A direct determination of the nuclear ground-state spin of ^{156}Eu," *Zeitschrift für Physik A Atoms and Nuclei*, vol. 302, pp. 181–182, June 1981.

[115] R. G. Lanier, R. K. Sheline, G. L. Struble, L. G. Mann, and J. A. Cizewski, "The ^{154}Eu(t,p) reaction: Some new systematics in the N = 90 spherical-deformed transition region," *Nuclear Physics A*, vol. 413, no. 2, pp. 236 – 246, 1984.

[116] M. K. Balodis, N. D. Kramer, P. T. Prokofjev, A. V. Afanasjev, T. V. Guseva, J. J. Tambergs, K. Schreckenbach, W. F. Davidson, D. D. Warner, J. A. Pinston, P. H. M. V. Assche, and A. M. J. Spits, "Level structure of the odd-odd nucleus ^{156}Eu," *Nuclear Physics A*, vol. 523, no. 2, pp. 261 – 299, 1991.

[117] J. A. Sheikh and K. Hara, "Triaxial projected shell model approach," *Physical Review Letters*, vol. 82, pp. 3968–3971, May 1999.